An Experimental Investigation of Premixed Combustion in Extreme Turbulence

by

Timothy Michael Wabel

A dissertation submitted in partial fulfillment
Of the requirements for the degree of
Doctor of Philosophy
(Aerospace Engineering)
in the University of Michigan
2017

Doctoral Committee:

Professor James F. Driscoll, Chair
Assistant Professor Mirko Gamba
Assistant Professor Venkatramanan Raman
Professor Volker Sick

Timothy Michael Wabel

twabel@umich.edu

ORCID iD: 0000-0002-2360-5796

For my parents, who have always supported me

Acknowledgements

I can truly say that my time here at Michigan has provided some of the best moments of my life, and this is due largely to the people I have encountered along the way. I have had the incredible privilege to work with Professor Driscoll, and I will sure miss our weekly discussions about turbulence, combustion, and life. Prof. Driscoll has always provided sound guidance and direction, while also allowing a relatively free rein in the lab. I am deeply indebted to him for the countless resources he has provided. He will continue to be a role model, not just for how I conduct scientific research, but also for how I interact with and treat other people. I don't know how I got so lucky, but I could not have asked for a better advisor.

Professor Gamba has been an incredible resource during my time here, and I have greatly enjoyed our occasional discussions and ramblings about turbulence. I hope I can borrow some of his unique perspectives in problem solving. A big thank you also to Professors Venkat Raman and Volker Sick for serving on my thesis committee and being so generous with their time. Lastly, a special word of thanks to Dr. Jacob Temme, who was the ideal mentor to me when I started. For better or worse, I always ask myself "what would Jacob do?" whenever I approach a new problem. The tech staff has been exceptionally generous with their time and assistance, and I think I took more than my fair share from Tom, Aaron, Dave, and the late Marty Stenzel. Thank you all for keeping my lab running. Huge thanks also to Denise for helping me maneuver the bureaucracy of Rackham and keeping me on top of the various deadlines and requirements. Her relentless positivity kept me going on groggy
mornings.

The friends I have made at Michigan include some of the kindest and funniest people I have ever known. Drs. Patton Allison, Matt Fotia, and David Rosenberg provided excellent guidance to me when I first started. A big thanks to Kaihua Ding, Doreen Fang, Yuki

Shimizu, Steve Cast, Robin and Greg Hunt, Chris Marley, Chuky Mbagwu, Fabian Chacon, Jacob France, Yasin Abdul-Huda, and the late Abhinav Dasari for providing incredible mental and emotional support over the years. I will miss all of our late night pizza and karaoke sessions. Toronto has a lot to live up to. Last, but not least, thanks to my fiancée Soojin, who has been a rock for me through good times and bad.

TABLE OF CONTENTS

LIST OF FIGURES

LIST OF TABLES

ABSTRACT

An Experimental Investigation of Premixed Combustion in Extreme Turbulence

by

Timothy Michael Wabel

Chair: James F. Driscoll

This work has explored various aspects of high Reynolds number combustion that have received much previous speculation. A new high-Reynolds number premixed Bunsen burner, called Hi-Pilot, was designed to produce turbulence intensities in the extreme range of turbulence. The burner was modified several times in order to prevent boundary layer separation in the nozzle, and a large co-flow was designed that was capable of maintaining reactions over the entire flame surface. Velocity and turbulence characteristics were measured using a combination of Laser Doppler Velocimetry (LDV) and Particle Image Velocimetry (PIV). Flame structure was studied using a combination of formaldehyde (CH_2O), hydroxyl (OH), and the CH radical. Planar Laser Induced Fluorescence (PLIF). The spatial Overlap of formaldehyde and OH PLIF qualitatively measures the reaction rate between formaldehyde molecules and OH radicals, and is a measure of the reaction layers of the flame. CH PLIF provides an alternative measure of the reaction zone, and was measured to compare with the Overlap PLIF results. Reaction layers are the full-width at half-maximum of the Overlap or CH PLIF signal, and extinction events were defined as regions where the PLIF signal drops below this threshold. Preheat

structures were measured using formaldehyde PLIF, and are defined as beginning at 35% of the local maximum PLIF signal, and continue up to the leading edge of the reaction layer. Previous predictions of regime diagram boundaries were tested at the largest values of turbulent Reynolds number (Re_T) to date. The Overlap and CH PLIF diagnostics allowed extensive testing of the predicted broken reaction zones boundary of Peters. Measurements indicated that all run conditions are in the Broadened Preheat - Thin Reaction layers regime, but several conditions are expected to display a broken reaction zone structure. Therefore the work shows that Peters's predicted boundary is not correct, and therefore a Karlovitz number of 100 is not a valid criteria for broken reactions in the Bunsen geometry. Several measures of the turbulent burning velocity, including the global consumption speed and the extent of flamelet wrinkling, were measured at these conditions. Reaction layers for the burning velocity measurements were provided by the OH PLIF. The measurements showed that the global consumption speed continues to increase for all levels of turbulence intensity u'/S_L. In contrast, the flame surface wrinkling rapidly increases the flame surface area for $u'/S_L < 10$, but the flame surface area does not increase further at larger turbulence intensities. This indicates that the flame is not in the laminar flamelet regime, and the consumption rate per unit of flame surface area must be increased. The turbulent diffusivity is thought to be the mechanism enhancing the consumption rate, which is a scenario first hypothesized by Damköhler. The flame structure and burning velocity measurements motivated the measurements of the evolution of turbulence through regions of very thick preheat layers. This measurement utilized simultaneous PIV and formaldehyde PLIF in order to obtain conditioned statistics of the turbulence as a function of η, the distance from the reaction layer. Together, the results tell a consistent story, and deepen our understanding of premixed combustion at large Re_T.

CHAPTER 1

Introduction

1.1 Motivation

Modern power generation systems will continue to use combustion of fossil fuels for the foreseeable future. Despite growing progress in developing renewable energy sources, coal, petroleum, and natural gas still account for more than 75% of energy use in the United States [46]. Global energy demands grew substantially throughout the 20th century. For example, annual global consumption of fossil fuel rose from about 1 giga Ton in 1900 to 12 giga Tons in 2005 [65]. Needless to say, fossil fuel use has become a highly researched (and controversial) topic, and much of the work focuses on how to improve combustion efficiency and reduce harmful emissions (such as NO_x or unburnt hydrocarbons).

Design and optimization of combustion devices is typically performed using simulation tools such as computational fluid dynamics (CFD). There are many approaches to simulating combustion events, but two general categories are direct numerical simulations (DNS) and large eddy simulation (LES) [132]. DNS can directly compute the governing equations on a series of grid points that are spaced sufficiently close to resolve the smallest scales of the problem. Thus, DNS incorporates the full physics of the problem, and can produce exact solutions. Unfortunately, due to intensive computational costs, DNS domains are restricted to extremely small scales and fuel chemistry is often modeled using reduced chemical mechanisms. LES circumvents this problem by using a grid spacing large enough

to resolve the large scales of turbulence, where most of the kinetic energy is contained and where much of the "action" of turbulence resides (instabilities, mixing, etc.). The idea is that large scales of the flow generally depend upon the geometry of the system, while small scales are expected to be somewhat universal. In LES, all scales below the grid spacing cannot be directly resolved but are modeled. Because premixed combustion generally occurs at the smallest scales of turbulence [2], this means that combustion models must be used.

There are a large number of sub-grid scale combustion models for LES studies, but most models make assumptions of important flame characteristics given the turbulence conditions present. For instance, in weak-to-moderate turbulence, combustion can be expected to occur in thin, wrinkled sheets ("flamelets"), and therefore a flamelet sub-model would be used. Alternatively, to simulate Homogeneous Charge Compression Ignition (HCCI) engine conditions in the distributed reaction regime, a well-stirred sub-model (that might contain auto-ignition chemistry) would be a better choice [15]. Another fundamental combustion quantity, the turbulent burning velocity, will also vary depending on the model used. In order to obtain and apply correct models, we need to have an idea of how the flame behaves under various regimes.

Typically, boundaries between the different regimes of premixed combustion have been derived from theory and combined to form a regime diagram using a reduced set of boundary variable and initial conditions [94]. The construction of a regime diagram for premixed combustion has received considerable attention in recent years. Unfortunately, most studies to date have been done at either low turbulence intensities (u'/S_L, the r.m.s. velocity normalized by the laminar flame speed) or small integral length scales [41]. In particular, the boundary separating thin reaction zones from broken or distributed zones has only been studied using relatively small-scale experiments. The same can be said for measurements of the turbulent burning velocity, where experiments in Bunsen flames have been confined to turbulence intensity $u'/S_L < 25$ [140]. Therefore, there is a need to experimentally verify

regime predictions in realistic geometries and turbulence levels, such that the results may be more applicable to practical combustion devices.

To be useful, any model must be able to accurately predict fundamental combustion properties such as the flame structure and the turbulent burning velocity. Prior to the present study, it was unknown what would happen to a premixed flame when subjected to turbulence where both the turbulence intensity and integral scales are very large (large turbulent Reynolds number $Re_T = \frac{u'L}{\nu}$). This thesis utilizes the Hi-Pilot burner, a novel piloted Bunsen burner capable of producing large integral scales (from 6 mm to 41 mm) and extreme turbulence (where the extreme range is defined as $u'/S_L > 25$). This work represents an effort to further our understanding of the physics of large Reynolds number premixed combustion.

1.2 Outline

Background and theoretical grounding

The rest of this first chapter will be devoted to a review of the literature and relevant background pertaining to the thesis. Details of laminar flame structure and chemistry will be provided, including an overview of the chemistry pertaining to the preheat layer, the high temperature reaction zone (or inner layer), and the laminar burning velocity. Various theoretical formulations for the regimes of turbulent premixed flames will be reviewed, and previous experimental and computational results will be discussed. Numerous attempts have been made to derive theoretical formulations for the turbulent burning velocity, and numerous empirical correlations have been derived as well. The interactions of turbulent structures and a premixed flame surface will be analyzed, including the effects of flame stretch, wrinkling, and turbulent diffusivity. A summary will compare the various results to date, and the conclusions will help motivate the rest of the work, as it reveals several unresolved questions.

Experimental approach

The flow facility, the Hi-Pilot burner, and the laser diagnostics employed will be presented in Chapter 2. This thesis uses a number of laser diagnostics, including laser Doppler velocimetry (LDV), particle image velocimetry (PIV), and planar laser-induced fluorescence (PLIF) of the OH, CH, and formaldehyde (CH_2O) molecules. CH is a radical species that exists only in the region of the flame where high-temperature reactions occur, and the overlap of OH and formaldehyde will be shown to be an alternative marker of the heat release region. The relative merits of these diagnostics will be compared.

Characterization of the turbulence, co-flow, and flame structure

Chapter 3 will document characterization of the flow field in the Hi-Pilot burner. This was done using LDV, which measures a single component of velocity, and PIV which provides planar data. LDV was performed first, and provided measurements of mean and fluctuating velocities U and u', as well as the integral time scales. A correction to Taylor's hypothesis was applied to transform these time scales to integral length scales. The PIV data provides direct measurement of the longitudinal and lateral length scales, and therefore details the extent of anisotropy present in the experiment. It also allows us to quantify the accuracy of the correction to Taylor's hypothesis used in the LDV measurements.

Regimes of high Reynolds number premixed combustion

Results from the simultaneous acquisition of OH and formaldehyde PLIF will be presented in Chapter 4. It is shown that over a span of flow conditions ranging from weak to extreme turbulence ($7.5 < u'/S_L < 243$) the reaction zone structure remains effectively unchanged, despite a significant increase in flame surface area through the wrinkling mechanism. On the other hand, the preheat layer of the flame is found to broaden significantly, indicating the majority of test conditions fall in the Broadened Preheat - Thin Reaction zones regime. This is surprising, given the extremely large values of turbulence that exist upstream of

the preheat layer. It is hypothesized that the turbulence may not survive passage through these extensive regions of preheating, where kinematic viscosity ν increases and thermal expansion may act to attenuate the smaller scales of the flow.

Turbulent burning velocity in extreme turbulence

Measurements of the global consumption speed $S_{T,GC}$ and the increase in flame surface area A_T/A_L will be presented in Chapter 5, and implications for flame surface density models are discussed. Flame surface density measurements indicate an increase in the area of the heat release layers of 3-5 times the laminar value. However, the turbulent burning velocity increases by a factor of more than 20 times the laminar flame speed, and therefore flame surface area mechanisms cannot entirely explain the results. It appears enhanced turbulent diffusivity, which coincides with substantial broadening of the preheat zone, contributes to the burning velocity in these regimes. Large bending of the global consumption speed is observed, and it is thought that this may be due to the turbulence attenuation predicted above.

The Evolution of turbulence in a broadened preheat zone

Chapter 6 will document simultaneous measurements of formaldehyde PLIF and PIV, which provides details of the evolution of the turbulence through a broadened preheat layer. Measurements of mean velocity, turbulence level u', and the average eddy velocity U_θ show that the turbulence does not decay as it passes through the broadened preheat layer. Instead, it is shown that the turbulence levels measured at the jet exit are approximately the same as those impinging on the reaction surface. However, conditional integral scale measurements reveal that the integral scale increases through the flame, implying dissipation of small scales. These results will be used to explain results in the previous two chapters.

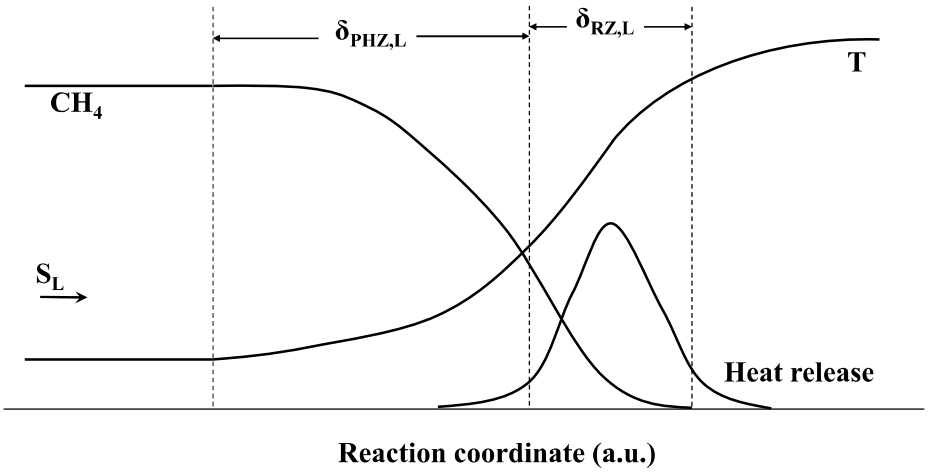

Figure 1.1: Illustration of a laminar premixed flame.

Conclusions

Finally, the results of these experiments will be summarized in Chapter 7, and applied back to the general question of the work - what happens to premixed flames in extreme turbulence? Although considerable work remains, it is shown that this thesis serves as a meaningful first step towards understanding the interaction of extreme turbulence and flame chemistry.

1.3 Laminar premixed flames

A brief review of laminar premixed combustion is necessary before we can explore the interaction of turbulence with a flame surface. A laminar premixed flame consists of perfectly mixed fuel and oxidizer streams, and for the steady-state case can be simplified to the one-dimensional problem shown in Figure 1.1. In the figure, the fuel is shown as methane, and the reaction coordinate corresponds to the dimension normal to the flame surface.

The vertical lines in Figure 1.1 indicate the preheat zone (PHZ) and the reaction zone

(RZ) boundaries. The preheat zone (also called the preheat layer) is the region where the larger molecules break apart, and low temperature reactions begin to occur. These are often referred to as pyrolysis reactions, and are where the temperature first begins to increase [70, 94]. The reaction zone is the thin, visible region where the majority of heat release occurs. The reaction zone is sometimes called the inner layer, and its structure can be defined many ways. Theoretical formulations often define the reaction layer thickness using the maximum temperature gradient as $\delta_{\Delta T,L} = \frac{T_{burned} - T_{unburned}}{dT/d\eta|_{max}}$, where η is the reaction coordinate. Alternatively, experiments typically define the reaction zone as the full-width at half-maximum of the heat release profile, or some species believed to approximate it.

The laminar burning velocity, or flame speed, S_L is defined as the relative velocity of the flame surface propagating normal to the cold reactants. In the steady, one-dimensional case given in Figure 1.1, S_L is simply the velocity of the gas upstream of the preheat layer. Flame stretch can introduce local variations of the propagation rate of the flame, which in a Bunsen flame can be several times greater or smaller than the measured value S_L. It is useful to distinguish between the unstretched laminar flame speed S_L^0, and the stretched laminar flame speed S_L, as one is determined purely from the chemistry and the other depends on the flame configuration and turbulence. The two are related as $S_L = S_L^0 - \ell * \kappa$, where ℓ is the Markstein length, and κ is the curvature of the flame surface.

The laminar flame thickness is usually called $\delta_{F,L}$, and the total flame thickness is the summation of the preheat and reaction layers as

$$\delta_{F,L} = \delta_{RZ,L} + \delta_{PHZ,L} \tag{1.1}$$

The flame thickness is a length scale that measures how quickly chemical reactions can occur against the oncoming flow. Therefore, it is proportional to $\delta_{F,L} \sim \alpha_0/S_L$, where α_0 is the thermal diffusivity before any preheating occurs. An unstretched laminar flame thickness can be defined similar to the flame speed as $\delta_{F,L}^0 \sim \alpha_0/S_L^0$. From this we see that both the flame thickness and flame speed are proportional to the thermal diffusivity.

Lastly, it is useful at this point to define the term *flamelet*, as it will be referred to frequently throughout this thesis. Williams first defined a flamelet to be a flame where the gradients in temperature, heat release, etc., are much larger in the flame-normal direction than the tangential direction [137] [94]. A *laminar flamelet* is a flamelet which propagates locally at the laminar burning velocity S_L. In this regime, the combustion time scales are very fast relative to the turbulence, such that the reactions are able to occur in thin layers [91].

Flamelet concepts have been extremely popular with modelers, especially in LES contexts, because all of the chemistry can be calculated from that of a laminar flame. Flamelet models typically utilize a conservation equation of either flame surface density Σ (see Section 1.5.1.1) or the G-equation, which is defined on the flame surface and describes the motion of the flame front. These are advantageous because they de-couple the flame chemistry from the modeling of the turbulent flow.

Laminar flamelets can persist in very turbulent flows; in fact, a survey of the literature reveals that the vast majority of turbulent combustion experiments have revealed flamelet-like structures [41]. However, the distinction is made here between a laminar flamelet, which propagates locally at the stretched laminar flame speed S_L, and a flamelet-like structure, which only requires that the composition gradients are much larger in the direction normal to the flame. A flamelet structure may persist in very high levels of turbulence, but if the turbulent diffusivity is sufficiently large the flame may propagate at a turbulent flame speed that is greater than the laminar value, $S_T/S_L > 1$.

1.4 Regimes of premixed combustion

1.4.1 Regime diagrams

Numerous attempts have been made to divide premixed flames into different regimes of combustion [1, 19, 93, 96]. Regime boundaries are typically derived from the ratio of tur-

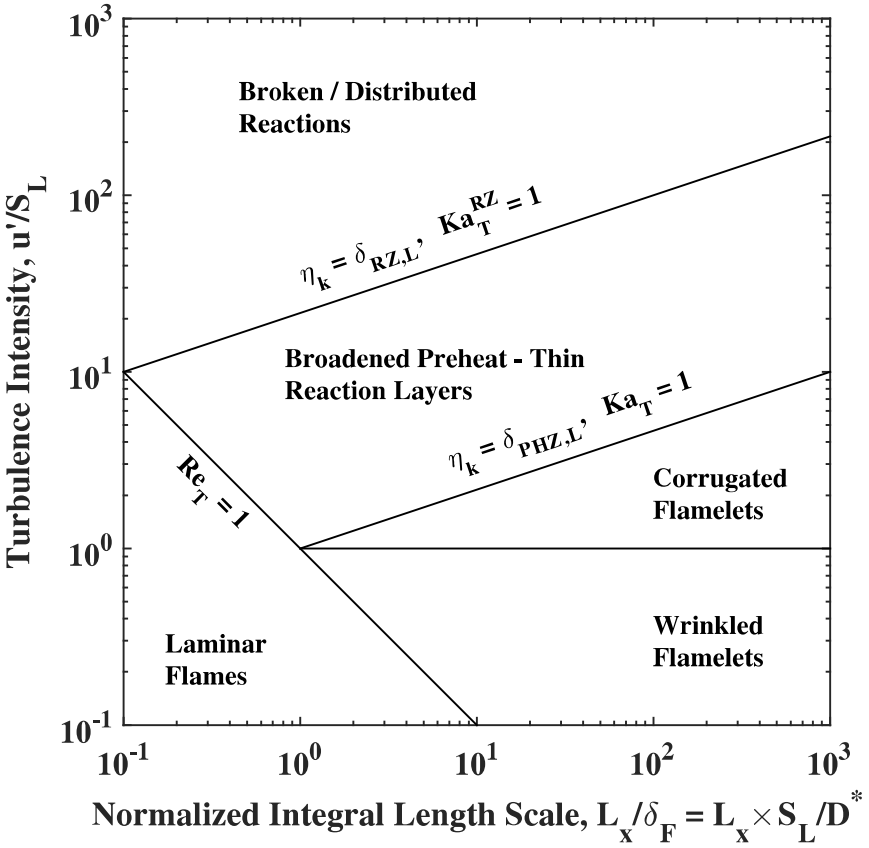

Figure 1.2: Regime diagram as proposed by Peters [93, 94]

bulence and chemistry time scales, and they attempt to predict the structure of the reacting flow (flamelets, local extinction, distributed reactions, etc.). The most common regime diagram was proposed by Peters [93] and plots the normalized integral length scale $L/\delta_{F,L}$ against the turbulence intensity u'/S_L. This version of the regime diagram is given in Fig. 1.2.

The regime diagram separates flames into various structures depending on the turbulence intensity and integral scale. Laminar flames exist for $Re_T < 1$, where both u'/S_L and $L/\delta_{F,L}$ are small. As the turbulence is increased, turbulent motion distorts the flame surface, and stretch acts to elongate local flame elements. Vortical structures then redistribute the increased flame surface into wrinkles - this is the wrinkling mechanism [120]. Thus, the turbulence wrinkles the flame and increases the total area of the exothermic layers. When

the turbulence level u' is less than the laminar flame speed S_L, the flame will be a mildly wrinkled flamelet. As the turbulence level exceeds the local burning rate, $u'/S_L > 1$, the flame cannot keep up with local turbulent fluctuations, and the wrinkling process becomes more complex. This regime is called corrugated flamelets.

If the turbulence is continually increased, smaller and smaller scales of motion will be present in the flow. It is usually thought that a turbulent eddy larger than the width of the flame will not be able to disrupt the chemistry, it can only interact with the flame sheet through wrinkling and strain mechanisms. It has been observed that the large-scale strain exerted on a flame element can cause local thinning on the layer, and this is one mechanism for flame extinction [38]. On the other hand, if a turbulent eddy is able to penetrate the flame structure, it will be able to circulate hot gas from near the reaction layer upstream, which will then increase the reaction rate upstream due to the elevated temperatures. In regime diagram analyses it is typically argued that this occurs when the Kolmogorov scale is able to penetrate the flame. This will lead to the broadening of the flame, specifically the preheat layer upstream of the primary reactions, as chemical reactions occur over a wider region, and it is also expected that the burning rate will increase [103]. This regime contains flames that have a broadened preheat - thin reaction layer structure.

Likewise, if the Kolmogorov scale is able to penetrate the reaction layer, the chemistry of the reaction layer should be disrupted. However, in this regime it may be possible to extract heat from the reaction surface faster than the chemistry can sustain. Therefore, this regime is predicted to sustain either broken or distributed reactions. It remains unclear under what conditions distributed reactions can exist, as well as the conditions separating them from broken reactions.

At this point, a few words are needed regarding the construction of the regime diagram, as much of this work is focused on validating the predicted boundaries shown in Fig. 1.2. In order to construct the regime diagram, it is assumed that:

- The Schmidt number is unity: $Sc = \nu/D = 1$, where D is the mass diffusivity of the

reactants.

- The flame thickness is taken to be $\delta_{F,L} = D^*/S_L$. Because the diffusivity will be increased near the flame, we use a modified diffusivity D^* which is evaluated at an elevated temperature [92]. This is a simplification, as the exact relation will contain an empirical constant. Also, from this: $t_F = D^*/S_L^2$.

- The criterion for finite-rate chemistry effects - that is, the point where the flame chemistry can be disrupted by the turbulence - is when the Kolmogorov time scale t_η equals the chemistry time scale. This is analogous to stating that Kolmogorov scale eddies of size η are able to penetrate the flame and disrupt the chemical reactions. At this point the flame will either broaden or extinguish.

The turbulent Reynolds, Damköhler, and Karlovitz numbers are then defined as:

$$Re_T = \frac{u'L}{S_L \delta_{F,L}} \tag{1.2}$$

$$Da_T = \frac{S_L L}{u' \delta_{F,L}} \tag{1.3}$$

$$Ka_T = \frac{t_F}{t_\eta} = \frac{\delta_{F,L}^2}{\eta^2} = \frac{u_\eta^2}{S_L^2} = \sqrt{\frac{u'^3 \delta_{F,L}}{S_L^3 L}} \tag{1.4}$$

In his derivation, Peters then re-writes Eqn. 1.2 (the turbulent Reynolds number) and introduces a second Karlovitz number, based on the reaction layer thickness.

$$Re_T = Da_T^2 Ka_T^2 \tag{1.5}$$

$$Ka_T^{RZ} = \frac{\delta_{RZ,L}^2}{\eta^2} = \left(\frac{\delta_{RZ,L}}{\delta_{F,L}}\right)^2 Ka_T \tag{1.6}$$

Eqn. 1.6 states that the relevant Karlovitz number at the reaction zone must use $\delta_{RZ,L}$,

not $\delta_{F,L}$. Essentially, by assuming $\delta_{F,L} = D^*/S_L$, we are able to say that the Karlovitz number is simply the ratio of flame and Kolmogorov length scales squared. Therefore, when $Ka_T > 1$, this theory would predict that the flame would begin to broaden. Likewise, when $Ka_T^{RZ} > 1$, we would expect the reaction zone to be disrupted. It is noted in passing that several definitions have been used for the Karlovitz number, but this has become most common in recent years [41]. Returning to Eqn. 1.2, we can re-arrange terms and utilize Eqn 1.5:

$$\frac{u'}{S_L} = Re_T \left(\frac{L}{\delta_{F,L}}\right)^{-1} = Ka^{2/3} \left(\frac{L}{\delta_{F,L}}\right)^{1/3} \tag{1.7}$$

Using Eqn. 1.7 the lines on the regime diagram in Fig. 1.2 can be constructed. As an aside, it is assumed that the reaction layer thickness is approximately one tenth of the flame thickness. This result is arrived at using activation energy asymptotic analysis [106], but is not a very accurate approximation. CHEMKIN simulations and most experiments show that the reaction layer is typically about one-quarter to one-half of the flame thickness. This distinction will be returned to in Chapter 4 when the regime diagram is assessed. Using this approximation, the required Karlovitz number for broken reactions is $Ka_T^{RZ} = \left(\frac{\delta_{RZ,L}}{\delta_{F,L}}\right)^2 Ka_T = 100 Ka_T$. Thus, the boundaries for BP-TR flames and for Broken Reactions correspond to a Karlovitz number Ka_T equal to 1 and 100, respectively.

1.4.2 Experimental evidence for non-flamelet combustion

A goal of the thesis is to evaluate the predicted boundaries for flamelet combustion and, if necessary, suggest modifications or improvements. This section will discuss the relevant measurements and simulations of turbulent premixed flame structure. The vast majority of the experimental literature reports thin flamelets [41]. In a review by Driscoll, all of the twenty papers examined showed evidence of flamelet structure. Shepherd et al [112], Buschmann et al [26], Dinkelacker et al [38], and Soika et al [117]] all measured the preheat

thickness using Rayleigh scattering and found the layers were thinner, ranging from $0.4 < \delta_{PHZ,T}/\delta^0_{PHZ,L} < 1$. The turbulence intensities in these studies ranged from $0.5 < u'/S_L < 34$, and the Karlovitz number ranged from $0.1 < Ka_T < 44$. However, no discernible trend was observed between these turbulence quantities and the flame properties. For instance, the thinnest preheat measurement corresponded with the lowest values of u'/S_L and Ka_T, while the second thinnest flame had among the largest turbulence levels, with a Karlovitz number of 13 and u'/S_L of 23.

In contrast, Chen and Bilger [31] [30], O'Young and Bilger [89], and Mansour et al. [75] also used Rayleigh scattering over similar turbulence conditions and observed slight thickening of the preheat layers, with measured layers between one and three times the laminar value.

While there have been many studies of the structure of premixed turbulent flames in the wrinkled flamelet regime [41] there have been relatively few in the broadened preheat regime. Numerous studies [7, 43, 105, 107, 108, 134, 143] have demonstrated that it is possible to substantially broaden the preheat region of a premixed flame, as small-scale eddies penetrate the flame. However, some work has seen broken or distributed reactions. Dunn et al [43] [44] used Rayleigh scattering in a high Karlovitz number, piloted, jet flame, and observed extinction and re-ignition events as well substantial broadening of the flame structure.

Zhou et al [143, 144] has obtained the only experimental evidence to date of distributed reactions. Using a very small jet (~2 mm) and very large Karlovitz numbers Ka_T up to 1739, CH-PLIF images reveal relatively uniform heat release across the jet core. Zhou et al. [145] also applied CH-PLIF diagnostics to swirl-stabilized flames and observed distributed reaction zones in the downstream region. Both of these instances of distributed zones revealed reaction layers that varied significantly over the flow domain. The layers are very thin near the base of the Bunsen and swirl flames, but broaden significantly downstream, indicating a dependence on the non-dimensional residence time x/U. Formalde-

hyde PLIF was also recorded in order to quantify the preheat thicknesses for both of these configurations. The results showed much more rapid broadening of the preheat layers than the reaction zones, and a similar residence time dependence.

A number of recent direct numerical simulations (DNS) have explored a similar turbulence regime as Zhou et al [143, 144]. Interestingly, a DNS study recently attempted to replicate the result of the high Ka_T jet burner [135]. The flame surface density and curvature measured in the DNS agreed well with the experiment, and the simulated Overlap signal areed with the flame structures measured by Zhou. Savard et al performed DNS of a flame sheet in a channel and reported substantial broadening of the preheat layer along with some local extinction [107,108]. Their Karlovitz number was as high as $Ka_T = 280$. Studying lean hydrogen-air flames near lean blowoff, Aspden et al was able to produce Karlovitz numbers as high as $Ka_T = 1562$, and discovered evidence of distributed reactions [6, 8]. Both of these studies utilized very lean flames near blow-off, in order to lower the chemical reaction rate and increase u'/S_L and Ka_T within the constraints of a fully resolved DNS study.

1.5 Turbulent burning velocities

1.5.1 Definitions of the turbulent burning velocity

There are at least four alternative definitions of the turbulent burning velocity, and all of them are in somewhat common use [41]. Thus, there is a significant possibility for confusion if we do not specify what kind of burning velocity is being used. There is no correct definition of a burning velocity, and each can serve a useful purpose in certain applications. However, stating a measured "burning velocity" without elaboration is not useful, as the measured values can be quite different depending on the definition. Burning velocities can be defined in two general categories: displacement speeds and consumption speeds. Each of these can be further divided into local and global quantities. The global consumption

speed measures the rate at which the reactants are consumed, and is defined as [48]:

$$S_{T,GC} = \frac{\dot{m}_r}{\rho_r A_F} \tag{1.8}$$

In Eqn. 1.8, $\dot{m}_r$ is the mass flow rate of the reactants passing through the flame surface, ρ_r is the density of the unburned reactants (before any preheating occurs), and A_F is the flame surface area of a certain iso-contour. A_F is most commonly taken at the $\overline{c} = 0.5$ iso-contour, where $\overline{c}$ is the mean progress variable of the flame, a measure of how probable a given point in space contains burned products. This form gives a measure of how rapidly reactants are converted into products, and is therefore very useful from engineering and design perspectives. Alternatively, a local measurement of the consumption speed is more typical to DNS studies due to the availability of heat release and mass fraction details that the experimentalists cannot easily acquire. The local consumption speed defined using the heat release rate would be defined as [70, 94]:

$$S_{T,LC} = \frac{1}{\rho_u} \int_{-\infty}^{\infty} \dot{w}_r d\vec{n} \tag{1.9}$$

This can be easily evaluated in a DNS study of , for example, a freely propagating flame in a channel. However, it is very difficult to measure $\overline{w}_r$ in experiments. Instead, a global consumption speed $S_{T,GC}$ is typically what is measured in experimental studies. However, this can only be applied to geometries where the mass flow of burned reactants is known, such as an envelope flame where all reactants pass through the flame surface. In a V-flame or a Bunsen flame with an open flame tip (where some of the reactants can escape the measurement domain avoiding the flame) this measurement cannot be adequately determined.

The flame speed discussed in section 1.3 was the relative velocity of the flame propagating into the unburnt reactants, and this is the definition of the displacement speed [126]:

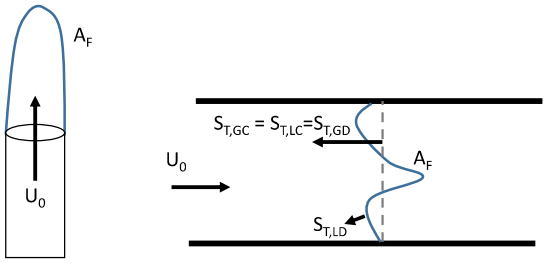

Figure 1.3: Two different geometries for which the burning velocity may be defined. On the left is an envelope Bunsen flame, for which a global consumption speed is often defined using the flame area A_F and the reactant density and mass flow rate. On the right is a flame sheet in a channel, which will be propagating locally at a velocity $S_{T,LD}$, which may or may not be equal to the laminar burning velocity S_L. Using the $\bar{c} = 0.5$ contour, several different forms of burning velocity can be defined.

$$\overrightarrow{n} \cdot S_{T,D} = \overrightarrow{u} \tag{1.10}$$

In Eqn. 1.10, $\overrightarrow{u}$ is the relative velocity vector between the flame surface and the reactants, and $\overrightarrow{n}$ is the flame surface normal vector. This is typically defined locally, with $S_{T,LD}$ measured as the velocity of the reactant gas upstream of the flame. Difficulties with this measurement include accounting for thermal expansion if the velocity is measured at a point in the preheat layer. This requires transforming the measured velocity at the flame into the equivalent value prior to thermal expansion, $u = \rho^* u^* / \rho$, where ρ^* is the gas density at the temperature of the measurement location, while ρ is the density in the cold reactants upstream [119]. Additionally, defining an iso-surface in a highly turbulent flame with broadened preheat zones quickly becomes a difficult task. Therefore, this measurement is most often constrained to relatively weakly turbulent flames. There is also a global displacement speed $S_{T,GD}$, which would measure an average flame surface identical to A_F in equation 1.8 and the average velocity field U. To obtain $S_{T,GD,}$ you would then apply Eqn. 1.10 to over the extent of A_F.

1.5.1.1 Flame surface density

An important concept in flamelet theory is the flame surface density, commonly abbreviated as FSD or Σ. It is formally defined as the average area of the flame sheet that is present within a unit volume. For planar measurements, it has an analog that is the average length of the flame segment (measured in the plane of the laser sheet) within a unit area.

$$\Sigma = \frac{\delta L}{(\Delta x)^2} \tag{1.11}$$

where δL is the ensemble-averaged length of flame surface within an interrogation box, and Δx is the length of one side of the interrogation box. The accuracy of the 2D approximation of Σ in Eqn. 1.11 was assessed by Bell et al. [13], and it was shown that the uncertainty of the planar measurement was $\pm 10\%$. Therefore, the value for Σ measured from the planar measurements is approximately equal to the true three-dimensional value. Using these concepts, the turbulent burning velocity can be derived from the flame surface density following [22]:

$$\frac{S_{T,F}}{S_L^0} = I_0 \frac{A_T}{A_L} = I_0 \int_{-\infty}^{\infty} \Sigma d\eta \tag{1.12}$$

$$I_0 = \frac{S_L}{S_L^0} = 1 - Ma * Ka \tag{1.13}$$

In Eqn. 1.13, the definition of the stretched flame speed was used, and Ma is the Markstein number, $Ma = \ell / \delta_{F,L}^0$, and $Ka = \kappa \delta_{F,L}^0 / S_L^0$. The stretch factor I_0 is approximately unity in lean, turbulent, methane-air flames [113]. The turbulent burning velocity of Eqn. 1.12 is called the flamelet velocity, because it describes the burning velocity of a laminar flamelet (i.e., the increases are purely due to flamelet wrinkling). Because most DNS studies and experiments to date have studied flames in the corrugated flamelet regime, this has often been referred to simply as the burning velocity, but it is important to note that it only applies

if the flame is propagating locally at the laminar flame speed.

1.5.2 Turbulent burning velocity theory

The observation that turbulence can increase the consumption rate of combustible reactants dates back at least to Mallard and Le Chatelier, who observed the effect of turbulence in increasing reaction rates in 1883 [73]. However, the modern theoretical grounding for burning velocity is rooted in the work of Damköhler, who in 1940 proposed two hypotheses for the evolution of the turbulent burning velocity [36]. In his formulation, there would be two limiting cases of turbulence-flame interactions: a large scale and a small scale limit. In the large scale limit, the turbulence can only wrinkle the flame surface, increasing the area of the exothermic layers as described in 1.4.1. The geometry of this case is given for a simplified, single flame-vortex interaction in Fig. 1.4. In this case, the total burning rate of the flame is dependent on the increase of the reaction zone surface area relative the laminar case, A_T/A_L. Note that in flame-wrinkling nomenclature, a wrinkle is defined as the wavelength of the wrinkle formed by a vortex, so in Fig. 1.4 the wrinkle size would be the distance λ indicated, which is essentially the wavelength of a sine wave fitted to the distorted flame surface.

In the large-scale limit depicted in Fig. 1.4, the wrinkling A_T/A_L is independent of length scale, and is assumed to depend only on the turbulence intensity u'/S_L. Shchelkin [67, 111] derived a geometric relationship between the turbulence intensity and A_T/A_L by assuming the wrinkles were conical. This relationship, which is expected to govern the turbulent burning velocity in the large-scale limit, is:

$$\frac{S_T}{S_L^0} = \frac{A_T}{A_L} = \sqrt{1 + A\left(\frac{u'}{S_L}\right)^2} \tag{1.14}$$

In Eqn 1.14, S_T/S_L will change from a square-root to a linear dependence on u'/S_L as the turbulence is increased. In the small scale limit, finite-rate chemistry is expected to

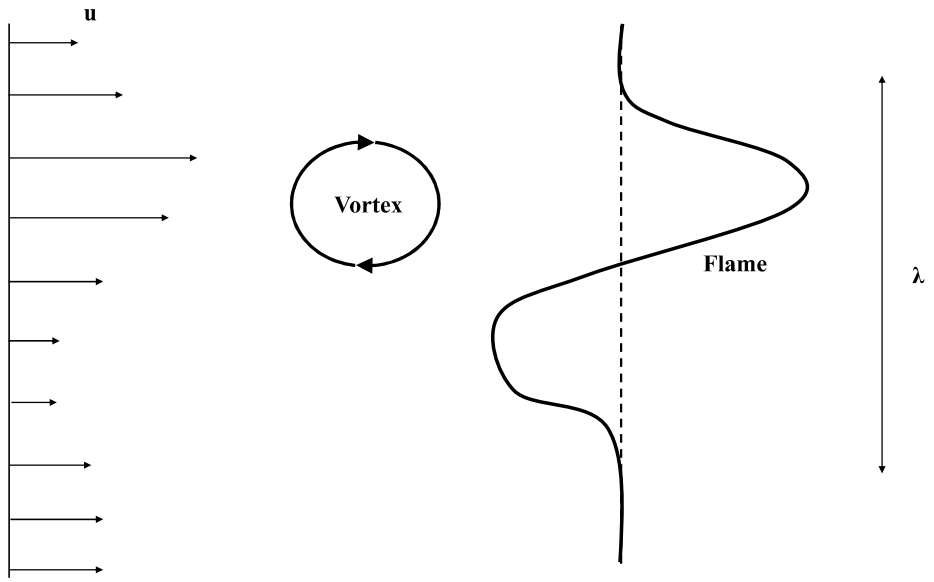

Figure 1.4: Flame vortex interaction illustrating the wrinkling phenomena. Adapted from Lewis and von Elbe [36]

impose greater influence. As the smallest turbulent eddies penetrate the flame structure, they will act to diffuse hot gas from the reaction zone upstream at a rate comparable to the chemistry time scale. This coincides with the Broadened Preheat - Thin Reaction layer regime, and suggests the turbulent burning velocity should depend to some degree on the enhanced diffusivity. Damköhler illustrated this [93, 94] by analogy with the laminar case, as:

$$S_L \sim (D/t_c)^{1/2} \tag{1.15}$$

$$S_T \sim (D_T/t_c)^{1/2} \tag{1.16}$$

$$\frac{S_T}{S_L^0} \sim \left(\frac{D_T}{D}\right)^{1/2} \sim \left(\frac{u'}{S_L}\frac{L}{\delta_{F,L}}\right)^{1/2} \sim Re_T^{1/2} \tag{1.17}$$

In Eqns 1.15 and 1.16 t_c is the time-scale of combustion, and D_T is the turbulent dif-

fusivity, which is proportional to the product of the turbulence level and integral scale as $D_T \sim u'L$. In Eqn 1.17 it can be further assumed that $\nu = D$, and therefore S_T/S_L is expected to follow a square-root Reynolds number dependence in this limit. A turbulent flame containing distributed reactions would be expected to depend only on the turbulent diffusivity, since there would no longer be a "flame" surface to wrinkle, and Eqn 1.14 would be undefined.

1.5.2.1 Other theoretical formulations of the burning velocity

The above discussion only considers limiting conditions, as real combustion devices will contain flamelet wrinkling occurring simultaneous with enhanced turbulent diffusivities, for example in a flame in the Broadened Preheat - Thin Reaction layer regime. Thus, a correct formula for the burning velocity must account for contributions from both terms. This sub-section will briefly look at several theoretical formulations that have been developed.

Kolla et al [64] derived an expression for S_T using Kolmogorov-Petrovskii-Piskunov (KPP) analysis. In their analysis, the KPP theory produces:

$$S_T = 2\sqrt{\frac{\nu}{\rho_r S c_c}\left(\frac{\partial\bar{\dot{\omega}}}{\partial\bar{c}}\right)_{\bar{c}\to 0}} \tag{1.18}$$

Where Sc_c is the Schmidt number of a reaction progress variable, and the relationship for the turbulent burning velocity is:

$$\frac{S_T}{S_L^0} = \sqrt{\frac{18C_\mu}{(2C_m-1)\beta}\left[[2K_c^* - \tau C_4]\left(\frac{u'L}{S_L\delta_{F,L}}\right) + \frac{2C_3}{3}\left(\frac{u'}{S_L}\right)^2\right]} \tag{1.19}$$

Eqn 1.19 incorporates the theoretical formulations outlined above, and assumes an additive relation between the enhanced diffusivity and the flame wrinkling. In the limit of small u'/S_L, the relation becomes proportional to Re_T, while in limit of large u'/S_L, S_T/u' scales with $\sqrt{1+Da_T}$.

In a separate analysis, Peters derived an expression for the turbulent burning velocity in

large and small-scale turbulence using a level-set approach and the G-equation [93]. Peters also utilizes a term depending on $\sqrt{Re_T}$, however the formulation is different from Kolla as the integral scale is thought to play a larger role than u'/S_L:

$$\frac{S_T}{S_L^0} = 1 - \frac{0.39}{2}\frac{L}{\delta_{F,L}} + \sqrt{\left(\frac{0.39}{2}\frac{L}{\delta_{F,L}}\right)^2 + 0.78\frac{u'L}{S_L^0\delta_{F,L}}} \tag{1.20}$$

Abdel-Gayed and Bradley obtained another expression for S_T/S_L which utilized a two eddy theory, assuming only the largest and smallest eddies need modeling and that the burning rate for each eddy size is the product of the eddy decay rate and the amount of mixture chemically reacted during the eddy lifetime [2]. In another work comparing a wide range of previous burning velocity measurements, Bradley found that the product of the flame stretch rate and Lewis number provided a good fit for a majority of the data [21]. Likewise, in a review by Andrews et al [4], a large number of previous experiments (predominantly in the spherically expanding geometry) were analyzed and S_T/S_L demonstrated substantial bending when plotted against u'/S_L, however it was found to follow a near-linear dependence on Re_T. They found this to be independent of the chemical composition.

1.5.3 Measurements and simulations of the turbulent burning velocity

An important question is how the turbulent burning velocity S_T/S_L varies with fundamental turbulence parameters, such as u'/S_L and $L/\delta_{F,L}$. A related question is how much the surface area of the exothermic layers increases through flamelet wrinkling. In other words, is there an effective limit for A_T/A_L beyond which flame surface destruction effects (such as flamelet merging) balance out further increases in flame area through wrinkling. Previously, it was shown that in the laminar flamelet regime the turbulent flame surface area A_T/A_L should be equal to the turbulent burning velocity S_T/S_L. As the reaction layers become broadened, turbulent diffusivity is expected to enhance the local burning rate. Therefore there are two potential contributors to S_T/S_L:

(1) increased surface area of the exothermic layers (A_T/A_L) due to turbulent wrinkling; and

(2) enhanced burning rate per unit area, due to increased turbulent diffusivity.

It has not been conclusively proven when S_T/S_L will exceed A_T/A_L, i.e., when turbulent diffusivity will contribute to the turbulent burning velocity. This section will provide a brief review of the relevant computational and experimental results.

1.5.3.1 Variation of S_T/S_L

Envelope flames

In the envelope flame geometry, Filatyev et al. [48] measured the global consumption speed $S_{T,GC}$ using planar laser induced fluorescence (PLIF) of the CH radical, a radical which has been shown to adequately track the reaction layer [39]. Turbulence levels were fairly low, with flames operating in the corrugated flamelet regime and $u'/S_L < 9$, and significant bending was observed. Bending refers to a decrease in the sensitivity of S_T/S_L on u'/S_L as the turbulence level is increased. The results of Filatyev indicated a decrease in S_T/S_L at the largest turbulence levels, and the ratio of A_T/A_L was found to match the turbulent burning velocity, indicating the flames were in the laminar flamelet regime.

Gulder has extensively studied burning velocities in round Bunsen flames of various integral scales. Smallwood et. al. [116], Gulder et. al. [56, 57], Yuen et. al. [140–142], and Tamadonfar [122, 123] have all consistently found that global consumption speeds (measured variously using Mie scattering and Rayleigh scattering) continue to increase with turbulence intensity up to $u'/S_L = 24$. They also found that the integral of flame surface density $\int_{-\infty}^{\infty} \Sigma d\eta$ was much less than the consumption speeds, and typically plateaued to a constant value as turbulence intensity increased. Integral length scale was found to be important, as burning velocities generally increased with integral scale.

Kobayashi et. al. [63] studied Bunsen flames at atmospheric pressure and at high pressure up to 1 MPa. Consumption speeds were measured with OH-PLIF, and the 0.05, 0.1,

and 0.5 contours were selected for analysis. Using the 0.1 contour, and in the range of u'/S_L up to 4, they found that the atmospheric pressure flames had a consumption speed $S_{T,GC}/S_L^0$as high as 10. At 1 MPa, the turbulence intensity was as high as $u'/S_L = 9.5$, and the burning velocities increased to $S_{T,GC}/S_L^0 = 27$. Bending in the burning velocity curves was observed for $u'/S_L > 2$.

Low-swirl burners

Using a low-swirl burner, Shepherd, Cheng, Bedat, and Talbot [12], [114], [33] found a nearly linear dependence of $S_{T,GD}/S_L$ versus u'/S_L, contrasting with the result of Bradley [4], Filatyev [48], and others. Turbulence levels were reported as large as $u'/S_L = 27.6$. In these works, Rayleigh scattering or OH PLIF was used to identify the flame surface, and a displacement speed was obtained by measuring the velocity (using PIV or LDV) in the reactants just upstream. Flame surface densities were measured using the measured flame surfaces to evaluate A_T/A_L, and it was found that the displacement speeds exceeded A_T/A_L.

Direct numerical simulations

In a DNS study by Savard et al. [107, 108], a flame sheet propagating in a channel was analyzed. Turbulence levels were as high as $u'/S_L = 21$, and a significant difference was observed between unity and non-unity Lewis numbers, highlighting the importance of differential diffusion effects, suggesting that *Le* should be incorporated into burning velocity models. Aspden et. al. [7, 9] also studied turbulent flames in a channel, and as mentioned in Section 1.4.2 some distributed reactions were observed. They observed that as the transition to distributed burning occurred, the measured local consumption actually decreased. In related work, Aspden et al. [5] has also found that the Lewis number *Le* is capable of explaining large variations in the burning velocity at moderate turbulence.

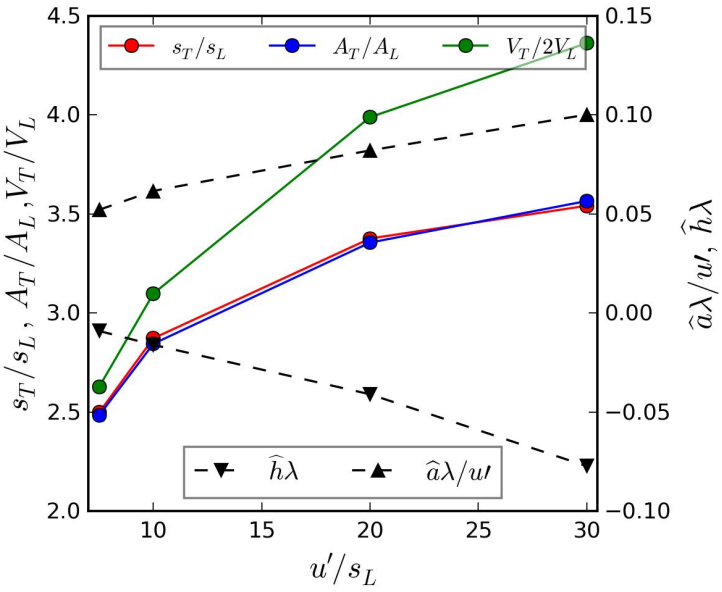

Figure 1.5: Nivarti and Cant. This corresponds to Fig. 7 in [85].

1.5.3.2 Variation of the flame surface area A_T/A_L

Generally, direct numerical simulations have found that the normalized turbulent flame surface area A_T/A_L is proportional to S_T/S_L. Recently, Nivarti and Cant [85] studied lean methane-air flames under a wide range of turbulence intensities ($1.5 < u'/S_L < 30$) using DNS of a flame element in a channel with forced turbulence and periodic boundary conditions. They observed that the burning velocity S_T/S_L plateaued to a value slightly larger than 3.5. Their simulations showed that the flame surface area ratio A_T/A_L matched S_T/S_L exactly at all measurement points, as illustrated in Fig. 1.5. Their analysis showed that the large degree of bending observed in the S_T/S_L curve is not due to local flame quenching. Rather, in high-intensity turbulence, mechanisms favoring destruction of flame surface area (such as flamelet merging) are favored. It is interesting that their study extends to a very large value of $u'/S_L = 30$, which is comparable to the most turbulent experimental measurements of S_T in the Bunsen geometry. The integral scales in this study were 0.99 mm, and when normalized by the laminar flame thickness $L/\delta_{F,L} = 2.75$.

The research group of Omer Gulder has performed numerous studies with round Bun-

sen flames. Smallwood et al [116] measured $S_{T,GC}$ by recording Mie scattering images of oil droplets that evaporated at the reaction front. They measured the fractal parameters of the flame surface wrinkling (a measurement of A_T/A_L) and found it to be significantly below the measured value of $S_{T,GC}/S_L$. This indicates departure from laminar flamelet theory, and these results were later replicated by Gulder and Smallwood [57] and Yuen and Gulder [140] who used OH-PLIF and Rayleigh scattering, respectively, to compute the flame surface density. They found that the integral of flame surface density, which is another measure of A_T/A_L, plateaued at approximately 3 for $u'/S_L > 5-10$, while $S_{T,GC}/S_L$ continued to increase for turbulence levels up to $u'/S_L = 24$. The integral scales for these flames were all less than $L = 1.79$ mm, with $L/\delta_{F,L} = 4$. It is very interesting to compare this result with the finding of Nivarti and Cant above, who studied turbulence conditions that are approximately the same. It may be important that the geometries were very different, as an envelope Bunsen flame may not behave the same as a flame sheet in a channel. In the case of the Bunsen flame, the turbulence will pass obliquely through the reaction layer at most locations, while the DNS configuration constrains the turbulence to intersect the flame orthogonally. Note that in both of these studies, the ratio A_T/A_L asymptoted to a similar value that was less than 4.

Similarly, Chen and Bilger [32] measured the integral of flame surface density in turbulent Bunsen flames for integral scales $L/\delta_{F,L}$ between 12 and 20, and they observed a near linear increase in the integral of FSD with maximum values of approximately 3, which is about the same value seen by both Yuen et. al. and Nivarti et. al. Turbulence intensities u'/S_L were varied between 2.5 and 7.

Sankaran et al [106] studied turbulent Bunsen flames using direct numerical simulation, which should allow a more proper comparison with the experimental work as the geometry is the same. However, Sankaran et al reported a result that was similar to that of Nivarti and Cant. Sankaran et al. observed a linear variation of $S_{T,GC}/S_L$ with turbulence intensities for $3 < u'/S_L < 10$. In their work, the flame surface area ratio A_T/A_L was equal to the

values of $S_{T,GC}/S_L$, indicating the flames remained in the laminar flamelet regime. The integral scale to flame thickness ratio was approximately 1.5.

Therefore, there appear to be some discrepancies in the burning velocity literature. Essentially, DNS studies suggest that A_T/A_L can fully explain increases in the turbulent burning velocity, but at large values of u'/S_L bending occurs as flamelet merging balances wrinkling, and the ratio A_T/A_L plateaus at approximately 3.5. The experimental work agrees that the turbulent flame surface area A_T/A_L will saturate at approximately 3-4, however the results of Yuen and Gulder and others show that the burning velocity continues to increase beyond this point. Geometry may play a role, as the residence time of the eddies will change whether the flame is a freely propagating segment in a channel (DNS) or a Bunsen flame. Another distinction is that the turbulence interacts differently throughout the surface of the Bunsen cone, with little wrinkling near the base (due to large mean shear) and large wrinkling near the tip, where the flow-flame interaction more closely approximates the DNS configurations.

However, a more likely explanation may be the role of the integral length scale. Poinsot et al [79] used DNS to show that the ability of turbulence to stretch a flame surface increases with the size of the turbulent eddy. Fig. 1.6 is the result from Meneveau and Poinsot, which plot the total flame stretch acting on a flame $\langle K \rangle$. Because wrinkling is a two-step process with flame stretch being the first component, it is probable that larger eddies will also be better able to wrinkle a turbulent flame surface. For instance, from Meneveau and Poinsot, the flame surface area present after a certain time t_q (in the absence of quenching) is $A(t_q) = A_0 e^{\langle K \rangle t_q}$. Therefore, a given turbulence interaction will cause a greater increase in A_T/A_L as the eddy size increases. The literature appears consistent that there is a limit beyond which the ratio A_T/A_L cannot increase, although the exact value of this limit has not yet been quantified. It may be that turbulence conditions with larger integral length scales, due to their better efficiency in stretching the flame, are able to reach this saturation limit of A_T/A_L, while smaller integral scales are not. This may explain the discrepancies

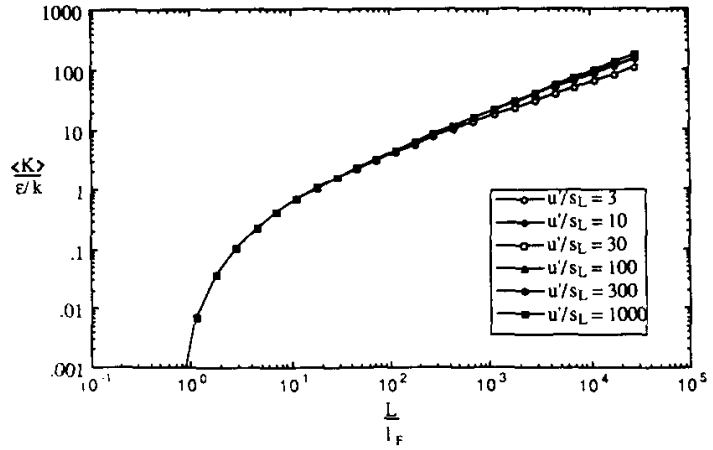

Figure 1.6: Stretch efficiency function of Poinsot [79]. For large integral scale ($L/\delta_F > 1$) the stretch increases approximately logarithmically. Note that the stretch has almost no dependence on u'/S_L when normalized by the strain of the largest scales of the flow $\langle\epsilon\rangle/k$.

seen between some experiments and the DNS, and suggests that computational work must continue to work in the direction of simulating larger integral scales.

1.6 Objectives of the thesis

This introductory chapter has attempted to present an overview of the theory describing premixed flame structure and burning velocities, and how the theory compares to experimental results. Based on this analysis, it is clear that there has been substantial progress in low to moderate Reynolds number combustion, and even some recent developments in very large Karlovitz number flames (small length scales but large turbulence intensity). However, the behavior of turbulent flames subjected to large length scales and turbulence intensities (and thus large Re_T) has been relatively unexplored. This work addresses the question of what happens to a premixed flame in high Reynolds number turbulence. For example, does the turbulent burning velocity continue to increase in extreme turbulence, and if so, is bending observed with increasing turbulence? Do flamelets persist in extreme turbulence, or do the layers become broken or broadened?

The Hi-Pilot burner, to be described in the next chapter, is capable of turbulence in-

tensities as large as $u'/S_L = 243$ and turbulence Reynolds numbers of $Re_T = 99{,}000$. This allows an unprecedented opportunity to explore premixed flame behavior. The first goal of this work was to test the predicted broken reaction layer boundary of Peters. To this end, two reaction layer visualizations techniques were employed, namely the overlap of OH and CH_2O PLIF (referred to as the Overlap method) and CH PLIF. Another objective was to evaluate the turbulent burning velocity in extreme turbulence, which in the Bunsen geometry has been restricted to $u'/S_L < 25$ [140]. Measurements of an average progress variable were recorded using OH PLIF, and compared with several measurements of A_T/A_L to evaluate how much of the increase in the burning velocity is due to flamelet wrinkling.

It will be seen in the following chapters that the preheat layers in the Hi-Pilot are extremely thick, often exceeding 20 mm. Thus, this work offers a prime opportunity to investigate the behavior of turbulent features as they progress through the preheat zone. Simultaneous planar measurements of velocity (PIV) and preheat zone structure (CH_2O PLIF) will provide conditioned statistics of mean velocity U, turbulence level u', and mean eddy rotational velocity U_θ. The integral length scale will also be evaluated, in order to quantify the extent of dissipation of the small-scales as well as the evolution of the turbulent diffusivity (which should scale as $D_T \sim u'L$).

This research provides the first database of measured flame properties at large Re_T utilizing modern laser diagnostics. Measured flame properties include the preheat and reaction layer structure, extinction events in the reaction zone, turbulent burning velocities, and the extent of flamelet wrinkling. Such a database is essential for constructing an accurate regime diagram and for the development of better combustion models.

CHAPTER 2

Experimental Approach

In order to address the questions set out in Chapter 1, very large values of turbulence were required. To this end, the Hi-Pilot, a high Reynolds number piloted, premixed jet burner was created. The flow field and turbulence properties were characterized using a combination of laser Doppler velocimetry (LDV) and particle image velocimetry (PIV). The former allows temporally resolved measurements of velocity data at a single point just above the jet exit on centerline. However, obtaining an integral length scale from this data requires invoking Taylor's hypothesis, also known as the frozen flow approximation. This states that for any time series measurement τ, a length scale L can be obtained as $L = \tau * U$, where U is the mean velocity of the flow. This assumes that the turbulent structures do not change appreciably as they are convected past the measurement point, and that their convective velocity is equal to the mean velocity of the flow. This is generally a good approximation only for $u'/U \ll 1$, but does not hold in this experiment. A standard correction to Taylor's hypothesis was applied to obtain a more accurate convection velocity, and thus integral length scale. Planer velocity measurements were obtained using particle image velocimetry (PIV) which provide a direct measurement of the longitudinal and lateral integral scales and turbulence levels, and allow an evaluation of the performance of Taylor's hypothesis.

Measurements of flame structure require high resolution spatial information of some marker of the flame chemistry. The most popular method is probably planar laser induced

fluorescence (PLIF), and this thesis applies PLIF of formaldehyde (CH_2O), OH, and CH respectively. The Overlap method consists of simultaneously acquired OH and CH_2O PLIF images, which mark the product region and the preheat region, respectively. The PLIF signal is proportional to the total quantity of the excited species, and therefore the pixel-by-pixel product of these images gives a quantity proportional to the forward reaction $CH_2O + OH \rightarrow HCO + H_2O$, which happens to coincide spatially with the primary heat release region. This measurement was checked by performing CH PLIF, which is an alternative marker of the reaction zone that has been shown to adequately trace the heat release region.

Following these general flame structure measurements, the turbulent burning velocity was measured using OH PLIF, which is formed rapidly at the leading edge, and can therefore be used as a marker of the flame location if the reaction layer is thin and unbroken, which the flame structure measurements will confirm. Lastly, simultaneous PIV and CH_2O PLIF will be performed to measure the evolution of the turbulent features through a broadened preheat layer. This chapter will first provide details of the Hi-Pilot burner, and then explain the principles and application of each of the diagnostics used.

2.1 The Hi-Pilot Burner

The Hi-Pilot experiment is a piloted, premixed burner capable of reaching very large values of turbulence Reynolds number Re_T. It consists of a long plenum with flow straightening elements and turbulence generating slotted plates placed upstream of a converging diverging nozzle. A schematic of the burner with plenum is shown in Fig. 2.1.

The flow straightening elements consist of a honeycomb plate supporting several rows of marbles, in order to provide uniform flow to the test section. The slotted plates, detailed in Fig. 2.2, were first used by Marshall et al [76], and are placed just upstream of a strong contraction section. This produces shed vortices from the slotted plate that are then subjected to a large mean shear as the flow accelerates through the contraction. The presence of this mean shear produces elongated turbulent eddies, as can be seen by examining the

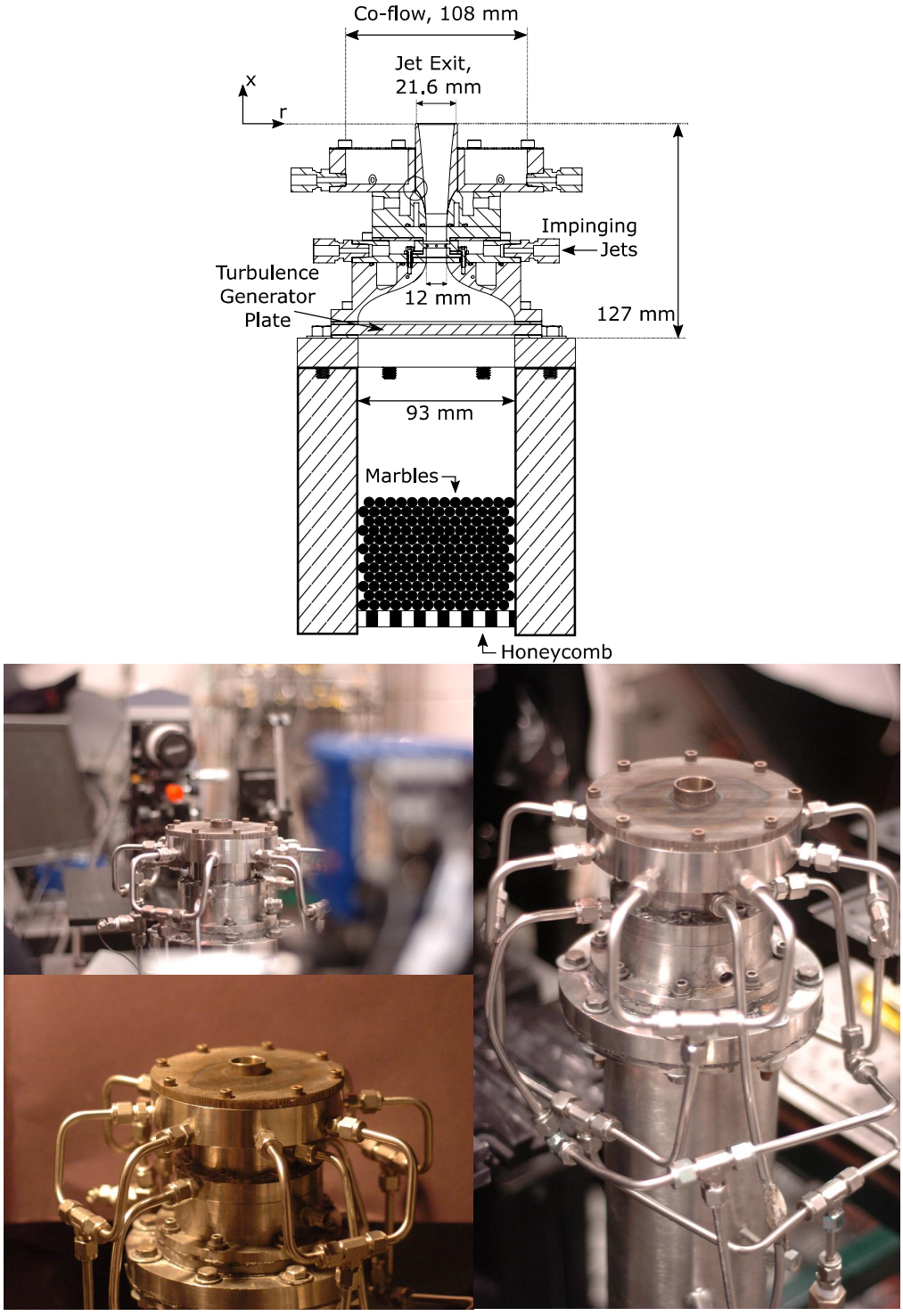

Figure 2.1: Schematic of the Hi-Pilot Burner. Note that the coordinates are centered with r = 0 over the centerline of the jet exit.

vorticity transport equation:

$$\frac{\partial \omega_i}{\partial t} + u_j \frac{\partial \omega_i}{\partial x_j} = \omega_j \frac{\partial u_i}{\partial x_j} + \nu \frac{\partial^2 \omega_i}{\partial x_j \partial x_j} \tag{2.1}$$

The left hand side of Eqn 2.1 is the total derivative of the vorticity vector ω, which describes the total rate of change of vorticity for a fluid particle. The first term on the right hand side is the vortex stretching term, which describes how vortical structures are stretched or rotated due to gradients in the mean velocity. The last term on the right hand side is the viscous term. The vortex stretching term demands that eddies are elongated in the direction of positive mean shear, and contracted in negative mean shear. Thus, with large positive values of dU_x/dx passing through the contraction, the turbulent eddies will become elongated in the flow direction. Similarly, the vortex stretching mechanism enhances the longitudinal turbulence level u' while decreasing the lateral term v'. Thus, although the turbulence generating system is capable of producing extremely large values of longitudinal integral scales L_x and turbulence levels u', some degree of anisotropy is introduced. The extent of anisotropy, and how it varies with turbulence level and slot width is the subject of section 3.2.3.

Varying the turbulence generators among the three slotted plates shown in Fig. 2.2 can produce very different levels of fluctuation velocities, integral scales, and velocity profiles. This allows access to a wide range of flow conditions at a single mass flow rate of reactants. A pair of impinging jets are located at the throat of contraction section, and serve to enhance the total turbulence level and integral scale. These were operated at 6% the total flow rate of reactants issuing from the plenum. The effect of the jets will be detailed in section 3.1. Flow rates were monitored using choked orifices, and pressure was also monitored just downstream to ensure choked flow. The equation for the mass flow rate through a choked orifice is:

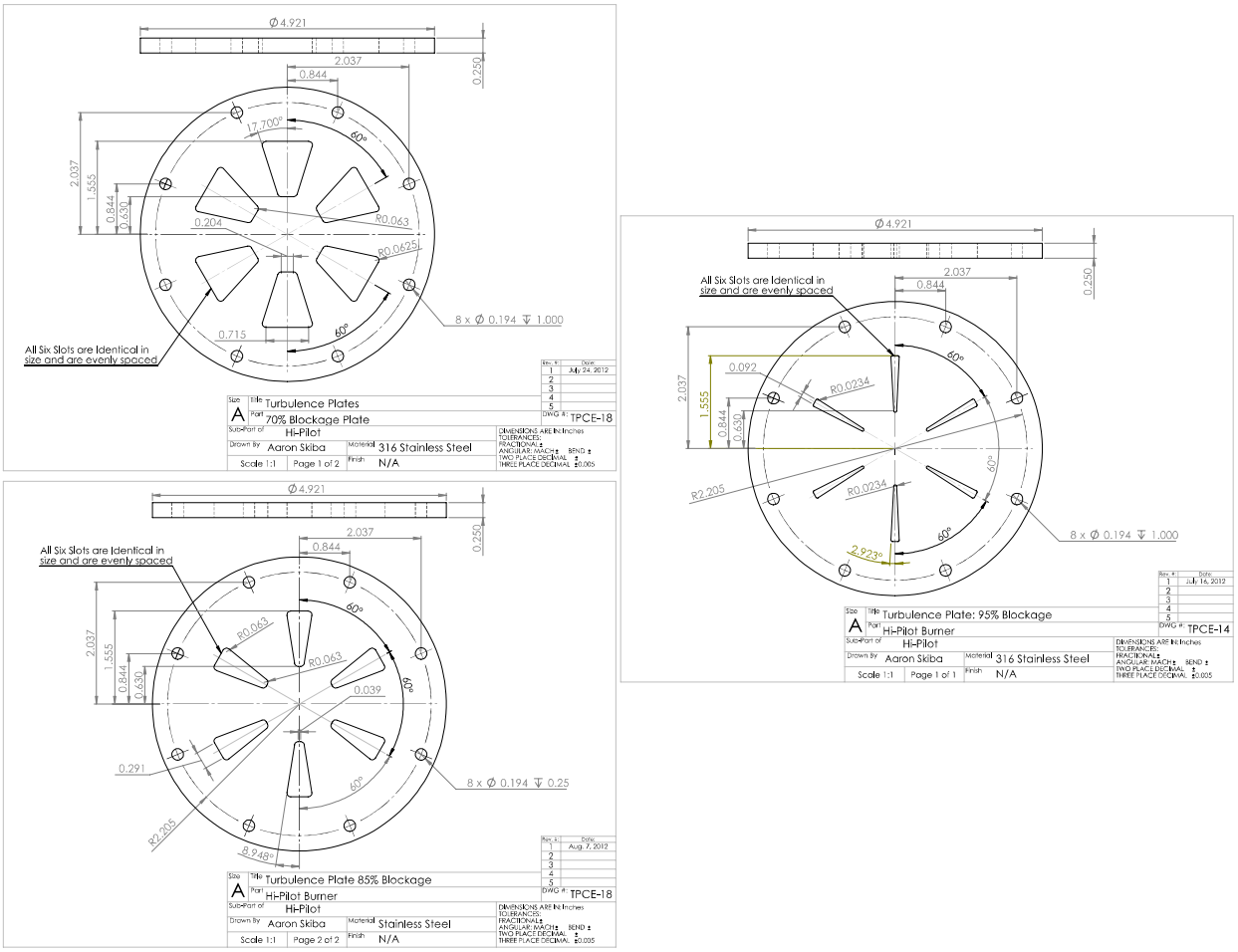

Figure 2.2: Turbulence generating slotted plates. The plate with the largest slots is called plate “a”, and while the one with the smallest slots is called plate “c”.

Table 2.1: Run Conditions for the Hi-Pilot Burner for $\phi = 0.75$

Case	Main Air	Main Fuel	Jet Air	Jet Fuel	Co-Flow Air	Co-Flow Fuel	$\frac{m_r}{\rho_r A}$
	(g/s)	(g/s)	(g/s)	(g/s)	(g/s)	(g/s)	(m/s)
1	2.24	0.098	-	-	25.4	1.11	5.2
2	4.60	0.200	-	-	25.4	1.11	10.7
3	9.10	0.402	0.61	0.026	25.4	1.11	22.6
4	13.2	0.579	0.87	0.037	25.4	1.11	32.6
5	21.6	0.942	1.37	0.060	25.4	1.11	53.3
6	29.5	1.300	1.90	0.084	25.4	1.11	73.0

$$\dot{m} = \sqrt{\frac{\gamma}{R_g}\left(\frac{2}{\gamma+1}\right)^{\frac{\gamma+1}{\gamma-1}}} \frac{p_0 A^*}{\sqrt{T_0}} \tag{2.2}$$

In Eqn. 2.2, γ is the specific heat ratio of the gas (methane or air), R_g is the gas constant, A^* is the orifice area. The room temperature T_0 was approximately 297 K, and the operating back pressure p_0 varied between 93.5 psi and 250 psi depending on the orifice and flow rate desired. The Hi-Pilot mass flow rates are listed in Table 2.1, and the measured run conditions are given in Table 2.2. Note that the turbulent Reynolds number is defined here as $Re_T = u'L/\nu$. The measured values are explained later in Section 3.1.1.

The version of the Hi-Pilot shown in Fig 2.1 is the result of several design iterations. The first model utilized a narrow ring of hydrogen pilot surrounding a central jet that had a much more aggressive expansion angle. It was observed that this produced separation for some of the higher flow rate cases, which was corrected by making the nozzle longer and slightly narrower. In addition, hot products from the pilot only persisted to approximately half the average flame heights, due to large amounts of entrainment of cold air by the central jet. This brought cold air into contact of the downstream edge of the flame, quenching reactions and producing an open flame tip. A closed flame tip is essential in this work, both to ensure measured extinction events are due to the turbulence issuing from the Hi-Pilot (instead of poor back-support downstream of the flame) and to obtain an accurate measure of the global consumption speed. Measuring $S_{T,GC}$ requires knowledge of the mass flow

Table 2.2: LDV turbulence measurements for the Hi-Pilot burner

Case	Jets?	U (m/s)	u' (m/s)	τ (ms)	$L_{x,Taylor}$	$L_{x,cor}$	Re_T	η_k (μm)
1a	No	7.7	1.7	1.13	8.6	9.6	1,000	120
1b	No	6.0	1.6	1.05	6.3	7.3	760	120
1c	No	8.5	1.2	0.68	5.8	6.1	480	140
2a	No	14.1	2.9	0.48	6.8	7.5	1,400	74
2b	No	9.2	3.1	0.68	6.2	7.8	1,600	72
2c	No	15.5	2.3	0.47	7.3	7.6	1,100	90
3a	No	29	5.4	0.22	6.3	6.9	2,400	46
	Yes	32	6.0	0.59	19	20	7,900	55
3b	No	17	5.9	0.37	6.3	7.9	3,000	44
	Yes	21	7.1	0.35	7.3	9.2	4,200	40
3c	No	30	4.8	0.24	7.1	7.6	2,400	51
	Yes	32	5.7	0.27	8.6	9.3	3,400	48
4a	No	39	8.6	0.22	8.6	9.5	5,300	35
	Yes	44	10	0.51	22	25	16,000	40
4b	No	23	8.3	0.25	5.6	7.2	3,900	34
	Yes	28	9.3	0.24	6.7	8.4	5,000	32
4c	No	40	7.6	0.17	7.1	7.7	3,800	37
	Yes	44	9.0	0.21	9.3	10	6,000	35
5a	No	56	17	0.23	13	16	1,800	24
	Yes	64	24	0.44	28	37	5,800	23
5b	No	38	15	0.15	5.6	7.5	7,400	21
	Yes	45	20	0.17	7.4	10	13,000	19
5c	No	64	20	0.17	11	14	18,000	20
	Yes	64	25	0.22	14	19	32,000	19
6a	No	80	30	0.15	12	15	30,000	15
	Yes	78	37	0.36	28	41	99,000	17
6b	No	48	23	0.10	4.6	7	10,000	15
	Yes	72	29	0.12	8.6	12	22,000	15
6c	No	86	30	0.11	9.3	12	23,000	15
	Yes	89	38	0.13	12	17	41,000	13

rate of reactants, which can not be identified if some fraction is escaping through the tip of the flame unburned. This problem was avoided by building the larger co-flow shown in Fig 2.1, which has a diameter approximately five times that of the central jet.

To illustrate the problem, examples of an insufficient co-flow and a sufficient co-flow [62] are shown in Fig. 2.3. The left column shows CH-PLIF and the right shows OH-PLIF, which mark the reaction layer and the products region, respectively. In the top row, OH-PLIF is seen downstream of all of the reaction surfaces, providing back-support to the flame by way of hot radicals and elevated temperature throughout the products region. In contrast, significant gaps are seen in the OH-PLIF signal in the lower row, indicating entrainment of cold air that is being brought into contact with the reaction surface. This disrupts the 1-D laminar chemistry that would ideally exist in a flame with sufficient back-support. The result is extensive extinction of the CH-PLIF reaction layers. By using a large co-flow in the Hi-Pilot experiment, this problem is avoided; the temperature is sufficient downstream of the reaction layer such that a one-dimensional profile of the flame temperature and species should be equal to that of the laminar flame.

2.2 Laser Doppler Velocimetry

The axial component of velocity U, turbulence level (R.M.S., or fluctuation, velocity) u', and integral scale L_x were evaluated using Laser Doppler Velocimetry (LDV). The measurement principle makes use of the fringe pattern that will occur when two laser beams intersect obliquely. Fig 2.4 illustrates the fringe pattern phenomena. The region where the beams intersect is called the probe volume, and the measurement is an average over this domain. The flow is seeded with tracer particles, which are assumed to follow the flow exactly. As the particles pass through the fringes, they will scatter the light at a frequency proportional to their velocity. Therefore the particle velocity can be computed as $u = f * d_f$, where d_f is the fringe spacing.

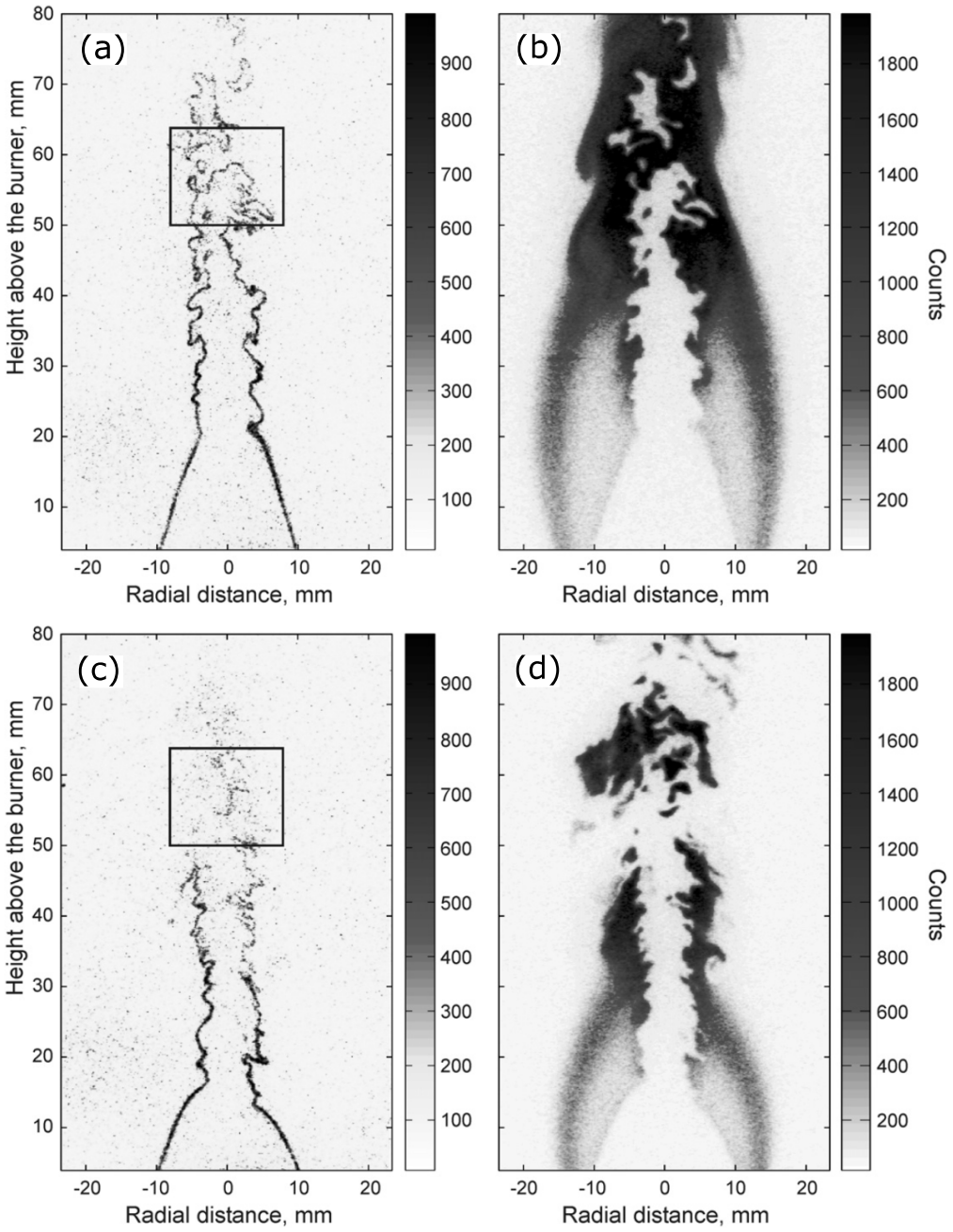

Figure 2.3: Example of a co-flow that is (a) insufficient, producing extinction events, and (b) sufficient, such that the reactions are maintained across the flame surface and there is a uniform region of OH downstream of the flame. The figure is taken from [62].

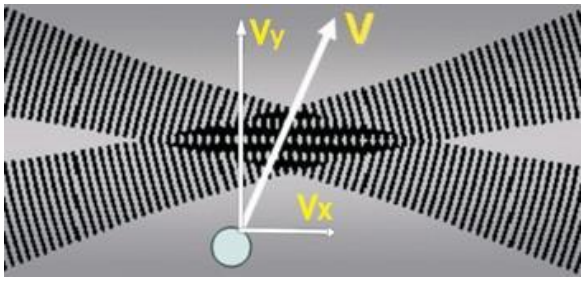

Figure 2.4: LDV fringe pattern. Courtesy of Per Petersson. [95]

In Fig 2.4, note that only the component of velocity normal to the fringe pattern will be detected; thus, it is possible to underestimate the velocity if the laser beams are misaligned. It is also important to note that particles with negative velocity cannot be detected in the standard setup; if the two intersecting beams have the same wavelength, the fringe pattern will be stationary, and a backwards and forwards moving particle would be indiscernible. This problem is often avoided by using a Bragg cell, which is an acoustic modulator that increases the frequency of one of the laser beams, typically by around 40 MHz. This creates a moving fringe pattern, providing a surplus frequency to the measured signal in addition to that due to particle motion. Thus, a particle can move counter to the mean flow and still be detected, so long as the scattered frequency is less than the frequency shift of the Bragg cell. A Bragg cell was not used in this work; however, due to the very large jet velocities, it is not expected that negative axial velocities will occur very frequently, and is therefore unnecessary.

The laser/optic assembly consisted of an Argon-Ion laser emitting continuous-wave 514.5 nm at 0.56 W, which was passed through a beamsplitter and focused to a focal volume over the test section with a 249.5 mm lens. This provided a fringe spacing of 2.58 micrometers. Doppler-shifted Mie scattering from the particles was collected with a photomultiplier tube affixed with a 124.5 mm lens. TSI optical lenses and PMT were used, and the particle bursts were processed with TSI Flowmaster hardware and software. Light was detected by the PMT in forward scattering mode, in order to maximize the collected signal. Maximum scattering intensity occurs approximately 180 degrees from the angle of inci-

dence for small particles, however placing the PMT in the path of the laser beam provided unwanted measurement noise. Therefore, the PMT was typically placed at about 10-15 degrees off axis, which compromises some signal but greatly reduces the noise.

2.2.1 LDV Tracer Species Considerations

PIV particles must be sufficiently small to track the turbulent fluctuations while being large enough to provide sufficient light scattering for a strong signal. Melling [78] shows that for an excitation wavelength λ (532 nm in this case), the Mie scattering obtained from particles of $d_p \geq \lambda$ is generally adequate. The tracer species chosen were 0.5 µm alumina oxide (Al_2O_3) particles from Microgrit. Thus the 0.5 µm (or 500 nm) particles provided sufficient scattering. The flow-tracking condition can be evaluated by comparing the characteristic settling time of a particle to the time scale of the flow. The particle settling time is determined by assuming the spheres are in a regime of Stokes flow due to their small diameters ($Re_D < 1$). Under this assumption, the characteristic particle time is the Stokes time [37]:

$$\tau_p = \frac{\rho_d d_p^2}{18\mu}. \tag{2.3}$$

Using the appropriate particle density and diameter, and evaluating the viscosity of air at 298 K, the resulting particle time is $\tau_p \sim 3.65\ \mu s$. The characteristic flow time is estimated for PIV measurements by Melling [78] as:

$$\tau_f = 10\frac{\delta}{\Delta U} \tag{2.4}$$

In the above, δ should be taken as the smallest resolved length scale of the PIV measurements (see Section 2.3), while ΔU is the largest estimated velocity. The corresponding values in this experiment are approximately 0.288 mm and 89 m/s, thus providing a flow time of $\tau_f \sim 32.36\ \mu s$. Taking the ratio of the two time scales, and defining the Stokes Number:

$$Stk = \frac{\tau_p}{\tau_f} \sim 0.11 \tag{2.5}$$

Clemens and Mungal [34] suggest a criterion for PIV measurements that Stk < 0.5, which is satisfied for the current conditions. This analysis can be assumed to apply approximately to the LDV measurements as well, and therefore the particles chosen can be trusted to faithfully track the flow. LDV measurements were performed for all test cases in Table 2.1, and the results will be presented in the following chapter.

2.2.2 Integral scale measurements

A fundamental measure of the structure of a turbulent flow is the integral length scale, and some background discussion of this topic is required here. The LDV measurements provide a temporal measurement of the axial velocity at a single point, allowing computation of the temporal autocorrelation. The autocorrelation is a function that describes the structure of the turbulence, and is essentially a measure of how correlated a turbulent quantity remains over a certain interval in time or space Δ [98]. The temporal autocorrelation is defined here using the fluctuating velocity $u'(t) = U - u(t)$ and is:

$$R(\Delta t) = \frac{\overline{u'(t)\,u'(t+\Delta t)}}{\sqrt{\overline{u'(t)^2}}\sqrt{\overline{u'(t+\Delta t)^2}}} = \frac{\overline{u'(t)\,u'(t+\Delta t)}}{u_{rms}^2} \tag{2.6}$$

In Eqn. 2.6 the denominator is re-written as u_{rms} on the right-hand-side, the root-mean-square of the fluctuating velocity. It is assumed that the turbulence is stationary and therefore does not change with the lag time Δt. The autocorrelation describes the correlation of a point with its surroundings, and therefore decays from unity until it reaches zero. In weakly turbulent flow, nearby regions will remain relatively strongly correlated, while very turbulent flow becomes uncorrelated much more quickly. Fig 2.5 illustrates this difference for small and large turbulent Reynolds numbers, respectively. Note that a spatial autocorrelation performed with PIV may appear like the low Re_T case at small values of Δt because

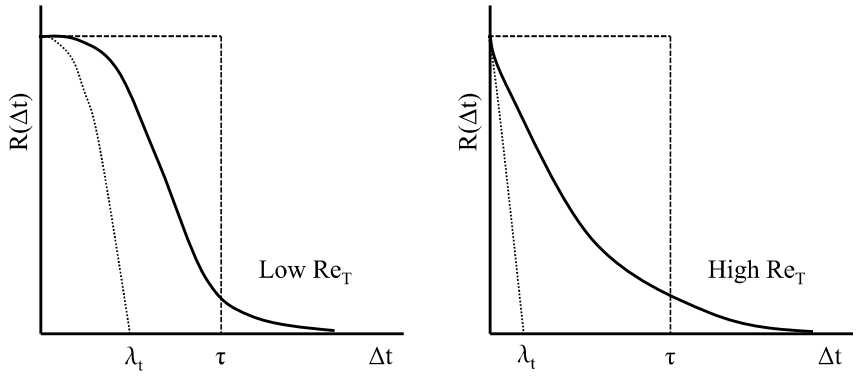

Figure 2.5: Example temporal autocorrelation function for low and high turbulent Reynolds number cases

the method averages velocities over the size of the interrogation window, therefore imposing correlation on the data. The question of resolution requirements in PIV measurements will be addressed later in Section 2.3.3.

The temporal integral scale is defined as the integral of the autocorrelation over its full domain. That is:

$$\tau = \int_0^\infty R(\Delta t)\, d\Delta t \tag{2.7}$$

As can be inferred from the physical meaning of the autocorrelation function, the integral scale measures the distance required for a turbulent quantity to *become* uncorrelated. It has an analog, called the Taylor scale, which measures the maximum distance over which a turbulent quantity *remains* correlated. The Taylor scale is defined as:

$$\lambda_t^2 = -2/\left(\frac{d^2R(\Delta t)}{d\Delta t^2}|_{\Delta t=0}\right) \tag{2.8}$$

Fig 2.5 shows that it can be physically inferred from the shape of the autocorrelation function as a parabola beginning at (0,1) having identical curvature at the origin as $R(0)$. The Taylor scale is an important quantity for PIV measurements, and will be returned to in

section 2.3.3.

Eqn 2.7 provides a measure of the temporal integral scale, which is measured directly from the LDV. However, the quantity of interest in most turbulence and combustion applications is the integral length scale, L_x. The subscript x denotes the longitudinal (flow) direction, which in this case provides a longitudinal integral scale. As an aside, a longitudinal integral scale is one in which the velocity component in the autocorrelation function is identical to the direction of integration. A lateral scale would, using two-dimensional spatial measurements for example, require integrating the autocorrelation function $R_u(x,y)$ over the radial direction r. Because these LDV measurements only measure a single component of velocity, only longitudinal integral scales may be obtained. PIV measurements to be discussed later will measure longitudinal and lateral scales.

In order to convert temporal scales to spatial scales, it is common to employ Taylor's hypothesis, which assumes that the turbulent features are frozen as they convect past the probe volume. The formal definition begins by considering a fluctuating velocity (in an arbitrary direction-i) $u_i^{'}$ in a turbulent field being convected locally in the x_1-direction by mean velocity U_1. Using index notation:

$$-\frac{\partial u_i^{'}}{\partial t} = U_1 \frac{\partial u_i^{'}}{\partial x_1} + u_j^{'} \frac{\partial u_i^{'}}{\partial x_j} \tag{2.9}$$

If the turbulence level is small relative to the mean velocity, $u'/U \ll 1$, the third term in Eqn 2.9 becomes insignificant. This is Taylor's hypothesis, and is written as:

$$-\frac{\partial u_i^{'}}{\partial t} = U_1 \frac{\partial u_i^{'}}{\partial x_1} \tag{2.10}$$

Eqn 2.10 states that a temporal derivative of u' is proportional to its spatial derivative through the mean velocity U. The form that is often used for converting temporal scales to length scales is $L_x = \tau U$. However, a turbulent flow will be embedded with a wide range of eddy sizes, all propagating at a different velocity, with the smallest scales generally moving

very slowly. The mean velocity U is an average over the entire turbulence spectrum, and therefore the convection velocity of the largest (integral scale) eddies may be much larger than the flow's mean velocity. Using this concept, Heskestad derived [59] a correction to Taylor's hypothesis by modifying the mean velocity in Eqn. 2.10. Essentially, this correction accounts for the difference between the eddy convection velocity and the flow mean velocity, which should be a function of fundamental turbulence quantities. The analysis of Heskestad relates mean-square time derivatives with their spatial equivalent, but can be applied to measured integral scales [52, 59, 66, 86, 138]:

$$L_x = \tau U \left[1 + \frac{\overline{u'^2}}{U} + 2\frac{\overline{v'^2}}{U^2} + 2\frac{\overline{w'^2}}{U^2} \right] \tag{2.11}$$

If the flow can be approximated as isotropic, then this can be simplified to:

$$L_x = \tau U \left[1 + \frac{\overline{u'^2}}{U} + 4\frac{\overline{v'^2}}{U^2} \right] \tag{2.12}$$

Eqn. 2.12 was used to transform the measured temporal integral scale τ into a longitudinal integral length scale L_x. However, it should be noted (and will be discussed in detail in the following chapter) that although Taylor's hypothesis will underestimate the integral length scale, the approximation of Eqn. 2.12 will *overestimate* L_x if the flow is not isotropic [136].

2.2.3 Calibration in a turbulent pipe

The LDV system was first tested in a fully developed turbulent pipe flow in order to compare the measurement and processing procedure with a relatively well-understood problem. A ½" Swagelok tube was used, along with compressed dry air and a previously built seeder [3]. 5 micrometer alumina-oxide Zerospheres (manufactured by 3M) were used as the seed particles. As was discussed in Section 2.2.1, these are larger particles than were used to seed the Hi-Pilot experiment, but were found to adequately track the less turbulent

$U(m/s)$	u'/U	$L_x(mm)$	L_x/D
78.3	4.15%	3	27%

Table 2.3: Measurements

flow in the pipe.

A 0.104" diameter choked orifice from O'Keefe was used to meter the flow, and a pressure tap taken downstream confirmed the critical pressure ratio across the orifice was met. Data was collected at 5 flow rates, but only the highest flow rate was selected for analysis. The measurement consisted of 4 runs, each of which collected 100,000 data points. At low velocities, the measured velocity matches the mass-average velocity well. However, the values diverge at higher flow rates. This may imply that the orifice coefficient is not properly calibrated.

Data was independently sampled with a digital oscilloscope (taken post bandpass filtering), and it was found the frequency of the Doppler bursts matched closely with the mean Doppler frequency reported by the system. This confirmed proper operation of the burst correlator device. Integral length scales were calculated using the method outlined above. Note that for the relatively weak turbulence of this case, the correction to Taylor's hypothesis did not change the measured value of L_x.

Due to convective-acoustic instability, it was necessary to low-pass filter the data at 4700 Hz to avoid erroneous correlations. The turbulence intensity for the combined data sets was 4.15%. The integral length scale was computed to be approximately 3 mm, which is roughly 30% of the pipe exit diameter. This value, along with the measured turbulence intensity, is in line with the data reported in Hinze [60].

2.3 Particle Image Velocimetry

Planar two-component velocity measurements were computed on centerline using particle image velocimetry (PIV). This measurement served three purposes: (1) to provide velocity

data within a broadened preheat layer, which will be the subject of Chapter 6, (2) to measure the degree of anisotropy in the Hi-Pilot, with a direct measurement of the longitudinal and lateral integral scales L_x and L_r, and (3) to estimate the accuracy of the isotropic correction to Taylor's hypothesis (Eqn 2.12) in the LDV turbulence measurements.

2.3.1 Principle of PIV

The PIV technique utilizes successive images of flow tracer species, typically oil droplets or metal particles illuminated by a laser sheet. A sensor array that records the images (CCD CMOS or, formerly, film) is then divided into smaller regions called interrogation boxes [99]. The PIV method requires finding the most probable displacement of that interrogation box between the two frames. Fast Fourier Transform-based (FFT) correlation algorithms compute the probability of each possible particle displacement, and generate a three-dimensional probability map with the elevation z corresponding to the probability of the displacement at that $x-y$ location. In a good PIV data set with minimal particle drop-out (where particles in frame 1 convect out of the plane of the laser sheet and are not present in frame 2) and an average particle displacement of approximately 7 pixels, the correct peak (that is, the peak corresponding to the true particle displacement) should be much larger than the neighboring displacement values. This process is illustrated in Fig. 2.6.

2.3.2 Experimental details

In this experiment, a pair of Nd:YAG lasers were used to provide 532 nm sheets, and a LaVision Imager Pro 2048x2048 pixel CCD camera recorded the elastically scattered light from the particles. The seed particles were different from that used by the LDV. After some trial-and-error, it was found that the 0.03 μm Al_2O_3 (activated alumina-oxide to minimize agglomeration) particles from Electron Microscopy Sciences optimized seed density and tracking ability while minimizing agglomeration. These particles were smaller than those

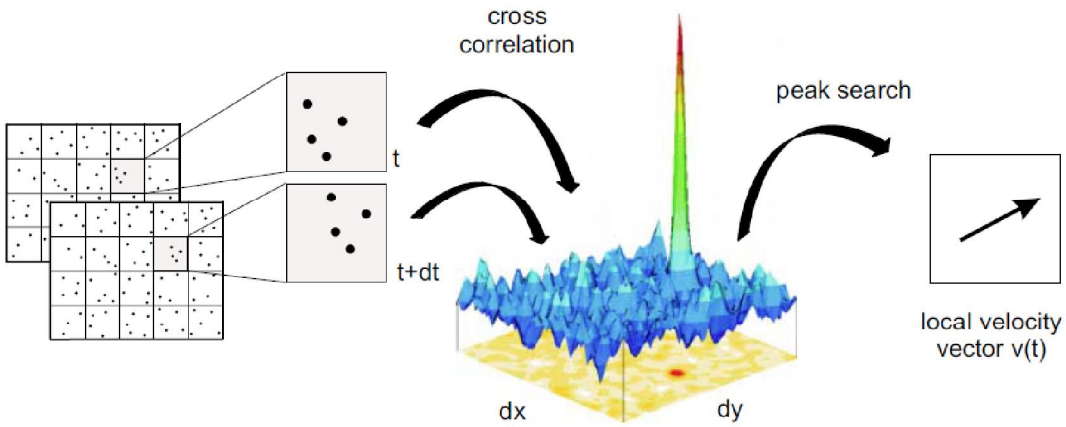

Figure 2.6: Illustrative example of the PIV method. Particles are identified and interrogation regions are selected. A FFT algorithm computes the probability of each displacement. The highest peak in the resulting elevation map corresponds to the velocity vector, which is an average over the interrogation box domain. Taken from LaVision Flowmaster manual [68].

used in the LDV measurements, so the critical Stk number analysis applies here as well.

2.3.3 Resolved scales of the PIV

Accurate PIV measurements requires sufficient resolution of the large and small scales in the flow. However, in a highly turbulent flow fully resolving both the largest and smallest scales is not a simple task. With increasing turbulence, Table 2.2 shows that the integral scale generally increases, due to the larger mean velocity. However, the larger Re_T at these conditions increases the separation between the largest and smallest scales of the flow, meaning that a field of view capable of capturing the integral scale L_x may not have the resolution required to capture the Kolmogorov scale η_k.

Lavoie et al [69] suggest a domain approximately five integral scales in length is necessary to resolve L_x. O'Neill et al [87] performed a comparison between integral scales computed from PIV, with a domain length three times L_x, and DNS results in which the domain from which integral scale computation was performed was reduced progressively from eight to two times L_x. O'Neill found a difference in the shape of the autocorrelation

computed from the DNS data when changing from a domain that was $4.5L_x$ to $8L_x$, suggesting that the smaller domain is not sufficient. In addition, the autocorrelation for the PIV rolled off faster than the DNS, even when the DNS used the smallest domain of $2L_x$, suggesting the PIV measurements could not capture the largest scales with a domain of $3L_x$. However, although the shape of the autocorrelation function was clearly different, the magnitude of difference of the integral (i.e., L_x) was similar. In this work, it is assumed that a field of view twice the L_x is sufficient to capture the integral scales.

In turbulence theory, the Kolmogorov scale is the smallest scale in the velocity field over which a gradient may be sustained [128]. However, experiments have shown that resolution of the Kolmogorov scale is not necessary to accurately measure velocity gradients, and that the actual scale where dissipation of kinetic energy occurs (and hence the smallest "real" scales in the flow) is the viscous scale λ_v [69, 104]. The viscous scale is computed using [24, 25]:

$$\lambda_v = \Delta L Re_L^{-3/4} \tag{2.13}$$

where $\Delta = 11.2$ and is determined empirically, and L is the integral scale computed using the full width of 5% of the maximum of the velocity profile of the jet. The relationship between the viscous scale and the Kolmogorov scale is given by Friehe et al [50] who examined kinetic energy dissipation data in a round jet and found $\lambda_v = 6\eta_k$, where η_k is the Kolmogorov scale [128]. Therefore, it is argued that the turbulence is fully resolved with a resolution sufficient to capture the viscous scale, even if the Kolmogorov scale is not resolved, because the viscous scale corresponds to the smallest physical scale in the flow. In the Hi-Pilot, these range in size from approximately 335 μm to 64 μm. Thus, in order to resolve the smallest scales of flow for the most turbulent run conditions, the Nyquist sampling criteria requires a PIV interrogation window of at most 32 μm. Lastly, it is noted that the requirement for accurately measuring the mean velocity field in PIV is an interrogation box size of one-half the Taylor scale λ_t [51].

Thus, we can outline the resolution requirements for a PIV experiment under two cases. In the case that the measurement must capture all scales of turbulence (in order to measure velocity gradients such as dissipation), the largest and smallest scales must both be resolved. This means that the field of view must be at least $2L$ in length, combined with an array size and interrogation box combination suitable to resolve the viscous scale λ_v. In the case that the experiment only needs to measure the mean velocity, the turbulence level u' and the integral scale, then only the Taylor scale λ_t need be resolved. In a turbulent flow with a wide separation of scales this is a significantly relaxed requirement [51].

Due to the very large separation of scales in this experiment, several of the run conditions could not be fully resolved by the PIV. For example, a representative integral scale for Case 5 will be shown to be at least $L_x > 10$ mm with a turbulence level u' around 25 m/s (see the following chapter). Thus, the smallest possible acceptable field of view would be 20 mm, and if the interrogation window is 16x16 pixels, the smallest resolved scale would be approximately 300 μm (the camera CCD array consists of 2048x2048 pixels). This is sufficient to capture the Taylor scale, which would be about 425 μm. However, this is much larger than the viscous scale $\lambda_v$which is less than 80 μm.

2.3.3.1 Integral scale measurements in PIV

The autocorrelation function was previously defined for temporal measurements as $R(\Delta\tau)$. The spatial autocorrelation is defined similarly, and is written as:

$$R_u(\Delta x \Delta r) = \frac{\overline{u'(x,r)\,u'(x+\Delta x, r+\Delta r)}}{\sqrt{\overline{u'(x,r)^2}}\sqrt{\overline{u'(x+\Delta x, r+\Delta r)^2}}} = \frac{\overline{u'(x,r)\,u'(x+\Delta x, r+\Delta r)}}{u_{rms}^2} \tag{2.14}$$

The spatial autocorrelation function R_u is presently defined in the axial direction, as it contains only velocities in the $x-direction$. It can also be defined using velocity fluctuations in the $r-direction$, and would then be called R_r. The longitudinal integral scale is

defined as the integral of the spatial autocorrelation function in the same direction as the component for which it was defined. The lateral (or transverse) integral scale is defined by integrating in the orthogonal direction to the component for which R is defined. For an autocorrelation function R_u, the integral in the $x-direction$ is the longitudinal integral scale, and integrating in the $r-direction$ provides the lateral integral scale. Using this nomenclature, the longitudinal integral scales L_x and lateral integral scales L_r are defined as:

$$L_x = \int_{\Delta x=0}^{\infty} R(\Delta x, \Delta r = 0) d\Delta x \tag{2.15}$$

$$L_r = \int_{\Delta r=0}^{\infty} R(\Delta x = 0, \Delta r) d\Delta r \tag{2.16}$$

2.4 Planar Laser Induced Fluorescence

Modern laser diagnostics are capable of high resolution measurement of combustion radicals, and the most popular technique is currently Planar Laser-Induced Fluorescence (planar LIF or PLIF). Fluorescence is the spontaneous emission of radiation from an upper energy level of an atom or molecule after it has been excited in some way [45]. This is most often applied in combustion diagnostics through laser-induced excitation (almost always in the ultra-violet) of an electronic energy state. Typically the wavelength of the emitted light is shifted from that of the excitation source, but this is not required.

If the laser irradiance is much less than what will saturate the fluorescence, then the measurement is in the linear regime and the LIF signal is proportional to the amount of the species present in the probed sample. The governing LIF equation in this regime [45] is given in Eqn 2.17

$$F = \frac{h\nu}{c} \frac{\Omega}{4\pi} \ell A N_1^0 B_{12} I_\nu \frac{A_{21}}{A_{21} + Q_{21}} \tag{2.17}$$

where F is the fluorescence signal power, h is Planck's constant, ν is the frequency of the emitted signal, Ω is the collection solid angle, and ℓ is the distance along the laser propagation axis over which fluorescence is collected. A is the focal area of the laser beam, N_1^0 is the species population in the electronic ground state prior to excitation, B_{12} is the Einstein coefficient for absorption, I_ν is the irradiance of the laser beam, A_{21} is the Einstein coefficient for spontaneous emission, and Q_{21} is the collisional quenching rate constant.

If all of these can be accurately measured, than it is possible to precisely measure the quantity of the LIF species. However, the goal of this work is to identify the flame structure, and how it evolves in extreme turbulence. Although quantitative PLIF measurements would provide a measure of the heat release rate (of a given reaction), it would not change the qualitative observed trends of whether a layer is broken or the thickness that exists. Therefore, the PLIF measurements in this work will accurately report if a species (or reaction) is occurring, and the PLIF intensity provides a qualitative sense of the relative concentration. However, no quantitative species concentration or reaction rate data can be extracted from this measurement.

2.4.1 Simultaneous OH and CH_2O PLIF

2.4.1.1 Overlap Chemistry

The flame structure was visualized using simultaneous OH and formaldehyde (CH_2O) PLIF. The reaction zone thickness is defined to be the width of the CH_2O-OH overlap layer at 50% of its maximum value (FWHM). Previous studies [10, 11, 16, 47, 61, 82, 83, 90, 101, 102, 130, 139] have also used the overlap of OH and CH_2O or HCO to define the reaction layer. This is because the primary pathway for HCO production (and subsequently heat release) involves reactions with CH_2O and OH. Specifically, OH + CH_2O => HCO + H2O, and thus the rate of production of HCO is proportional to [OH]x[CH_2O]. Figure 2.7 shows CHEMKIN profiles calculated for a freely propagating, laminar, premixed methane-air flame (ϕ = 0.75). The simulations show that the heat release profile nearly coincides

with the Overlap profile. However, it should be noted that the PLIF signals are uncorrected for electronic quenching or Boltzmann population fraction. The thickness of the reaction layer ($\delta^0_{RZ,L}$) was found to be 0.18 mm in the CHEMKIN simulations of a premixed laminar flame.

Li et al. [71] showed that CH_2O can also be used as a marker of the preheat zone. The leading edge of the preheat zone is defined to be where CH_2O concentration is 35% of its maximum, and CHEMKIN simulations indicated that the gas temperature here is 550 K. This temperature establishes the upstream boundary of the preheat zone. The preheat zone thickness is then defined as the width of the CH_2O signal from the leading edge on the reactant side to the start of the reaction zone (defined above as the local half-maximum value on the reactant side). The un-stretched, laminar value of the preheat zone thickness ($\delta^0_{PH,L}$) computed by CHEMKIN was 0.36 mm.

2.4.1.2 Overlap Diagnostics

Simultaneous planar laser induced florescence (PLIF) images of the formaldehyde molecule (CH_2O) and the hydroxyl radical (OH) were acquired using two Andor iStar intensified CCD cameras binned (2 x 2) to 512 x 512 pixels and firing at 2.5 Hz. The formaldehyde (CH_2O) was excited by the third harmonic of a Spectra-Physics Nd:YAG laser operating at 355 nm and approximately 135 mJ/pulse, through a series of pQ transitions in the 4^1_0 vibrational band. The returning CH_2O fluorescence was filtered using a high and low pass filter (Semrok BLP01-364R and FF01-533/SP, respectively) transmitting wavelengths between 364 and 533 nm.

The OH beam was excited using a second Spectra-Physics Nd:YAG laser pumping a Sirah dye laser. The dye was tuned to output 568 nm and then doubled using a BBO crystal to 284 nm, to excite the $P_1(5)$ transition of OH in the $A^2\Sigma^+ - X^2\Pi(1,0)$. Typical laser power for the OH excitation was 4.5 mJ/pulse. The camera capturing OH fluorescence was equipped with an Asahi Spectra bandpass filter centered at 310 +/- 5 nm. Gate times

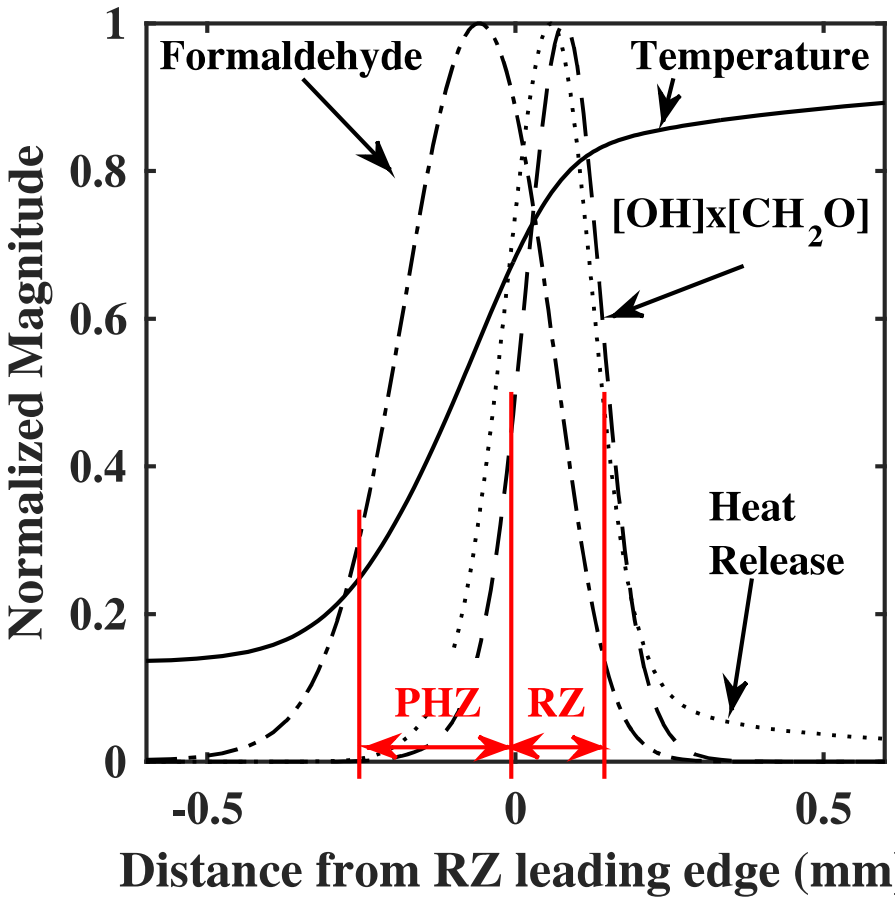

Figure 2.7: CHEMKIN simulation for a laminar methane-air flame ($\phi = 0.75$). Note that the Overlap profile coincides with the heat release region, formaldehyde marks the preheat layer very well, and the preheat zone is only approximatley two or three times the reaction zone thickness.

for both cameras were limited to 100 ns to minimize flame chemiluminescence, and the laser pulses were separated by 200 ns to avoid cross-talk [100]. A diagram depicting the simultaneous PLIF imaging setup is provided below in Figure 2.8. Note that for the sake of clarity only one set of sheet forming optics is shown; however, the OH and CH_2O laser sheets were formed with two separate sets of sheet-forming optics, and were overlapped before being focused over the burner centerline.

In order to obtain accurate Overlap measurements, a small FOV providing high resolution was required. The FOV for these measurements was 30 × 30 mm^2, and the spatial resolution (derived from the binned pixel size and laser sheet thickness) was 59 × 59 × 200 μm^3. The resolving power of the camera is different from the binned pixel size, and was measured using the scanning knife edge technique [35]. The resolving power of the formaldehyde and OH cameras was approximately 150 μm. Recall that the CHEMKIN simulations showed a reaction zone thickness for the lean methane-air flame of approximately $\delta^0_{RZ,L}$ = 180 μm. Thus, the resolving power of the system should be adequate to capture the thin layers. However, as will be shown below, the actual reaction layer thickness in most experiments (including this one) is much larger than predicted by CHEMKIN. This means that the estimate of the system resolution is relatively conservative.

2.4.1.3 Background corrections

PLIF images were first processed with a series of background corrections. The sources of noise in a recorded PLIF image are discussed by Clemens [35] and are (1) the "dark" noise in the CCD circuit, which is reduced by water-cooling the intensified cameras; (2) scattered light from the laser (either Rayleigh signal or reflections) that is captured during the recording; and (3) luminosity from the flame. The noise signal generated by laser scattering and flame luminosity are measured by taking a set of images with the laser present and no flame, and with the flame present with no laser, respectively. These are called the laser background B_{laser} and flame background B_{flame}. The dark noise is measured by taking a

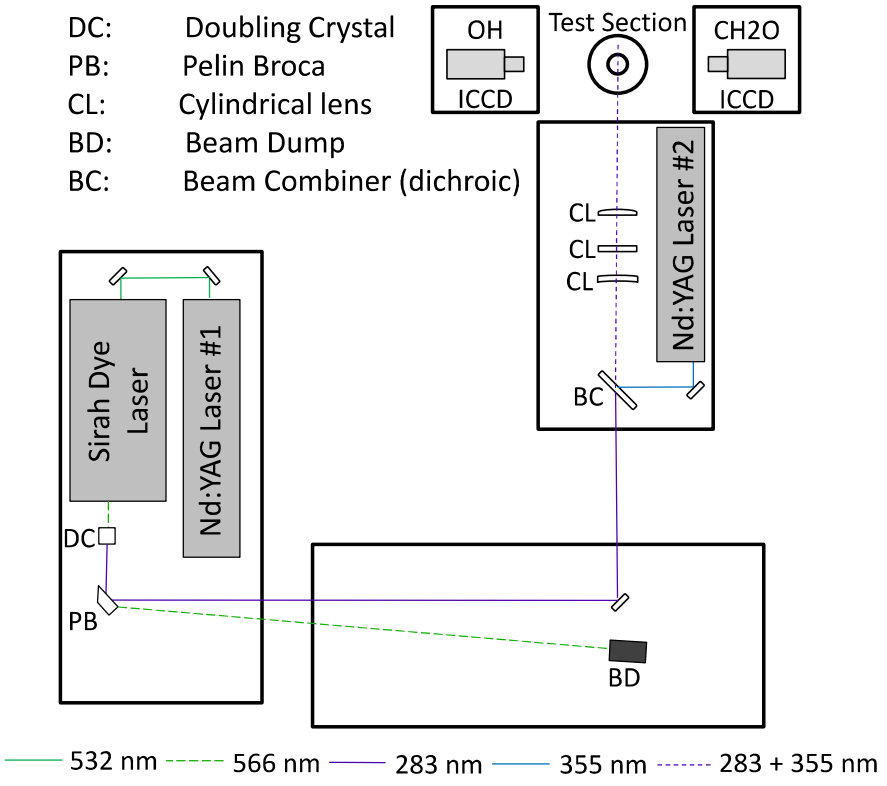

Figure 2.8: Schematic of the Michigan OHxCH_2O Overlap diagnostic system

set of images with the room lights off and the lens cap covering the camera lens, and is called the dark background B_{dark}. However, the dark noise B_{dark} is present any time the CCD is active, which means that it is superimposed on both B_{laser} and B_{flame}. Therefore, if the measured intensity of the CCD is I, the corrected signal S can be obtained as [109]:

$$S = \frac{I - (B_{laser} + B_{flame}) + B_{dark}}{LW} \tag{2.18}$$

In Eqn. 2.18, L is the laser sheet profile, which was recorded using a dye cell following each data campaign, and W is the white background. W is measured by imaging a uniform surface (such as a panel of frosted glass or a back-lit display) and represents how much variation is produced on the image from a non-varying source. This can be particularly significant in the corners of the image due to the vignetting effect of the optical system.

2.4.1.4 Image Processing

The reaction layer thickness is defined using the full-width at half-maximum of the pixel-by-pixel product of the OH and CH_2O images. However, due to noise present in the raw PLIF images as well as large spatial variation in signal intensity, the raw Overlap signal is not of a desirable quality. Fig. 2.9 below illustrates the issue. In (a) and (b) are the raw OH and CH_2O PLIF images, respectively, after application of the background corrections of Eqn. 2.18. The raw Overlap signal is given in (c), and in this case a global threshold (50% of the maximum Overlap signal in the image) is used. It would be very difficult to extract any useful measurements from this reaction layer. There is Overlap signal far way from the flame surface, for instance in the right-hand region of the image where the OH PLIF signal is clearly at zero. Additionally, the large pocket region (approximately three quarters of the way up in the center) is entirely filled with signal, and it is difficult to tell by inspection if this is accurate. Part of the problem is understood by referring back to the one-dimensional flame chemistry, given in Fig. 2.7, which shows that the OH concentration is at a maximum where the formaldehyde signal should be zero (fully consumed in the

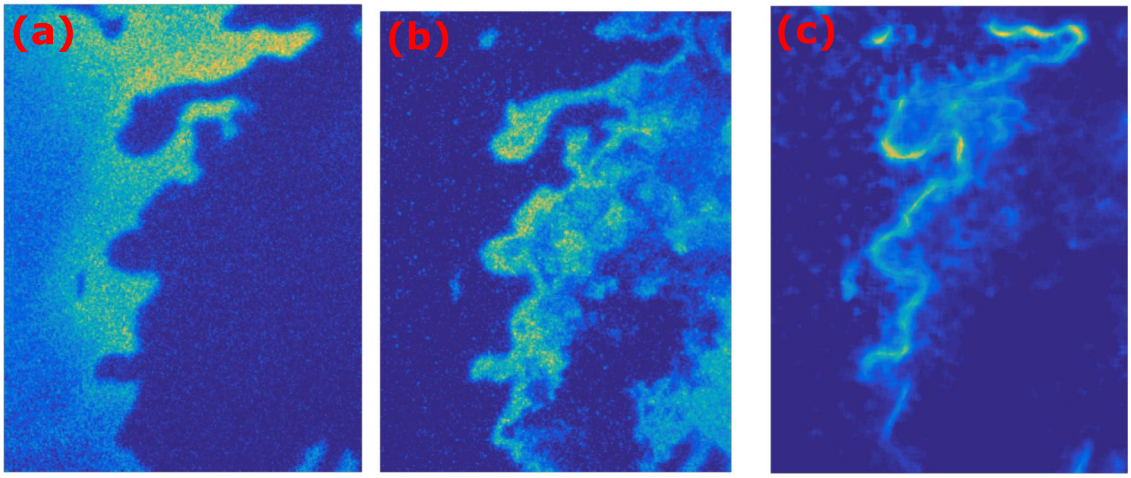

Figure 2.9: Example of image processing problems. (a) raw OH and (b) raw CH_2O PLIF images, after background subtraction. (c) raw Overlap signal.

products), and vice versa. However, if there is a noise "floor" below which the signal cannot drop, then this noise will be greatly amplified in regions even very far way from the flame. This is particularly challenging in pocket/cusp regions, where this error can produce a flamelet-like reaction layer that appears like a distributed region.

In order to overcome these inherent difficulties to the Overlap method, a novel image processing algorithm was developed. To eliminate salt-and-pepper noise in the raw OH and CH_2O PLIF images, the background correction of Eqn. 2.18 was followed by a 5 pixel $\times$ 5 pixel median filter. Level-set filtering was then applied in order to enhance the signal-to-noise of the PLIF images. Level-set filtering is a non-linear filtering technique similar to anisotropic diffusion filtering, which was used by Bockle [16] to produce high quality Overlap images. The effect of the level-set filtering on the measured layer thicknesses will be addressed below in Section 2.4.1.6. It is found that the filtering causes a net change of approximately 1% to the Overlap layers.

At this point, the OH images were transformed onto the reference frame of the CH_2O image, so that the pixel-by-pixel product could be obtained. To do so, an imaging target consisting of a series of crosses was imaged with each camera. The corresponding cross was identified in each target image, and a transformation matrix was generated that prop-

erly registered the OH image onto the CH_2O image. The precision of the transform was evaluated by comparing the transformed OH target-image with the CH_2O target-image, and it was found that the method produced sub-pixel accuracy ($> 59\,\mu m$).

The Overlap layers are then obtained from the pixel-by-pixel product of the background-corrected, filtered, and transformed OH and CH_2O images. A local thresholding technique was developed, and this consisted of three steps. First, a watershed algorithm [80] was applied to the Overlap signal in order to produce a series of ridge points. The watershed algorithm essentially considers the Overlap signal as an elevation map, and finds the locus of points from which water would drain if the surface were covered with water. These ridge points form a skeleton along which the Overlap signal is a local maximum. Next, the signal of each point in the Overlap image is compared with the signal at the nearest ridge point; if it is less than 50% of this local maximum, the signal at the point is set to zero. Lastly, these steps are iterated two additional times, with the updated (thresholded) image from the previous iteration as the input for the next cycle. The result is a locally-thresholded image that accurately captures the full-width at half-maximum of the Overlap layers. This technique is illustrated in Fig. 2.10.

In Fig. 2.10(a), the raw Overlap signal is used in the first iteration of the local-thresholding method. In (b), a skeleton of ridge points is obtained from (a). Finally, the Overlap image (a) is thresholded using the skeleton of (b), in order to produce the locally-thresholded Overlap layer of (c).

Once the Overlap images were properly thresholded an average reaction layer thickness was calculated for each image as follows. First, the distance between each pixel on the skeleton and the nearest pixel on an edge of the reaction zone was determined (i.e., the distance is half the thickness). Then, these distances where multiplied by a factor of two to account for the fact that the skeleton lies along the center of the reaction zones. Finally, summing these distances over the whole skeleton in a particular image and subsequently dividing this summation by the length of that skeleton produced an average thickness value

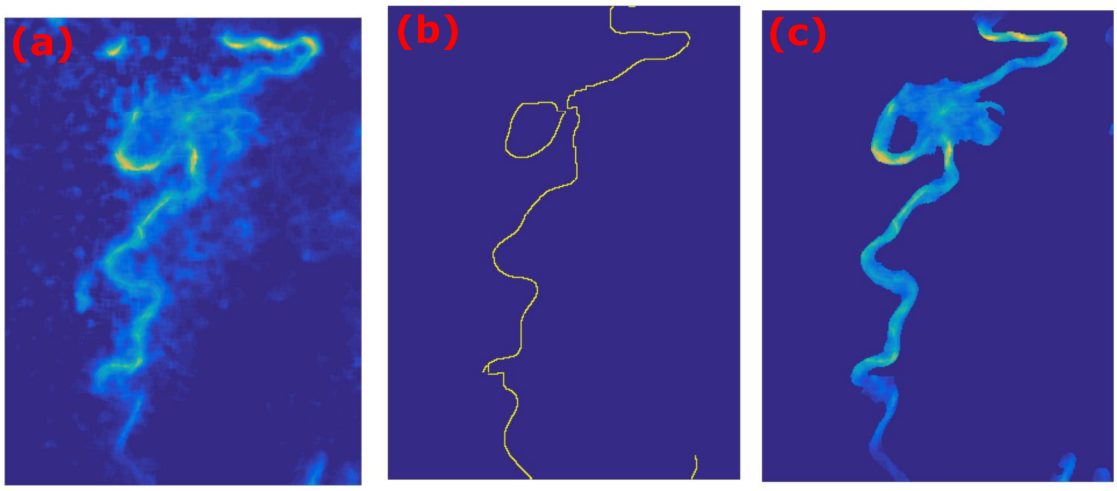

Figure 2.10: The solution to the obtaining an accurate Overlap signal entails local thresholding using a skeleton containing local maximas. (a) is the raw Overlap signal, (b) is the skeleton for the raw Overlap signal, and (c) is the resulting processed Overlap signal using the skeleton of (b) to provide local thresholding.

for that image.

2.4.1.5 Obtaining the preheat layers from the Overlap PLIF measurements

The preheat zone region corresponds to the CH_2O PLIF signal, as discussed in Sec. 2.4.1.1. In order to obtain the preheat layers from the Overlap PLIF measurements, the CH_2O images are processed following the steps outlined in Sec. 2.4.1.4, that is they are background-corrected and filtered. The preheat zone is defined as beginning at 35% of the local maximum of CH_2O signal, and continues up to the leading edge of the reaction zone. Therefore, the local-thresholding algorithm described in Sec. 2.4.1.4 was applied to the CH_2O PLIF images, except they were thresholded at 35% of the local maximum. The processed Overlap images were then subtracted from the resulting thresholded CH_2O PLIF signal, producing an image of the preheat zone. The average preheat zone thickness for a specific image was computed in a similar fashion as to the reaction layers.

		$\phi = 1.05$	$\phi = 0.65$
δ_{RZ}	Measured	0.36	0.52
	CHEMKIN	0.15	0.22
δ_{PHZ}	Measured	0.39	0.45
	CHEMKIN	0.24	0.49

Table 2.4: Measured and simulated laminar layer thicknesses in millimeters

2.4.1.6 Laminar flame calibration of the Overlap PLIF diagnostics

To assess the accuracy of the Overlap diagnostic, a calibration study was conducted with a laminar conical Bunsen flame. The laminar calibration flame data showed that in the Overlap region the product of the OH and CH_2O PLIF signals was a Gaussian profile that had a peak value that was constant and continuous along the flame. Example laminar flames for $\phi = 0.75$ and 1.05 are given in Fig. 2.11. However, as was noted in the previous section, the turbulent flame displayed significantly more spatial variation in Overlap signal intensity, which necessitated the local thresholding. The typical signal-to-noise ratio in the laminar flame was 130 for the CH_2O and 250 for the OH after median and level-set filtering, and 33 for the processed Overlap images. Here "noise" is defined to be the R.M.S. signal fluctuations in a region of the the laminar flame where the OH and CH_2O concentrations are uniform. Table 2.4 lists the measured layer thicknesses from the Bunsen flame compared to the CHEMKIN simulations. All turbulent measurements of Overlap thickness and preheat layer thickness are normalized by the measured value of the laminar flame given in Table 2.4.

The effect of the spatial filtering on the resulting layer thicknesses was also tested. Because median filtering is an edge-preserving technique, it did not significantly change the measured layer thickness. Likewise, the level-set filtering was found to change the measured layer thicknesses by only approximately 1%.

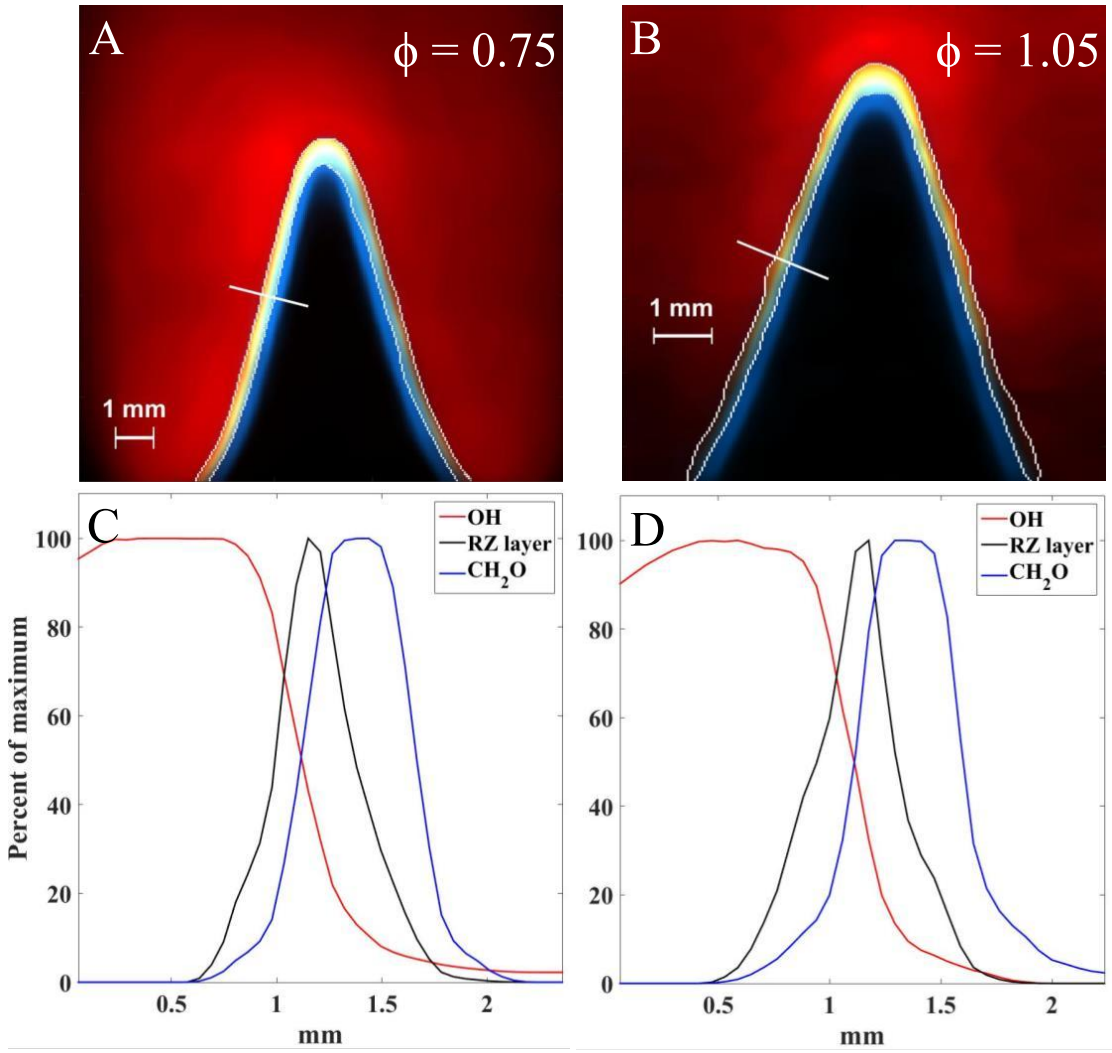

Figure 2.11: Laminar methane-air flame for equivalence ratio (a,c) $\phi = 0.75$ and (b,d) $\phi = 1.05$. The white line intersecting the flame in (a) and (c) represents the distance along which the profiles in (c) and (d) are taken.

2.4.1.7 Uncertainty in the Overlap PLIF diagnostics

As was discussed in Sec. 2.4.1.4, the PLIF images were corrected for background noise arising from ambient light, laser scattering, and flame chemiluminescence. It was observed that considerable variation in the laser pulses could occur from one shot to the next, however shot-to-shot variations in the laser sheet were not measured in this work. Although they would be desirable, they were inhibited by facility limitations. The question of quantifying the uncertainty in the Overlap layers is an important one, but also somewhat challenging.

First and foremost, the Overlap images are expected to track the heat release region of the primary reactions, and so we would like to know how well it performs. Section 2.4.1.6 showed that in the laminar flame the Overlap signal corresponds with the heat release region nearly exactly. Likewise, the work of Nikolaou [84] compared the Overlap and heat release profiles in the DNS databases of freely propagating methane-air flames, and found that the Overlap reaction rates generally showed good spatial agreement with the global heat release. However, when global heat release was at zero, the Overlap reaction rate was still positive (approximately 10% of the maximum). Therefore, extinction may be present even if the Overlap reaction is still occurring. However, the threshold for determining extinction in this work is 50% of the local maximum; the low level reaction rate seen in the DNS is not detectable with current diagnostics. This means that even if the Overlap reaction rate is proceeding at 10% of the maximum rate, the measurement will not be able to detect it, and the layer will appear extinguished. Therefore, global extinction can be assessed from the Overlap signal. However, [84] also showed that there are several other reaction pathways through which heat release can occur. In particular, reactions can proceed through the alternative pathway of $CH_2O + H$. This means that if there is no Overlap signal, it does not necessarily imply that there are is no heat release, it only proves that one particular reaction has ceased. Therefore, the presence of Overlap signal is both a necessary and sufficient condition for establishing that a reaction layer is present; however, absence of Overlap

signal is a necessary but insufficient condition for determining that the flame is quenched.

There are two forms of uncertainty present in any measurement: statistical (or random) error, and bias error. The statistical error will approach zero as the number of measurement samples increases, but the bias error will always be present. The statistical error of the reported thicknesses can be addressed by considering the histograms of layer measurements. Each data set consists of approximately 400 images, each providing a single layer thickness (averaged over the instantaneous image). The standard deviation of these layer measurements provides an adequate measure of the statistical uncertainty of the average thickness. Note that because the reaction layer varies spatially (depending on local strain, roll-up, etc.), there is not a single universal thickness for any given case. Rather, a distribution will always exist even if an infinite number of samples are collected. But the statistical error around the true distribution will approach zero in that case. For the measured layer thicknesses reported in Chapter 4, the thickness profiles follow a Gaussian distribution. For a Gaussian profile, approximately 67% of the data falls within one standard deviation, and approximately 95% falls within 2 standard deviations. For all measured values, error bars representing 2 standard deviation around the mean value will be shown, corresponding to 95% confidence in the mean value.

The bias error in the measurements consists of two parts: resolution (after accounting for image blur through the optical collection system) and flame misalignment with the laser sheet. For the laminar flame, the reaction layer is measured to be anywhere from 0.36 mm to 0.52 mm, depending on the equivalence ratio (Table 2.4). This is approximately two times the laser sheet thickness and resolving power of the optical system, both approximately 200 μm. Therefore, the layers are said to be adequately resolved in this case (uncertainty in the resolution will be further addressed in Section 5.4).

However, it is noted that three-dimensional effects will always be present in a planar scalar measurement, particularly at higher turbulence levels, therefore some bias error is inherent to the measurement. The effect of flame-sheet misalignment is illustrated in Fig.

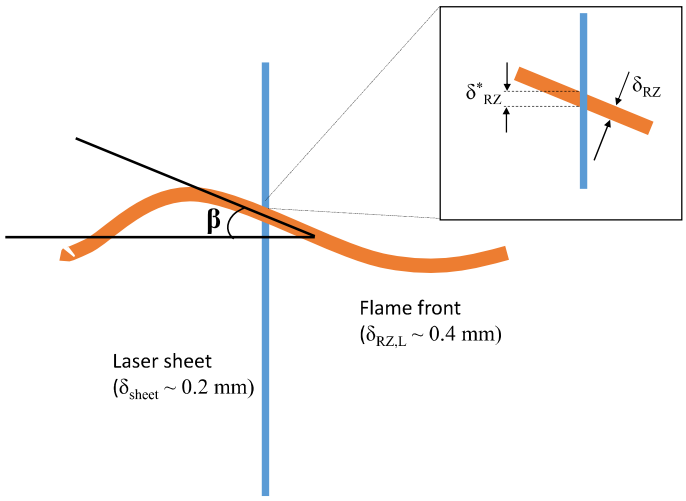

Figure 2.12: Effect of flame mis-alignment with the laser sheet.

2.12. If the instantaneous flame surface is not aligned orthogonal to the laser sheet, the measured thickness δ^*_{RZ} will be larger than the true thickness of the layer δ_{RZ}. This effect can be corrected for if the probability of the intersection angle α is known. The angle β was measured by Chen and Bilger [32] using dual plane PLIF measurements in a turbulent Bunsen flame. Their result for the probability of the magnitude of β is given in Fig. 2.13. The function is $P(\beta) = \frac{2}{\pi} cos^2(\beta)$, for $-\pi/2 < \beta < \pi/2$, and was derived theoretically for a turbulent planar flame brush.

The result of Chen and Bilger shows that the turbulent flames all follow approximately the same distribution for β. Therefore, this result will be used to estimate the uncertainty in the misalignment angle in the PLIF measurements. Although this error will introduce an additional uncertainty in the value of the measured thicknesses, the effect should be relatively constant across all run conditions. Therefore, the technique is still capable of answering the question posed, which only requires measuring the change in the layer structures as the turbulence is increased.

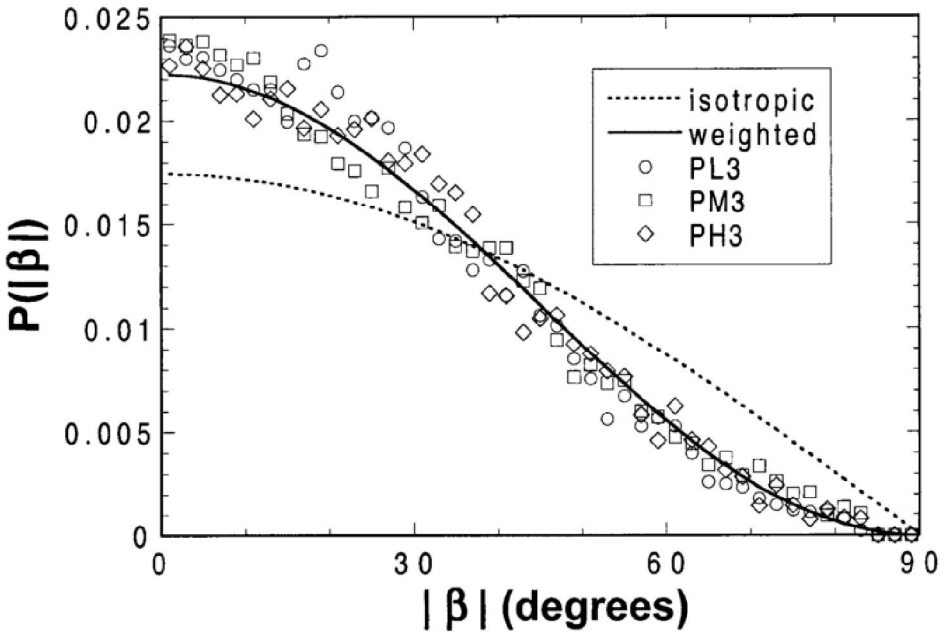

Figure 2.13: Probability distribution for the flame misalignment angle $P(|\beta|)$ as a function of $|\beta|$. Taken from Chen and Bilger [32].

$$\overline{\delta}_{RZ} = \overline{\delta^*_{RZ}} cos(\overline{|\beta|}) \tag{2.19}$$

The integral $\int_0^\infty |\beta| P(|\beta|) d|\beta|$ was computed and found to be 26.7 degrees, which is the average misalignment angle for a turbulent flame, $\overline{\beta}$. The uncertainty due to this misalignment can be calculated as $cos(26.7\,deg) = 0.893$. Therefore, the expected bias error in the flame thickness measurements is estimated to be approximately 10.7%.

2.4.2 OH-PLIF for turbulent burning velocity measurements

Turbulent burning velocities were computed using OH-PLIF to record the location of the instantaneous flame surface. If the reaction layers consist of thin flamelets, with rapid production of the OH radical at the flame-front, then the leading edge of the OH-PLIF signal will correspond approximately to the location of the reaction layer. Note that if the reaction layers are broadened or broken, then the location of the heat release zones

will not necessarily correspond to the measured OH distribution. As will be shown in Chapter 4, reaction zones in the Hi-Pilot are thin (they do not exceed two times the laminar layer thickness) and continuous for all run conditions. Therefore, OH is an adequate flame surface marker in this experiment.

The time-averaged flame boundary was determined from 400 simultaneous hydroxyl (OH) PLIF images. OH was excited with a Nd:YAG laser emitting 300 mJ at 532 nm, which pumped a dye laser operating on Rhodamine 6G dye. The dye output at 568.14 nm was doubled to generate ~ 4 mJ at 284.07 nm. The sheet was 220 mm tall and 0.200 mm thick. A square field of view (FOV) between 150 and 200 mm per side (depending on the height of the flame) was imaged using an intensified CCD camera with a gate time of 100 ns and a spatial resolution of 250-350 μm/pixel depending on the field of view. Background light was rejected using a bandpass filter centered at 310 nm. Formaldehyde (CH_2O) was also recorded in order to ensure that all reactants were consumed within the measurement domain. Formaldehyde was excited by the 355 nm output of a second Nd:YAG laser. The CH_2O fluorescence was collected with a second intensified CCD camera admitting light between 364 and 533 nm, with similar FOV and resolution.

With the location of the instantaneous flame surface suitably identified, an average progress variable can be computed by taking the ensemble average of all binarized OH-PLIF images in a data set. Binarization of the OH-PLIF followed the same algorithm as discussed in 2.4.1.4, and a threshold of 25% was used. The local thresholding was necessary due to the numerous pockets and cusps present in the turbulent surfaces. Although the selection of 25% was arbitrary, results do not change with different thresholds due to the sharp gradient in OH concentration near the flame front. The progress variable thus defined is the mean progress variable of OH, which is:

$$\overline{c}_{OH} = \frac{1}{N}\Sigma_{n=1}^{N} img(n) \tag{2.20}$$

Fig. 2.14 shows the $\overline{c}_{OH} = 0.5$ contour superimposed on an instantaneous OH PLIF

Figure 2.14: Example of an instantaneous flame surface for Case 3b (reactants in gray, products in white). The contour of average flame position is shown in black. This line indicates $\bar{A}_F$ used in evaluating $S_{T,GC,1}$.

image, showing that the diagnostic is successful in capturing the pockets and cusps present in the flame surface. In Eqn. 2.20, N is the total number of images required and *img* is the binarized OH-PLIF image. It is important to note that the progress variable of OH is not identical to the mean progress variable as defined, for instance, in the Bray-Libby-Moss (BML) model [94]. Typically, the mean progress variable refers to the progress of temperature from the unburnt reactants to the products. In this case, the reaction layers remain thin, and therefore the flame can be approximated as a step function with the instantaneous c_{OH} rising from 0 to 1 where the OH-PLIF signal is present. Thus, for the flames in this work the progress variable of OH is approximately equivalent to the mean progress variable of temperature. An example mean progress variable of OH is given in Fig. 2.15.

The turbulent burning velocity can be computed using the concepts of Section 1.5. The following forms of S_T were measured in this work:

1. $S_{T,GC,1}$: Global consumption speed based on the average flame surface position. This is defined using the $\overline{c}_{OH} = 0.5$ contour. In order to obtain the flame area $\overline{A}_f$, the 2-D contour was convoluted about the $x-$axis using a standard formula [115] producing

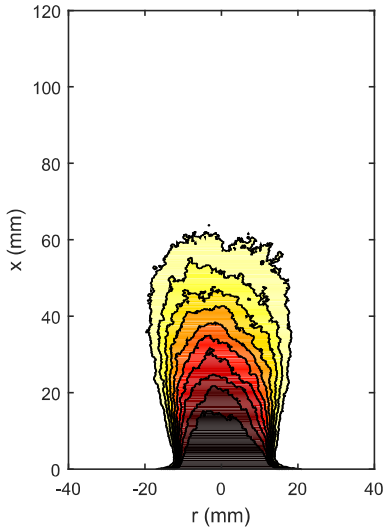

Figure 2.15: Mean progress variable for Case 3b. Note the smoothly varying contours separating the reactants at $\bar{c}_{OH} = 0$ and products at $\bar{c}_{OH} = 1$.

a three-dimensional surface.

2. $S_{T,GC,2}$: Global consumption speed based on the leading edge flame surface position. This is defined using the $c_{OH} = 0.2$ contour.

3. $S_{T,F} = S_L^0 I_0 \int_{-\infty}^{\infty} \Sigma d\eta d\xi$: The integral of flame surface density Σ. η is the flame-normal direction, and ξ is the flame tangent. This integral is a measure of the extent of flamelet wrinkling, A_T/A_L. The quantity is averaged over the entire average flame surface because it is a local quantity that varies from near unity at the base to quite large (~5-10) at the tip [106, 125]. The flame surface density Σ is computed from Eqn 1.11. The flame segments are obtained by applying Canny edge detection to the binarized OH-PLIF images, resulting in a line tracing the heat release layers. Variation of the size of the interrogation box Δx between 1 mm and 4 mm produced changes in the measured flame surface density Σ of less than 10%, indicating the flame surface density did not depend on box size. This is shown in Fig. 2.16, and was previously demonstrated by Filatyev [48]. This is because the length of the flame segment within a region increases in proportion with the size of the interrogation box,

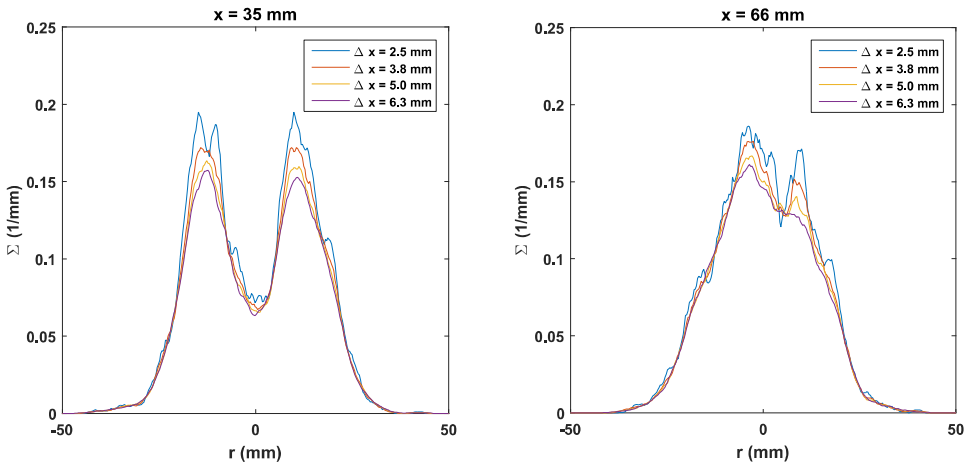

Figure 2.16: Variation of Σ for Case 6b for two downstream distances, demonstrating that the flame surface density does not change significantly with box size.

such that the resulting Σ is insensitive to the box size. Δx was approximately 4-5 mm (16 pixels), depending on the requisite field of view, for the measurements reported in this work. The normal direction was computed at each point along the skeleton of the $c_{OH} = 0.5$ contour, and integration was performed in each direction. The integration was computed until the edge of the domain on the downstream side of the flame, and was computed until either the edge of the domain or the centerline, whichever came first, on the reactant side. The measurement was performed at each point along the skeleton, and the ensemble average was taken for $S_{T,F}$. Note that the stretch factor I_0 is assumed to be unity and constant in this work. For lean methane-air flames at high turbulence, this is a good approximation [114]. As a corollary, because $I_0 = 1$, S_L^0 and S_L will be used interchangeably.

4. A_T/A_L, an alternative measurement of the extent of flame surface wrinkling was also computed. This was evaluated directly from the OH-PLIF images. A_T is computed as the ensemble average of all of the heat release layers (obtained as described in 3, above), and A_L is defined as the average flame position $\overline{c}_{OH} = 0.5$.

2.4.3 CH PLIF

An alternative measure of the reaction zone, and a technique that is somewhat more common in the literature, is imaging of the CH radical. The most common technique was outlined by Carter et al [27] and consists of tuning an Nd:YAG-pumped dye laser system to the $Q_1(7.5)$ transition of the $B^2\Sigma^- - X^2\Pi(v' = 0, v'' = 0)$ band near 390.3 nm. This technique is useful for its ease of access with commonly available laser diagnostics as well as its application for simultaneous particle image velocimetry; however, it is often hampered by relatively poor signal to noise. With this in mind, a novel method of probing the CH radical was developed [28] which instead excites the overlapping $Q_2(2)$ and $Q_2(6)$ transitions from the $C^2X^+ - X^2\Pi(0,0)$ band near 314 nm. The significant advantage of this technique is the excellent signal-to-noise that can be achieved, illustrated in Fig. 2.17. The image is a raw PLIF image - that is, no background or laser sheet correction has been applied. Even in this preliminary state, the quality of the PLIF image is outstanding. For high-repetition rate PLIF imaging, the laser intensity per pulse is limited; therefore, the resonant PLIF transition at 314 nm provides a unique opportunity to image temporally resolved CH reaction layers.

CH-PLIF was acquired at 10 kHz in coordination with Drs. Cam Carter and Steven Hamack, Prof. Tonghun Lee, and Aaron Skiba. Measurements were made at the Air Force Research Laboratory at Wright-Patterson Air Force Base in Dayton, Ohio. The CH-PLIF was used to provide an alternative reaction layer measurement to compare with the Overlap method. To generate the laser sheet at 314.415, the second harmonic from an EdgeWave Innoslab Nd:YAG laser pumped a Sirah Credo dye laser. Then, an integrated second harmonic generator doubled the output from the dye laser to produce the 0.2 mJ CH excitation beam. Finally, this beam was directed through a series of optics that produce a 50 mm × 0.23 mm sheet, which covered the 47 mm × 47 mm FOV. Fluorescence resulting from the incident laser-light was captured with a Photron SA-Z CMOS camera with an array size of 1024 ×1024 pixels. This provided a spatial resolution of 91 × 91 μm^2 in the imaging

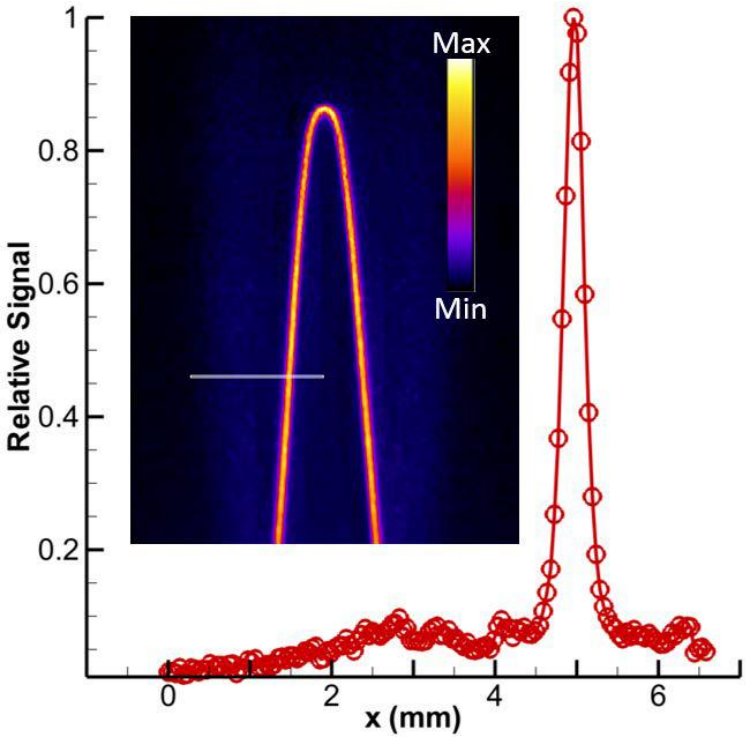

Figure 2.17: Example image of CH-PLIF from Carter [28].

plane. The laser sheet thickness was 230 μm, and provided the resolution in the direction normal to the imaging plane. The camera was equipped with a LaVision HS-IRO intensifier fitted with a Cerco 100-mm f/2.8 lens. Additionally, a Schott UG-5 filter and a 1-m focal length UV close-up lens were attached to the Cerco lens to suppress flame luminosity and eliminate the need for extension rings, respectively.

The CH-PLIF images underwent a processing scheme similar to the Overlap PLIF. The raw CH-PLIF images were binned to a 512 ×512 pixel array size, giving a nominal pixel size of 91 μm ×91 μm. These images are then flat-field corrected and divided by an average CH-PLIF profile, which corrects the images for non-uniformities in the laser sheet. Following these operations a 5-pixel-radius median filter was applied to the CH-images resulting in signal-to-noise ratios (SNRs) of ~14. Here, SNR is computed by dividing the average by the standard deviation of the signal within a region of relatively uniform signal. Note that a laser and flame background subtraction was found unnecessary given the very

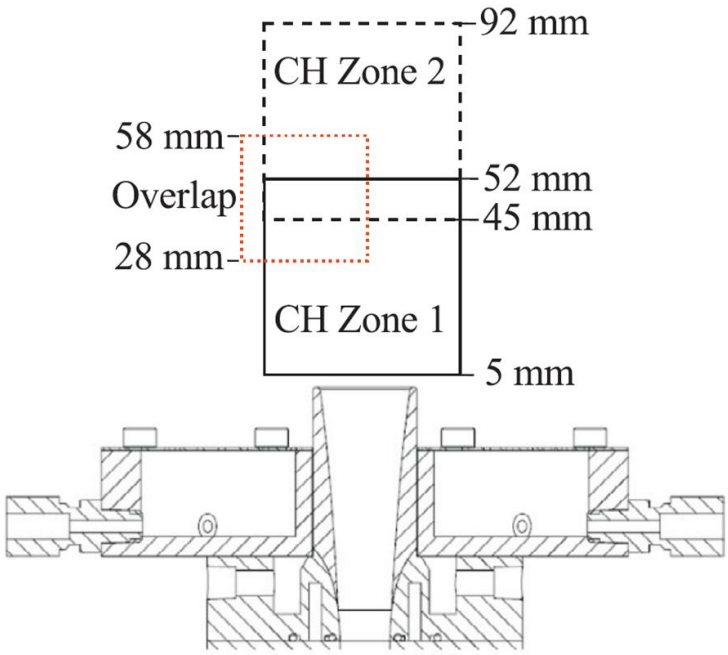

Figure 2.18: Schematic of the measurement locations for the CH PLIF, in comparison to the Overlap field of view.

high signal-to-noise inherent to the resonant PLIF transition; rather, a median image was composed for each data set, and found to adequately bring the background noise to near zero.

2.4.3.1 "Two-tone" Combined CH-OH PLIF

During the CH-PLIF measurements, a related measurement was performed. The technique is outlined in [29], and makes use of the nearby OH excitation band $A-X(1,1)$ band $Q_1(6)$ transition. By tuning the laser wavelength to 314.425 nm, both the CH $Q_1(7)$ and the OH $Q_1(6)$ transitions can be excited, so that OH and CH are both present in the PLIF image. This technique is valuable for probing flame-extinction events, as it allows investigation of the product region downstream of the reaction layer. An example of this technique is given in Fig. 2.19 for a turbulent Bunsen flame. In this work, the combined CH-OH PLIF technique will be used to examine the degree of back-support in the turbulent Hi-Pilot flames, and explore the effect of cold air entrainment into the product gases downstream of

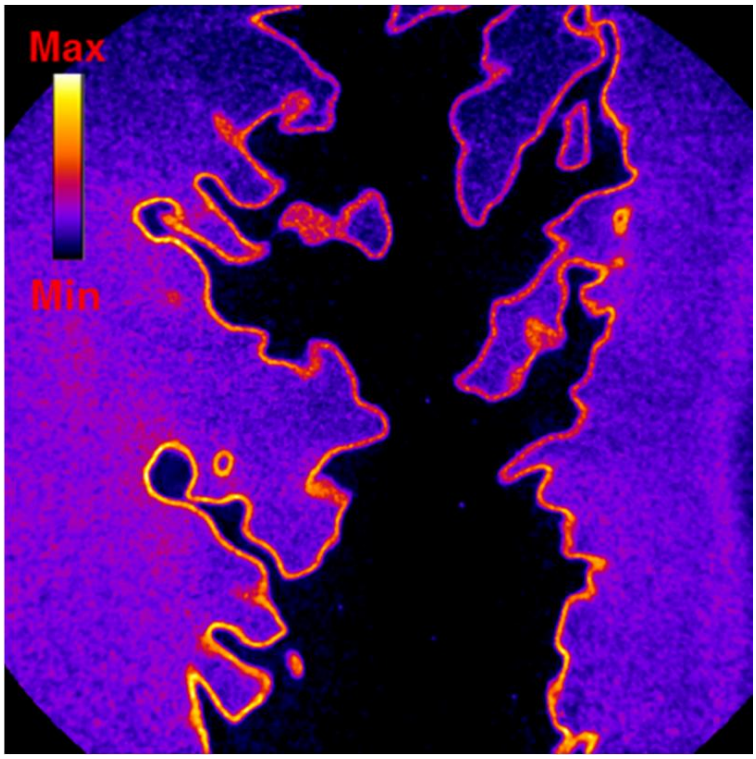

Figure 2.19: Two-tone combined CH-OH PLIF in a rich (ϕ = 1.07) Bunsen flame. Taken from [29].

the flame. Because all of the diagnostics in this measurement were identical to that of the CH-PLIF, the resolutions and sheet thickness given in Section 2.4.3 apply here as well.

2.5 Simultaneous PIV and CH_2O PLIF

Two planar velocity measurements (PIV) will be presented in this work: a turbulence characterization study over a range of test cases, and simultaneous PIV and CH_2O-PLIF to obtain turbulence statistics conditioned on the distance from the reaction zone. The formaldehyde PLIF arrangement and detection system was identical to that described in Section 2.4.1.2. Velocity measurements are made using a pair of Spectra Physics Nd:YAG lasers operating at approximately 120 mJ at 532 nm. Laser light is elastically scattered off of 0.3 micron Al_2O_3 particles, and captured by a LaVision ImagerPro 4M camera. Laser sheets were carefully aligned prior to each data campaign, and sheet thicknesses were approxi-

mately 1 mm and 0.2 mm for the PIV and PLIF sheets, respectively. Velocity vectors were obtained throughout the entire field of view, including the products region. It was necessary to seed the co-flow to accomplish this, as rapid mixing downstream of the reaction zone, combined with the drop in seed density in the products due to thermal expansion, made vector computation impossible if only the reactants were seeded. The PIV field of view for the turbulence characterization measurements was 20x20 mm and the CCD array size was 2048x2048 pixels. For the simultaneous PIVxPLIF measurement, the field of view was approximately 9.3 mm, and two run conditions (Case 3b and 4b at equivalence ratio $\phi = 0.75$) were extracted for analysis. These cases were chosen due to the ability to resolve most of the important scales of turbulence, while maximizing the values of u'/S_L. For Case 4b, the smallest interrogation box size that produced less than 5% missing vectors was 32x32 pixels. Vector errors mainly arose in the products region for this case.

Using a window size of 32x32 pixels, the physical size of the window was $\Delta = 144\,\mu m$, meaning that only scales larger than approximately 144 μm were resolved. This is because any scale smaller than the interrogation box is inherently filtered, as PIV gives the average velocity within the interrogation region. Buch and Dahm have shown [24, 25] that the smallest scales that must be captured to fully resolve the flow turbulence are $\lambda_v = C\delta Re_\delta^{-3/4}$, where δ is the integral length scale and C is an empirical constant equal to 11.2, although the specific number is open to some debate [128]. In a detailed study of the ability of PIV measurement to resolve all relevant scales, Lavoi et al. [69] showed that for a spatial resolution of $\Delta = 3\eta_k$, velocity gradients are accurately captured. Additionally, they found that the dissipation associated with small-scale structures is within 5% of the true value.

For the two cases studied, the relevant viscous scales are approximately $\lambda_v = 116\ \mu m$ and $\lambda_v = 75\ \mu m$, respectively, and the Kolmogorov scales are $\eta_k = 24\ \mu m$ and $\eta_k = 16\ \mu m$. Using a 32x32 pixel window, the relative size of the interrogation region was $\Delta = 6\eta_k$ and $\Delta = 9.3\eta_k$ for Case 3b and 4b, respectively. Thus, the smallest scales of the flow were not completely resolved for the conditioned velocity measurements. However, it is expected

that most of the turbulence is governed by the larger eddies, as the smallest scales of the flow are relatively weak. Additionally, for Case 3b the particle images were sufficient to produce 16x16 pixel interrogation regions. This improves the resolution to $\Delta = 3\eta_k$ for this condition, which is the upper limit proposed by Lavoi et al. This higher resolution measurement was utilized as a check on the results obtained using the lower resolution vectors.

CHAPTER 3

Turbulence Characterization

This chapter will describe the characterization of the flow field and turbulence of the Hi-Pilot burner. The discussion will be broken into two sections. The LDV measurements will be presented first, which provided mean and fluctuating velocities for all cases, as well as integral time scales which were transformed to length scales using Taylor's hypothesis (see section 2.2.2). Then the results of the PIV measurements will be introduced, in order to quantify the anisotropy suggested from the previous LDV results, as well as to evaluate the accuracy of the time-length scale transform employed in the LDV.

3.1 Laser Doppler Velocimetry

LDV measurements were performed for the run conditions in Table 2.1 in Chapter 2. Measurements were taken approximately 5 mm above the jet exit on centerline, with just the oxidizer lines flowing (that is, non-reacting conditions with no fuel flow). The angle of the crossing beams limited how close the focal volume could be placed to the exit plane. Mean velocities were corrected for gate-time bias. This was necessary because LDV is a flux-weighted measurement that inherently over-samples faster moving structures [58,127]. For instance, consider an imaginary flow that contains, in equal parts, particles moving at x units/sec and $2x$ units/sec. In this case, roughly twice as many of the faster moving particles would pass through the probe volume during any given recording duration. Gate-time weighting corrects for this as:

$$U = \frac{\sum_{i=1}^{N} u(i)\tau_i}{\sum_{i=1}^{N} \tau_i} \tag{3.1}$$

Where τ is the gate-time of the instantaneous measurement (that is, the duration of the particle burst, provided by the TSI hardware), u is the measured velocity of the burst, and U is the corrected mean velocity. Between 750,000 and 1,000,000 data points were collected at each measurement condition. Due to the random arrival time of a tracer particle at the LDV focal volume, the sampling frequency is highly variable. This poses problems for deriving a temporal autocorrelation; the problem is well summarized by Benedict et al [14]. Autocorrelations were computed using the fuzzy slot technique described by Marshall et al [76, 77, 129, 131], which circumvented the problem.

A sample autocorrelation for Case 5a is given in Fig. 3.1. The y-axis is the autocorrelation function $R(\tau)$ and the x-axis is the lag time τ. Note that the function decays exponentially to zero, but some residual noise remains in the data. The noise increases at large lag times, and asymptotes to a slightly positive value for the most turbulent cases. This poses some difficulty in extracting integral length scales, as there are a number of options regarding how to integrate such an autocorrelation. For instance, a least-squares fit can be applied to the data, and the integral could be performed either up to the point where the autocorrelation function plateaus slightly above zero, or integrated to the end of the domain. However, in this measurement, the autocorrelation function should go to zero, and only high-frequency noise prevents it from decaying completely. Therefore, a fitting function that follows this high frequency region is not desired. Instead, a two-term exponential function is used that fits the majority of the data during the roll-off, but does decay to zero at large separation Δt. The exponential fit is given as the solid black line in Fig. 3.1 and is of the form:

$$f(x) = a\,exp(-bx) + (1-a)\,exp(-cx) \tag{3.2}$$

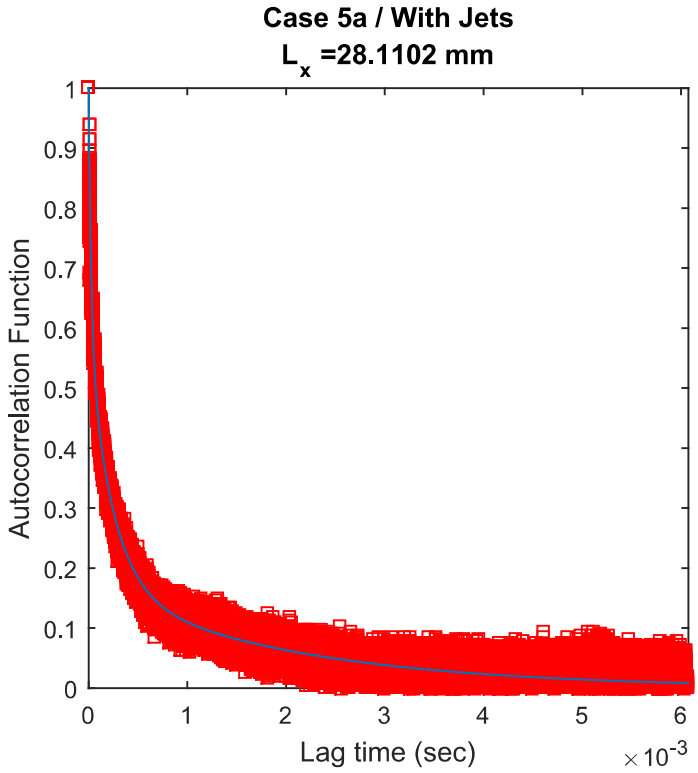

Figure 3.1: A sample autocorrelation for Case 5a. Note that the function decays exponentially to zero, but there is some noise in the data. The noise increases at large lag times, and asymptotes to a slightly positive value. The two-term exponential function fits the majority of the data and does decay to zero.

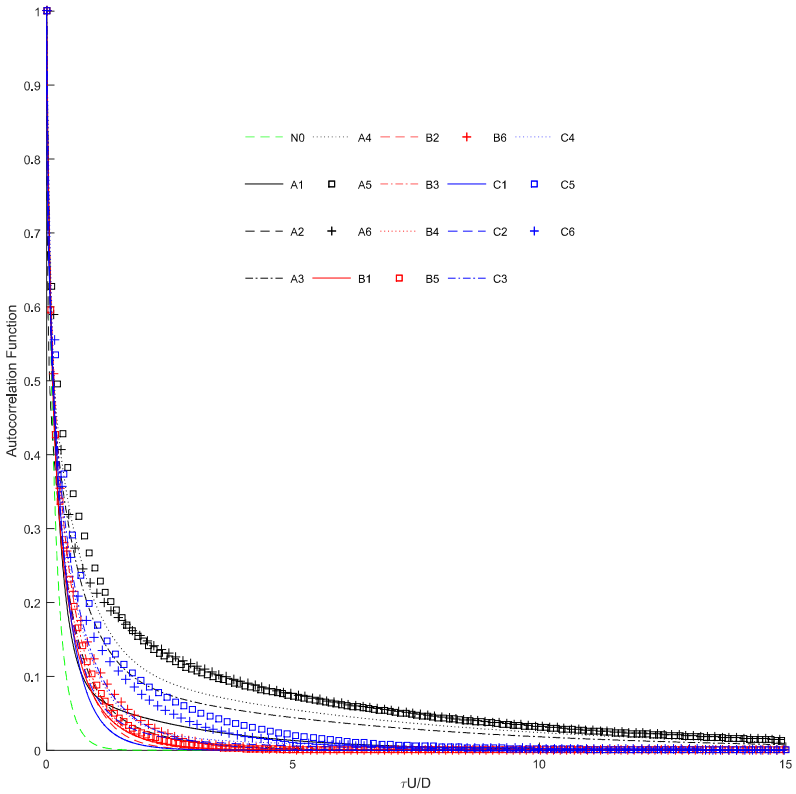

Figure 3.2: Illustration of the autocorrelation for all 18 Hi-Pilot test cases and a laminar pipe calibration case. Flow is non-reacting.

3.1.1 LDV measurements in the Hi-Pilot

LDV measurements were made for the 18 nominal Hi-Pilot run conditions, and the computed autocorrelations for each case are given in Fig. 3.2, along with the autocorrelation for the calibration measurement performed in a round pipe (indicated as $N0$). The x-axis is normalized by the mean velocity as $\tau U/D$. While the autocorrelations for the medium and small slot collapse nearly to a single profile, the functions for the large slots (given in black) do not. For the large slot, the autocorrelation increases with increasing flow rate.

The mean velocity U, fluctuation velocity u', and integral time scale τ are given in Table 2.2 (Chapter 2). The integral length scales are computed using both Taylor's hypothesis ($L_{x,Taylor}$) as well as the correction described in Chapter 2 ($L_{x,cor}$). Turbulence Reynolds

number Re_T and Kolmogorov scales are derived from L_x and u' and are included as the final two columns. Note that for the calculation of Re_T and η_k, the integral scale $L_{x,cor}$ was used. For the Case title, the number refers to the flow rate (given in Table 2.1) and the letter corresponds to the turbulence generator plate. The largest slotted plate is assigned 'a', and the smallest is denoted 'c'.

Note that for most conditions, $L_{x,Taylor}$ and $L_{x,cor}$ are approximately equal; for example, Case 4c (with jets) shows an integral scale between 9.3 mm and 10 mm depending on the method. However, for the higher turbulence cases, generally above Case 5, the differences can become significant. The accuracy of the correction for Taylor's hypothesis will be explored in detail in section 3.2.3, where two-dimensional velocity measurements will be used to assess the assumptions used to compute $L_{x,Talylor}$ and $L_{x,cor}$.

It is observed that the integral length scales generally increase with mean velocity, presumably due to the stretching mechanism discussed in Section 2.1. The turbulence levels reach extremely large values of $u' > 30$ m/s, and the turbulence intensity u'/U approaches 40% for several cases. The integral length scales generally are increased with the impinging jets running, which may be due to the increased flow rate. The turbulence Reynolds numbers are very large for the most turbulent cases, with six run conditions of $Re_T > 20,000$, and the most turbulent case of $Re_T = 99,000$. To the author's knowledge, this is the most turbulent Bunsen-flame experiment reported in the literature.

3.1.2 Uncertainty in the LDV measurements

The uncertainty in the LDV measurements was determined using the 95% confidence interval around the mean combined with the uncertainty in the mass flow rates. At least 500,000 samples were taken for all run conditions, so the 95% confidence interval in the mean is determined as

$$\sigma_{\overline{U}} = \frac{1.96 * u'}{\sqrt{N-1}} \tag{3.3}$$

Due to the very large sample sizes, the magnitude of $\sigma_{\overline{U}}$ was less than 2% of the mean value $\overline{U}$ for all run conditions. The uncertainty in the flow rates is given by the uncertainty in the sonically choked orifices, which is:

$$\frac{\Delta \dot{m}}{\dot{m}} = \sqrt{\left(\frac{\Delta P_0}{P_0}\right)^2 + \left(\frac{\Delta A^*}{A^*}\right)^2 + \frac{1}{4}\left(\frac{\Delta T_0}{T_0}\right)^2} \tag{3.4}$$

The resolution of the pressure gauges was approximately 1 psi with nominal back-pressures of around 150 psi, the assumed error in the orifice diameters was 2%, and the variation in room temperature is assumed to be 3%. Eqn. 3.4 then gives a combined uncertainty in the flow monitoring of approximately 3.7%. The total uncertainty in the mean velocities is then the root-sum-of-squares of the above: $\frac{\Delta \overline{U}}{\overline{U}} = \sqrt{\frac{\sigma_{\overline{U}}}{\overline{U}} + \frac{\Delta \dot{m}}{\dot{m}}} = 4.2\%$.

There was an additional uncertainty in the integral length scale arising from uncertainty in the fit of the autocorrelation function. This is primarily due to the non-zero asymptotes present in the most turbulent run conditions that was discussed earlier. The R-square value of the exponential fits were typically greater than 0.95, indicating that the fit explains more than 95% of the total variation of the data about the mean. As can be seen from the sample autocorrelation in Fig. 3.3, the scatter is typically relatively small during the decay of R_{uu}, and it is only in the roll-off region and beyond ($R_{uu} < 0.3$) that the scatter increases significantly. In order to evaluate the uncertainty of the exponential fit, the 95% confidence interval for the coefficient fit was determined, and the lower bound was integrated until the first zero crossing (the lower dotted curve in Fig.3.3). This produced an estimated lower bound for the integral length scale produced by the fitting function, and was compared with the measured value of L_x reported in Table 2.2. The change in L_x using the 95% confidence band was approximately 35%, which is the estimated uncertainty in the integral length scale measurements.

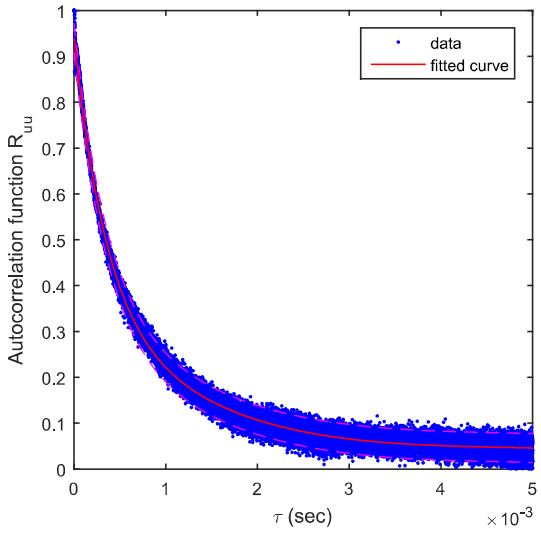

Figure 3.3: 95% confidence bands in the autocorrelation measurements. The lower band was extracted and integrated to the first zero crossing in order to estimate the uncertainty in the measured value of L_x.

3.2 Particle Image Velocimetry

Particle image velocimetry (PIV) was performed using the diagnostics described in Section 2.5. This section presents PIV measurements of the Hi-Pilot co-flow and several run conditions of the non-reacting central jet. The goal of these measurements was to characterize the velocity field and turbulence attributes and to provide a comparison with some of the previous LDV measurements.

3.2.1 Characterization of the co-flow

The co-flow of a turbulent Bunsen flame is important for maintaining reactions globally, and has been modified several times for this experiment. If the co-flow is too weak, cold air will be entrained by the central jet and brought into contact with the reaction surface, quenching the flame. The purpose of the co-flow in this experiment is to produce a region of uniform products downstream of the thin reaction zones, such that a one-dimensional temperature or species profile should resemble the laminar case. However, it is important

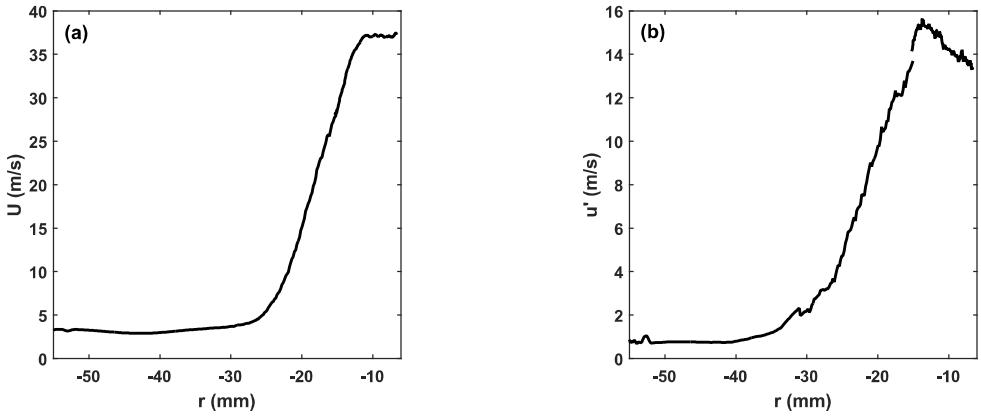

Figure 3.4: Radial profiles of (a) mean velocity U and (b) fluctuation component u' for the co-flow for Case 3b.

to characterize the strength of the shear layer between this stronger co-flow and the central jet. In Bunsen geometries, it is typically assumed that all of the turbulence acting on the flame surface is generated within the reactants, often measured on centerline at the jet exit. Because the flame surface resides within the jet core, it is expected that the effects of the shear layer will be much less than what may be seen in a free turbulent jet measured in the fully developed region far downstream. However, at high jet velocities this shear layer may still be substantial, and if the average flame surface is located within the shear layer then it could increase the effective turbulence acting on the flame to a level above that which is generated within the reactants. Figure 3.4 shows radial profiles at 1 diameter (21.6 mm) downstream for average velocity U and the fluctuating velocity component u' for Case 3b.

Figure 3.4 shows velocity measurements for Case 3b with the main flame reacting. Velocity measurements are not conditionally sampled on the reactants or products; i.e., velocity measurements are made throughout the flame zone. The data is a composite of measurements taken from the downstream location (where the simultaneous PIVxPLIF was taken, Chapter 6) and from a much larger FOV taken to characterize the full width of the co-flow velocity. The two data sets agree well, with the mean velocity increasing at an approximately constant velocity gradient of $dU_x/dx = 2,850$ 1/s, and is constant at about 4 m/s in the co-flow. The turbulence intensity does not drop to zero in the co-flow due to tur-

bulence from the shear layer, but decays to less than 1 m/s. It is also interesting to note that the turbulence intensity reaches a sharp maximum in the shear layer between the co-flow and central jet. The effective turbulence intensity u' appears to be a superposition of that deriving from the turbulence generating plates in the central jet (which would resemble an error function) and that arising from the shear layer (which would have a Gaussian function). The resulting profile of u' therefore a combination of these two profiles, explaining the shape of the curve.

3.2.2 Characterization of the velocity field for non-reacting conditions

PIV measurements were performed for a number of the run conditions listed in Table 2.2, however resolution limits were imposed due to the very large separation of scales. The field of view for these measurements was approximately 20 mm x 20 mm, and was centered evenly over the jet exit. Velocity measurements were made with just the main air running; i.e., non-reacting conditions. The co-flow was not run for these measurements as the variation of the turbulent quantities on centerline was the primary concern. Also note that the impinging jets were not run for any of the PIV measurements. This was because the impinging jets were not seeded, and thus when they were run they disrupted the seed density of the flow producing pockets of unseeded fluid.

Figs. 3.5 and 3.6 present axial and radial profiles of the mean and fluctuating components of velocity for Case 3b and 4b. Note that these two run conditions will be selected for study in Chapter 6. It is seen that Case 3b is very symmetric, with the maximum velocity centered over the jet exit, and little variation of either u' or U_x over the central 80% of the burner. There is a slight increase in u' in this case as the shear layer of the co-flow is approached, as discussed in Section 3.2.1.

However, Case 4b exhibits significant asymmetry, with the maximum velocity occurring around $r = -7$ mm, and substantial radial variation of mean velocity. This asymmetry is present in most of the highest velocity run conditions (generally above Case 4 for all

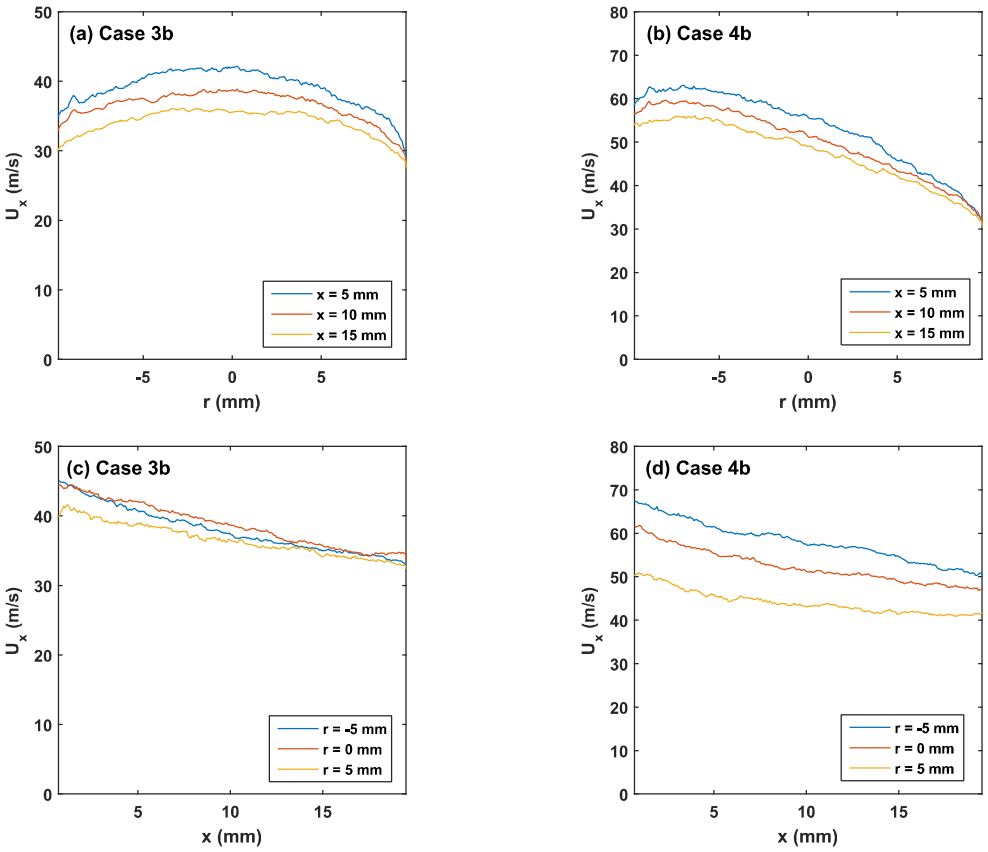

Figure 3.5: Mean velocity profiles for Case 3b (left) and Case 4b (right)

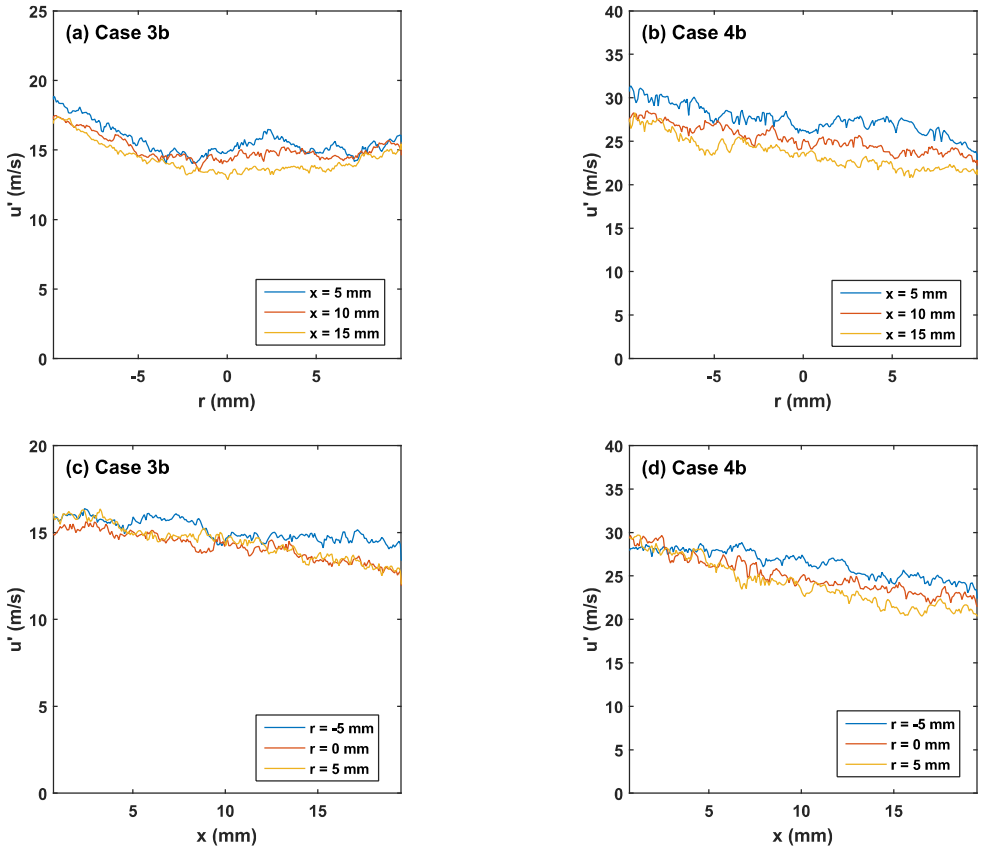

Figure 3.6: Fluctuating velocity profiles for Case 3b (left) and Case 4b (right)

slotted plates), and intensifies worse with increasing integral length scales. Despite a number of attempts to straighten the flow, perfect symmetry in the jet was never achieved. It is likely that a slight manufacturing defect in the converging section or the nozzle produces a flow asymmetry, and the very strong contraction accentuates the problem.

However, despite the significant asymmetry in the mean velocity, the fluctuating velocity u' does not vary nearly as significantly. Although there is asymmetry in the radial profiles in Fig. 3.6(b) (decreasing u' with r), the gradient is very small. Also, the fluctuating velocity in Case 4b has approximately the same slope for $\partial u'/\partial x$ downstream as for Case 3b. Note that these measurements are all taken well within the jet core ($5-6D \sim 108-130$ mm), and therefore far-field scaling relations for free turbulent jets do not apply here.

Together, these measurements show that despite asymmetry in the mean velocities, the

turbulence levels are approximately homogeneous and isotropic over a small region (less than ~ 10 mm). With this in mind, the simultaneous PIV and formaldehyde PLIF measurements are performed at a relatively small field of view (less than 9.5 mm) in order to ensure relative homogeneous turbulence.

3.2.3 Integral length scales

The LDV measurements described in Section 3.1 produced very large integral length scales and indicated significant anisotropy at the jet exit. This is suspected to be a product of the strong contraction (and thus high mean shear) used in this configuration. An analysis of the vorticity transport equation reveals that this effect allows the vortex stretching term to significantly elongate eddies in the flow direction [133]. PIV measurements were used to evaluate the degree of isotropy in the turbulence (u' and v') and the integral length scales (L_x and L_r). Details regarding the definitions and computation of the autocorrelation function and the corresponding integral length scales were described in Section 2.3.3.1. An example spatial autocorrelation $R_u(\Delta x,\Delta r)$ for Case 4a is shown in Figure 3.7. The relative size of integral scales L_x and L_r is given in the shape of the spatial autocorrelation function, and the ellipsoidal structure of the contours given in Fig. 3.7 illustrates that the flow is anisotropic and that L_x is several times larger than L_r.

The measurement domain extended from $-10\,mm < r < 10\,mm$ and $0\,mm < x < 20\,mm$, and each test case was evaluated at 1 mm above the jet exit on centerline. Not all spatial autocorrelations decay to zero within the measurement domain. In these cases, an exponential function was fit to the data points to extrapolate the trend to zero.

The PIV measurements were able to resolve 11 of the 18 nominal Hi-Pilot run conditions, and the results are given in Table 3.1. Cases a, b, and c correspond to decreasing slot size in the turbulence generating slotted plates. For the more turbulent run conditions, the optical system was unable to resolve both the Taylor and integral scales within a single measurement domain, and therefore measurements at those conditions were not possible.

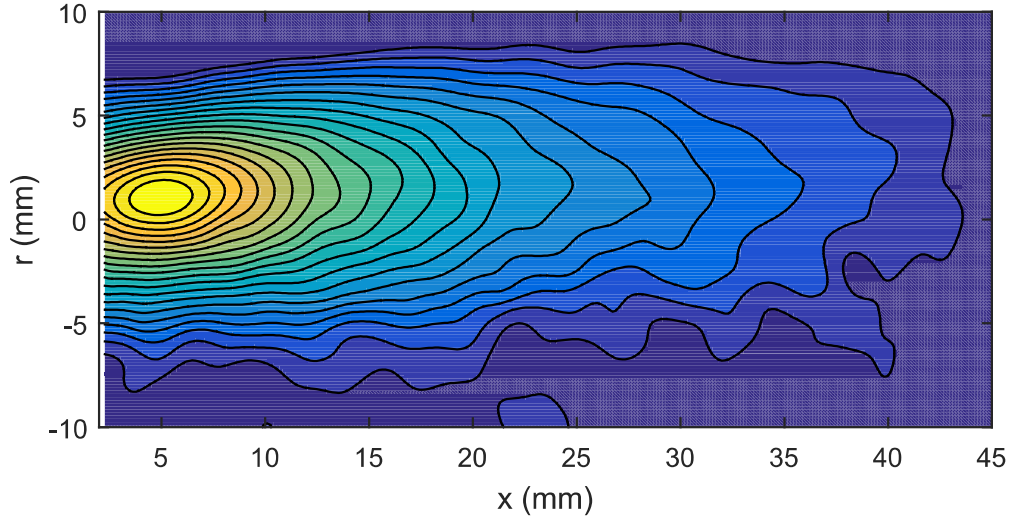

Figure 3.7: Spatial autocorrelation for Case 4a. Darker contours correspond to decreasing R_u.

Case	U_{CL} (m/s)	u'_{CL} (m/s)	v'_{CL} (m/s)	u'/v'	L_x (mm)	L_r (mm)	L_x/L_r	L_{HD} (mm)
1a	16.1	3.1	2.3	1.3	8.2	1.8	4.5	2.7
1b	11.0	3.6	2.5	1.4	7.8	2.2	3.5	3.2
1c	16.7	2.5	2.0	1.3	5.3	1.6	3.3	2.3
2a	34.2	6.4	4.8	1.3	9.9	1.9	5.1	2.9
2b	22.7	7.7	5.5	1.4	10.0	2.3	4.4	3.4
2c	34.5	5.4	4.2	1.3	6.5	1.8	3.7	2.6
3a	58.5	16.6	11.4	1.5	11.8	2.9	4.1	4.3
3b	44.2	15.5	11.2	1.4	12.6	3.2	4.0	4.7
3c	61.5	12.3	11.0	1.1	6.1	2.0	3.0	2.9
4b	52.0	28.6	19.6	1.5	13.3	3.3	4.0	4.8
4c	93.8	26.8	17.5	1.5	6.2	2.1	3.0	2.9

Table 3.1: Run conditions and results of the integral length scale measurements

For Case 3b, the longitudinal scale is approximately 12.6 mm, and the lateral scale is 3.2 mm. These results can be combined using a hydraulic diameter:

$$L_{HD} = \frac{4L_r L_x(64 - 16E^2)}{(L_r + L_x)(64 - 3E^4)} \tag{3.5}$$

$$E = \frac{L_x - L_r}{L_x + L_r} \tag{3.6}$$

For Case 3b we can then obtain a hydraulic diameter of the integral scale of approximately L_{HD} = 4.7 mm. The hydraulic diameter of the integral scale describes the effective size of the eddys that interact with the flame. Because the reactants pass tangentially through the flame over most of the surface, L_{HD} may be more representative of the scale of turbulence which actually interacts with the reaction layer.

From Table 3.1, it is seen that u'_{CL}/v'_{CL} is approximately 1.4 for all conditions. The anisotropy of integral scales is measured by L_x/L_r and illustrated in Fig. 3.8, and the quantity is between 3 and 5 at all conditions. This indicates that the turbulence is not isotropic and the deviation from isotropy is approximately the same for all cases. The hydraulic diameter is plotted against u' in Fig. 3.9. The hydraulic diameter increases non-linearly with u' for all cases, but for Cases 1-4c the change is much smaller than for Cases

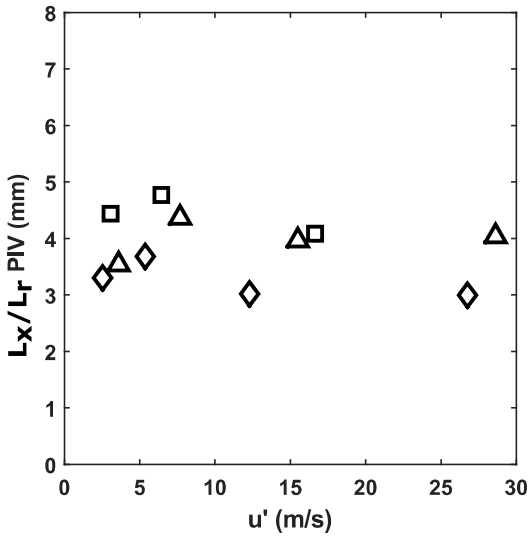

Figure 3.8: Variation of the anisotropy of integral length scales L_x/L_r versus axial velocity fluctuations u'.

a and b.

3.2.4 Assessment of the validity of Taylor's hypothesis in extreme turbulence

It was discussed previously that the LDV measurements require a temporal-spatial correlation in order to compute an integral length scale. Typically, almost all turbulence measurements are made in the time domain (using LDV or a hotwire anemometer, for example) and converted into the spatial domain assuming that the turbulence is frozen; i.e., $L = \tau U$. Taylor's hypothesis assumes that the convective velocity of the energy-containing (integral scale) eddies is approximately equal to the mean velocity of the flow. However, this can be an inaccurate approximation in highly turbulent flows with a wide range of scales. In a highly turbulent flow, the mean velocity averaged over all scales in the flow can be considerably smaller than the convective velocity of the energy-containing eddies. The criterion generally used to apply Taylor's hypothesis is $u'/U \ll 1$, but the LDV measurements show that the turbulence intensity exceeds 35% for some run conditions in this work. Therefore,

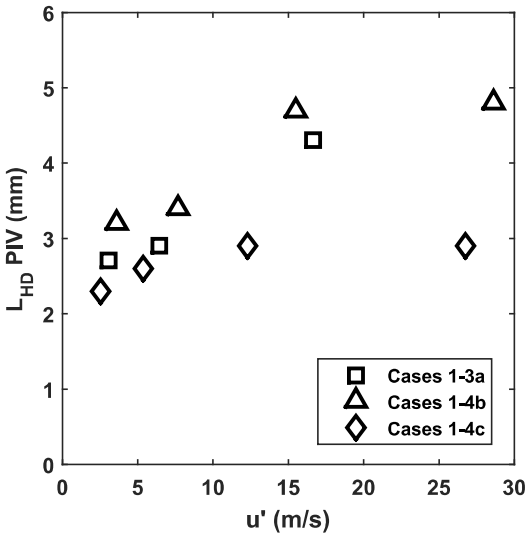

Figure 3.9: Variation of hydraulic diameter L_{HD} versus u'.

applying Taylor's hypothesis in these conditions can result in significantly underestimated integral length scales. The correction for Taylor's hypothesis was discussed in Section 2.2.2, as well as the reduced correction assuming isotropic flow:

$$L_x = \tau U \left[1 + \frac{\overline{u'^2}}{U^2} + 4\frac{\overline{v'^2}}{U^2} \right] \tag{3.7}$$

$$L_x = \tau U \left[1 + \frac{\overline{u'^2}}{U^2} + 4\frac{\overline{v'^2}}{U^2} \right] \tag{3.8}$$

The LDV measurements of L_x in Table 2.2 used the isotropic correction to Taylor's hypothesis, Eqn. 3.8. However, although Taylor's hypothesis can underestimate the length scales in a highly turbulent flow, the presence of mean shear often implies substantial anisotropy. This means that the isotropic correction to Taylor's hypothesis can overestimate the length scales [136]. Using the planar velocity data from the PIV measurements, we can visualize the error associated with obtaining L_x from τ in extreme turbulence for these two methods. The error associated with Taylor's hypothesis and with the isotropic correction to Taylor's hypothesis are given in Fig. 3.10.

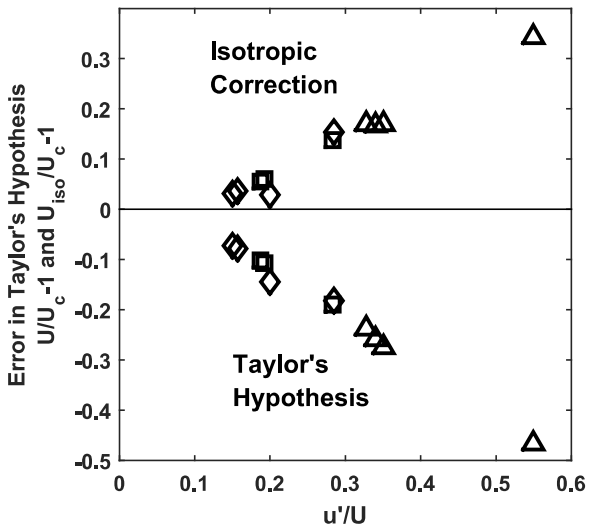

Figure 3.10: The performance of Taylor's hypothesis and the isotropic correction versus turbulence intensity u'/U. The error associated with both of these temporal-spatial transformation increase linearly with turbulence intensity, however the error in the isotropic correction is approximately one-third less than Taylor's hypothesis.

In Fig 3.10, it is observed that Taylor's hypothesis can underestimate the integral length scale by nearly 50%, while the isotropic correction to Taylor's hypothesis can overestimate the length scale by about 35%. The error associated with both Taylor's hypothesis and the isotropic correction increases linearly with turbulence intensity u'/U, however the magnitude is about a third less using Taylor's hypothesis. From the results, it appears that the isotropic correction is reasonable for $u'/U < 0.3$ (about 10% error), however it becomes significant for larger turbulence. This highlights the importance of multi-component velocity measurements in extreme turbulence.

CHAPTER 4

Regimes of Premixed Flames in Extreme Turbulence

This chapter contains measurement results of premixed flame structure in extreme turbulence, and the implications for a regime diagram. As described in the introduction, several theories have been developed describing the interaction of turbulent structures with a premixed flame surface. Laminar premixed flames (and flames in weak-to-moderate turbulence) have chemical time and length scales that are very short, with all of the heat release occurring in a region of space less than half a millimeter for atmospheric flames. In this case, the flame chemistry is 'frozen' relative to the much larger time scales of the incoming turbulence. Theory typically predicts finite-chemistry effects (i.e. broadening or extinction of the chemical reactions due to turbulent transport or strain) when the time or length scale of the turbulence becomes comparable to that of the flame.

The regime diagram predicted by Peters assumes that these effects will become significant for the preheat layer and reaction zone at Karlovitz numbers of approximately 1 and 100, respectively. This corresponds to the Kolmogorov scale of turbulence penetrating the preheat or reaction layer structure, utilizing several assumptions regarding the scale of the laminar flame structure as outlined in Chapter 1. Although several previous works described in the introduction have explored regimes of $Ka_T > 100$ and observed evidence of broken or distributed burning, none of these studies have studied flames subjected to any

appreciable integral length scales. For instance, the distributed reactions seen by Zhou et al were obtained on extremely small jet burners with an exit diameter less than 2 mm, and the exit velocity exceeded 400 m/s. Although this was capable of producing non-flamelet-like behavior, it is not representative of any practical combustion operating conditions. Rather, most devices use moderate-to-large integral length scales. For instance, the integral length scale in a gas turbine combustion chamber may be approximately 20 mm. In this case, it is the turbulent Reynolds number $Re_T = u'L/\nu$ that is large, rather than the Karlovitz number Ka_T. As described in Chapter 3, the Hi-Pilot is capable of producing turbulent Reynolds numbers up to 99,000, which is 5-6 times the largest value previously obtained, and several of these test conditions fall well into the predicted regime of broken/distributed reactions. This chapter will examine the variation of flame structure across all operating conditions, and compare the measured values to the predictions made by Peters. Conclusions regarding the regime diagram, and potential improvements or modifications, will be discussed.

4.1 Run conditions and regime diagram locations

Chapter 3 documented the run conditions and turbulence levels attainable in the Hi-Pilot burner. There are six possible flow rates and three possible turbulence generating plates, producing eighteen nominal run conditions. Equivalence ratio for flame structure measurements was either $\phi = 0.65$ or $\phi = 1.05$. Figure 4.1 shows the resulting thirty-six possible run conditions and their position on the Peters regime diagram. Note that there are several conditions well beyond the predicted boundary for broken reactions. Therefore, the measurements will allow a strong conclusion regarding the validity of Peters broken reaction zone boundary. Additionally, another set of cases are just above the Klimov-Williams boundary. Because the Hi-Pilot cannot sustain flames below the Klimov-Williams line this boundary cannot be evaluated directly. However the preheat structure measurements will provide a check of the Klimov-Williams prediction.

The reaction and preheat zones were imaged using the Overlap PLIF technique as well

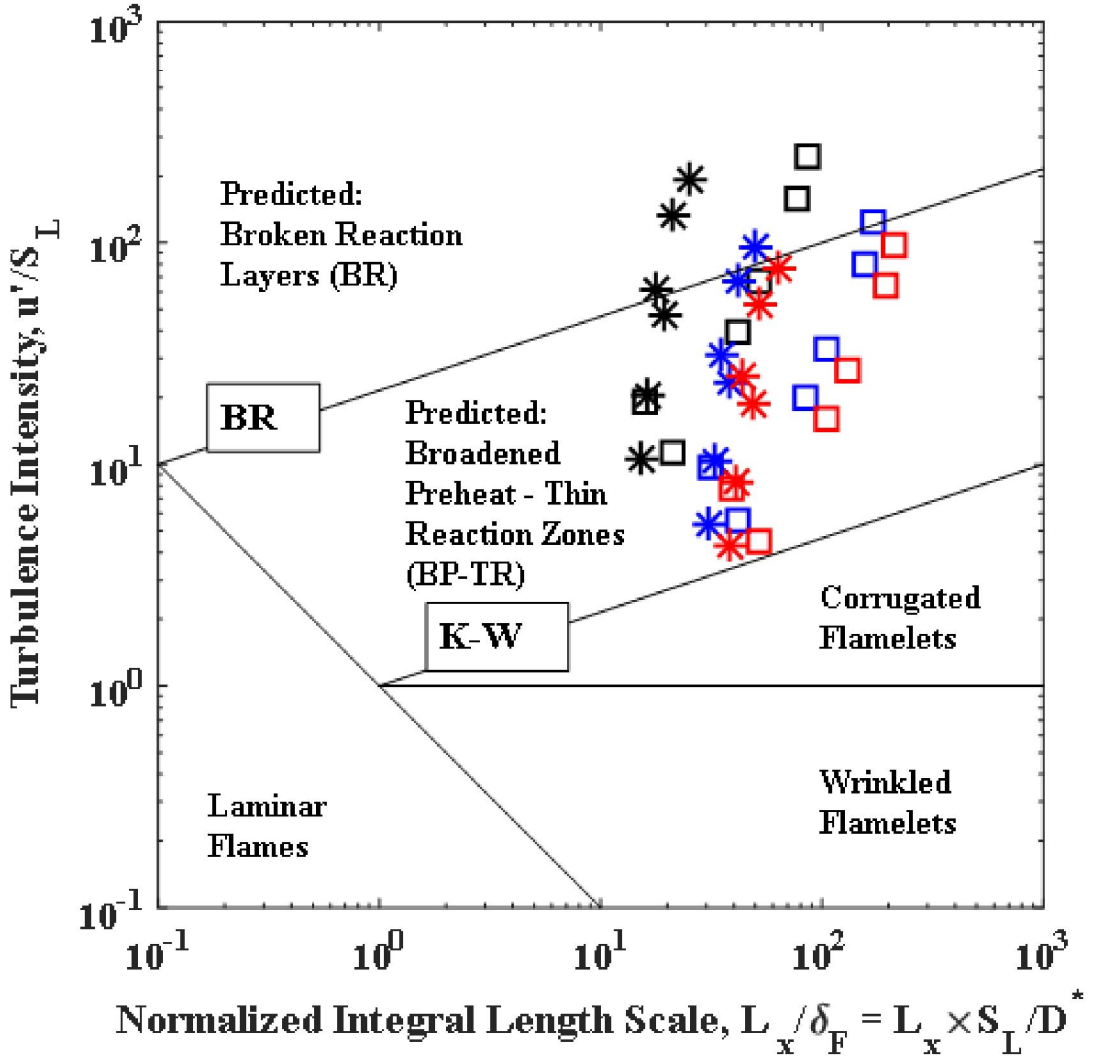

Figure 4.1: Borghi regime diagram as predicted by Peters [20, 92, 94]. Theoretical regime boundaries are labeled K-W (Klimov-Williams) and BR (Broken Reactions). Square symbols indicate the present measurements.

Table 4.1: Run conditions and parameters for the flame structure measurements

Case	ϕ	U_0 (m/s)	u' (m/s)	L_x(mm)	Re_T	Da_T	Ka_T	u'/S_L	$L_x/\delta_{PHZ,L}$
2a	1.05	14	2.9	7.5	1,440	25	4.7	7.5	31
3a	1.05	32	6.0	20	7,900	33	8.5	15	84
4a	1.05	44	10	25	16,500	25	16	26	105
5a	1.05	64	24	37	58,200	15	50	62	154
5a	0.65	64	24	37	58,200	2.3	275	157	75
6a	0.65	78	37	41	99,000	1.7	503	243	83

as CH PLIF described in Chapter 2. Results from two separate measurement domains will be presented. First, results from a preliminary, relatively large field of view (FOV) of approximately 150×150 mm^2 will be discussed, as these provide a qualitative sense of the global flame structure. Then the flame structure results from the smaller, high resolution measurements will be presented.

Experiment and Run Conditions

Six run conditions were extracted from Table 2.2 that covered a range of $7.5 < u'/S_L < 243$ and $4.7 < Ka_T < 503$. The largest slotted turbulence generating plate, plate "a", was used to generate the turbulence, and impinging jets were used above Case 3. Equivalence ratio was slightly rich ($\phi = 1.05$) for Case 2a-5a, and the flame was run very lean ($\phi = 0.65$) for an additional two cases (Case 5a-6a). This was done in order to maximize the value of u'/S_L for these most turbulent cases. Note also that the integral scale varies over a wide range from $31 < L_x/\delta_{PHZ,L} < 154$. Both the normalized turbulence intensities u'/S_L and integral scales were significantly larger in this study than previous works. Conditions for all of the methane-air flames described in this chapter are given in Table 4.1.

4.2 Images of flame structure

It is illustrative to begin by presenting the large FOV PLIF results, which provide a qualitative sense of the flame structure. Figure 4.2 shows instantaneous preheat zones (blue) in the Hi-Pilot burner for Cases 2-5a ($\phi = 1.05$), together with OH images (red) and the

Overlap (yellow) signal. Preheat layers for Case 2a are continuous and in regions near the burner exit have a thickness that is close to the measured laminar value ($\delta_{PHZ,L}$) of 0.39 mm. For Cases 3-5a it is surprising to see the extremely thick preheat zones in Figures 4.2c and 4.2d. To the author's knowledge, preheat zones this thick have not been measured before. Case 4a, for example, shows a preheat thickness $\delta_{PHZ,T}$ (indicated by the white arrow in frame c) of 20 mm, which is more than ten times the laminar value. Figure 4.2 shows that $\delta_{PHZ,T}$ tends to increase with u'/S_L and with height (x) above the burner. Zhou et al. [143, 144] found similar trends. This suggests that residence time (which scales as x/U) is an important parameter, since $\delta_{PHZ,T}$ increases with (x/U) even though all locations experience about the same turbulence level and integral scales. This implies that some non-dimensional residence time should be considered when constructing a regime diagram.

4.3 Evolution of the preheat zone in extreme turbulence

Average preheat thicknesses were evaluated using the smaller (30×30 mm^2) FOV, and the measurement utilized local thresholding and the skeletonization described in Chapter 2. The distance between inner and outer boundaries is measured as twice the distance from each skeleton point to the nearest CH_2O edge (defined as the point where formaldehyde signal drops below 35% of the local maximum). Because the trailing edge of the preheat zone is defined as the start of the reaction layer, binarized Overlap images were used to set all CH_2O signal within the Overlap region to zero. Representative CH_2O PLIF images for a range of turbulence intensities u'/S_L are shown in Fig. 4.3.

For the laminar flame, the preheat layer is very thin and approximately one-third or one-half of the total flame thickness, depending on equivalence ratio, pressure, etc. As the turbulence is initially increased in 4.3(b), the scales of turbulence remain large relative to the flame, and the effect is only to wrinkle and distort the surface. Eventually, the turbulence is increased sufficiently such that the smallest scales of the flow are comparable to

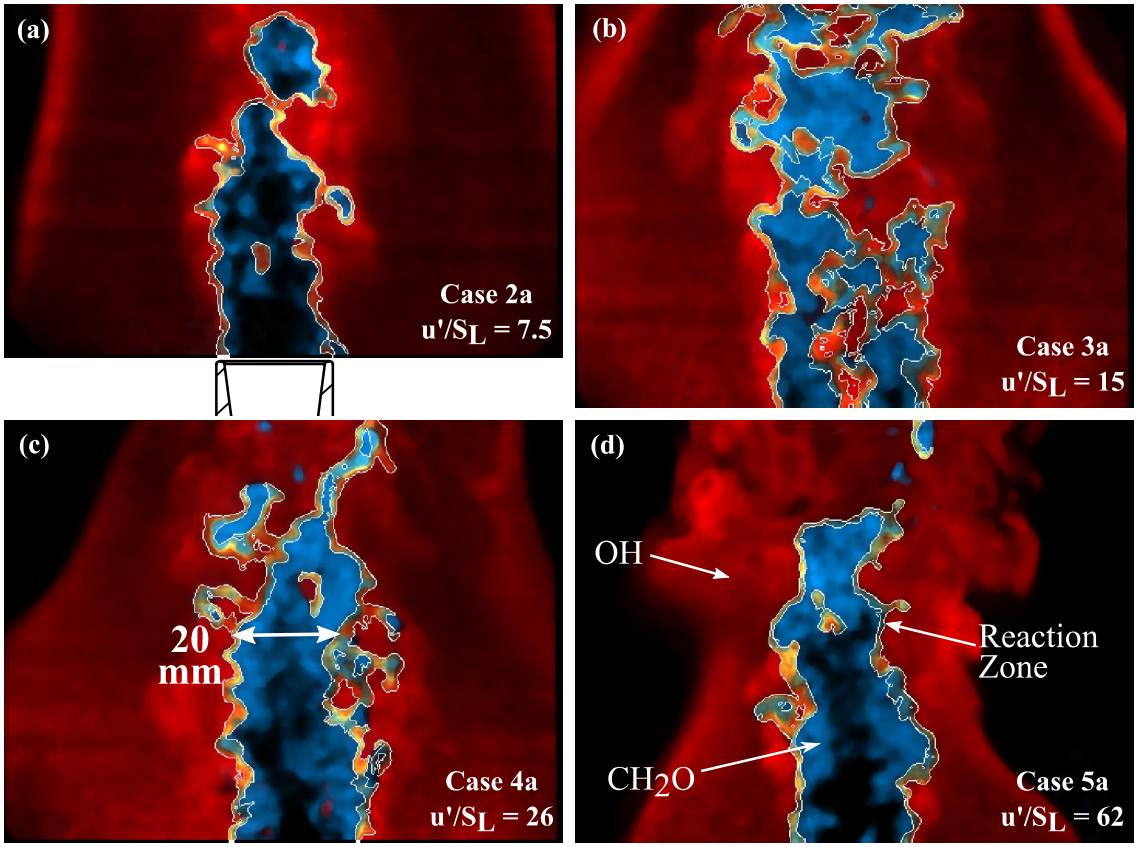

Figure 4.2: Simultaneous preheat zone (CH_2O, blue), reaction zone (yellow), and OH (red) instantaneous images for u'/S_L from 7.5 to 62 (ϕ = 1.05). White arrow in (c) indicates a preheat zone that is 50 times thicker than the laminar value ($\delta_{PHZ,L}$) of 0.39 mm. FOV in (a) is 69 mm (height)× 79 mm, in (b)-(c) it is 90 mm × 105 mm, and in (d) it is 115 mm × 130 mm

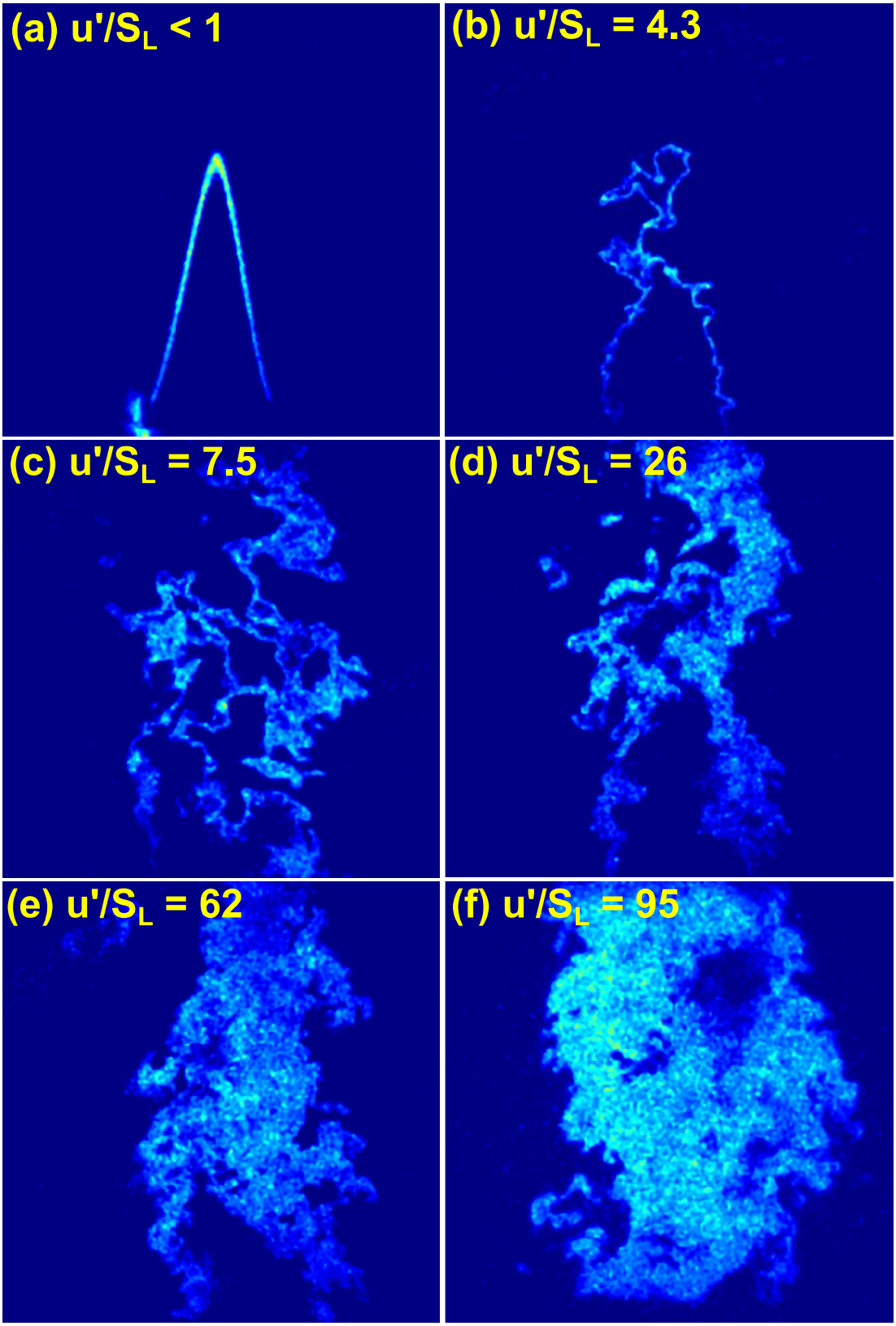

Figure 4.3: Evolution of the preheat structure with increasing turbulence intensity u'/S_L. (a) Laminar calibration flame, (b)-(f) Hi-Pilot flames

that of the preheat layer, and the low temperature chemistry is disrupted. This is manifested by substantial broadening of the preheat layer as turbulent transport is able to move hot gas near the reaction layer upstream. However, as the example in Fig. 4.3(c) shows, this is only a local phenomena at first, as regions with broadened preheat structures are juxtaposed with preheat structures that are approximately the laminar thickness. Increasing turbulence intensity u'/S_L causes the broadening effect to become more substantial throughout the flame, and eventually this thickening causes the preheat structures on either side of the Bunsen cone to merge (4.3(e)). If the turbulence continues to increase beyond this point, the location where the two sides of the preheat layer merge will move upstream, as seen in 4.3(f) where the location of preheat structure merging has moved nearly to the exit plane. At this point the preheat layer can be considered fully broadened, because it has expanded to occupy all available space within the flame cone. From the CH_2O PLIF, it is unknown what effect increasing the turbulence beyond this point will have; it may be that further increases in turbulence are still more effective in distributing hot gas near the flame upstream, and would allow the entire preheat region to attain a higher (and more uniform) temperature. Because the PLIF measurements of CH_2O concentration in this work are qualitative, this question cannot be directly answered at present, and will require either temperature field measurements through Rayleigh scattering or quantitative CH_2O PLIF.

The measured preheat zone thicknesses are shown in Figure 4.4. The thickness $\delta_{PHZ,T}$ reaches nearly thirty times the laminar value ($\delta_{PHZ,L}$). There is, of course, a limit to how much broadening can occur once the two sides of the Bunsen cone merge, as in Fig. 4.3(e) and 4.3(f). This limit is the width of the jet, which can be approximated as one-half the burner exit diameter, which gives a theoretical maximum $\delta_{PHZ,T}/\delta_{PHZ,L} \sim (21.6/2)/0.322 = 33.5$, which is approximately the maximum layer thicknesses measured in Fig. 4.4

All cases fall within the "broadened" preheat zone regime, defined as $\delta_{PHZ,T}/\delta_{PHZ,L} > 2$. The Klimov-Williams criterion has often been cited as the boundary separating corrugated flamelets from Broadened Preheat - Thin Reaction layers (BP-TR) [94]. This cri-

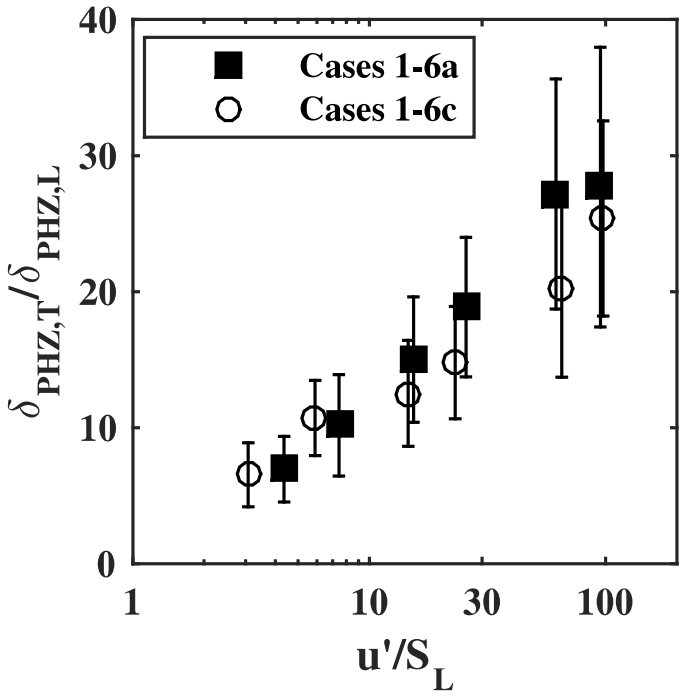

Figure 4.4: Average preheat zone and thicknesses normalized by the measured laminar thickness as computed as a function of u'/S_L.

terion is based on the assumption that the preheat layer will broaden as the Kolmogorov scale of turbulence becomes small enough to penetrate the flame ($\eta_k < \delta_{PHZ,L}$). In this regime, it is thought that the reaction layer will remain unaffected by the turbulence, and retain laminar flame properties. The present study does not consider conditions below the Klimov-Williams criterion (corrugated flamelets), and therefore cannot evaluate the boundary conclusively. However, it is observed that all four of the flames which fall in the predicted BP-TR regime agree with the predictions of Peters. Thus, the present data supports (but does not validate) the Klimov-Williams criterion.

Fig. 4.4 shows that the preheat zone increases approximately linearly with the logarithm of u'/S_L, and is generally larger with increasing integral scale, particular in the extreme range of turbulence. It is useful to develop a correlation for the preheat layer thickness as a function of the turbulence conditions, as the works in Chapter 5 will measure turbulent burning velocities which depend in part on $\delta_{PHZ,T}/\delta_{PHZ,L}$. To this end, the

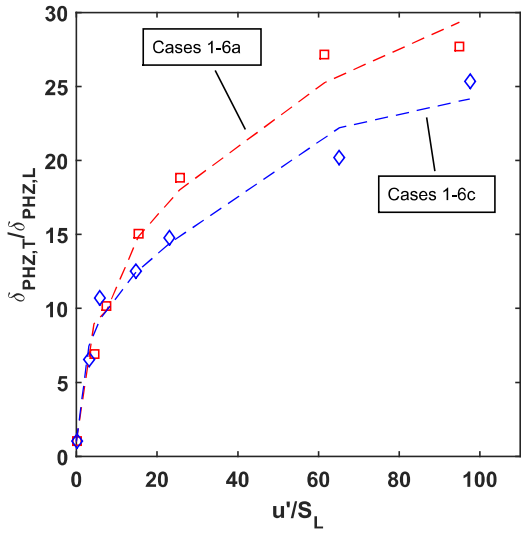

Figure 4.5: Performance of the correlation for the preheat layer thickness, Eqn. 4.1.

following correlation was found to approximate the measured preheat layers:

$$\frac{\delta_{PHZ,T}}{\delta_{PHZ,L}} = 1 + 2.2\left(\frac{u'}{S_L}\right)^{0.3}\left(\frac{L_x}{\delta_{PHZ,L}}\right)^{0.24} \tag{4.1}$$

The value for L_x was determined from the LDV measurements described in Chapter 3, and the performance of the fit is shown in Fig. 4.5.

4.4 Evolution of the reaction layer

4.4.1 Typical reaction layer images

Full-FOV Overlap reaction zones are shown as yellow regions in Figure 4.2 for Cases 2-5a ($\phi = 1.05$). For Case 2a there is significant large-scale wrinkling but no evidence of broken or distributed reactions. Case 5a also shows continuous and thin reaction layers despite a significant increase in u'/S_L. Reaction zone thicknesses were obtained by imaging the smaller FOV (30 x 30 mm^2), permitting the high resolution required for an accurate Overlap measurement. Typical reaction layers for Cases 2a, 4a, and 6a are given in Figures 4.6-

4.11. The turbulence intensities in the three run conditions are u'/S_L =7.5, 26, and 243, respectively. For each case, six representative reaction zones are presented in two separate figures. The first provides just the reaction layer against a white background and the second provides the OH and CH_2O signals on either side. In the second set of images, OH is in red, formaldehyde is blue, and the reaction layer is in yellow.

It is striking that there does not appear to be any significant change to the reaction layer structure across the span of run conditions, even at the extreme turbulence conditions of $u'/S_L = 243$. Figs. 4.7 and 4.11 show that formaldehyde and OH PLIF signals form a smooth, continuous interface, and the reaction layers (seen most clearly in Figs. 4.6 and 4.10) do not appear to be undergoing any significant change in either thickness or structure. The reaction layers in Case 6a appear to be approximately the same size as those in Case 2a, although there is more spatial variation at higher turbulence. Case 6a does exhibit some regions of extensive roll-up, where the reaction layers appear very thick. However, there are also regions where the layers appear much thinner than the lower turbulence levels conditions. This may be an illustration of the competing effects of flame strain: as large scales of turbulence stretch the flame tangentially (the preliminary step to wrinkle formation), the reaction layer is expected to become thinner. This effect was seen by Dinkelacker [38] in turbulent swirl flames. However, turbulence from small scale eddies is expected to broaden the flame, provided it is sufficiently small relative to the reaction zone structure. This work suggests that both actions are present in extreme turbulence.

A direct comparison between the reaction layers of Case 2a ($u'/S_L = 7.5$) and Case 6a ($u'/S_L = 243$) is provided in Fig. 4.12. The side-by-side comparison re-reinforces the remarkable consistency in reaction layer structure at two extremes of turbulence. For Case 6a there are occasional instances of broken reaction layers, this is evidenced by panel (c) in Figs. 4.10 and 4.11, and panel (f) in Fig. 4.12. The occurrence of extinction events is relatively rare, and will be quantified in section 4.4.4. It should be noted that local extinction of the Overlap signal does not necessarily imply that all reactions have ceased;

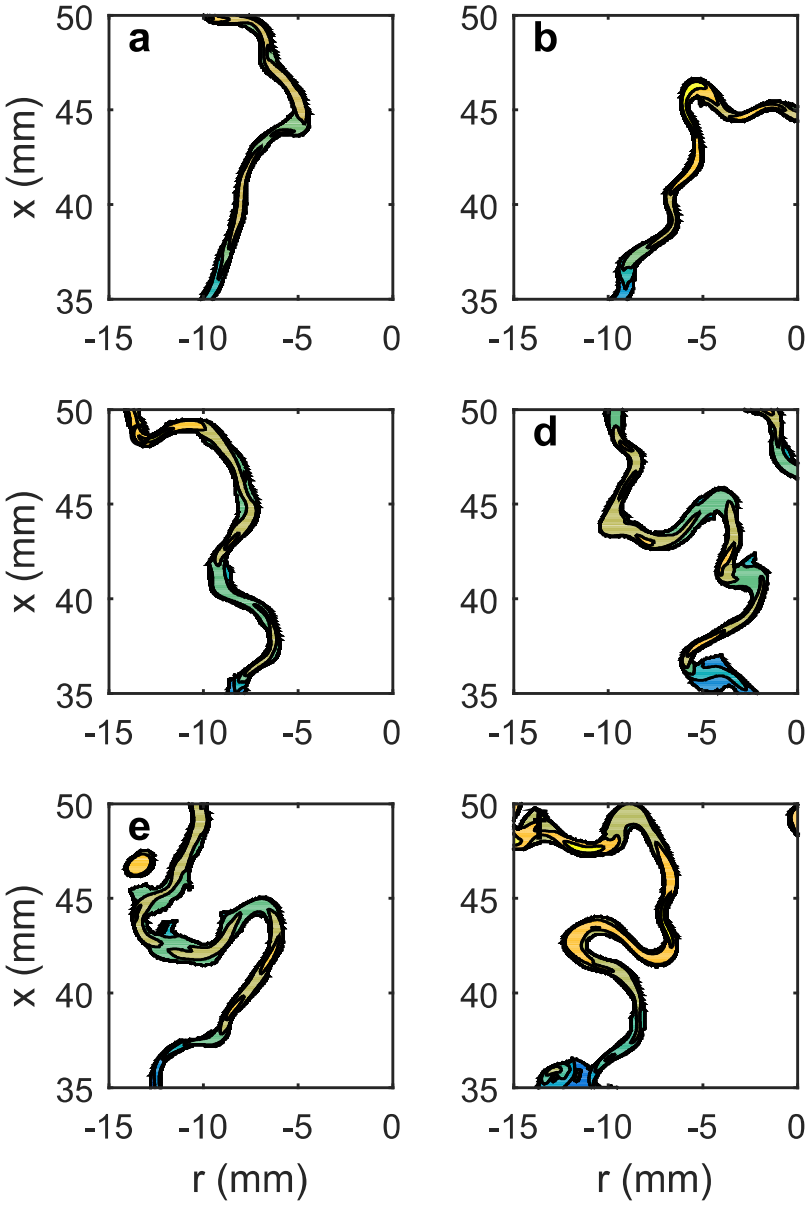

Figure 4.6: Example reaction layers for Case 2a. $u'/S_L = 7.5$.

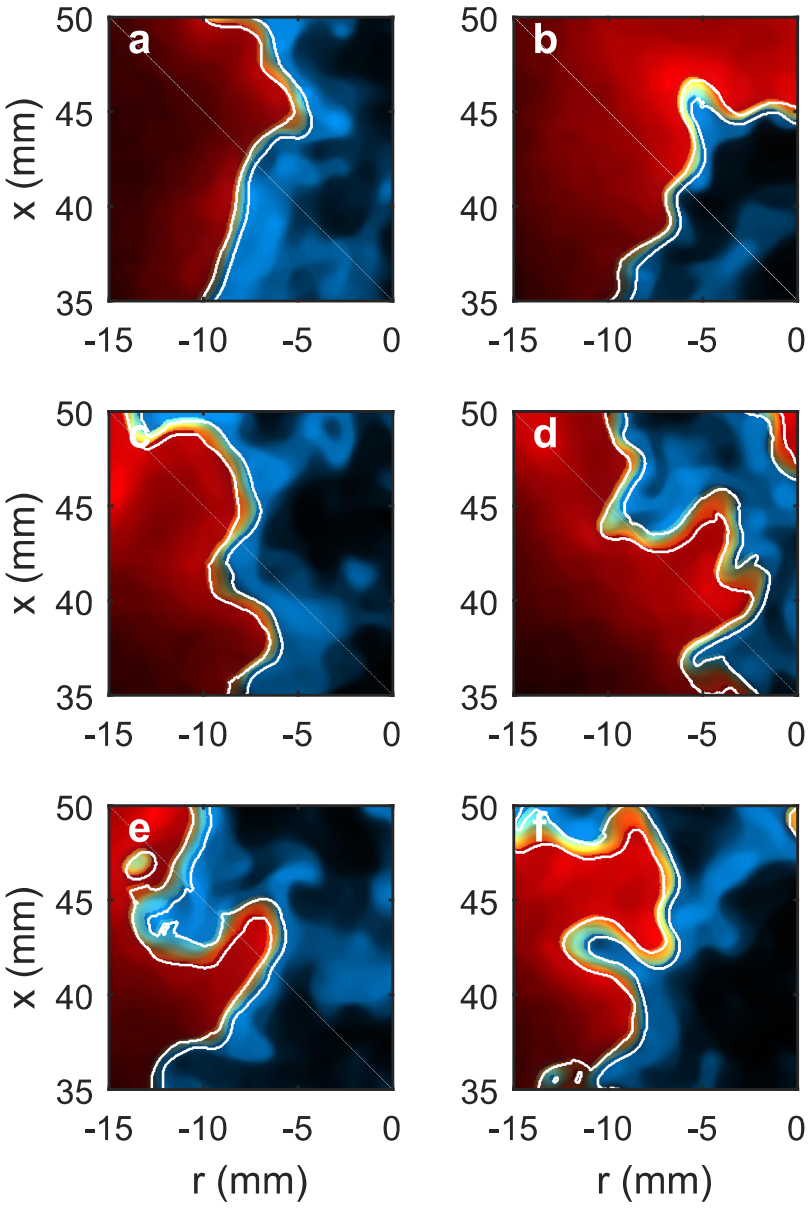

Figure 4.7: Example reaction layers for Case 2a. $u'/S_L = 7.5$. Red region is OH signal, blue region is formaldehyde signal, and yellow is the reaction layer.

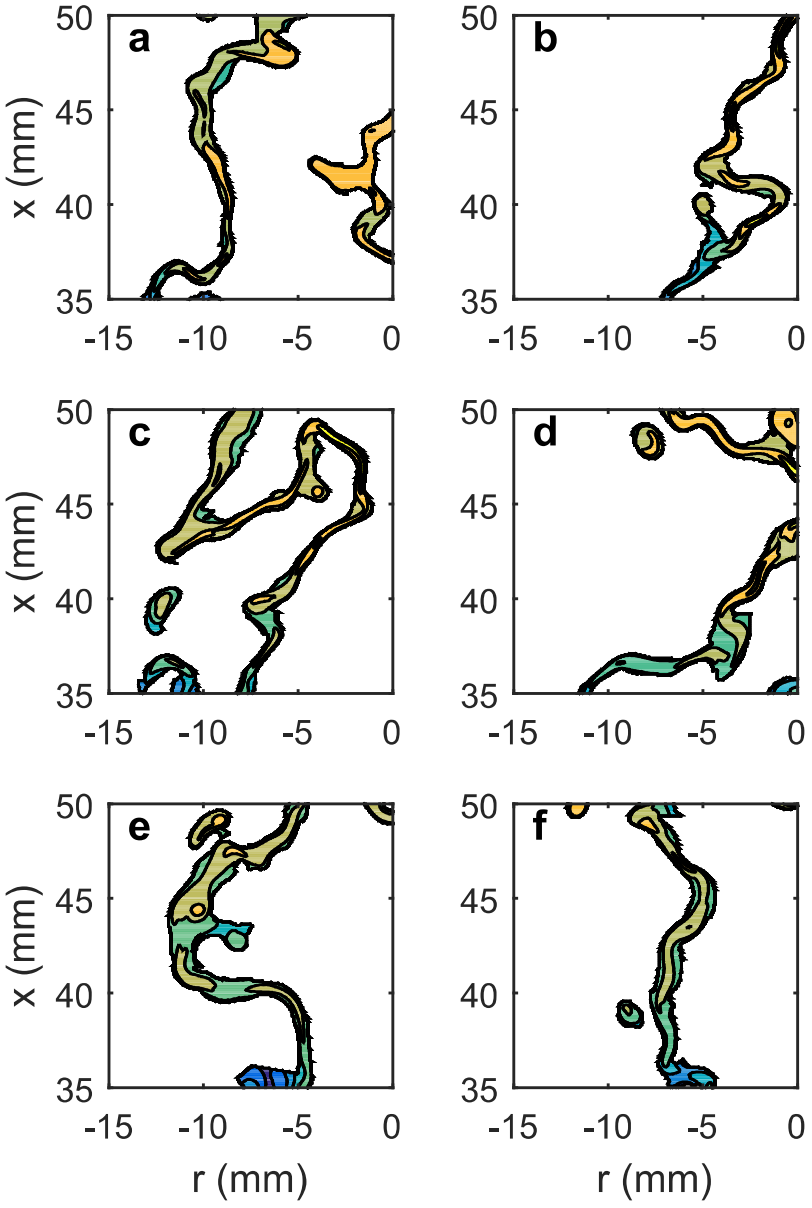

Figure 4.8: Example reaction layers for Case 4a. $u'/S_L = 26$.

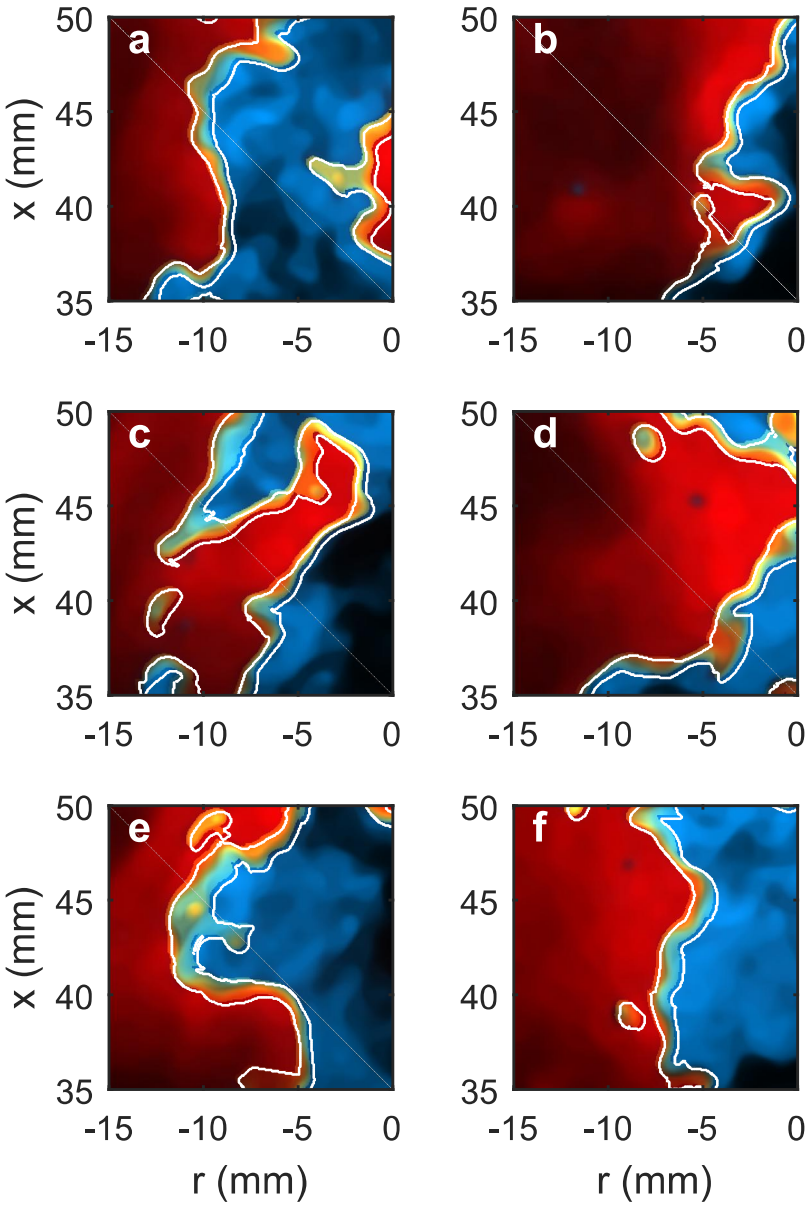

Figure 4.9: Example reaction layers for Case 4a. $u'/S_L = 26$. Red region is OH signal, blue region is formaldehyde signal, and yellow is the reaction layer.

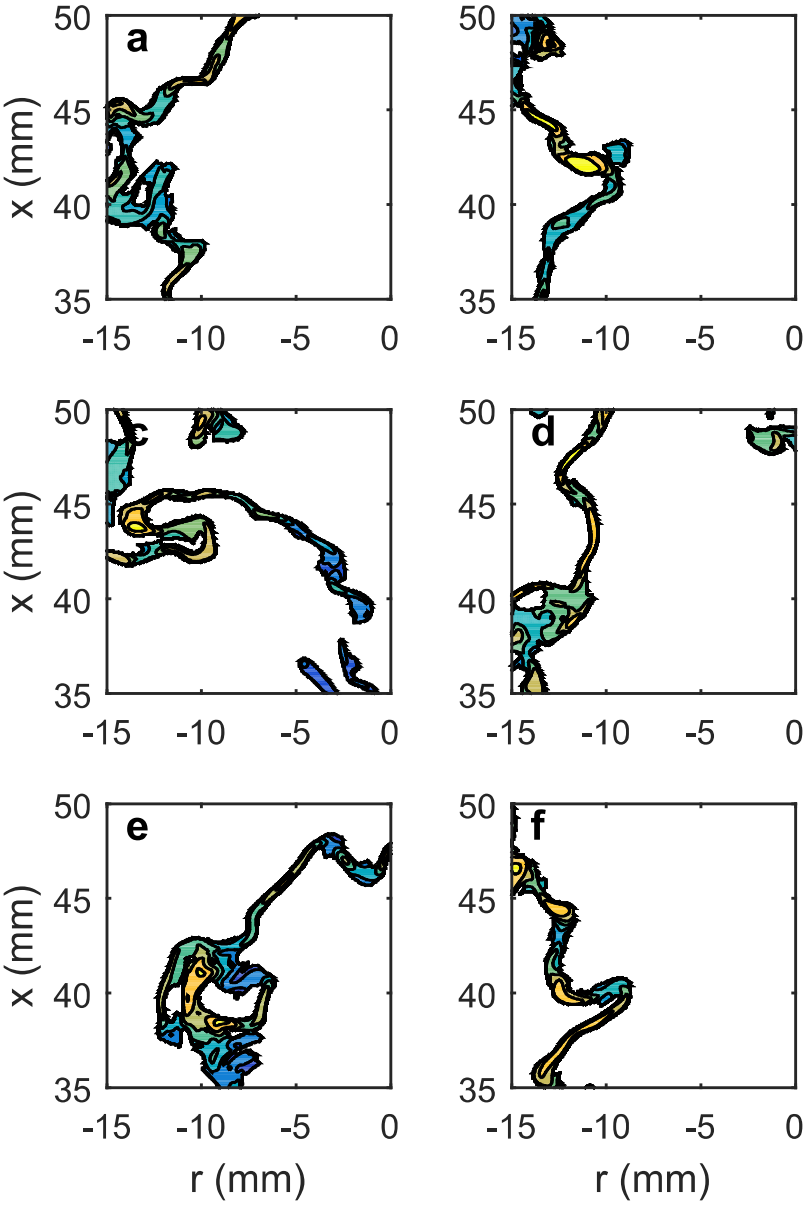

Figure 4.10: Example reaction layers for Case 6a. $u'/S_L = 243$.

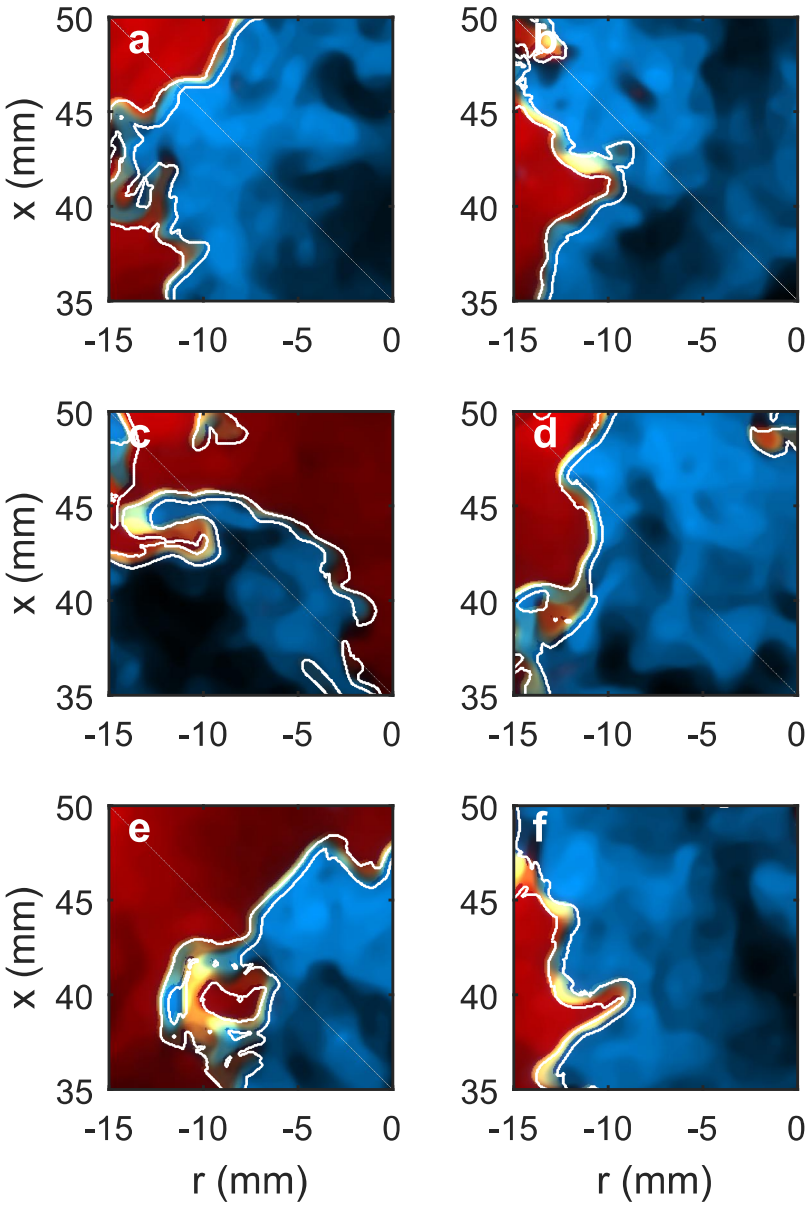

Figure 4.11: Example reaction layers for Case 6a. $u'/S_L = 243$. Red region is OH signal, blue region is formaldehyde signal, and yellow is the reaction layer.

rather the signal has simply dropped below the threshold used here (equaling 50% of the local maximum). See Section 2.4.1.7 for a discussion of how to interpret extinction events from the Overlap signal.

4.4.2 Average thickness of the reaction zones

The time-averaged reaction layer thicknesses were computed using the technique described in Section 2.4.1.4. Reaction layers are called "thickened" if their average thickness exceeds twice the laminar value. Figure 4.13 confirms the conclusions provided by the qualitative reaction layer images presented above, and shows that the normalized reaction zone thickness ($\delta_{RZ,T}/\delta_{RZ,L}$) does not exceed two, indicating no significant broadening. As the turbulence intensity is increased, the normalized reaction layer thickens gradually, however it remains less than two at all conditions, even at extreme turbulence levels of $u'/S_L = 243$ ($Re_T = 99{,}000$). There appears to be a decrease in $\delta_{RZ,T}/\delta_{RZ,L}$ in the last two measurement points, and this may be due to the different fuel chemistry in these flames. In order to obtain the highest possible value of u'/S_L, these two points were run at equivalence ratio $\phi = 0.65$, while the previous four data points were collected at $\phi = 1.05$ (see Table 4.1). Thus, it is possible that fuel chemistry parameters besides S_L and $\delta_{RZ,L}$ may be important; for instance, the Lewis number may important in these flames. Exploring these effects is an avenue for future work, and will be discussed in Chapter 7.

4.4.3 Percent of distributed regions

Although the Overlap signals are typically layer-like, there were occasions where non-flamelet like structures were observed. The percentage of flamelet-like reaction zones was calculated using a parameter that identified partially-distributed regions. We define a structure to be *partially-distributed* using Eqn 4.2.

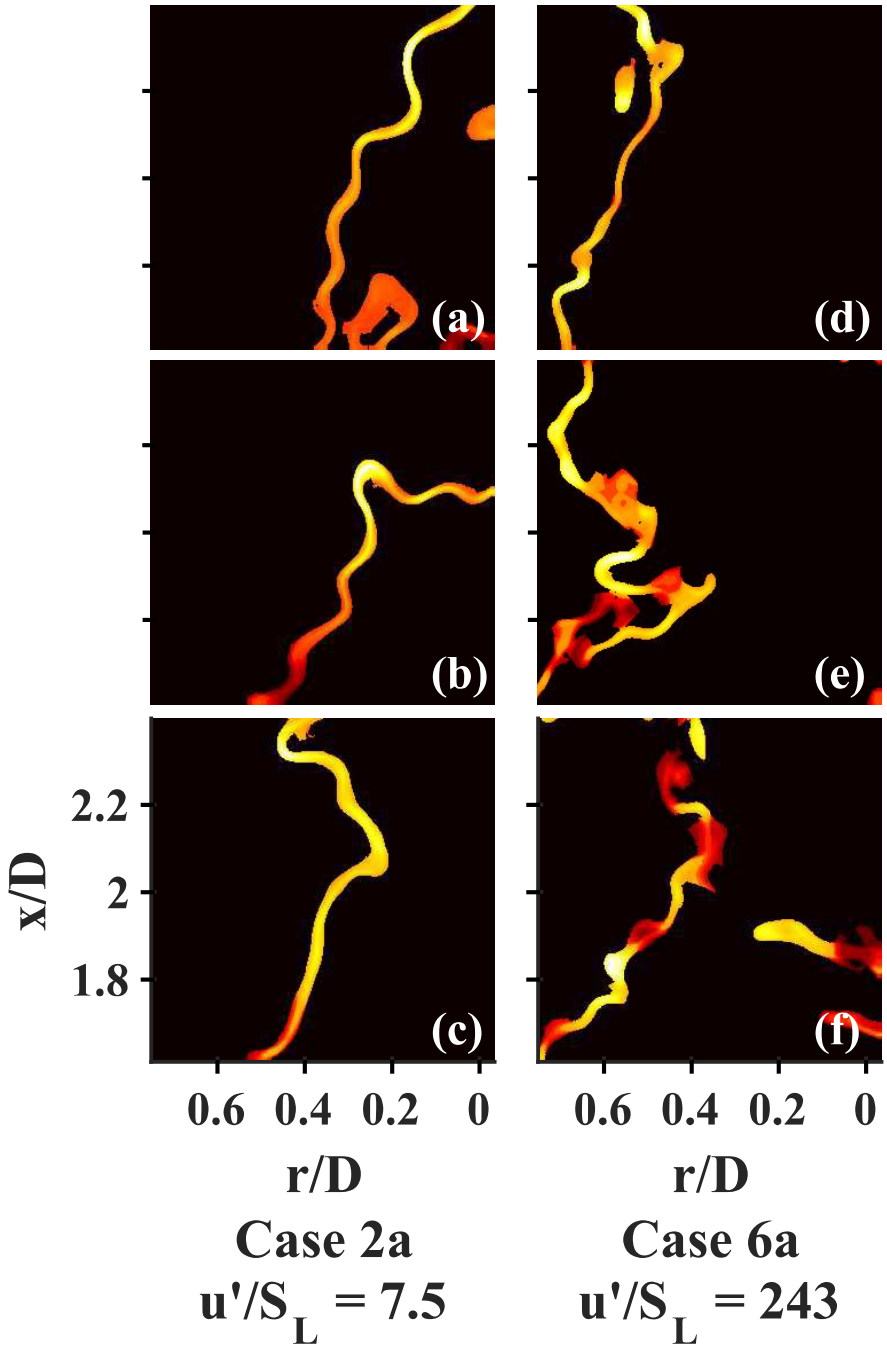

Figure 4.12: Reactions zones for the Case 2a (ϕ = 1.05, panels a-c) and Case 6a (ϕ = 0.65, panels d-f), at three random times.

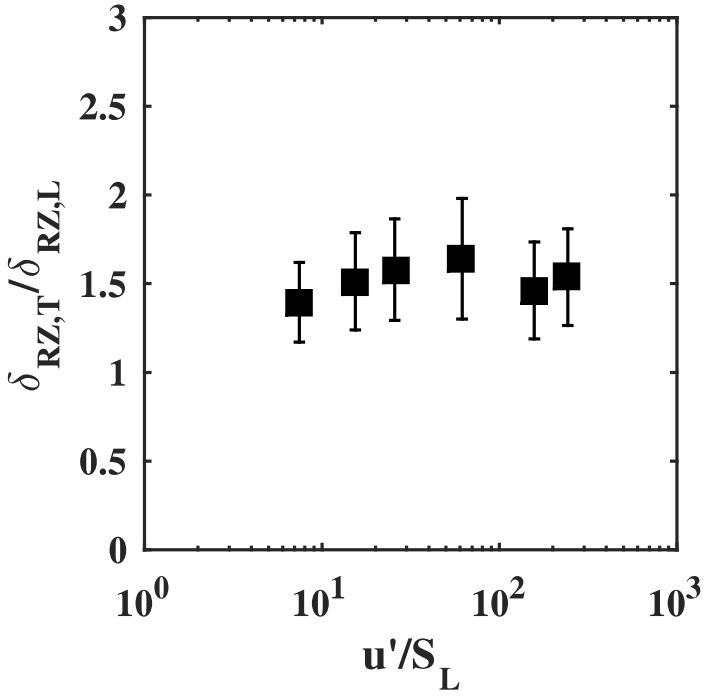

Figure 4.13: Average reaction zone and thicknesses normalized by the measured laminar thickness as computed as a function of u'/S_L.

$$locally\,distributed = \left\{ \begin{array}{c} \frac{\delta_{RZ,T}}{\delta_{RZ,L}} > 4 \\ \hline AR = \frac{Length}{\delta_{RZ,T}} < 4 \end{array} \right\} \tag{4.2}$$

In order to determine the aspect ratio AR, the length of a reaction layer (determined from the skeleton) was compared to the average thickness of the layer. See Fig. 4.14 for an example of how this method is implemented in a typical reaction layer image. The percentage of partially distributed layers ranged from 0 to 3%, indicating that distributed regions were not significant in any of the cases studied. Partially-distributed regions occurred predominantly in two situations: flame roll-up/merging events, where thin wrinkled flamelets come together and temporarily form a broad combustion zone; and pockets of combustion that occur far away from the primary flame sheet. Examples of both of these can be seen in the sample images provided in Figs. 4.6-4.11. It is noted that the observed pockets are likely to be a three-dimensional effect at least some of the time. Here, three-dimensional effect refers to a thin flame sheet that exists parallel to the laser sheet and is convected into the measurement plane during the acquisition time. This manifests itself as a blob of Overlap signal as the flame sheet is at first parallel with the laser sheet, and becomes a ring as the flame sheet continues to convect through (normal to) the laser sheet. This is seen most clearly in the CH-PLIF images, presented in Section 4.4.6

4.4.4 Measurement of the Burning Fraction to Quantify Local Extinction

An important quantity for turbulent flames is the likelihood of local extinction. The regime diagram given in Figure 4.1 predicts that at sufficient turbulence the reaction zones can no longer resist the strain of the flow and will either fully thicken into distributed reactions or break apart (broken reactions). The percentage of broken zones was quantified in the present data using the burning fraction, defined to be the amount of CH_2O on or near a reaction zone, divided by the total amount of CH_2O in the field of view:

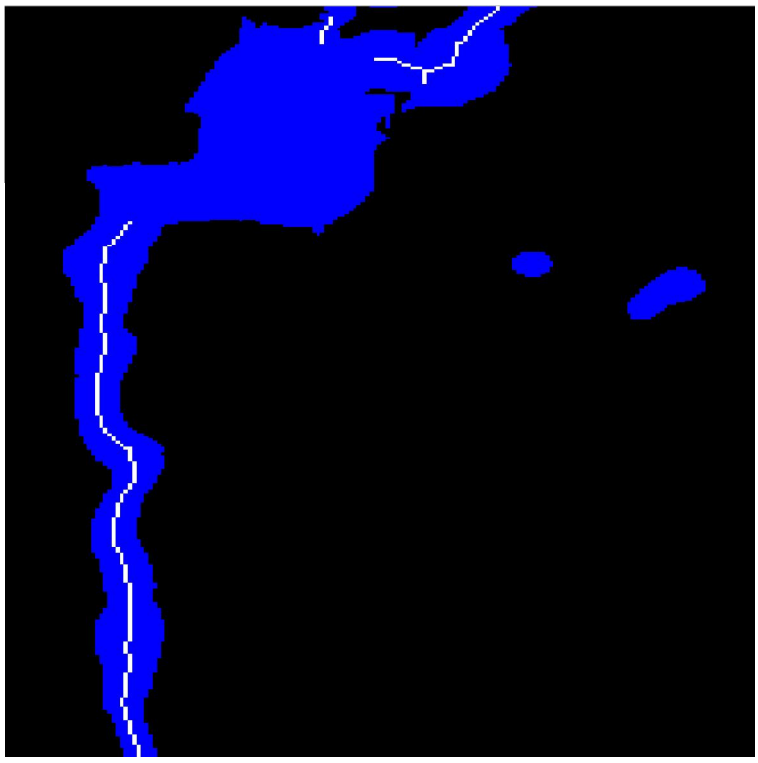

Figure 4.14: Example of locally distributed reaction zone parameter marking. Reaction layer is in blue. White skeleton lines indicate the region is locally a flamelet. The remaining regions are designated as locally distributed reactions.

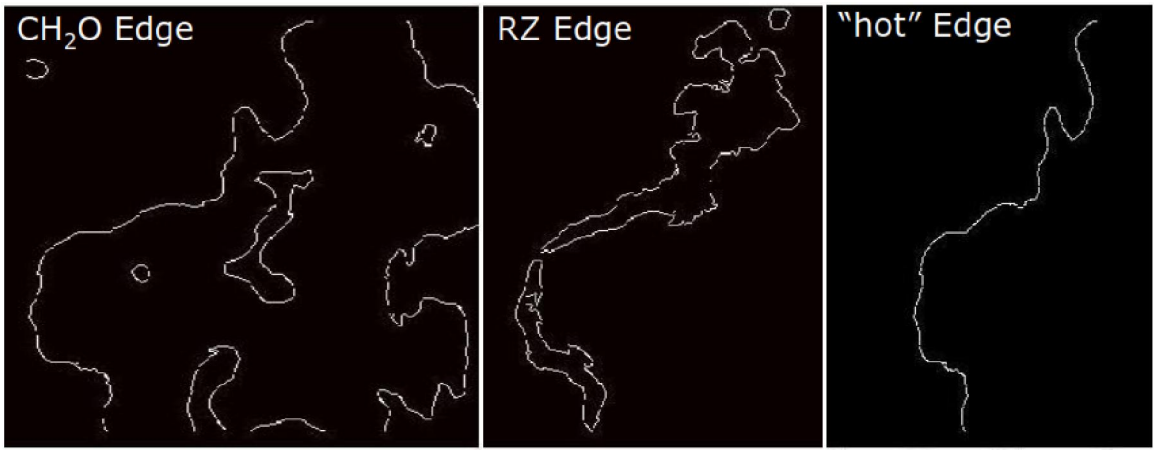

Figure 4.15: Illustration of how the burning fraction is determined.

$$BF = \frac{CH_2O\,burning}{Total\,CH_2O} \tag{4.3}$$

Of course, a large fraction of the CH_2O in any given PLIF image will consist of the "cold edge" boundary, marking the reactant side and the start of the preheat zone. Including this quantity in the denominator of Eqn. 4.3 would lead to an artificially low burning fraction, and a distorted view of the amount of extinction. The best solution was found to be breaking the image into multiple distinct objects and eliminating any objects not very near a reaction zone at some point along the surface. This procedure is illustrated in Fig. 4.15. On the left is the full CH_2O edge including the cold-side boundary, and in the middle is the reaction layer edge. Clearly, not every pixel in the CH_2O frame should be considered when evaluating the burning fraction. The right frame illustrates the processed CH_2O edge, refereed to as the "hot edge". It is clear that the procedure works as desired as it eliminates the "cold edges" from the image.

Once the CH_2O images have been processed as described above, the burning fraction is evaluated by taking the ratio of pixels on or near a reaction zone to the total number of pixels in the "hot edge" of the processed CH_2O image. The quantity is ensemble-averaged over all frames to derive a representative amount of local extinction for each run condition.

The burning fraction was found to be nearly constant at all conditions, with no cases falling below 0.98 (indicating less than 2% extinction). Therefore, all of the cases studied can be said to have nearly continuous reaction zones. Although some instantaneous flame segments were extinguished (panel (c) of Figs. 4.10 and 4.11, and panel (f) of Fig. 4.12), these events were rare.

Large-scale extinction in the Hi-Pilot was only possible when using a less robust co-flow. This allowed cold, ambient, room air to be entrained into the turbulent jet, quenching chemical reactions. All test cases in the present study used a sufficiently large co-flow to sheathe the flame with hot products, and the burning fraction was not computed for a condition with a weaker co-flow that produced global extinction (i.e., an open flame tip). However, large FOV formaldehyde and OH-PLIF images were recorded with a reduced co-flow and showed an open flame tip, indicated by the formaldehyde signal persisting downstream far beyond the trailing edge of OH-PLIF signal. Kiefer et al. [62] used simultaneous CH and OH-PLIF and observed identical results. This highlights the importance of co-flow geometry and temperature in maintaining combustion in extreme turbulence.

4.4.5 Broken reaction layers in the Hi-Pilot

The work above shows that reaction layers in the Hi-Pilot remain continuous and thin everywhere on the flame surface. However, there are two exceptions to this finding which merit discussion. The first is the observation that as the equivalence ratio is lowered to near the lean blow-off limit, the flame tip does not remain closed. In this, chemical reaction near the flame tip cannot keep up with the intense strain at the tip, as differential diffusivity in a lean Methane-air flame draws heat out of the region disproportionately [121].

The other instance where broken reactions were widely observed in the present work was described above in Section 4.4.4, and occurs in situations where the co-flow is not sufficiently strong. Here co-flow strength (sometimes called the back-support of a premixed flame) is defined using the concepts outlined in Sections 2.1 and 3.2.1. Much early work

performed in a previous version of the Hi-Pilot, with a much smaller co-flow, exhibited broken reaction zones. In this case, cold air was entrained near the reaction surface, disrupting the chemistry and quenching reactions. This would then lead to mixing of reactants and room air through the extinction region, producing reactants of unknown composition and temperature. The effect of co-flow strength on the global flame structure was illustrated in Section 2.1.

The process of reaction layer quenching due to entrainment is illustrated in Fig. 4.16 for a typical extinction event. Although extinction events were rare (less than 2% of the average flame surface), it was observed that quenching can occur in instances where there is an absence of OH-PLIF signal downstream of the reaction layer. The absence of OH-PLIF signal implies entrainment of cold air into the region downstream of the flame. Fig. 4.16 illustrates this using the two-tone PLIF method which was described in Section 2.4.3.1. This technique excites CH and OH radicals simultaneously with a single laser pulse, allowing imaging of the reactants and products in a single image. Thus, the variation of the products region near the flame prior to extinction events can be monitored. The figure shows a broad region of OH (and thus hot gases) downstream of the reaction layer at t = 0 ms. At t = 0.1 ms, the OH region downstream of the flame has thinned significantly, and cold ambient air is nearly in contact with the downstream surface of the reaction layer. This means that there is very little back-support downstream of the flame, which ideally would provide a uniform high temperature with plenty of combustion radicals. By the final frame t = 0.2 ms, the cold air has made contact with the reaction layer and quenched reactions at that point. Nearly all extinction events in the Hi-Pilot can be traced to this mechanism.

4.4.6 CH PLIF measurements of the reaction layer structure

The CH PLIF measurements were conducted at the Air Force Research Lab at Wright-Patterson Air Force Base, in coordination with Drs. Cam Carter and Stephen Hammack. The CH PLIF utilized a resonant transition at 314 nm, as described in Chapter 2. There

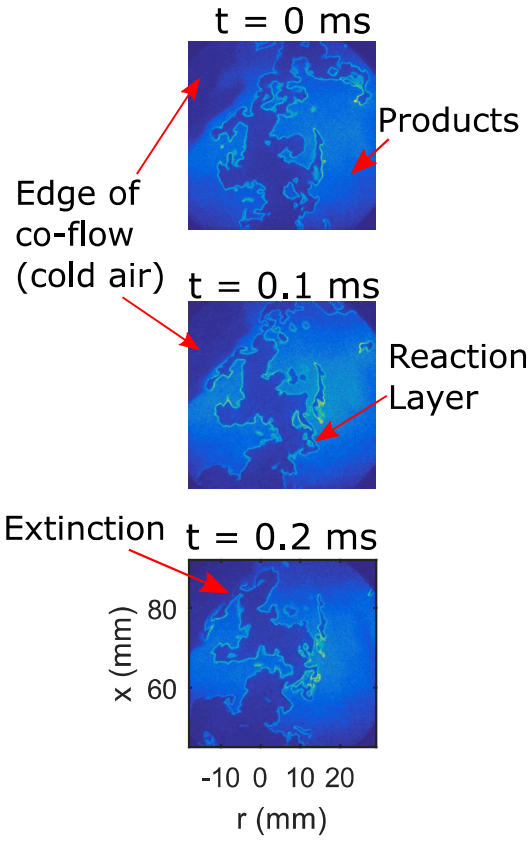

Figure 4.16: Example sequence of extinction in the Hi-Pilot burner. Case 5b ($\phi = 1.05$), $u'/S_L = 63.7$.

are several major advantages to this technique. First, the signal to noise is outstanding; with an excitation power on the order of 5-10 mJ/pulse, a signal-to-noise ratio exceeding 100 is common. Additionally, because the region where CH radical exists has been shown to coincide well with the heat release region, very little image post-processing is required; for the CH-PLIF, application of a straightforward thresholding algorithm will produce high quality reaction layer images. Because CH PLIF is a relatively more common tracer of the reaction zone, the high signal-to-noise, and the minimal need for post-processing enhancements as compared to the Overlap method, this was an ideal alternative marker of the reaction zones in the Hi-Pilot flames, and was used to validate the Overlap measurement.

Measurements for CH-PLIF were performed at Cases 2-5a in the Hi-Pilot burner. The CH-PLIF were generally found to remain thin and continuous at all measurement points, and exhibited an extremely densely packed structure. See Fig. 4.17 for an illustration of the CH-PLIF in a typical Hi-Pilot flame for Case 4a. The wrinkling is quite substantial and it is difficult to imagine that the flame surface area could increase much beyond this level, as flamelet merging is clearly occurring in the most densely populated regions. This is an important point, and it will be returned to in Section 5.3, where the maximum measured extent of flamelet wrinkling is discussed.

The CH thicknesses were measured using an identical processing algorithm as for the Overlap method, described in Section 2.4.1.4. The reaction layer thicknesses from the CH-PLIF are given in Fig. 4.18. Comparing the results with the measured Overlap layer thicknesses from Fig. 4.13, there is good agreement with the CH-PLIF. Both measurements indicated thin heat release zones, less than two times the measured laminar value. There does not appear to be a significant change in the reaction zone structure as the turbulence is increased, and a plateau is observed for both measurement techniques for $u'/S_L > 40$. Quantifying the degree of extinction is a more difficult task than in the Overlap PLIF, because there is not a layer edge to compare the reaction zones with (for instance, the burning fraction measurement described in 4.4.4 uses the formaldehyde edge as a reference;

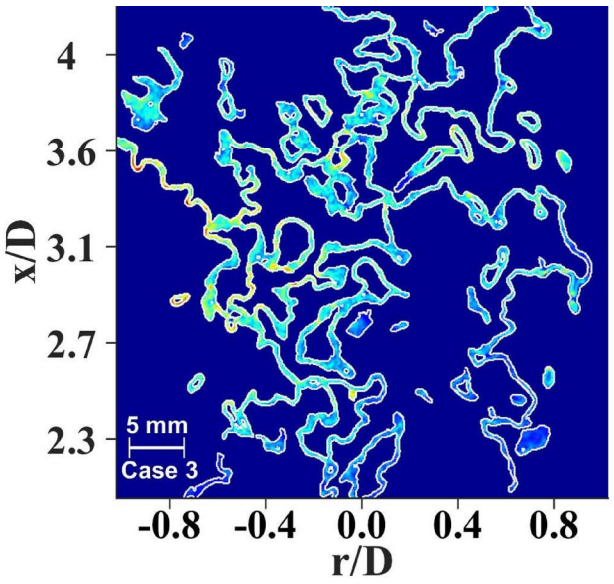

Figure 4.17: Typical image of CH radical for Case 4a. Note the 'distributed flamelets' (see text).

if a reaction zone is absent downstream of the preheat layer, it indicates an extinction event). Therefore, the burning fraction was not computed for the CH-PLIF. However, a visual inspection of the images (illustrated by the example in Fig. 4.17) shows very little extinction of the CH layers.

Taking the Overlap and CH-PLIF measurements together, we see a consistent story in the data. Despite substantial broadening of the preheat zones, no significant change is detected in the reaction layer structure. This is inconsistent with previous regime diagram predictions (ex, Peters), and is surprising given the extremely large turbulence intensities of $u'/S_L = 243$. The remainder of this chapter will discuss implications of these results on designing and interpreting regime diagrams.

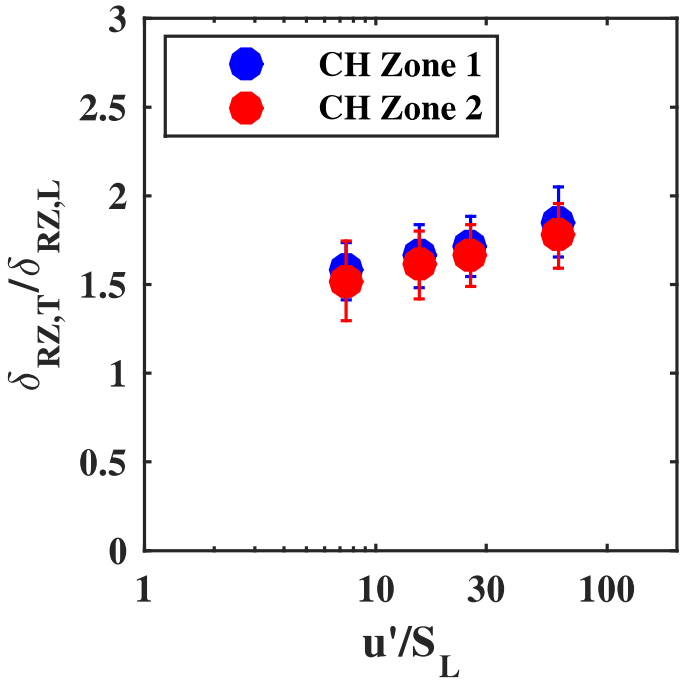

Figure 4.18: Average reaction zone thicknesses from the CH PLIF. The agreement with the Overlap thicknesses from Fig. 4.13 is very good, with all thicknesses less than twice the measured laminar value. Error bars represent two standard deviation of the thickness measurements, or 95% confidence in the mean.

4.5 Evaluation of regime diagram predictions and proposed modifications

The present work indicates some limited broken reaction zones (see Figure 4.12(f)), however these instances occur on average in less than 2% of the flame surface. Peters has predicted [93, 94] that as the turbulence intensity is increased beyond a critical value (see BR boundary in Figure 4.1), broken reactions will occur. However, the present work suggests this theory requires reconsideration, as several run conditions fell well above the predicted BR boundary, yet no significant change in flame structure was observed. There are several possible explanations for this discrepancy. The regime boundaries as drawn by Peters contain assumptions regarding both the turbulence and flame structure, which simplify the analysis but may not be valid. For instance, asymptotic analyses [106] predict the reaction layer should be about an order of magnitude thinner than the total flame thickness. However, CHEMKIN simulations and laminar flame measurements both show that the reaction layer is typically closer to one-half to one-third of the total flame thickness.

Additionally, the criterion for broken or distributed reactions ($\delta_{RZ} = \eta_K$) does not account for the attenuation of turbulence that will occur through a broadened preheat zone. Preheat zones greater than 20 mm in thickness (as observed in the Hi-Pilot) will present a large region of elevated temperature and viscosity across which turbulence will decay. The ratio of turbulence conditions (u' and L_x) measured upstream of the preheat layer and measured at the reaction front is the subject of the simultaneous PIV and formaldehyde PLIF measurements of Chapter 6. In the regime diagram of Peters, flame properties are evaluated at an elevated temperature when drawing the BR boundary, which will account for the increase in η_k through the preheat layer. However any attenuation of the turbulence beyond this preheating effect must be accounted for when constructing a regime diagram.

Based on the present results, it appears that this phenomenon makes it much more difficult to achieve fully broken or distributed reaction layers than previously believed. The

question of turbulence attenuation through the broadened preheat layer is the subject of Chapter 6, and discussion of that question is reserved for that section. However, the results indicate that the threshold for broken reactions is greater than the line of $Ka_T = 100$ that was predicted by Peters. We know that broken and distributed regions can occur, as the high Karlovitz number jet flames of Zhou et al [143, 144] and the DNS of Savard et al [107, 108] and Aspden et al [7, 8] demonstrated evidence of non-flamelet like combustion. However, the Karlovitz numbers in these flames was very large, exceeding $Ka_T = 1,000$ in the works of Zhou et. al. and Aspden et. al., which is well beyond the previously predicted limit. Thus, the present work shows that flamelet-like reaction layers exist for Ka_T up to 503. However, at larger Karlovitz numbers, broken and distributed layers have been obtained. Therefore, the results to date suggest that a new boundary should be used: $Ka_T = Ka_{T,crit}$, where $Ka_{T,crit}$ might be somewhat larger than 503. Chapter 6 will utilize the results of the simultaneous PIV and formaldehyde to address this question, and make a more quantitative prediction for the critical value of Ka_T.

Another important point that must be considered when comparing results is that differing geometries may not necessarily have the same values of $Ka_{T,crit}$ or $Re_{T,crit}$ to produce broken or thickened reaction zones. For example, Zhou et al performed measurements in a jet burner, where the turbulence is generated almost entirely from the shear layer developing between the very high velocity jet and the ambient air. In this case, the turbulence takes the form of a strong mixing layer that interacts with the flame downstream of the reaction zone. This is quite different from the canonical description of Peters, as well as the Bunsen-type flames such as the Hi-Pilot, where the turbulence is generated within the reactants and propagates into the reaction layer. There is no reason to expect that a Bunsen flame and a shear layer dominated jet flame will transition to broken or distributed zones a the same value of Re_T or Ka_T.

One objection that could be raised is that the turbulence at the jet exit is decaying downstream, and therefore the turbulence conditions at the flame front may in fact be in the

predicted BP-TR regime, and thus agree with the measurements. Therefore, it is an open question what value of turbulence should be used when considering a regime diagram. The measurement most consistent with Peters' theory would be to measure the local turbulence level at the reaction front, averaged over the entire flame surface. The regime diagram was conceived assuming turbulent eddies interacting normally with the flame, which would require the true turbulence statistics at the flame front. This would account for turbulent decay, as well as attenuation through the preheat zone which has been discussed previously. However, this has little use for practical applications. Instead, boundary conditions such as bulk flow velocity, inlet centerline velocity and turbulence intensity, and turbulence length scales should be used. Regime boundaries should be modified to account for any real-world effects (such as decay and attenuation), but use of a local (instead of global) variable defeats the purpose of a regime diagram, which is to predict combustion characteristics given a reduced set of boundary variables and initial conditions. Furthermore, the results of Section 3.2.2 showed that the turbulence levels in the Hi-Pilot are essentially constant over most of the flow field. Therefore even if this were accounted for, it would be unlikely to produce a significant change in the estimated location on the regime diagram.

The results of this work have significant implications for the modeling community, as it suggests that laminar flamelet concepts may be used in simulation tools such as LES models. For example, LES grids are typically much coarser than the reaction zone thickness, and are unable to resolve the details of the flame structure. A flamelet-like sub-model will assume a distribution for the flame surface density, burning velocity, and brush thickness for the unresolved reaction layers. The present results suggest that flamelet models can be used for extremely large turbulence intensities, over a much wider range than previously expected. However, it is emphasized that a "standard" flamelet model is not appropriate, because they do not account for the broadening of the preheat layers. Therefore, flamelet models can be used in extreme turbulence, however they must be capable of reproducing the physical results observed here, where the thin reaction zones are preceded by fully

broadened preheat layers.

CHAPTER 5

Turbulent Burning Velocity Measurements in Extreme Turbulence

This chapter will report on the turbulent burning velocity measurements performed in the Hi-Pilot burner. Turbulent burning velocities S_T have been reported for a wide range of burner geometries, however the integral scales and turbulence intensities have been restricted to $u'/S_L < 25$ and $L < 6$ mm (see Section 1.5.3 for an overview of the burning velocity literature). Four measurements of S_T will be reported in this chapter: the global consumption speeds $S_{T,GC,1}$ and $S_{T,GC,2}$, the integral of flame surface density $\int \Sigma d\eta$, and the flame surface area ratio A_T/A_L. The definitions of these terms were provided in sections 1.5 and 2.4.2.

For low-to-moderate intensity turbulence (generally assumed to be for $Ka_T < 1$), combustion will occur in thin sheets, and the reaction layers will retain their laminar properties for δ_{RZ} and S_L. As the turbulence increases, the total area of exothermic layers will increase due to the wrinkling mechanism. This will lead to an increase in the global consumption speed $S_{T,GC}/S_L$ that is proportional to A_T/A_L. Eventually, it is expected that the local consumption rate per unit area will also begin to increase, due to enhanced turbulent diffusivity of the preheat reactants. In this case, $S_{T,GC}/S_L$ will exceed A_T/A_L. The relevant questions this chapter will address are as:

1. Over what conditions is $S_{T,GC}/S_L$ proportional to A_T/A_L; that is, under what conditions do laminar flamelets persist?

2. Does the flame surface area A_T/A_L continue to increase, or does it saturate at some point? This saturation could be due to flamelet merging, residence time effects, etc.

3. When does the turbulent diffusivity begin to contribute to $S_{T,GC}$; that is, when do the curves for $S_{T,GC}/S_L$ and A_T/A_L begin to diverge? A parallel question is: does the global consumption speed $S_{T,GC}/S_L$ exhibit bending, as has been observed by others at large turbulence levels?

The Hi-Pilot burner affords measurement of Bunsen burning velocities at unprecedented turbulence levels. OH PLIF was used to identify the instantaneous flame surface and the mean progress variable of OH, $\overline{c}_{OH}$. The experimental setup and methodology was described in Section 2.4.2. The run conditions for the burning velocity measurements will be discussed in the next section. The global consumption speed measurements $S_{T,GC,1}/S_L$ and $S_{T,GC,2}/S_L$ will be presented first, and they will be compared with several alternative measures of the flamelet wrinkling factor A_T/A_L. After discussion, an attempt will be made to develop a correlation for the measured burning velocities and compare it with previous results in the literature.

5.1 Run conditions for burning velocity measurements

Burning velocity measurements were performed for all 18 nominal Hi-Pilot run conditions. These consisted of six different mass flow rates and three different slotted turbulence-generating plates, and impinging jets were used above Case 3. Recall that for the Case title, the number refers to the flow rate and the letter corresponds to the turbulence generator plate. The largest slotted plate is labeled 'a', and the smallest is denoted 'c'. Equivalence ratio for the measurements was chosen to be $\phi = 0.75$. The reason for this number is

Table 5.1: Run conditions and parameters for the turbulent burning velocity measurements

Case	U_0 (m/s)	u' (m/s)	L_x(mm)	Re_T	Da_T	Ka_T	u'/S_L	$L_x/\delta_{PHZ,L}$
1a	7.7	1.7	10	1,050	20	4.6	7.21	27
2a	14	2.9	7.5	1,440	9.0	12	12.6	21
3a	32	6.0	20	7,900	12	22	25.9	56
4a	44	10	25	16,500	8.8	42	43.4	70
5a	64	24	37	58,200	5.4	128	104	103
6a	78	37	41	99,000	3.9	232	160	114
1b	6.0	1.6	7.3	761	16	4.9	6.86	20
2b	9.2	3.1	7.8	1,580	8.8	13	13.4	22
3b	21	7.1	9.2	4,240	4.6	41	30.5	25
4b	28	9.3	8.4	5,050	3.2	64	39.8	23
5b	45	20	10	13,300	1.9	176	84.2	29
6b	72	29	12	22,300	1.4	304	126	32
1c	8.5	1.2	6.1	475	18	3.5	5.16	17
2c	16	2.3	7.6	1,140	12	8.2	9.83	21
3c	32	5.7	9.3	3,420	5.8	29	24.4	26
4c	44	9.0	10	5,980	4.0	55	38.6	28
5c	64	25	19	31,700	2.6	192	109	53
6c	89	38	17	40,900	1.5	377	163	46

that it maximized the values of u'/S_L while still maintaining a closed flame tip, which is essential to accurately determine $S_{T,GC}$. Run conditions are listed in Table 5.1. For these measurements, extreme levels of turbulence are generated, with u'/S_L reaching 163 and $L_x/\delta_{PHZ,L}$ exceeding 100. To normalize the data, values of laminar flame speed (S_L) and preheat thickness ($\delta_{PHZ,L}$) were determined from CHEMKIN to be 23.2 cm/s and 0.36 mm, respectively.

5.2 Global consumption speed

Measurements of the global consumption speed $S_{T,GC,1}/S_L$ using the $\overline{c}_{OH} = 0.5$ contour are plotted in Figure 5.1. The measurement points are shown as open squares, triangles, and diamonds, corresponding to turbulence generating plates a, b, and c in Table 5.1. Two measurement points are shown for the three largest run conditions where a second set of data was collected, and good repeatability is shown. Because $S_{T,GC,1}$ uses the average

flame position in its definition, it is the most conventional form of the global consumption speed, and is therefore a useful comparison between different experiment results. Included in the plot are data points from Yuen et al. [140], which had reported burning velocities at the largest turbulence intensities in the Bunsen geometry at the time. Their data points are shown as inverted blue triangles, and it is clear that they agree well with the current measurements for $10 < u'/S_L < 25$.

The current work measures the burning velocities at turbulence intensities u'/S_L that are more than six times larger than previous studies. It has been suggested that at large turbulence levels the burning velocity curve will flatten out and no longer increase with turbulence intensity. The proposed mechanisms include flamelet merging, residence time effects, and the onset of local quenching and extinction. The current work shows that for the Bunsen flame this is not the case. The global consumption speed is always increasing in Figure 5.1, and exceeds 25 times the laminar value at the largest turbulence levels. The burning velocity appears nearly linear in the range $0 < u'/S_L < 40$, however significant bending occurs as the turbulence intensity u'/S_L exceeds 40. The bending of the burning velocity curve will be discussed further later in this section.

The global consumption speed measured at the leading edge, $S_{T,GC,2}/S_L$, uses the $\overline{c}_{OH} = 0.2$ contour and is plotted in Fig. 5.2. It is seen that the global consumption speeds are much larger using the leading edge, and the largest measurements are approximately 70 times the laminar value. This is because the selected iso-contour of the mean progress variable of OH is closer to the jet exit, producing a smaller flame surface area which increases $S_{T,GC}$. It should be clear that the selection of an iso-contour of $\overline{c}_{OH}$ is entirely arbitrary, and therefore no definition of the global consumption speed is more correct than another. The selection of these two particular definitions was primarily motivated by the physical significance of using the average flame position and the leading edge of the flame, as well as the ability to compare with other studies that used similar definitions.

Comparing the two global consumption speeds, it is seen that $S_{T,GC,2}$ in Fig. 5.2 in-

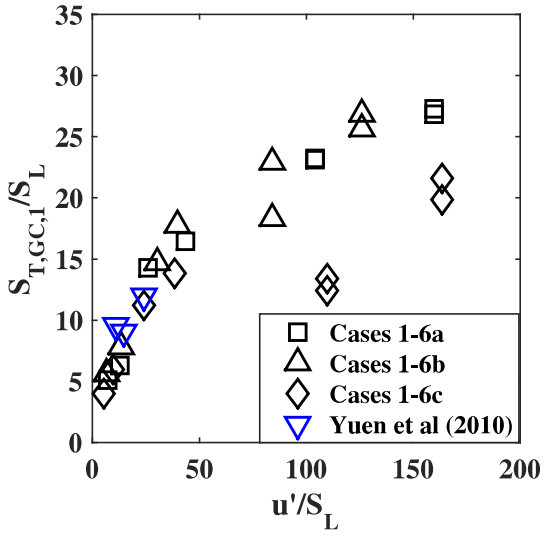

Figure 5.1: Global consumption speed $S_{T,GC,1}$ for the $\tilde{c}_{OH} = 0.5$ contour. Extreme levels of turbulence (u'/S_L between 25 and 160). Gülder's data for $u'/S_L < 25$ also shown.

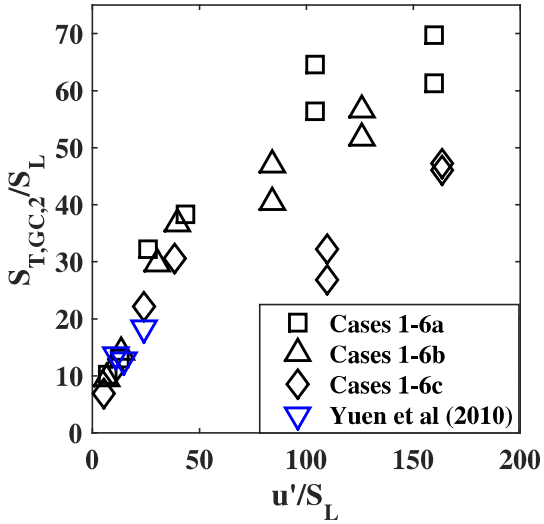

Figure 5.2: Global consumption speed $S_{T,GC,2}$ for $\tilde{c}_{OH} = 0.2$ contour.

creases with increasing integral scales, while values of $S_{T,GC,1}$ do not (recall from Table 5.1 that the square symbols represent the largest integral scales, and the diamond symbols represent the smallest integral scales). The differences due to integral scale are primarily observed at large turbulence intensity, while in the range of $u'/S_L < 20$ all measurements appear to collapse to a single curve.

The cases with the smallest slotted turbulence-generating plate (condition 'c', indicated by diamonds) produced the smallest global consumption speeds. This is believed to be due to the different velocity profile this slot produces; Table 4.1 shows that the centerline velocity U_0 for Case 6c is 14% larger than 6a. This is seen to produce a much taller flame, and thus lowers the global consumption speed. Additionally, the PIV measurements of section 3.2.3 showed that the hydraulic diameter of the integral scales for slot c was smaller than that of the other two turbulence generating plates. Fig. 5.3 plots the hydraulic diameter versus u', and it is seen that L_{HD} for the two larger slots collapse to a single curve, while the curve for the smaller slots is much lower. As will be shown later in this chapter, turbulent diffusivity is likely playing a significant role in the range of extreme turbulence $u'/S_L > 25$. Because the turbulent diffusivity is proportional to the square root of integral scale, it follows that the smaller integral scales produced by slot c will be unable to increase the burning velocity as substantially as the other slotted plates.

Figures 5.1 and 5.2 showed that the consumption speed evaluated at leading edge increased with integral length scale, but when conditioned on the average flame position there was no effect. To explain this result, a first hypothesis is that larger eddies might be better able to displace the instantaneous flame surface from its mean location, and therefore produce a broader turbulent flame brush. This would lead to a smaller area of the leading edge and cause the global consumption speed to be larger for larger integral scales. However, it was found that the normalized centerline brush thickness (δ_B/D, where δ_B is the distance between the 0.5 and 0.2 contours of $\overline{c}_{OH}$ on centerline) collapsed to a linear function (see Figure 5.4) of the normalized characteristic flame height (H/D). This indicates that the

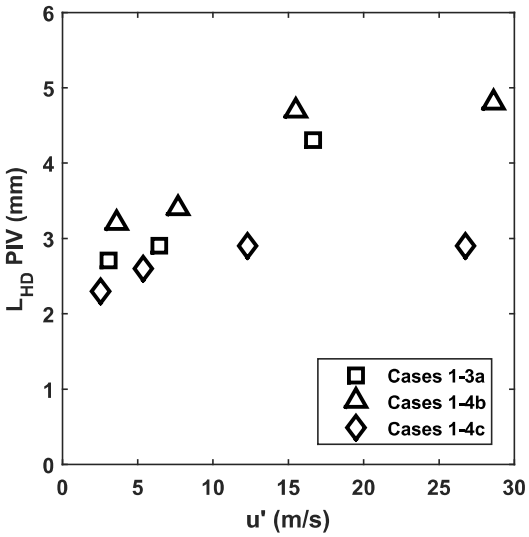

Figure 5.3: Variation of the hydraulic diameter L_{HD} of the integral scales with axial fluctuations u'. The largest two slots (Cases 1-3a and Cases 1-4b) produce integral scales that are approximately the same size. However, the smallest slots (Cases 1-4c) produce much smaller integral scales.

centerline brush thickness is not strongly dependent on integral scale.

This result surprising at first, because it conflicts with the geometric observation that the brush thickness must be increasing with L_x if the area of the average flame is independent of $L_x$but the leading edge surface area decreases with L_x. The resolution of this question arises from the observation that larger integral scales were observed to cause very large but relatively infrequent side-to-side displacements of the flame. This lateral displacement causes products to be located upstream of where the flame brush is normally positioned, thus reducing the effective flame area and increasing the measured burning velocity. Fig. 5.5 gives an example of this effect. An instantaneous flame image and the flame brush between the 0.2 and 0.5 contours of $\bar{c}_{OH}$ are shown for both a small and large integral scale. It is clear that for the smaller integral scale, the flame is highly wrinkled and contorted, but is generally present in the same location as the mean flame brush. However, at larger integral scales the flame brush is able to be moved much further from the mean brush location. Lateral motions are not found to alter the $\bar{c}_{OH} = 0.5$ contour as much as the $\bar{c}_{OH} =$

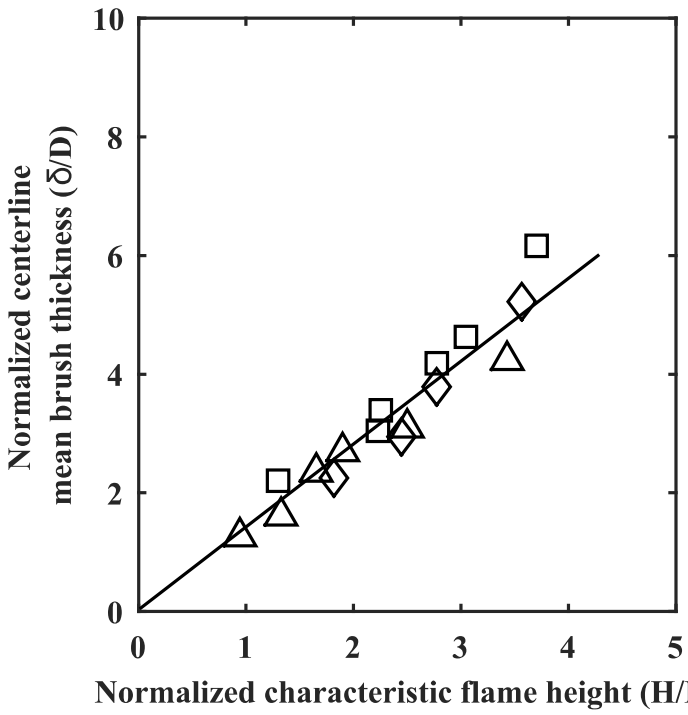

Figure 5.4: Normalized centerline flame brush thickness versus normalized flame height (H/D), where D is the burner exit diameter. Symbols are the same as for Fig. 5.1.

0.2 contour, which explains the differences between Figs. 5.1 and 5.2. The $\bar{c}_{OH} = 0.05$ contour also was analyzed (but not shown) and it was found that the trend continues as expected; an even greater integral scale effect was observed. However, these displacements predominately effect the edges (large distance from centerline) of the flame surface, while the brush thickness on centerline does not vary integral scale. This effect is seen clearly by the shape of the leading edge of frame (c) and (d) in Fig. 5.5, where the curvature for large radial distances is reversed for the small and large integral scale conditions due to these side-to-side motions. This example reinforces the necessity of planar measurements of the flame surface, as a measurement of the flame height alone would mask some of these details.

The bending of the curves in Figure 5.1 is found to occur when the preheat zone thickness becomes very large (typically greater than 20 mm, see Figure 5.6) [124]. The gray region in Fig. 5.6 is the preheat zone, which is identified by the presence of formaldehyde PLIF signal but no OH signal. CHEMKIN computations show that formaldehyde diffuses throughout the preheat zone in a laminar flame. The preheat zone in Fig. 5.6 begins where formaldehyde is 35% of its maximum value (corresponding to approximately 500 K) and ends where the reaction zone (marked by OH signal) begins. Based on this observation, it may be hypothesized that one factor that affects the bending is the ratio of the integral scale to the preheat thickness. If the preheat thickness is 20 mm and the largest eddies are 6 mm, it may be that the smallest eddies will not survive passage through the hot viscous preheat gases, and therefore cannot act on the flame surface. Furthermore, the response of the largest eddies in the flow is not known. Thus if the eddies do not survive, that may be a reason why increasing the turbulence level does not linearly increase the burning velocity and bending is observed. Moreover, cases with a larger integral scale see less 'bending' in Fig. 5.1b, while smaller integral scales begin to exhibit a plateau in flame speed more rapidly, suggesting larger integral scales are more resistant to preheat-turbulence attenuation. Our observed result was predicted by Lipatnikov, who estimated that only eddies larger than the

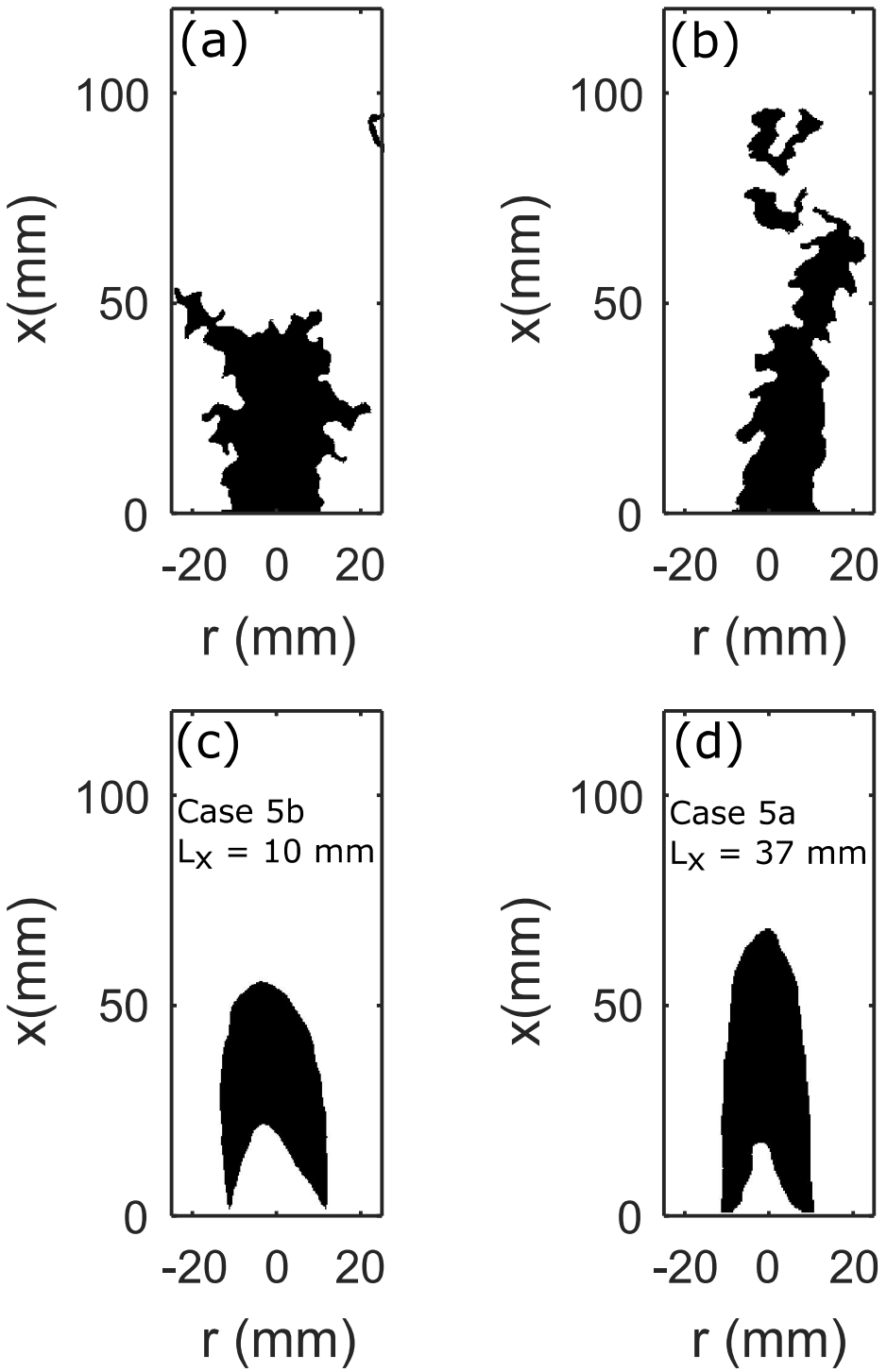

Figure 5.5: (a),(b): Instantaneous flame images for a small and large integral scale. Note that the flame with the large integral scale is displaced further from the average location. (c),(d): Mean flame brush, the distance between the 0.2 and 0.5 contours of $\overline{c}_{OH}$, for the small and large integral scale case. Note that the shape of the leading edge is very different for the two cases.

preheat zone thickness can survive the dissipative effects of the preheat region and modify the reaction layer and local burning rate [72].

This concept of eddy decay in the preheat zone can be stated in another way. Where the curves in Fig. 5.1 are linear, the preheat zone is thin so the turbulence level approaching the flame is nearly the same as the turbulence that traverses the thin preheat layer and reaches the reaction layer. Where the curves in Figure 5.1 are bending, the turbulence level (u') that survives and reaches the reaction layer is less than the upstream value of u' that is plotted on the horizontal axis. The effective turbulence acting on the reaction layer has been reduced by the preheat layer. This would shift the data points for large u' to the left in Figure 5.1, resulting in less bending. The work suggests that a new type of turbulence might be considered, called the effective turbulence, that differs from the upstream turbulence which is measured ahead of the preheat region. This observation, coupled with the observations discussed in Chapter 4, is the motivation for the simultaneous PIV and formaldehyde-PLIF measurements, to be described in Chapter 6. To foreshadow the results of that chapter, it does not appear that the turbulence level u' changes significantly during its passage through the preheat layer; however, the integral scale does appear to grow, implying that the smallest eddies are attenuated through either thermal expansion or viscous attenuation.

5.2.1 Effect of co-flow on the measured burning velocities

At this point, a critical observer may question how well the turbulence conditions that are actually impinging on the flame are described by the measurements of the cold flow issuing from the central jet. There is a shear layer between the co-flow and the central jet, and this will generate turbulence to some degree. This may mean that the value of u'/S_L indicated in Figs. 5.1 and 5.2 is significantly different from the true turbulence levels acting on the flame.

To evaluate the effect of the shear layer with the co-flow and its interaction with the central jet, Cases 1-3b were measured with a co-flow velocity twice that of the standard

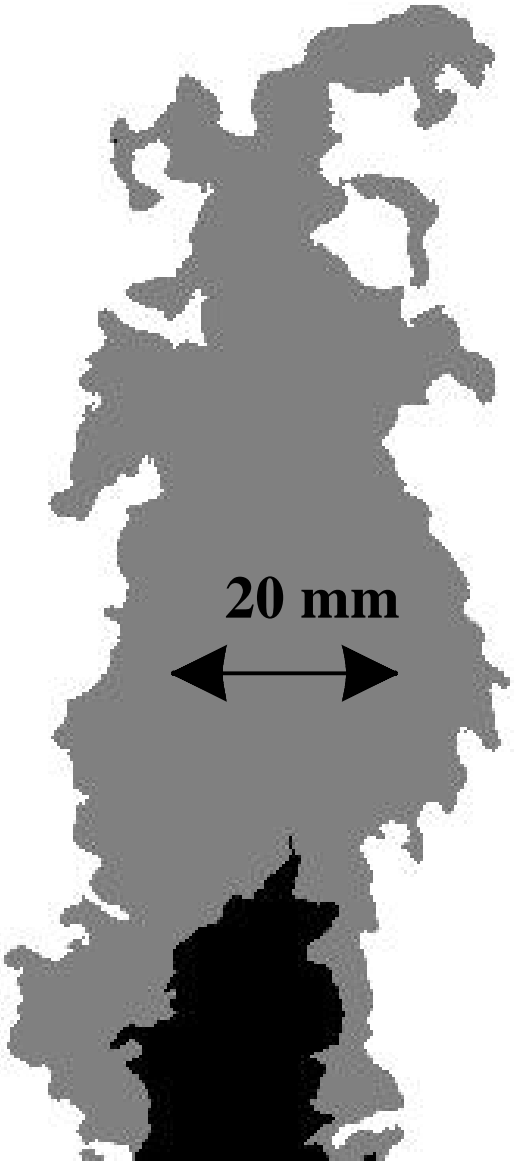

Figure 5.6: Illustration of broadening of the preheat zone for a representative flame (case 4a). Black indicates unburnt reactants, gray is preheated reactants (formaldehyde signal), and white is products.

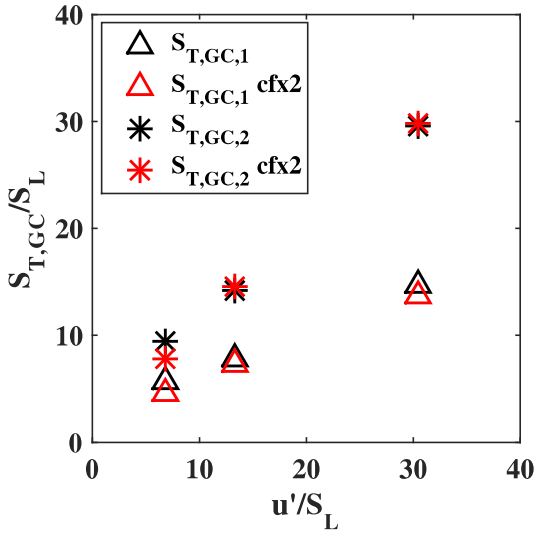

Figure 5.7: Effect of co-flow on the measured global consumption speeds.

conditions (accounting for thermal expansion, the mass-average velocity was increased from 9 m/s to 19 m/s). The results are given in Fig. 5.7, with red symbols corresponding to the doubled co-flow condition. The results show little change from the nominal condition, with Case 1 burning velocities reduced 10-15% and Cases 2-3 changing by less than 5%. The burning velocities decrease because the larger co-flow velocity is closer to the very large jet velocity, and therefore any shear-generated turbulence arising from the co-flow is reduced. This result indicates that the burning velocity $S_{T,GC}$ is not highly sensitive to the co-flow conditions, and suggests that the flame is positioned inside the shear layer. The contribution of the shear layer to the turbulence levels seen by the flame will be revisited in Chapter 6.

5.3 Contribution due to flamelet wrinkling

The contribution due to flamelet wrinkling ($S_{T,F}$) is defined as the integral of flame surface density $\int \Sigma d\eta$, and is a measure of the increase in flame surface area from the laminar value. The stretch factor I_0, which accounts for deviations in the laminar burning rate due

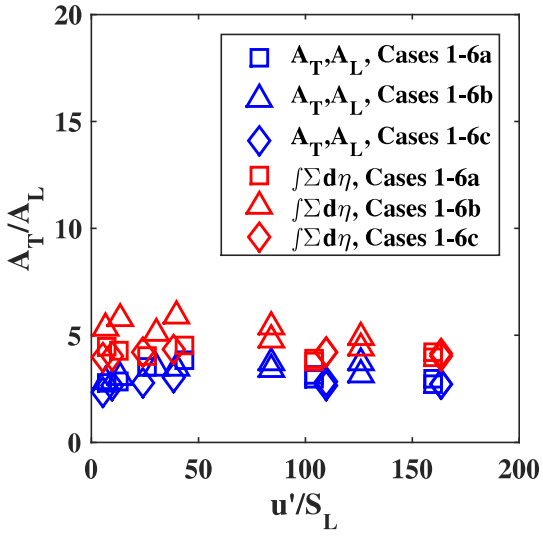

Figure 5.8: Two measures of the extent of flamelet wrinkling. Red data points correspond to $S_{T,F} = S_L I_0 \int \Sigma d\eta$. Blue data points correspond to the direct computation of A_T/A_L. Symbol notation is identical to Figure 5.1.

to kinematic stretch, is assumed to be unity. The increase in flame surface area can also be evaluated by directly computing the quantity A_T/A_L, by taking the ensemble average of measured reaction layer surface area and dividing by the area $\overline{c}_{OH} = 0.5$ contour. Further details regarding the methodology are described in Section 2.4.2. These two measurements are plotted in Fig. 5.8; the red symbols correspond to the $S_{T,F}/S_L = \int \Sigma d\eta$, and the blue symbols are the direct computation of A_T/A_L.

Fig. 5.8 shows that the flame surface area rapidly increases with u'/S_L, until it reaches approximately 3.5-5 times the laminar value. However, as the turbulence intensity is made larger, no further increase in the flame surface area is observed. The two measurements of flamelet wrinkling agree well, however the integral of flame surface density does produce slightly larger magnitudes at most values of u'/S_L. This may be because some amount of the flame surface density Σ on the reactant-side of the flame cone is double-counted , as the integration path of two separate measurement points may intersect. Alternatively, the value for A_L used to compute A_T/A_L in Fig. 5.8 was assumed to be the $\overline{c}_{OH} = 0.5$ contour, and this may underestimate A_T/A_L.

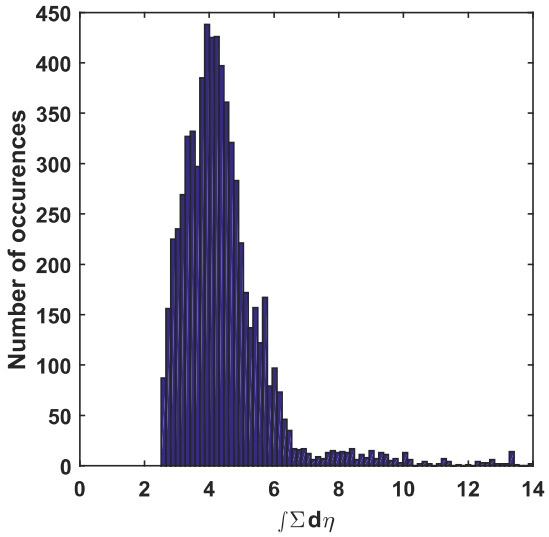

Figure 5.9: Distribution of the integral of flame surface density $\int \Sigma d\eta$. The distribution was similar for most cases, so the data was collected to a single set to show the number of occurrences per bin as $\int \Sigma d\eta$ is increased. The average is slightly greater than 4, and the frequency of occurrence for $\int \Sigma d\eta > 6$ is very small.

The value for $\int \Sigma d\eta$ was generally larger at the flame tip, where tangential strain is reduced and more wrinkling is possible. The histogram for the measurement $\int \Sigma d\eta$ is given in Fig. 5.9; the profile was approximately the same for all run conditions, so the entire data set was compiled to increase the population field in Fig. 5.9. The function has a tall and narrow peak, with a mean around 4-5. However, a long tail in the profile is visible, with some measurements producing values of $8 < \int \Sigma d\eta < 14$. These large values occurred exclusively in the tip region, where wrinkling was more extensive. This reinforces the notion that Bunsen flames are highly geometry dependent, as the burning rate (evidenced by $\int \Sigma d\eta$) will increase as the measurement domain moves from regions of high strain near the base to the freer propagation occurring near the tip [106].

An important result is that the flamelet wrinkling parameters do not continue to increase indefinitely in the extreme range of turbulence. Returning to the results of Section 5.2, it is clear that the measurements of $S_{T,GC}/S_L$ do not follow the same trend. The two measures of flamelet wrinkling are reproduced in Fig. 5.10, along with the global consumption

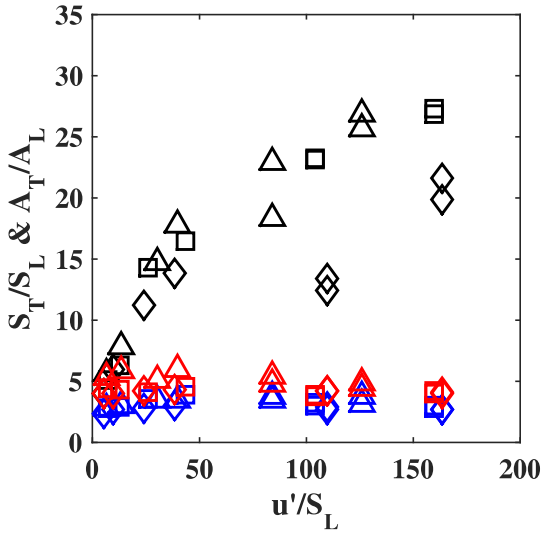

Figure 5.10: Mean flamelet velocity ($S_{T,F}$, lower curve), compared to global consumption speed ($S_{T,GC,1}$, upper curve). Symbol notation is same as Fig 5.1.

speed $S_{T,GC,1}/S_L$. It is seen that the flamelet wrinkling factor is much smaller than the consumption speed $S_{T,GC,1}$, and the lower curves are flat, indicating that it is independent of u'/S_L. This trend was previously seen by Gülder et al. [57] and Yuen et al. [140] for lower turbulence levels. This implies that the increases in the global consumption speed are not due to increases in flame surface area. Recall that there are two contributions to the burning rate: (1) the surface area of the exothermic layers, and (2) the local consumption rate per unit area of the layers. Therefore, because the flame surface area has plateaued yet reactants continue to be consumed more rapidly, the local consumption rate per unit area must be increasing.

The observed plateau of A_T/A_L can be explained by the transition from thin to broadened (or distributed) flamelets. Broadened here refers to the width of the flame brush, not the instantaneous reaction zone thickness which remains approximately constant (see Chapter 4). Despite the flame continuing to consume reactants at a greater rate, the total wrinkled flame area remains unchanged. That is, the peak flame surface density decreases, but the width of the flame brush increases. Expressed another way, the flame occupies a larger region of space, but the probability of a flame existing at any given location de-

creases; this leads to an integrated flame-surface density that is constant. The contribution due to flamelet wrinkling ($S_{T,F}$) is only useful as a burning velocity in the thin flamelet regime when it nearly equals the consumption speed.

In previous work, the formula $S_{T,F}/S_L = I_0 \int_{-\infty}^{\infty} \Sigma d\eta$ has been used to express the consumption speed, with the implicit assumption that $S_{T,GC}/S_L = A_T/A_L$ [125]. When the measured consumption did not match the flame surface area $A_T/A_L = \int \Sigma d\eta$, the stretch factor was assumed to be the difference, $I_0 = (S_{T,F}/S_L) / \int \Sigma d\eta$. In the cases of laminar flamelets this approach is valid, as the stretch factor is intended to incorporate changes in the local propagation speed due to mechanical stretch; i.e. the stretched laminar flame speed $I_0 = S_L/S_{L,0}$. Laminar flames measuring stretched burning velocities have shown that I_0 can be as large as 2, i.e. stretch can change the local propagation rate by a factor of 2 [21, 54]. However, in cases where the turbulent diffusivity ($D_T \sim (u'L)^{1/2}$) is increasing the local consumption rate, the burning velocity will exceed the stretched laminar flame speed, and this concept becomes less useful. As shown in Fig. 5.10, the global consumption speed greatly exceeds the flamelet wrinkling parameters in the present work, and therefore it is argued that $S_{T,F}$ is not useful for extreme turbulence.

At this point, it is useful to make a comparison with a recent experimental result from Osborne et al [88], who performed simultaneous PIV and OH and formaldehyde PLIF measurements in a version of the Hi-Pilot burner. They performed Lagrangian tracking of individual particles through the preheat zone (indicated by formaldehyde PLIF), and used the OH-PLIF boundary to mark the reaction layer. The transit time τ_c of these particles was measured, and by taking the ratio $\tau_c/\delta_{PHZ,T}$ from their measurements, they obtain a direct measurement of a velocity scale. They argue that this is essentially a measure of the local consumption rate, since it includes the time scale of the gas to pass through the measured thickness of the flame. Therefore, this is be denoted as S_i, and is a measure of the local consumption speed. Their result is shown in Fig. 5.11.

Fig. 5.11 shows the joint-PDF of S_i/S_L versus the measured normalized preheat zone

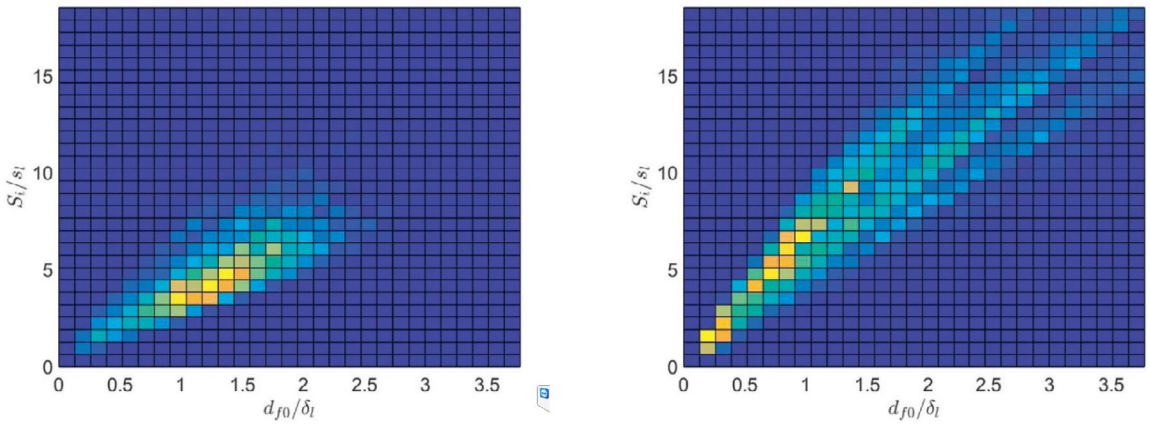

Figure 5.11: Experimental result of Osborne et al. Taken from [88]. Joint probability distribution for S_i/S_L versus d_{f0}/δ_L.

thickness d_{f0}/δ_L. Their Case 1 and Case 2 have $u'/S_L = 5$ and 20, respectively. The parameter S_i increases with the preheat layer thickness (the slope of the JPDF is positive), which indicates that the consumption rate increases with the local flame thickness. Furthermore the most probable value of S_i/S_L increased between Case 1 and 2, indicated by the increasing slop of the JPDF, which indicates that the average consumption rate is increasing with u'/S_L. This result supports the measured values of $S_{T,GC,1}/S_L$and A_T/A_L in Fig. 5.10, as it indicates that the consumption speed is increasing in regions of thick preheat zones and that the flames are not laminar flamelets. This provides an additional check on the measured burning velocities, because it was performed in the same burner and supports many of the conclusions mentioned previously.

5.3.1 Alternative measure of flamelet wrinkling from the CH-PLIF

Thus far, we have shown that the local consumption rates appear to be enhanced in extreme turbulence, presumably due to the increased turbulent diffusivity present in broadened preheat layers of the Hi-Pilot flames (section 4.3). The reasoning for this conclusion is that the measured global consumption speeds greatly exceed the increase in the measured flame surface area. However, a reader may question the resolution capabilities of the large FOV

PLIF images, from which the results of Fig. 5.8 were obtained.

In order to address this, the CH PLIF and Overlap PLIF measurements of Chapter 4 (described in Sections 2.4.1.2 and 2.4.3) were used to compute an alternative measure of the flame surface wrinkling. Both CH and Overlap PLIF were performed at high resolution capable of accurately resolving the reaction layer thickness. Therefore, these measurements provide an ideal check of the results of Section 5.3.

The flame surface densities were computed using a 0.91 mm and 1 mm box in the Overlap and CH-PLIF images, respectively. The integral of flame surface density was computed, but the integral was performed slightly differently. The integral of flame surface density is called Ω in these measurements, and is defined as

$$\Omega = \frac{1}{2}\int_{-\infty}^{\infty} \Sigma(x,r)dr \tag{5.1}$$

The reason for the change in definition is that the smaller field of views used in these measurements did not permit the use of the mean flame brush as used in the definition of $S_{T,F}$. Additionally, because these measurements were taken near the middle of the flame, the average flame brush was approximately vertical, so the results would not be expected to change significantly. This method is identical to the measurement of Ω_{CH} performed by Filatyev et al in a weakly turbulent slot burner. The parameters Ω_{OL} and Ω_{CH} were computed and are plotted in Fig. 5.12.

The results appear consistent with the conclusions of Section 5.3. The wrinkling increases approximately linearly in weak turbulence for $u'/S_L < 25$, but the results plateau and no increases in flame surface area are observed for at $u'/S_L = 62$. There appears to be a slight decrease in both Ω_{CH} and Ω_{OL} at the largest turbulence levels, which was also seen in Fig. 5.8 for $S_{T,F}$. These results suggest that lack of resolution of the smallest scales in the large field of view (used in the OH-PLIF) does not inhibit an accurate measure of the total flame surface wrinkling. This is because most of the area of the wrinkled surfaces is embedded in large scale wrinkles, with smaller scales contributing subsequently smaller

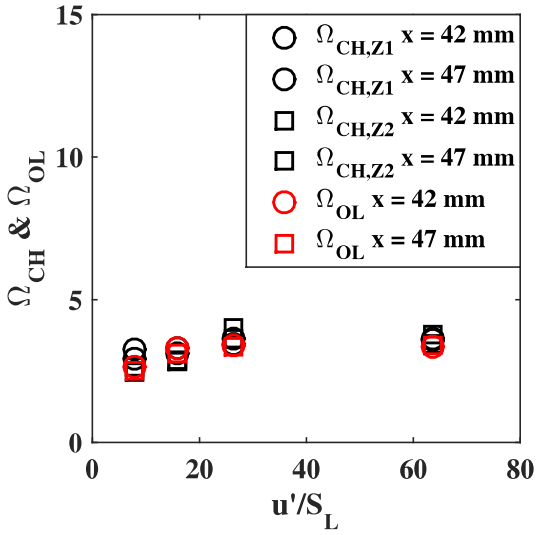

Figure 5.12: Wrinkling parameters Ω_{CH} and Ω_{OL} for the CH-PLIF and Overlap, respectively. Symbols correspond to cases 2a, 3a, 4a, and 5a described in Table 4.1 in Chapter 4.

amounts. This will be addressed in further detail in Section 5.4.1.

5.3.2 An aside on the maximum extent of flamelet wrinkling

Based on the current data here and in recent work by Steinberg and Gulder, it appears that there is a maximum extent of flame surface wrinkling. No work has been reported where the turbulent flame surface area exceeds three to five times the laminar value. This limiting value has been observed in DNS studies of [7,97,106], the turbulent swirl flames of Allison et al [3], and the Bunsen flames reported here and in [56, 88, 116, 140]. This suggests that after the point $A_T/A_L \sim 5$, flame surface destruction balances out continual increases in area, possibly due to flamelet merging. After the surface area of the exothermic layers has been maximized, the results here show that the burning velocity continues to increase, which must be due to enhanced burning rates per unit area (i.e., turbulent diffusivity). However, some DNS work has shown that even at very large turbulence intensities ($u'/S_L >$ 30), the flame surface area continues to determine the burning velocity, that is $S_{T,GC}/S_L = A_T/A_L$.

It is a hypothesis of this work that larger scales of turbulence are more effective at wrinkling the flame surface. Examining the DNS data, it appears that even though the burning velocity depends only on A_T/A_L even at very large turbulence levels, the magnitude of A_T/A_L remains small, less than 5 [97, 106]. Therefore, the small integral scales of DNS studies are not capable of wrinkling the flame sufficiently to saturate the flame surface area. As the integral scale is increased, more and more wrinkling will become possible, until eventually the saturation point will be reached. At this point, A_T/A_L can no longer increase, and any further enhancement of the burning rate must come from enhanced turbulent diffusivity.

5.4 Uncertainty in the measured burning velocities

The uncertainty in the measurement of $S_{T,GC}$ will derive from two factors. Recall that the global consumption speed is defined as $S_{T,GC} = m/(\rho A)$, and therefore any error in the determination of the mass flow rate of reactants or the average flame surface area will contribute to error in $S_{T,GC}$. The uncertainty in the mass flow rate is equal to the uncertainty in the choked orifice, which is:

$$\frac{\Delta \dot{m}}{\dot{m}} = \sqrt{\left(\frac{\Delta P_0}{P_0}\right)^2 + \left(\frac{\Delta A^*}{A^*}\right)^2 + \frac{1}{4}\left(\frac{\Delta T_0}{T_0}\right)^2} \tag{5.2}$$

which was discussed in Chapter 2 and was shown to be approximately 3%. The uncertainty in the flame surface area A_F derives from two sources: pixelization of the flame surface area, and out of plane leaning effects. The $c_{OH} = 0.5$ contour is an infinitely thin boundary that is represented in an image as a line one pixel in width. Therefore, the possibility for errors to arise does exist, especially when the surface is angled diagonally across the image, as pixelization will render a horizontal line that appears like a staircase. Additionally, wrinkles smaller than the resolution cannot be resolved, and therefore any increase in flame surface area beyond this point cannot be captured. The effect of pixelization has

been examined by Filatyev [110] and was shown to be approximately 3%. It is not expected that unresolved wrinkles will have any significant effect for two reasons: first, they do not change the mean position of the flame, they will only distort the local surface about a mean location; and second, due to the fractal nature of flamelet wrinkling, each successive scale will contain less of the total 'energy' of the flame surface. Therefore, the smallest wrinkles will not contribute significantly to the flame surface area, as most of the wrinkling comes from scales larger than the Taylor scale (see Section 5.4.1).

The last source of error is the most difficult to deal with, and cannot be adequately treated from the planar scalar measurements. If the flame is leaning significantly out of the plane of the laser sheet this can lead to a significant overestimate of $S_{T,GC}$, since you would essentially be measuring a contour of $\overline{c}_{OH}$ that has a much smaller area. However, two remarks will lend confidence to the measurement. First, the measure of $S_{T,GC}$ has shown to be repeatable, whereas the dynamics of the flow exit angle (relative to centerline) varies randomly each time the burner is re-configured (for example, changing out turbulence generator plates). This suggests that the average flame cone is not significantly off-center of the measurement plane. Additionally, only Cases 5a and 6a saw any noticeable amount of asymmetry about the centerline, therefore only these Cases have the possibility of significant out-of-plane effects. In order to ensure that these effects are accounted for, three-dimensional measurements would be required; either through multi-plane PLIF measurements or tomographic chemiluminescence.

To estimate the uncertainty arising from this effect, consider an average flame cone that is 70 mm tall and is displaced 2 mm from the centerline plane due to flow asymmetry. Note that the base diameter of the cone is given by the burner exit of 21.6 mm. For a circular cone, the surface area A is given by $A = \pi r s$, where r is half the base diameter, $s = \sqrt{r^2 + h^2}$is the slant height, and h is the height of the cone. In this case, the surface area A of the 70 mm tall cone is 2403 mm^2. If the cone is shifted by 2 mm out of plane (due to asymmetric leaning), the measured height would be 57 mm. The measured area of this cone

would then would be 1968 mm^2, which is 18% less. Therefore, a conservative estimate in the uncertainty in the measured flame surfaces is 18%. Note however that this corresponds only to a lower uncertainty limit. This is because any asymmetries in the flame surface will produce a smaller flame surface and therefore a larger consumption speed. There is also the question of the accuracy of the measured flame surface in the measurement plane, as it may be questioned whether the finest scales of wrinkles are fully resolved. This question is addressed in the following section 5.4.1.

5.4.1 Uncertainty in the flame surface wrinkling A_T/A_L

An important question is how accurate are the measures of flamelet wrinkling if the smallest scale wrinkles are not captured in the measurement. Conceivably, there may be lots of surface area generated at higher turbulence that is unresolved by the measurement, which would mean that the flame surface area may continue to increase with turbulence intensity, counter to the findings presented in 5.3. In this work four alternative measures have been provided for the extent of flame surface wrinkling: $\int \Sigma d\eta$ and A_T/A_L computed from the large field of view OH-PLIF, and Ω_{CH}, and Ω_{OL} from higher resolution measurements. All four measurements agree both qualitatively and quantitatively: the flame surface wrinkling does not change significantly over the range of conditions studied, and no flames indicate an increase in flame surface area $A_T/A_L > 5$. Thus, because the measured value does not change significantly as the resolution is varied, it would appear that the inability to resolve the very finest scales of turbulence does not affect the result.

However, it is important to quantify what fraction of the turbulent scales must be resolved in order to accurately capture the flame surface area, and how would the measurement change with full resolution. This can be addressed by considering the distribution of flame surface area caused by each scale, which has been extensively studied in the field of fractals [53]. To borrow an old statement of the problem, "how long is the coastline of Great Britain?". Of course, this will vary depending on the scale you use, as a map with

a resolution of a few meters will smooth over some of the surfaces (wrinkles). A surface can be measured using a polygon of N sides, with each side having a length of ϵ. The total length of the surface is then $N\epsilon$, and the interest in fractals arises from the fact that the quantity $N\epsilon$ tends to increase as ϵ is made smaller. Of course if the scale ϵ is larger than the scale of the smallest wrinkles, the reason for this behavior is clear, since the scale ϵ is simply filtering the surface.

A fundamental finding of fractal mathematics is as follows: the measured area of a fractal surface is proportional to the measurement scale according to ϵ^{2-D}, where D is called the fractal dimension [53]. From the work of Mandelbrot [74], if the measurement domain has a volume of L^3, then the area associated with a wrinkled surface is measured as:

$$A \sim \epsilon^{2-D} L^D \tag{5.3}$$

Again, the measured value of A depends on the measurement scale ϵ. For turbulent flames, the fractal dimension D is almost always between 2.35 and 2.6. Of course, if a scale ϵ is taken that is smaller than the reaction layer thickness, then A would not change further as ϵ is decreased. Therefore, a lower limit to ϵ is δ_{RZ}, and A is approximately constant below this point. When plotted on a log-log plot, the measured area is related to the measurement scale ϵ as given in Fig. 5.13.

Fractals have been measured experimentally by Gulder et al [56], who performed both OH PLIF and Mie scattering to measure the instantaneous Propane-air flame surfaces, and extracted fractal length scales. The resolution in their experiment was 350 μm in the OH PLIF and 150 μm in the Mie scattering, and the measured inner cutoff was found to vary with the size of the burner diameter. For a 22.4 mm Bunsen diameter, the inner cutoff was greater than 1.1 mm for all flames, and the outer cutoff was approximately 12-16 mm, depending on the measurement technique. For the smaller diameter burner, the inner cutoff was reduced but no less than 0.71 mm. Previous work by the [116] showed that the inner

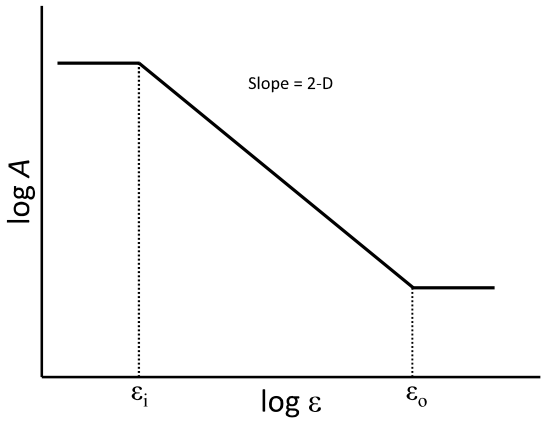

Figure 5.13: Variation of the measured flame surface area A in a box of volume L^3, using a measurement scale ϵ. The lower cutoff ϵ_i corresponds to the reaction layer thickness, and the outer cutoff ϵ_o corresponds to the integral scale.

cutoff ϵ_i for methane-air flames was approximately 1.5 mm, which is consistent with that of [56].

Assuming that the value for ϵ_i is approximately the same in the Hi-Pilot, then a conservative estimate of the resolution required to accurately measure the flame surface area is ϵ = 1 mm. For all measurement cases the resolution was much smaller than this limit; the worst resolution in the present measurements corresponds to the largest field of view in the OH measurements, which had a nominal pixel size of 0.3 mm. Therefore, the wrinkled flame surface should be adequately resolved. If the resolution were only half as accurate, and the scale ϵ is taken to be 2 mm, Fig. 5.14 shows that the error in the measured flame surface is approximately 15%.

Lastly, as an aside, it is sensible that scales smaller than approximately 1 mm should not contribute significantly to the flame surface area. The minimum measured laminar flame thickness occurred at ϕ = 1.05 and was $\delta_{F,L}$ = 0.76 mm. The scale of the reaction zone imposes a firm lower bound of $\epsilon_i \sim$ 0.4 mm, however any wrinkle less than ~ 1.5 mm is expected to be unstable. This is because a wrinkle of the size $\lambda = 2\delta_{F,L}$ will experience

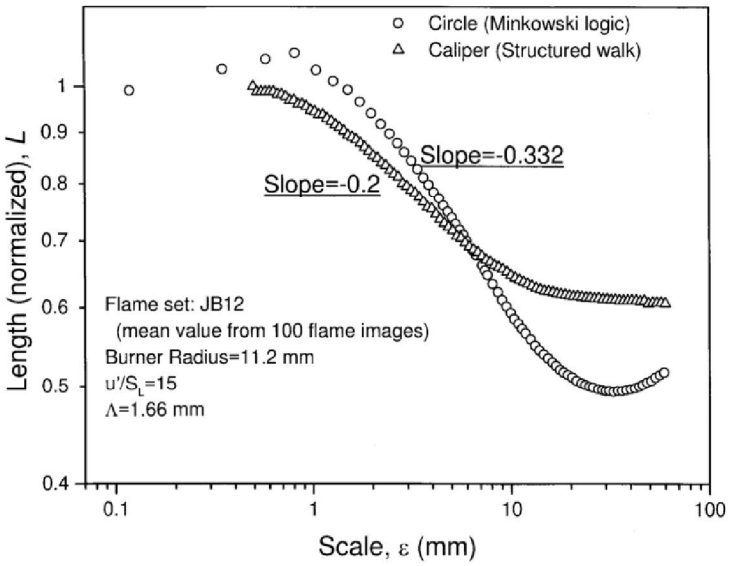

Figure 5.14: Experimental result from Gulder et al [56]

merging of the preheat layers and accelerated combustion. Likewise, any wrinkle smaller than $\lambda = 2\delta_{RZ,L} = 0.8$ mm will produce merged reaction layers, and the wrinkle will disappear.

5.5 Measured turbulent burning velocity correlations

As discussed previously, there are thought to be two general contributions to the turbulent burning velocity: (1) flamelet wrinkling which increases the surface area of the exothermic layers, and (2) increases in the local consumption rate per unit area of the layers, due to enhanced turbulent diffusivity. The conventional idea is that flamelet wrinkling and the resulting increase in flame surface area is the primary contribution to burning velocities at lower turbulence intensities. Kuo examines a geometric relation for burning velocity originally derived by Shchelkin [67], who assumed the wrinkling process can be viewed as flame surfaces becoming distorted into cones. The result is of the form:

$$\frac{S_T}{S_L} = \sqrt{1 + A\left(\frac{u'}{S_L}\right)^2} \tag{5.4}$$

In Eqn. (5.4) A is an experimentally determined constant. Bending (nonlinear behavior) has usually been observed in experiments [21, 41, 48, 140], and is not accounted for in this analysis. Possible causes for this effect are flame surface destruction by merging or local extinction, residence time effects (associated with increasing the overall turbulence level u' by increasing the bulk velocity U_0), or turbulence attenuation through a broadened preheat zone. The geometric analysis of Shchelkin predicts a linear relationship between burning velocity and turbulence intensity at large values of u'/S_L.

Section 5.3 provides evidence that increases in burning velocity at large turbulence levels are not due to increases in flamelet wrinkling. References [67, 94] discuss Damköhler's prediction that the turbulent burning velocity in the Broadened Preheat - Thin Reaction layers (BP-TR) regime is proportional to the square root of turbulent diffusivity $D_T \sim (u' L_x)^{1/2}$ multiplied by a reaction rate, based on analogy with the laminar case:

$$\frac{S_T}{S_L} = \frac{\sqrt{(\alpha + u' L_x) * RR_T}}{\sqrt{\alpha * RR_L}} \sim \sqrt{\frac{u' L_x}{\nu}} \sqrt{\frac{RR_T}{RR_L}} \tag{5.5}$$

Eq. (5.5) predicts that integral scale is a governing parameter. However the ratio of reaction rates in Eq. (5.5) can depend on flame stretch and the residence time during which the stretch rate is applied. This can introduce Karlovitz and Lewis numbers, as discussed by Andrews et al. [4], as well as the residence time (x/U_0) of eddies in the flame brush that is based on the mean velocity. Empirical correlations were designed to incorporate these physical models, and the suggested form is given in Eqn 5.6.

Table 5.2: Experimentally determined constants for Eqns. (5.6),(5.7)

Parameter	$S_{T,GC,1}/S_L$	$S_{T,GC,2}/S_L$	$\delta_{PHZ,T}/\delta_{PHZ,L}$
c_1	0.9	5.7	-
c_2	25	20	-
c_3	1.0×10^{-5}	2.0×10^{-5}	-
c_4	-	-	2.2
n	-	-	0.30
m	-	-	0.24

$$\frac{S_{T,GC}}{S_L} = \sqrt{1+c_1\left(\frac{u'}{S_L}\right)^2}\left(\frac{c_2}{c_2+\left(\frac{u'}{S_L}\right)}\right)* \left(1+c_3\sqrt{\left(\frac{u'}{S_L}\right)\left(\frac{L_x}{\delta_{PHZ,L}}\right)\left(\frac{L_r}{\delta_{PHZ,L}}\right)}\left(\frac{\delta_{PHZ,T}}{\delta_{PHZ,L}}-1\right)\right) \tag{5.6}$$

$$\frac{\delta_{PHZ,T}}{\delta_{PHZ,L}} = 1+c_4\left(\frac{u'}{S_L}\right)^n\left(\frac{L_x}{\delta_{PHZ,L}}\right)^m \tag{5.7}$$

Parameters $c_1 - c_4$, n, and m for the present data are given in Table 5.2. Note that values are listed that yield good curve fits for measured values of both consumption speeds $S_{T,GC,1}$ and $S_{T,GC,2}$. The square root factor that contains c_1 in Eqn. 5.6 is identical to Eqn. 5.4, and this factor dominates at low turbulence levels. The factor that contains c_2 is a bending term that is unity at low turbulence levels and becomes important at elevated turbulence levels. This factor is suggested by the analysis of Duclos et al. [42]; it arises due to the destruction term associated with flamelet merging in their flame surface density balance. The term that includes c_3 in Eqn. 5.6 is seen to be negligible when the preheat zone thickness ($\delta_{PHZ,T}$) is not much larger than its laminar value. For thick preheat zones, this term accounts for the enhanced diffusivity of heat (and thus the enhanced reaction rate) due to turbulence within the preheat zone, as was suggested by Damköhler.

It is observed that both the longitudinal and transverse integral scales are relevant to

determining the burning velocity, as they both contribute to the effective size of the turbulence. However, it was not possible to perform PIV measurements over all Hi-Pilot run conditions, due to the extremely large separation of scales. Therefore, the slot width of the turbulence-generating plates is used in Eqn. 5.6 as a proxy variable for the lateral integral scale.

In general, the quantities in Table 5.2 will be functions that depend on the composition of the reactants. Since composition was not varied in this work, these parameters are constants. The effect of Le and ϕ on the measured burning velocities are important questions that should be addressed in future work. The performance of Eqn. 5.6 for the two measured consumption speeds $S_{T,GC,1}$ and $S_{T,GC,2}$ is given in Fig. 5.15, and good agreement is observed for all conditions.

The present results suggest that the turbulence level and integral scale at the reaction layer differ from those in the upstream reactants. This has been predicted by the very high Ka DNS flames of Savard et al. [107, 108]. It is observed that our extreme levels of turbulence (u'/S_L up to 163) broaden the preheat layer dramatically to a thickness that is regularly greater than 20 mm. Additionally, the work of Osborne et al [88] shows that the local consumption speed is proportional to the preheat thickness. The elevated viscosity could reduce u' and modify L_x. This is a dynamic system, as the preheat thickness depends on the same variables as burning velocity; as the preheat layer broadens with increasing turbulence, it may attenuate some of the eddies acting on the reaction layer downstream. This possibility was discussed previously in Chapter 4. Thus it is suggested that the preheat zone thickness is a variable that indirectly modifies the burning velocity by modifying the incoming turbulence. The work points out the need to measure the variation of turbulence level and integral scale as a function of distance through a thickened preheat zone, which is the subject of the simultaneous PIV and formaldehyde PLIF measurements of Chapter 6.

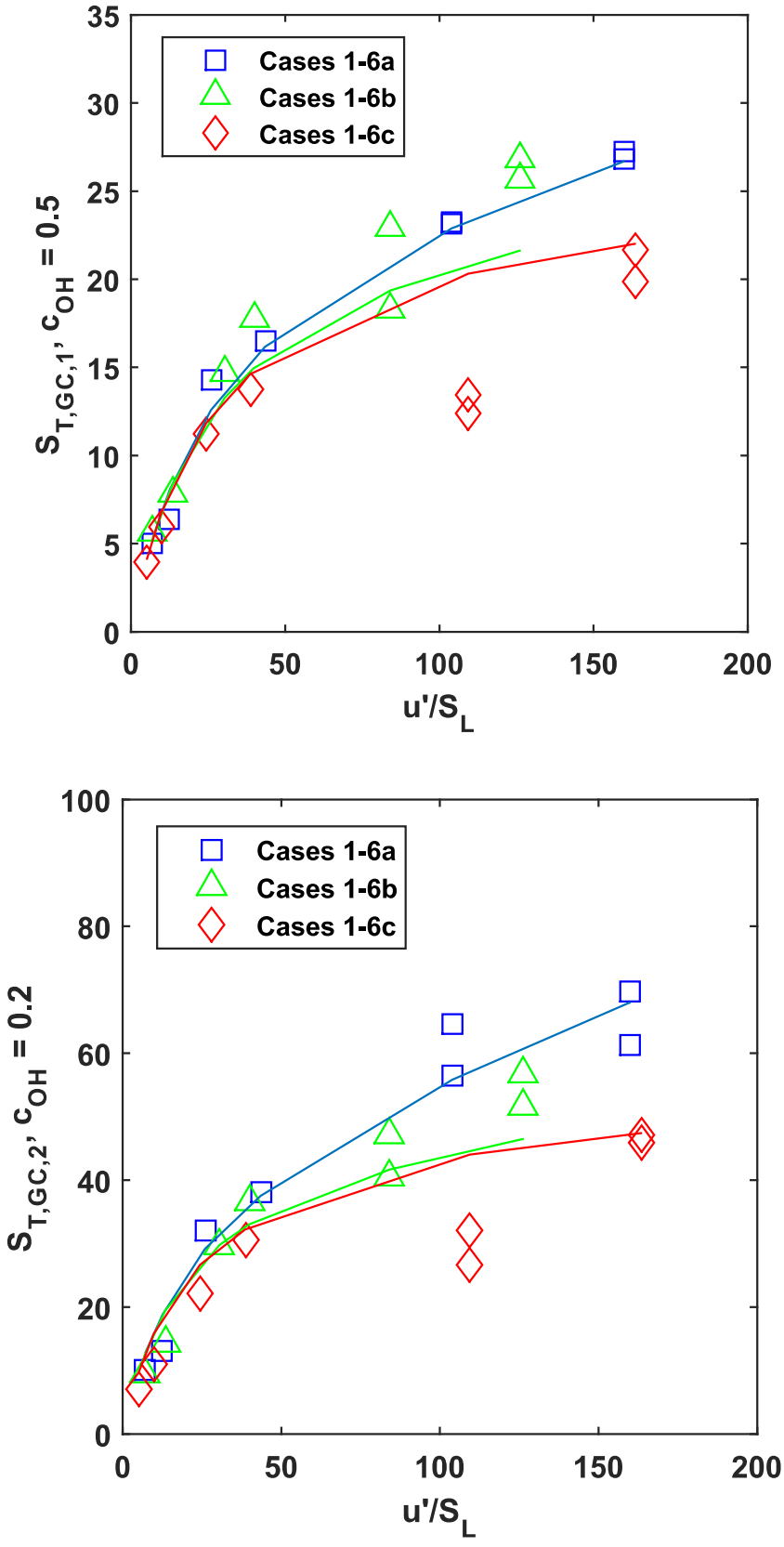

Figure 5.15: Correlations for burning velocity

5.6 Conclusions of the burning velocity measurements and implications for modeling

Three types of turbulent burning velocity were measured in the new range of *extreme turbulence* (defined as $u'/S_L > 25$), and turbulence levels exceeded six times that of previous work. The conventional consumption speed $S_{T,GC,1}$ (based on the area of the $\tilde{c}_{OH} = 0.5$ contour) and the leading edge consumption speed $S_{T,GC,2}$ (based on the $\tilde{c}_{OH} = 0.2$ contour) increase with increasing turbulence levels. Both consumption speed curves displayed bending, and values of $S_{T,GC,1}/S_L$ exceeded 25.

Several measurements of flamelet wrinkling were performed, and it was observed that increasing u'/S_L in the extreme range of turbulence does not cause further increase in A_T/A_L, indicating flame surface destruction balances further increases in wrinkling in this regime. This is consistent with data of Gülder [116, 140] who considered lower turbulence levels. Thus $S_{T,F}$ and A_T/A_L are not good metrics of the burning velocity in the extreme turbulence range, because $S_{T,F}$ is based on thin flamelet assumptions that are no longer valid.

The results of this work should be useful to the modeling community, for whom accurately capturing the turbulent flame speed is an essential component of any model. The results show that despite the reaction zone maintaining a flamelet-like structure (Chapter 4), the flames are not laminar flamelets. This is because the burning velocity is enhanced due to the actions of turbulent diffusivity, and therefore the local propagation rate exceeds the value of S_L that can be expected using stretched flame concepts. The work shows that any modeler who wishes to accurately capture the turbulent flame speed must have both a flamelet wrinkling (flame surface density) sub-model, as well as a turbulent diffusivity sub-model, as both terms are significant in extreme turbulence.

CHAPTER 6

Simultaneous Measurements of Velocity and Preheat Structure

The work of this thesis thus far has shown that the flames in the Hi-Pilot have a structure consisting of wrinkled, thin flamelets, but the preheat layer is fully broadened (meaning it has thickened sufficiently to extend to all reactants within the flame cone). The turbulent burning velocities are increasing due to mechanisms of turbulent diffusivity, and flamelet wrinkling is saturated for $u'/S_L >\sim 20$, where further increases of u'/S_L do not increase A_T/A_L. However, these results conflict with the analysis of Peters [92–94] which would predict that a number of our flames should be in the broken reaction layers regime. One possible explanation for this discrepancy is that the turbulence is weakened during passage through the preheat layer, which may be due to attenuation of u' or dissipation of the small scales (and therefore growth of the η_k). Or, it may be that disruption of the reaction layer requires very strong, small eddies. Peters's criterion only requires that eddies are small enough to fit inside the reaction layer, but does not state how strong the eddies must be to broaden or break it. A corollary to this is that the reaction layers may be much more resilient to turbulence than previously expected, possibly due to the enhanced diffusivity that will occur when the preheat layers are broadened.

The fact that broadened or broken reaction zones are not observed at the very large turbulence levels of $u'/S_L = 243$, as well as the simultaneous broadening of the preheat layers

that corresponds with large-scale bending of the $S_{T,GC}$ curves, suggests that the broadened preheat layers are interacting with and modifying the incoming turbulence impinging on the reaction surface. If turbulence levels u'/S_L are attenuated or fine-scale structures are dissipated during passage through the broad preheat layers, that would provide an explanation for the results observed in Chapters 4 and 5.

The works of Dunn et al [43, 44], Zhou et al [143–145], Savard et al [107, 108], and Aspden et al [7, 8] are among the only studies that have shown evidence of non-flamelet like behavior. Thus, although they show that it is possible to produce broken or distributed zones, all of them utilized relatively small scale experiments and the results have yet to be observed in larger configurations. The DNS of Savard et al observed some dissipation of fine-scale structures as the preheat layer broadened, but the effect of this mechanism at larger scales has not been tested. Therefore, there is a gap in turbulent combustion theory, which this chapter will address.

This work marks the first experimental study to test whether turbulence decays and integral scales increase within the preheat layer due to viscous decay and/or thermal expansion, which was predicted by the analysis of Lipatnikov and observed in the DNS results of Aspden et al and Savard et. al. Simultaneous PIV and formaldehyde PLIF measurements were performed in order to obtain conditioned statistics of the turbulence as a function of the distance from the reaction surface. There are few previous attempts to measure conditioned turbulence statistics in this way. Frank et al [49] performed simultaneous OH-PLIF and PIV measurements in weakly turbulent ($2 < u'/S_L < 9$) methane-air flames stabilized on a 36 mm piloted Bunsen burner. Their results showed a transition from counter-gradient to gradient diffusion occurred as u'/S_L increased. Bohm et al [17, 18] applied simultaneous particle image velocimetry (PIV), particle tracking velocimetry (PTV), and OH-PLIF to obtain conditional flow field statistics in partially premixed opposed jet flames. Their results were used to obtain profiles for turbulence statistics such as turbulent kinetic energy and vorticity through the reaction layer.

The goals of the conditional velocity measurements are to show how the turbulence level u' and integral scales vary across the broadened preheat zones in order to determine the turbulence level that finally reaches the reaction layer. This should help us better understand why the reaction layers are not broadened or extinguished in extreme turbulence, and may also help explain the observed bending of the measured consumption speeds $S_{T,GC}$.

6.1 Definition of Conditioned Velocity

Conditioned velocities in the present study are defined to be velocities that are conditioned on η, the distance from the reaction layer boundary. Thus $\eta = 0$ is the upstream boundary of the reaction layer and positive values of η represent locations in the preheat layer. Negative values of η occur in the products. For each pixel in each recorded image, the value of η is determined. An ensemble is created of velocities associated with a certain value of η (plus or minus $\Delta\eta$) and the average of this ensemble is computed. The value of u' where η is positive represents turbulence in the reactants. The value of u' for negative values of η represents turbulence in the products. The reaction layer is idealized to be an infinitely thin sheet, which was shown by the flame structure measurements of Chapter 4 to be a reasonable approximation.

Bray et al. [23], Gulati and Driscoll [40, 55], and Shepherd et al. [112] have demonstrated the need to know conditioned velocities in premixed turbulent flames. Velocity fluctuations (u') at a point P have three contributions: one is due to u' recorded at times when reactants are present at P (positive values of η), and a second is recorded at times when only products are present at P (negative values of η). A third contribution to the unconditioned value of u' is due to flamelet crossing, but this third contribution to u' is not turbulence. Consider a laminar flame that oscillates over point P (see Fig. 6.1). The measured value of u' will be large because the velocity oscillates between the velocity of the reactants and the larger velocity of the products, but the measured value of u' in this case does not represent turbulence. Thus, the unconditioned value of u' in a premixed tur-

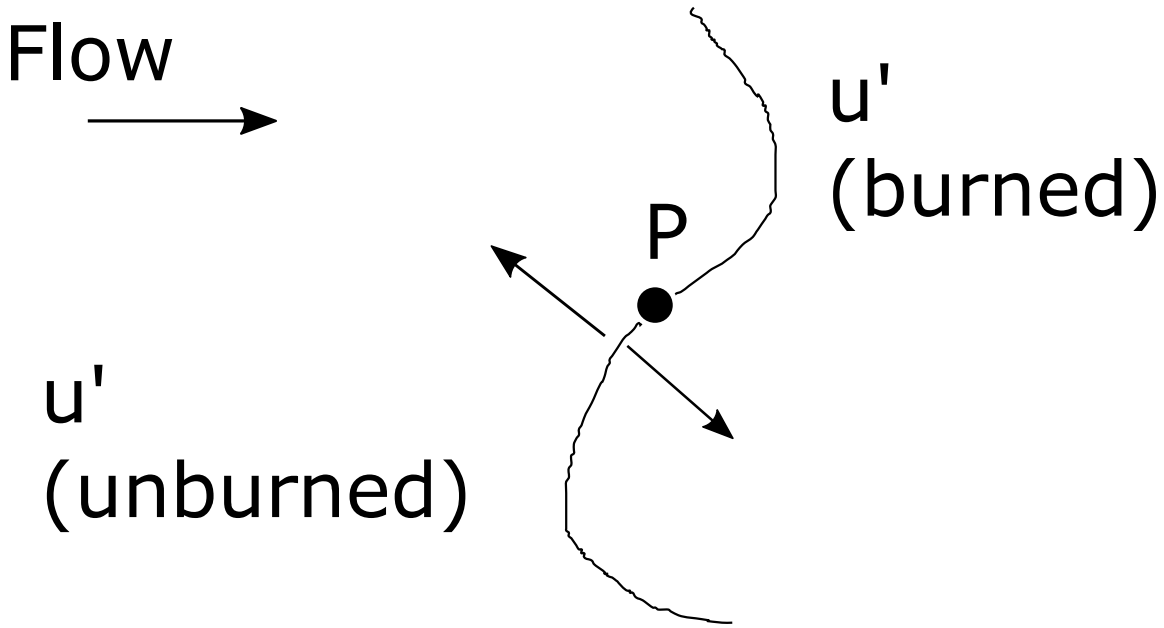

Figure 6.1: Illustration of the contributions to velocity fluctuations u' at a point P that is near the flame surface. Fluctuations of the flame surface about the point P will produce measured values of u' that are very large, but are not physical. Conditional sampling of velocity in the reactants and products eliminates this source of error.

bulent flame is not a measure of the turbulence in either reactants or products. In this work, the conditioned velocity measurements prevent this fictitious turbulence due to flamelet crossing from contributing to u'.

6.1.1 Identification of the local distance from the reaction layer

Obtaining turbulence measurements conditioned on the local distance from the reaction layer required generating a map for each image that assigned every velocity vector a distance from the flame front. This required first marking the products in each simultaneous PIV-CH_2O image. The products are distinguished from cold reactants by the combination of absence of formaldehyde signal, a sharp gradient in formaldehyde, and a drop in seed particle density due to gas expansion. A computer code was written to identify these regions, and each image was verified (and if necessary, corrected) by hand in post-processing. Data sets consisted of 1,000 raw images, and approximately 750 were used for data anal-

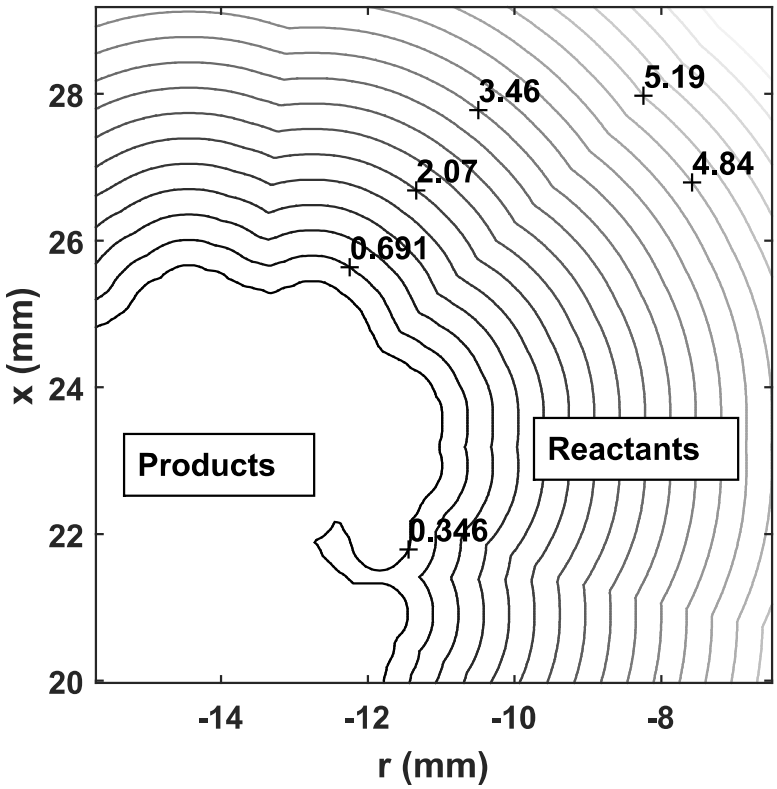

Figure 6.2: Example of contours of local distance from the reaction zone. Change colormap to white in products

ysis. The remainder were discarded due to either ambiguity distinguishing products from reactants, or difficulty identifying the leading edge of the formaldehyde structure (i.e., the edge was outside of the field of view). At this point, the formaldehyde edge is separated into two segments - one which faces the reactants (the preheat zone edge) and one which faces the products (the reaction zone). For each pixel in an image, the distance to the nearest reaction zone edge is identified, and this value is assigned to the corresponding velocity vector or turbulence statistic at that location. An example of a resulting distance map is provided in Figure 6.2. The white region is the product region, and the contours show increasing distance from the reaction zone.

At this point, all velocity vectors have been associated with a local distance from the reaction layer. The velocity measurements are then conditionally sampled in order to obtain

profiles through the flame. To do so, the distance from the reaction surface is discretized into bins of 0.05 mm (50 μm). That is, all velocity vectors within 0.05 mm of the reaction layer are collected into one group, all vectors between 0.05 mm and 0.10 mm are collected into another group, and so on. Typical bin sizes exceed 100,000 vectors, and the minimum bin size for computation was 10,000 vectors. From these conditionally sampled vectors, a mean velocity $\widetilde{U}$ is computed for each bin, with the tilde indicating the conditional mean. Next, fluctuation velocities $\tilde{u'} = \sqrt{\overline{\left(u - \tilde{U}\right)^2}}$ are defined, producing the turbulence level conditioned on the local distance from the reaction layer.

6.2 Run conditions and measurement location

The Hi-Pilot burner was used for the simultaneous PIV and formaldehyde PLIF measurements. The run conditions studied in this measurement are Case 3b and 4b, with equivalence ratio set to $\phi = 0.75$. Fig. 6.3 displays the progress variable of OH (measured from the OH-PLIF described in Chapter 5) for Cases 3b and 4b, and the measurement location is superimposed in red. The field of view is positioned to capture approximately the middle of the flame brush, with the $\overline{c}_{OH} = 0.5$ contour passing through the middle of the black box in Fig. 6.3. This corresponded to positions in the lab coordinates relative to centerline above the jet exit plane of $-15.7\,mm < r < -6.5\,mm$ and $20.0\,mm < x < 29.2\,mm$.

Note that the flame heights for the measured test cases are approximately 60-70 mm, while the jet core should extend to approximately 5*D = 125 mm. Therefore, the flames studied are well within the jet core. The co-flow flame sits below the exit plane of the central jet, and is run at a flow rate sufficient to produce a region of uniform hot products downstream of the main flame. The laser diagnostics and experimental setup for the simultaneous measurements are detailed in section 2.5.

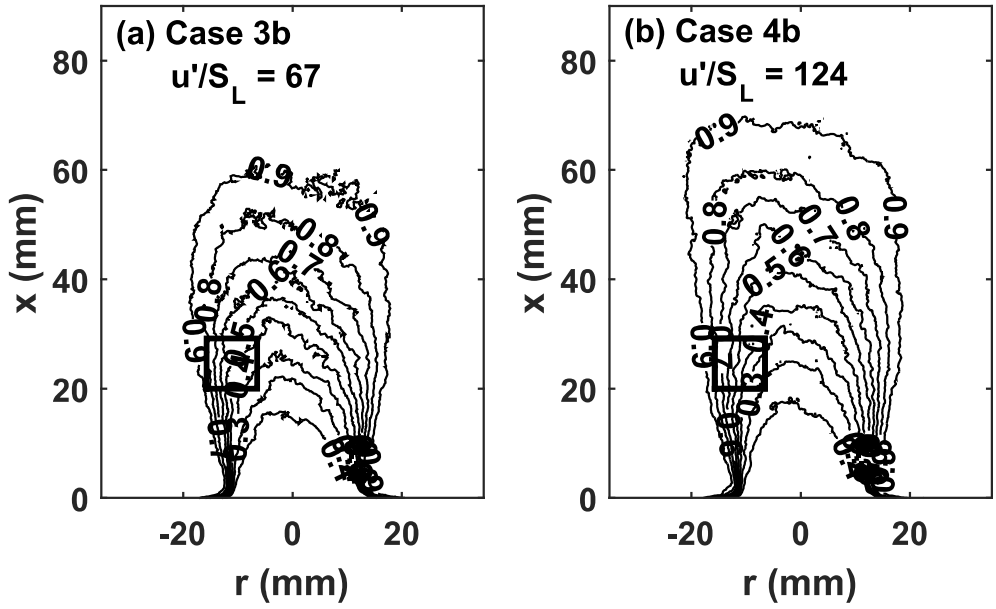

Figure 6.3: Contours of the mean progress variable of OH ($\overline{c}_{OH}$) for the two test cases studied. Contour lines are levels of constant $\overline{c}_{OH}$ from 0.1 to 0.9 in increments of 0.1. The thick black box corresponds to the measurement location of the simultaneous PIV and formaldehyde PLIF.

6.3 Conditioned velocity measurements through the flame

Conditioned velocity measurements are conditioned on the distance to the reaction layer (η), as explained in Section 6.3. Positive values of eta correspond to the preheat layer while negative values of eta correspond to the products. Figure 6.4 presents conditioned velocity and turbulence statistics for Cases 3b and 4b relative to the distance from the reaction zone. The turbulent kinetic energy k is computed as $k = \frac{1}{2}u'^2 + v'^2$, with the assumption that the unmeasured out-of-plane component of velocity w' is approximately equal to the radial fluctuation v'. The reaction coordinate is positive in the reactants and negative in the products. The reaction zone boundary is indicated by the solid vertical line, and the average preheat zone boundary is indicated by the dashed vertical line. The preheat thicknesses were measured from the instantaneous formaldehyde PLIF following the procedure of Section 2.4.1.4. The average thicknesses of the preheat layers was found to be 1.37 mm for Case 3b and 1.59 mm for Case 4b. Note that this measurement is conditioned on the field of view; because the field of view is fairly small, the magnitude of the measured preheat thickness is biased toward smaller values. It is important to note that the preheat layer thickness varies dramatically both from image to image and in different regions within a frame; therefore, although the average preheat zone extends only approximately 1.5 - 1.75 mm, some fraction of the measurements at $\eta = 6$ mm will exist in the preheat layer. Likewise, a small fraction of measurement samples at $\eta < 1$ mm will be upstream of the instantaneous preheat layer.

Figure 6.4 shows that the mean velocity U and turbulence level u' are approximately constant upstream of the average preheat layer, but there is a substantial drop in the mean velocity U as the reaction zone is approached. It appears that U begins to decrease at approximately the location of the average preheat layer edge, although the gradient $\partial U_x/\partial\eta$ is maximum at $\eta \sim 0$ for both flames. In contrast to the mean velocities, the turbulence intensity remains fairly constant throughout the preheat region. It is observed that there is a slight decrease in the longitudinal rms velocity u' as it enters the preheat layer, but this

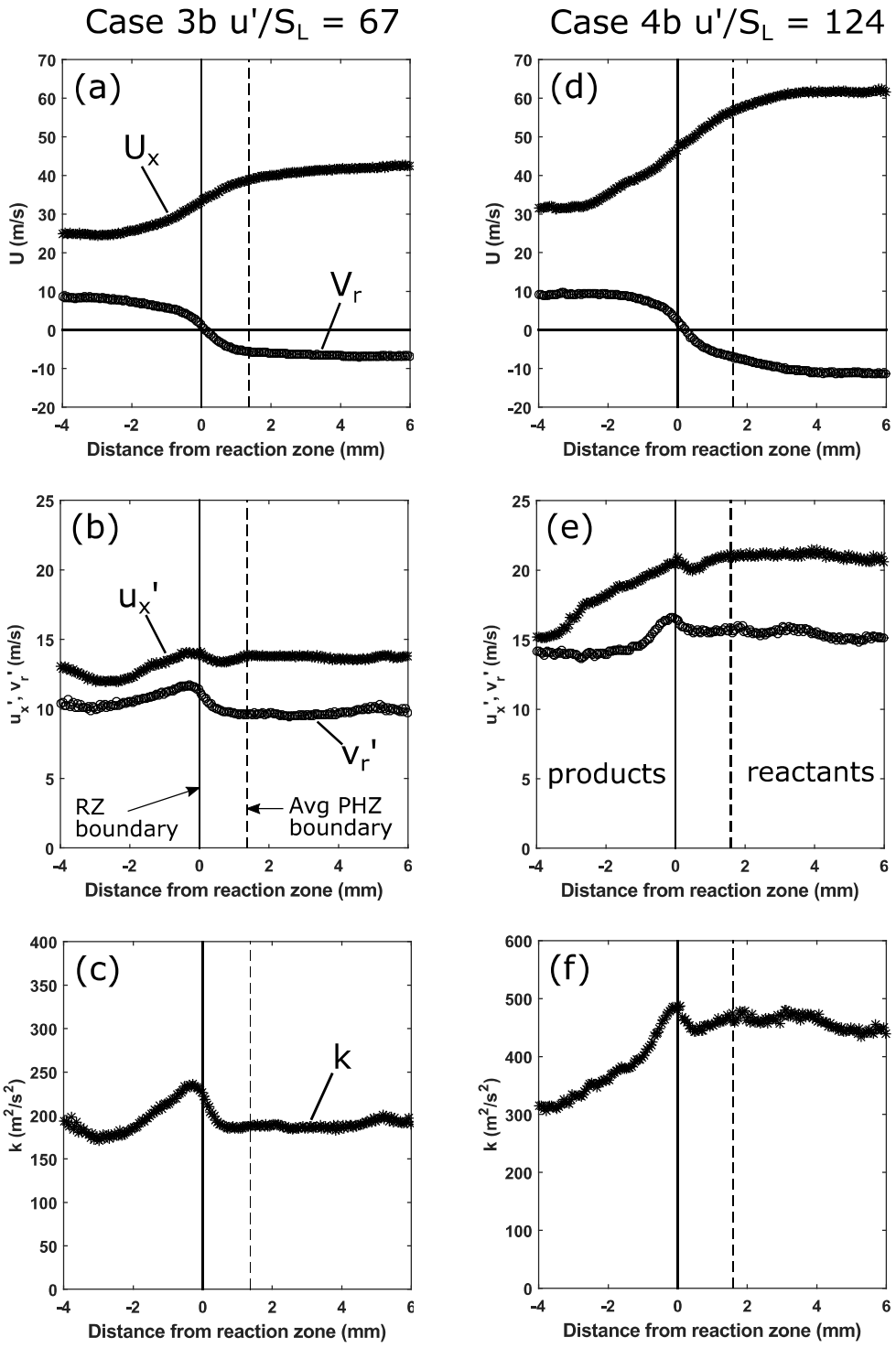

Figure 6.4: Turbulence statistics conditioned on distance from the reaction zone. a,d: Conditioned mean velocity, b,e: conditioned r.m.s. velocity fluctuations, c,f: conditioned turbulent kinetic energy k.

effect is very small. The decrease is countered by the large increase in turbulence intensity that begins approximately 1 mm before the flame. For Case 3b, the turbulent kinetic energy k returns to approximately its pre-flame values downstream of the reaction layer. However, for Case 4b k continues to decrease after the flame. This effect is much stronger in the longitudinal velocity fluctuation u', while the lateral fluctuation v' is approximately constant for $\eta < -1$.

6.3.1 Change in mean velocity through the flame

Figure 6.5 shows an instantaneous image of the velocity and preheat zone structure for Case 3b. Figure 6.5(a) shows every 10th velocity vector in red superimposed on the formaldehyde signal in white. Figure 6.5(b) shows contours of velocity magnitude for the same image, with the preheat zone outlined in white. The regions containing reactants and products are labeled accordingly in (b). What is striking in the image is that the kinetic energy $(u^2+v^2)^{1/2}$ is significantly larger in the reactants, and drops progressively through the flame region. This is indicated by the regions in (b) corresponding to velocity magnitudes of ~ 60 m/s, while the average velocity magnitude in the preheat layer is approximately ~ 30 m/s. The significant drop in velocity near the leading edge of the formaldehyde PLIF signal was suggested by the mean velocity profiles in Fig. 6.4 (a) and (d), and is seen consistently across the data sets. That is, high velocity gases are almost exclusively contained in the reactants, and the preheat boundary typically exists in the region where the velocity begins to decrease.

Figure 6.6 gives PDFs of axial velocity u measured in the preheat layer and in the cold flow upstream. The mean in the cold flow is approximately 45 m/s, and decreases to 35.7 m/s in the preheat layer, and is in agreement with the profiles given in Fig. 6.4. This result may be somewhat surprising, since the elevated temperature of the preheat layer would be expected to produce gas expansion. This drop in velocity as flow enters the preheat zone suggests that the flame may be located near the shear layer separating the co-flow from the

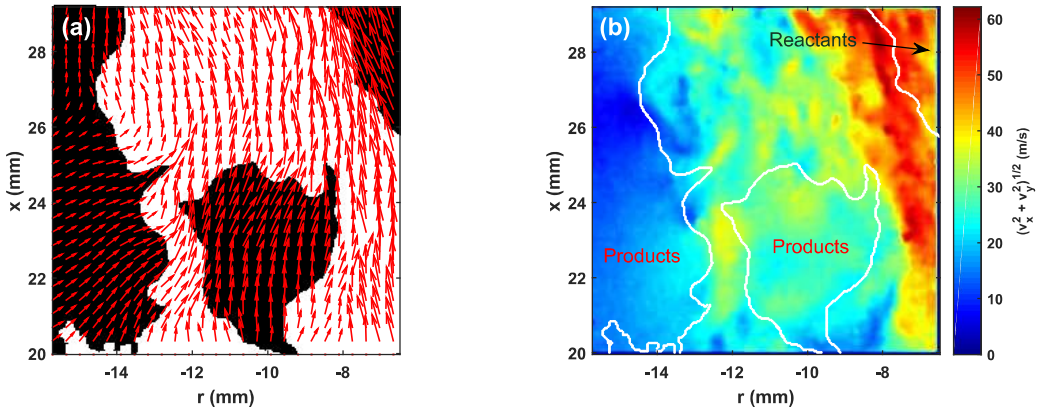

Figure 6.5: Instantaneous images of velocity (left) and kinetic energy (right). On the left, formaldehyde signal is in white, with every 10 velocity vectors in red. It is clear that the flame region is associated with reduced values of all measured quantities.

central jet. Given the extremely large turbulence intensities produced in the Hi-Pilot burner, it is not unreasonable to expect the flame would position itself relative to the incoming flow to be in regions of lower strain.

6.3.2 Conditional measurements of velocity through the preheat layer

An effort was also made to measure the conditioned turbulence values as a function of distance through the preheat layer. For this measurement, identical processing steps were performed for the conditioned velocity statistics. However η was instead defined as η_{PHZ}, which is zero on the preheat zone edge and is increasing in the direction of the flame. Note that η_{PHZ} is undefined in the cold reactants (upstream of the preheat layer), i.e., it is only positive.

The results are given in Fig. 6.7 and generally agree with the profiles through the reaction layer from Fig. 6.4. Mean velocity progressively decreases through the preheat zone, but the turbulent fluctuations u' and v' are approximately constant. It is interesting that there appears to be a rapid increase in the lateral fluctuation velocity v_r' within the first 1 mm of entering the preheat zone, but it remains relatively constant for larger values of η_{PHZ}.

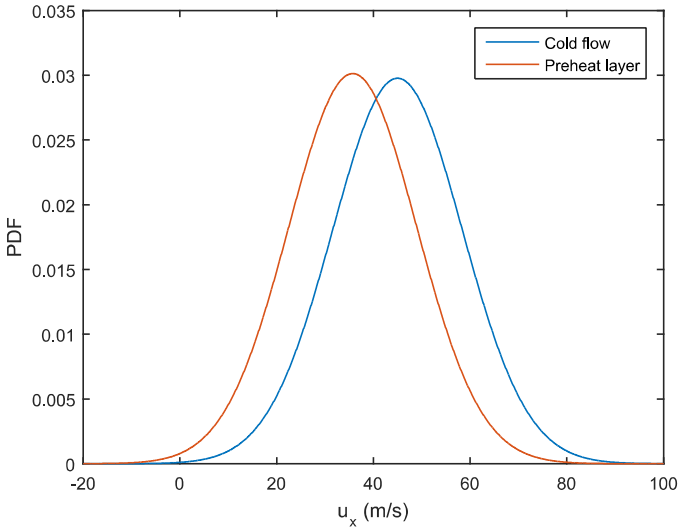

Figure 6.6: PDF of streamwise velocity u_x in the preheat layer and in the cold flow upstream for Case 3b. The velocity is larger upstream of the preheat layer.

Note, however, that making direct comparisons between the measured values at specific locations, for example at the average preheat layer boundary $\eta_{PHZ} = \delta_{PHZ,T}$ and $\eta = \delta_{PHZ,T}$, do not give identical values. This is because the conditional sampling is defined differently depending on whether measurements are desired as a function from the reaction layer or as a function of distance through the preheat layer. This is because an instantaneous velocity vector may be located on the leading edge of the preheat layer, corresponding to $\eta_{PHZ} = 0$, but the instantaneous preheat thickness varies significantly, meaning η may take any value and is unlikely to be exactly $\delta_{PHZ,T}$.

6.3.3 Evolution of Strain and Enstrophy through the flame

The variation of the strain rate and enstrophy as a function of η were also evaluated for Case 3b. Because these quantities depend on velocity gradients, higher resolution was required than the 32x32 pixel interrogation box could provide. Therefore, a 16x16 pixel interrogation window was used. Case 4b was not considered in this case because the vectors obtained from the smaller interrogation window were deemed inadequate in the products

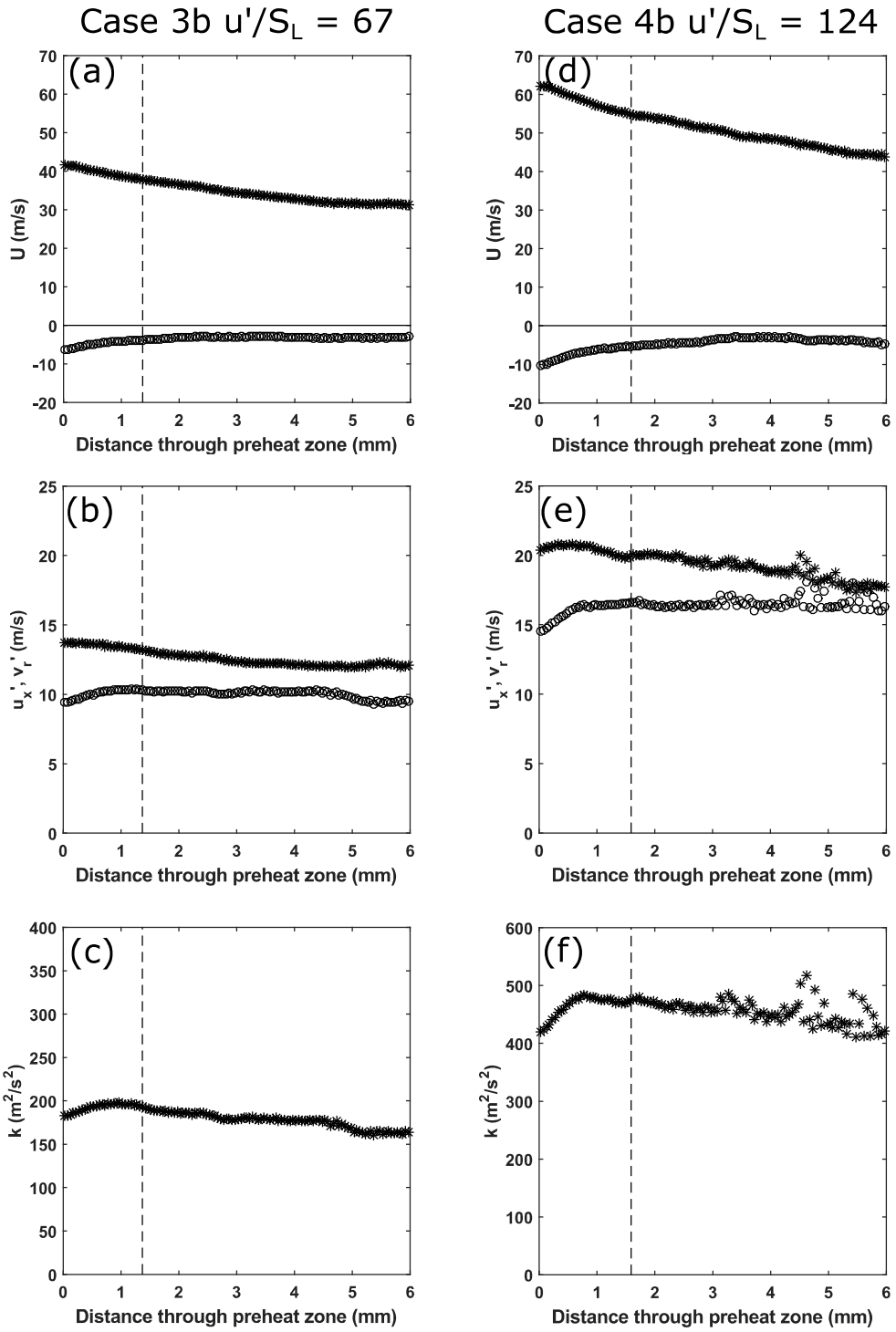

Figure 6.7: Turbulence statistics conditioned on distance through the preheat zone. a,d: Conditioned mean velocity, b,e: conditioned r.m.s. velocity fluctuations, c,f: conditioned turbulent kinetic energy k.

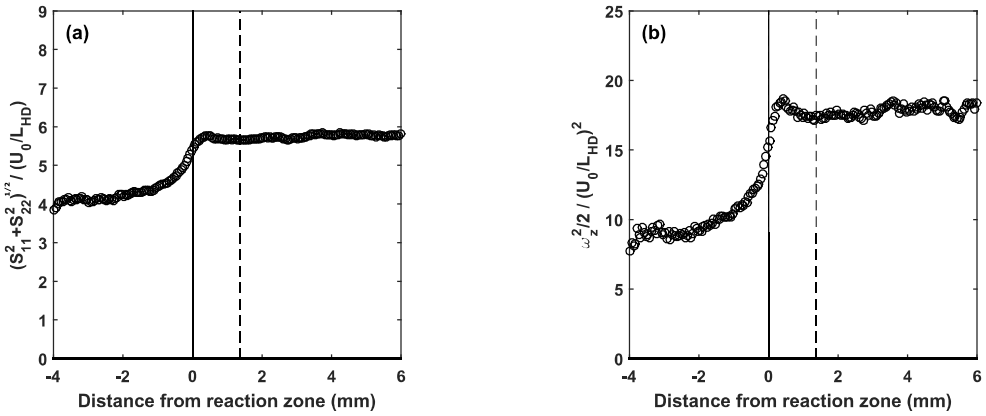

Figure 6.8: Variation of the normalized (a) principle strain rates and (b) enstrophy as a function of η, the distance from the reaction zone for Case 3b.

region. For further discussion of the uncertainty associated with the PIV measurements, see Section 6.3.6. The strain rate tensor is defined as:

$$\underline{S} = \begin{bmatrix} \frac{\partial u}{\partial x} & \frac{1}{2}\left(\frac{\partial u}{\partial y}+\frac{\partial v}{\partial x}\right) & \frac{1}{2}\left(\frac{\partial u}{\partial z}+\frac{\partial w}{\partial x}\right) \\ \frac{1}{2}\left(\frac{\partial u}{\partial y}+\frac{\partial v}{\partial x}\right) & \frac{\partial v}{\partial y} & \frac{1}{2}\left(\frac{\partial v}{\partial z}+\frac{\partial w}{\partial y}\right) \\ \frac{1}{2}\left(\frac{\partial u}{\partial z}+\frac{\partial w}{\partial x}\right) & \frac{1}{2}\left(\frac{\partial v}{\partial z}+\frac{\partial w}{\partial y}\right) & \frac{\partial w}{\partial z} \end{bmatrix} \tag{6.1}$$

The PIV measurements can only resolve the four terms in the upper left-hand corner of the strain rate tensor. The strain rate tensor can always be transformed such that the tensor is diagonal, and the eigenvalues of $\underline{S}$ represent the principal strain rates S_1, S_2, and S_3. The norm of the principle strain rates in the measurement plane was taken as $\sqrt{S_1^2+S_1^2}$ and then normalized by (U_0/L_{HD}). This result is plotted in Fig. 6.8(a). It is clear that the strain rate is approximately constant for all values of η in the reactants, although there is a slight increase just before the reaction zone. This is followed by a rapid decrease through the reaction layer before returning to a steady value in the products region.

The enstrophy was also computed as $\frac{1}{2}\omega_z^2 = \frac{1}{2}\left(\frac{\partial v}{\partial x}-\frac{\partial u}{\partial y}\right)^2$ and normalized by $(U_0/L_{HD})^2$, and is plotted in Fig. 6.8(b). The enstrophy follows a very similar trend as the strain rates, with relatively homogeneous magnitude both in the products and reactants, but a rapid decay in strength as the flow passes through the reaction layer. Together, these results

reinforce the conditioned turbulence measurements discussed in Section 6.3, and illustrates that the turbulence structures does not change significantly as it passes through the reaction layer.

6.3.4 Analysis of the shear layer

The results of the conditionally sampled mean velocity profiles suggest that the dynamics of the shear layer between the co-flow and central jet may be important. The co-flow was characterized previously in section 3.2.1, and the mean velocity gradient was found to be approximately $dU_x/dx = 2,850$ 1/s. Comparing this result to the measured gradient in conditional mean velocity, we find a velocity gradient of $\partial U/\partial\eta = 5,100$ 1/s for Case 3b and $\partial U/\partial\eta = 6,000$ 1/s for Case 4b.

The turbulence intensity u' approaching the flame is approximately 14 m/s for Case 3b and 21 m/s for Case 4b (Fig. 6.4 (b) and (e)). These values are extremely close to the previous velocity measurements reported in Section 3.2.2. There, the non-reacting velocity field was measured from $-10\,mm < r < 10\,mm$ and $0\,mm < x < 20\,mm$. For this measurement, neither the main fuel nor the co-flow were run. The turbulence intensity u' at $r = -7\,mm$ and $x = 20\,mm$, which corresponds to the boundary of the smaller field of view used for the simultaneous PIV and formaldehyde PLIF measurements, was found to be approximately 15 m/s for Case 3b, and 25 m/s for Case 4b. The turbulence intensity was approximately constant through the field of view, as the value of u' on centerline at $x = 1$ mm was approximately 16 m/s for Case 3b and 29.5 m/s for Case 4b. Some decay of u' occurred downstream, and it increased slightly (less than 20%) as the shear layer with the co-flow was approached.

Comparing, then, the measured turbulence intensities impinging on the reaction layer and the values measured at the jet exit, we see that there is not a significant change in u'. For Case 3b, a regime diagram would predict that the turbulence level impinging on the entire flame surface is approximately 16 m/s for Case 3b and 29.5 m/s for Case 4b. We see from

Fig. 6.4 (b) and (e) that these are reasonable approximations, as the turbulence is relatively homogeneous throughout the jet core. Relative to the measured jet-exit turbulence levels, the turbulence that acts on the flame front is only 10% less for Case 3b and 26% less for Case 4b.

Therefore, we can say that turbulence levels upstream of the flame do not change significantly until the post-flame region, which indicates that the co-flow shear layer lies downstream of the flame brush. However, the shear layer appears to lie relatively close to the downstream boundary of the flame. Thus the shear layer affects the turbulence level just downstream of the flame, but does not appear to significantly affect the turbulence level that is upstream and incident upon the flame. It is important to quantify what fraction of the total turbulence level u' impinging on the flame surface is due to the shear layer. The turbulence level u' for Case 3b at x = 20 mm and r = 0 mm (taken from the larger field of view discussed in section 3.2.2) is approximately u' = 12 m/s. Because this is inside the jet core and on centerline, this value should be entirely unaffected by the shear layer. Fig. 6.4(b) demonstrates that the turbulence level seen by the flame is 14 m/s. Therefore, this analysis suggests that for Case 3b, 85% of the total u' that interacts with the flame is due to the turbulence generated within the reactants, and 15% is due to the co-flow shear layer. Likewise, for Case 4b the turbulence level u' on centerline at x = 20 mm is approximately 22 m/s, and the value of u' acting on the flame is 21 m/s. Therefore, for Case 4b 95% of the turbulence impinging on the flame is generated within the reactants, and only 5% is due to the shear layer. This is an intuitive result: as the turbulence levels issuing from the burner become more extreme, effects of the shear layer become less significant.

6.3.5 Variation of the average eddy velocity U_θ through the preheat layer

The results presented thus far do not appear to support the hypothesis that substantial attenuation of turbulence intensity occurs through broadened preheat zones. As shown in

Fig. 6.4(c) and (f), the turbulent kinetic energy k is approximately constant for $1 < \eta < 6$, indicating that the turbulence upstream of the preheat layer is approximately the same as what interacts with the reaction zone.

This means that we must search for an alternative explanation as to why the turbulence is unable to modify the reaction layer structure. It may be the case that as the turbulent eddies pass through the preheat layer, they grow in size. This has previously been shown in single vortex-flame interactions [81]. Through conservation of angular momentum, if the vortex grows larger its angular velocity must decrease. A reduced angular velocity would imply a weaker eddy, which is less capable of disrupting the chemical reactions. In order to evaluate this hypothesis, the average eddy velocity U_θ was determined from the PIV data, and conditional measurements of U_θ were performed similar to Fig. 6.4.

To measure the rotational velocity, vorticity was first calculated from the PIV data. Individual vortical structures were identified using the Q-criterion. The Q-criterion is a tool used to distinguish rotation and strain elements in a turbulent flow [46]. For example, in flows with high mean shear, the magnitude of vorticity will be large; however, these do not correspond to actual vortical structures, rather it is shear-generated vorticity. The Q-criterion eliminates these shear-generated structures, and is defined for incompressible flow for $Q = \frac{1}{2}(||\Omega||^2 - ||S||^2) > 0$, where Ω is the rotation tensor and S is the strain tensor, the anti-symmetric and symmetric terms of the velocity gradient tensor, respectively. The Q-criterion is positive when the local rotation is larger than the strain, and therefore is a good qualitative measure of rotational structures. For each image, all rotational structures were identified using the Q-criterion, and the average vorticity ω of each structure was recorded. A hydraulic diameter for each structure was then computed using $D_h = \frac{4A}{P}$. Finally, the eddy rotational velocity was evaluated as $U_\theta = \omega D_h$, and is plotted in Figure 6.9 in a similar manner as the other turbulence statistics.

Figure 6.9 shows that the average rotational velocity decreases approximately linearly during its passage through the preheat layer, but the change is small. The eddy velocity

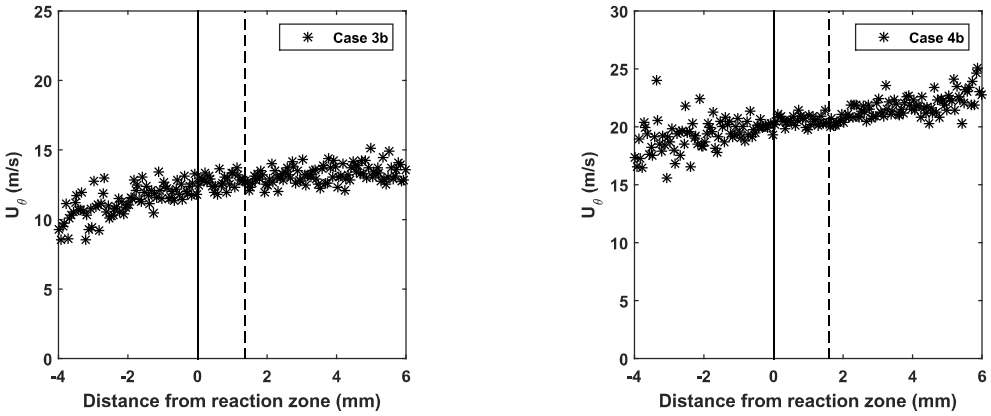

Figure 6.9: Average eddy rotational velocity conditioned on distance from the reaction zone.

U_θ decreases from 14 m/s to 10 m/s for Case 3b, and from 23 m/s to 18 m/s for Case 4b, and the gradient $dU_\theta/d\eta$ is approximately the same for the two cases. The spread about the mean in Figure 6.9 is fairly large, due to the much smaller sample size for rotational velocity; while each image will have hundreds of velocity vectors, there may only be twenty or thirty rotational structures. However, the scatter in Figure 6.9 is useful for visualizing the statistical (random) error in the measurement, which is +/- 2-3 m/s.

The eddy velocity appears to decrease somewhat faster downstream of the reaction layer, where the temperature is much larger. Taking the difference in U_θ over the range $\eta = 6$ to $\eta = 0$, we see that U_θ only decreases by approximately 7% for Case 3b (14 m/s to 13 m/s), and 10% for Case 4b (23 m/s to 20.5 m/s). It is conjectured that it is unlikely that a change in U_θ of such a small magnitude would be sufficient to prevent the turbulence from disrupting the reaction layers. Thus, it appears that attenuation of eddy strength (measured by U_θ) does not adequately explain the inability of the turbulence to perturb the reaction surface.

6.3.6 Uncertainty in the conditioned velocity measurements

At this point, it is useful to discuss the uncertainty that is associated with the conditioned velocity measurements of Figs. 6.4, 6.7, and 6.9. The precision (statistical error) of the conditioned velocity measurements can be approximated using the 95% confidence interval of the mean velocity, Eqn. 3.3. The confidence interval in the mean velocity was +/- 0.294 m/s for Case 3b and +/- 0.43 m/s for Case 4b. These uncertainties represent approximately 1% of the mean velocity.

To assess the accuracy of the conditioned velocity measurements, the PIV interrogation box size was reduced from 32x32 pixels to 24x24 pixels and 16x16 pixels. If the small scales are sufficiently resolved, the PDF profiles of velocity should not change significantly as the box size is varied, as such would imply that important information in the flow is not resolved in the measurement. Gamba and Clemens [51] have shown that the critical length scale required to meet this condition is the Taylor scale λ_t. The resulting PDF's of the x-component of velocity are given in Fig. 6.10 for Case 3b. It is clear that the profiles do not change significantly with varying box size, implying that the measurements adequately resolve the necessary scales of the flow.

With the exception of the strain rate and enstrophy measurements (Section 6.3.3), the conditioned turbulence statistics were measured using a relatively large 32x32 pixel interrogation window. This size provided the highest quality vectors in both the reactants and products, while permitting resolution below the Taylor scale. As shown in Fig. 6.10, the measured velocities do not change with interrogation box size, and resulting conditioned turbulence profiles for Case 3b were independent of interrogation box size. However, the smallest scales of the flow are not captured with this larger resolution. Although this does not effect the measurement of mean velocity or its fluctuation, it will change the measured vorticity, as the small-scale gradients are filtered.

The effect of interrogation window size on the measured eddy velocity U_θ is shown in Figure 6.11. As the resolution improves, the magnitude of the eddy velocity decreases, as

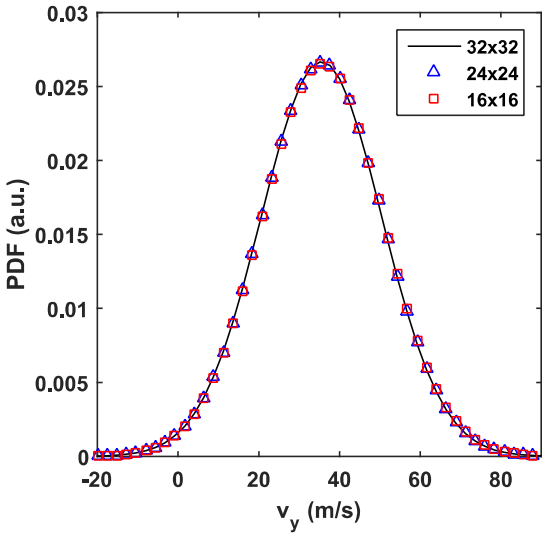

Figure 6.10: PDF's of the x-component of velocity for Case 3b with PIV interrogation box sizes of 32x32 pixels, 24x24 pixels, and 16x16 pixels.

smaller (slower moving) scales are added to the statistics. However, there is little change between the two smallest interrogation box size, and Fig. 6.11 shows that the conclusions are not changed by using a smaller box. Note that the 16x16 box is sufficient to resolve the estimated size of the viscous scale λ_v (using the assumption from Buch and Dahm that $\lambda_v/\eta_k \sim 11.6$). However, the box size is still approximately 3 times the estimated Kolmogorov scale or, by the Nyquist sampling criterion, 6 times the minimum size necessary to resolve the Kolmogorov scale. The 16x16 window box could only be computed for Case 3b, due to reduced seeding density at the more turbulent run condition.

6.4 Conditional integral length scale measurements through the flame

From the results presented thus far, it appears that the incoming turbulence in the cold reactants ahead of the flame is not significantly attenuated as it passes through the higher temperatures of the preheat region. Measurements show both the turbulence levels u' and

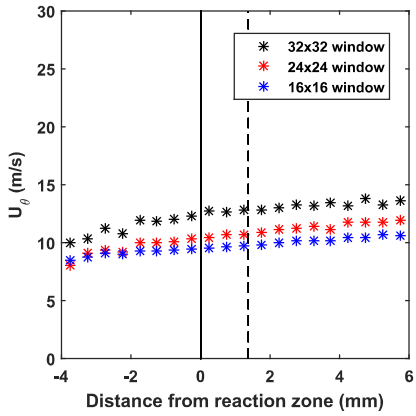

Figure 6.11: Variation of eddy velocity with interrogation window size

average eddy velocities U_θ that impinge on the flame surface are approximately the same as the upstream values. However, it is known that the large scale structures are dominant in determining the turbulence intensity, and scales of turbulence smaller than the Taylor scale λ_T do not contribute significantly to measured values of U or u'. [51, 118]. Therefore, if some dissipation of the finer-scales of turbulence occurs, it may not be detected by measurements of u', which are governed by large-scale phenomena.

In some DNS work [107, 108] fine-scale structures appear attenuated in broadened-preheat regimes. Also, it has been shown that most combustion events occur at the smallest turbulent scales [2]. Therefore, attenuation of these fine-scale elements could have implications for the ability of the turbulence to disrupt the flame chemistry. This may be an explanation for the inability of extreme turbulence to produce broken or distributed reactions at large Re_T.

The goal of this section is to measure the variation of the integral length scales through the flame. In doing so, we can then evaluate whether the smallest scales of the flow are attenuated. In addition, Chapter 5 has suggested that increased turbulent diffusivity may be essential in increased turbulent burning velocities in the Thin-Reaction, Broadened-Preheat regime. Because turbulent diffusivity scales as $D_T \sim u'L$, an increase in the integral length scale would support this result. In homogeneous, isotropic turbulence (HIT), the integral

length scale can be computed from the autocorrelation function, measured at a single point in the flow field. The autocorrelation function was defined in Section 2.3.3.1 and is written as:

$$R_u(\Delta x \Delta r) = \frac{\overline{u'(x,r)\,u'(x+\Delta x, r+\Delta r)}}{\sqrt{\overline{u'(x,r)^2}}\sqrt{\overline{u'(x+\Delta x, r+\Delta r)^2}}} = \frac{\overline{u'(x,r)\,u'(x+\Delta x, r+\Delta r)}}{u'^2_{rms}} \tag{6.2}$$

In HIT, the integral of the autocorrelation function has a precise physical meaning corresponding to the average size of the energy-containing eddies - the integral length scale L. If we can measure the integral length scale in the products, the preheat layer, and in the cold flow upstream, we can then conclude how much, if at all, the smallest scales are attenuated. If the smallest eddies disappear, the integral must increase to some degree.

However, attempting to compute an integral length scale in a flame raises some important questions. Due to changes in gas composition, temperature, and velocity throughout the combustion region, the flow will not be homogeneous or isotropic. Eqn. 6.2 defines R_u at a single point (x,r) for all possible separation distances Δ in the x and r directions. However, if the autocorrelation is measured at a single point, it will be located in a preheat layer in only a fraction of the images, and it may occur at any distance from the edge. Thus, it is difficult to get a measure of the integral scale in the preheat layer using this method because the measured region is not homogeneous. In order to probe a region of the flow that is relatively homogeneous, the autocorrelation in the preheat layer was computed at the point corresponding to the center of the instantaneous formaldehyde PLIF image. Likewise, the measurement in the cold flow will be computed at the point that is furthest from both the formaldehyde edge and the edge of the measurement domain. That is, in the preheat layer the measurement point will be taken in the center of the largest region of formaldehyde PLIF signal, and likewise in the cold region and in the products. This is illustrated schematically in Fig. 6.12.

Therefore, this work computes the autocorrelation at a different point (x,r) in each

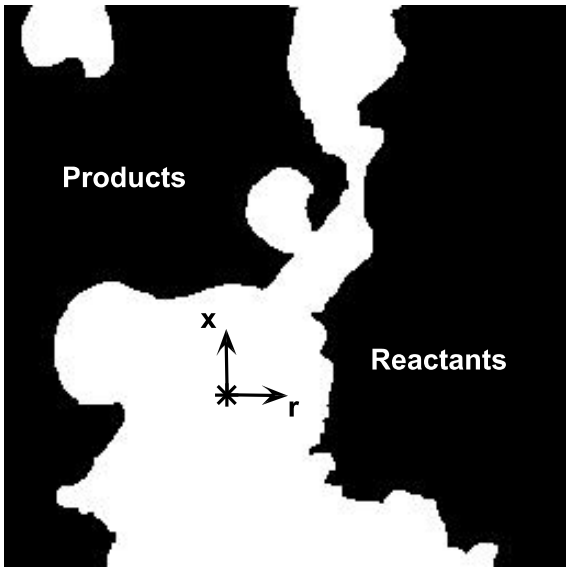

Figure 6.12: Example of identification of the measurement location (x, r) in the conditional autocorrelation measurement for an instantaneous image. The white region is the preheat zone, and the products and reactants are labeled accordingly. The autocorrelation R_{tt} is integrated in the x and r directions, which are shown on the figure.

image. The autocorrelation R_u is computed in the products, reactants, and cold region, respectively, for all images in the data set, and the ensemble average is calculated. Integral length scales are computed in the standard way by fitting an exponential function and integrating to the first zero crossing. Thus, the computation of the autocorrelation R_u is the same, except the reference point (x, r) is varied in each image. The implicit assumption in this measurement is that the turbulence levels and integral scales of the non-reacting flow do not vary significantly over the measurement domain. The velocity measurements of Section 3.2.2 showed that the turbulence conditions are approximately constant over small regions, and the field of view here is less than 10 mm, which permits this assumption.

It should be noted that this measurement is not precisely a spatial autocorrelation, which by definition requires the computation at a single point over all data sets (i.e., the correlation of a single point with its surroundings). Rather, this is a conditional autocorrelation, conditioned on the maximum thickness of a scalar quantity in an image. Therefore, the measured length scale is not equivalent to the integral length scale; it is instead defined as a conditional integral length scale.

Figure 6.13 below illustrates the autocorrelation measured in the standard way, and the method used here, which is labeled as a roaming method in the legend. Although the measurement is less smooth, the conditioned autocorrelation is similar in shape, and the resulting integral length scale is approximately the same. Note that the lateral scale typically decays much nearer to zero, while the longitudinal scale is only resolved to $R_{uu} \sim 0.3 - 0.5$. Thus, extrapolation (performed using exponential fitting) must be done to obtain integral length scales. This procedure introduces some level of uncertainty in the measured length scales. All of the measured conditional autocorrelations are fit with a multiple-term Gaussian function, and the fit is varied until the 95% confidence band around the function is minimized. The uncertainty of the measured values will be discussed in Section 6.4.2.

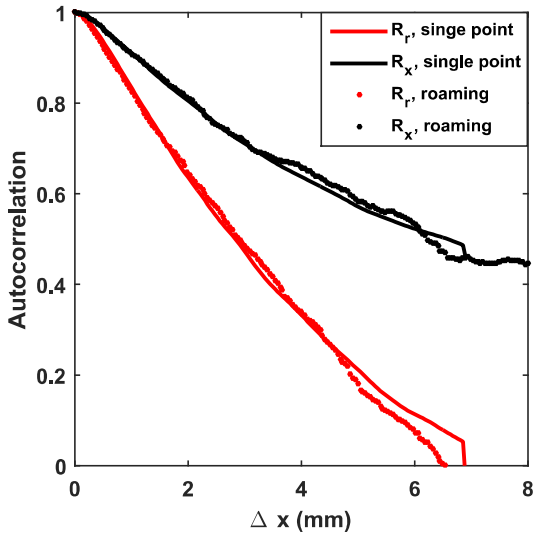

Figure 6.13: Autocorrelation, computed in the standard way (solid line) and using the roaming point method (dots)

6.4.1 Conditional integral length scale results

The conditional integral length scales were measured for Cases 3b and 4b using the techniques described above. For this discussion, the conditionally sampled measurements in the unburnt reactants upstream of the preheat layer will be called the 'cold' measurements. This distinguishes the measurement from the preheat layer and product regions. Note that this does not imply non-reacting flow, merely the cold region of reactants upstream of the flame. Fig. 6.14 displays the autocorrelation R_u in the x-direction (that is, $R_u(\Delta x, \Delta r = 0)$) for Case 3b in the cold flow, preheat layer, and products. The profiles indicate that at the edge of the measurement domain, the autocorrelation function is largest in the conditionally sampled preheat measurements, while it has decayed most rapidly in the cold flow. It is interesting to observe that the profiles of R_u have a similar shape in the products and in the cold flow, but different in the preheat layer. The autocorrelation drops below 0.8 faster in the preheat layer than either the products or the cold flow, however the turbulence remains approximately correlated ($R_u \sim 0.5$) over a wider range.

The autocorrelation profiles in the x and r directions were fitted with Gaussian functions

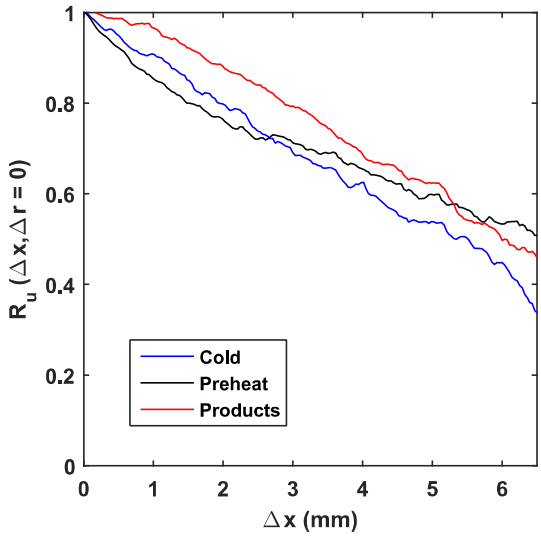

Figure 6.14: Longitudinal profiles of the conditional spatial autocorrelation R_u for Case 3b. Blue is conditionally measured in the cold flow upstream of the preheat layer, black is measured in the preheat layer, and red is measured in the products.

and integrated. The results are given in Figure 6.15, where L_x and L_r have been combined using the hydraulic diameter (Eqns. 3.5-3.6). The results are plotted against η, similar to the profiles from Fig. 6.4. Note that in order to obtain the value for η in the products, preheat layer, and cold flow, the average distance to an edge was determined from the data set. Here, 'edge' refers to the reaction layer in the products, and the formaldehyde edge in the preheat layer and cold flow. For the products and preheat measurements, this value was taken as η. For the cold flow, this value was added to the mean preheat layer thickness.

The value for L_{HD} in the cold region was approximately 4 mm for Case 3b and 4b, which is very close to the measured value of 4.7 mm reported in Table 3.1. The measured integral scales are slightly smaller here due to the restricted field of view. However, although the magnitude of L_{HD} is aliased toward smaller values, the change is not large. Therefore, the measurement should be capable of accurately capturing the integral scale variation through the flame.

Fig. 6.15 shows that the conditional integral scale grows as the flow approaches the flame, and decreases slightly in the products. This is consistent with the profiles of R_u

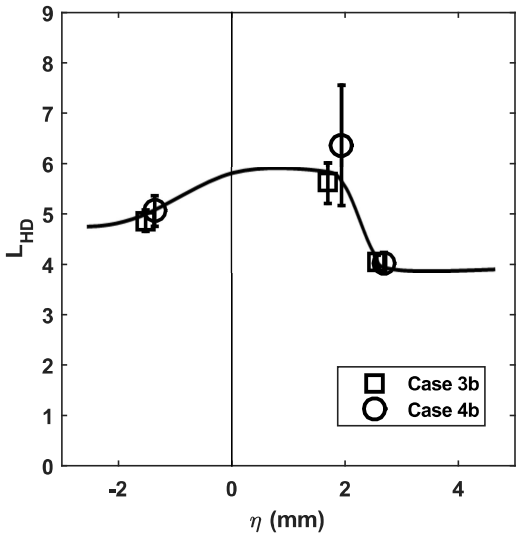

Figure 6.15: Integral length scale measurement in the cold flow (left) and the preheat zone (right)

given in Fig. 6.14. Although the magnitude of the change is not large (both run conditions demonstrate approximately a 50% increase in L_{HD} in the preheat layer), this implies that the small scales of turbulence are dissipated in the broadened preheat layers. This also supports the observation that the turbulent diffusivity should increase in the broadened preheat layers, which was suggested by the burning velocity results. Therefore, this appears to be an explanation of how the turbulence cannot perturb the reaction zone structure, despite Kolmogorov scales substantially smaller than the reaction layer thickness.

6.4.2 Uncertainty in the conditional integral length scale measurements

There are two general sources of uncertainty in the measured conditional integral length scales: the random deviations of the autocorrelation function R_u that arise due to the computation method; and the uncertainty in the Gaussian fit that is applied to the data, including the extrapolation to zero. The random error associated with the computation method was assessed by comparing the conditional integral length scale with the a computation of the integral scale performed in the standard way, i.e. computing R_u at a single point in the im-

age. To do so, a non-reacting data set was examined, and R_u was computed at a single point. The measurement was then repeated, but with R_u computed from a random point (x, r) in each image. The result of this procedure was given previously in Fig 6.13, where the lateral and longitudinal profiles of R_u are shown using these two methods. The results showed that while the conditional measurement generally overlaps with the traditional autocorrelation, there is scatter above and below at large separation distances Δ. The reason for this error is the lower number of samples at large separation distances. When R_u is computed at a single point, all separation distances Δ within the field of view will yield the same number of data points; however, when the interrogation point (x, r) moves randomly, the point will be in the center of the domain some fraction of the time, and near the domain boundary at other times. This produces a maximum separation distance Δ_{max} that varies depending on (x, r), and therefore a decreasing number of samples as the separation is increased. The result of this is noise near the edges of the domain as the sample size decreases. The regions of low sample sizes were eliminated from the profiles of R_u, so that the remaining autocorrelation is relatively smooth. This typically corresponded to removing approximately the final 20 separation points Δ in a data set consisting of 236 points. The random error of the conditional autocorrelation R_u was not assessed, because it was much smaller than the uncertainty associated with the Gaussian fit of the data.

The conditional autocorrelation functions were fit with Gaussian functions. In order to quantify the uncertainty of the fit, multiple functions were attempted for each autocorrelation. Gaussian functions consisting of two, three, four, or five terms were fit to the data, and only the resulting curves that decayed smoothly to zero were considered. The uncertainty of the fit was assessed by integrating each profile and then comparing the resulting largest and smallest conditional integral scales. This range is estimated to represent the possible variation of the true conditional integral length scale. The value for L_x and L_r in Fig. 6.15 is halfway between the largest and smallest values obtained using the different fitting functions. The minimum uncertainty in the fit occurred in the cold flow where R_u

typically decayed much closer to zero, and varied between 1% and 10%. The uncertainty is largest in the preheat layer where the conditional autocorrelation is largest, and therefore the Gaussian fit must extrapolate over a larger region. The uncertainty in the preheat regions varied between 10% and 26%

6.4.3 Turbulent kinetic energy spectrum

The results presented thus far suggest that although there is little change in the turbulence level u' approaching the flame, the smallest scales of turbulence may be dissipated through the broadened preheat layers. However, the dissipation of the small scales is only shown indirectly from the conditional integral scale measurements discussed in Section 6.4.1. To explore this mechanism more fully, turbulent kinetic energy spectra were analyzed for Case 3b in the preheat layer and in the cold flow upstream. Recall that the interrogation box size for analysis in previous sections (32x32 pixels) was coarser than the expected size of the smallest scales. Therefore, a higher resolution interrogation box size of 16x16 pixels was used. However, this was still slightly larger than one-half of the expected size of the viscous scale, which is the requirement to fully resolve the flow (here $\Delta_{PIV} = 3\eta_k \sim 0.62\lambda_v$). Thus, by the Nyquist sampling criterion, we cannot resolve the smallest scales.

Figure 6.16 illustrates the distribution of turbulent kinetic energy across the wavenumber k. The energy spectrum is normalized by the area under the curve, which is equal to the rms velocity u'^2. Almost all scales occur in the inertial range of turbulence, which is to be expected given the small field of view. Note that domain length is approximately 9.2 mm and the measurement can only resolve one-half of that scale (4.6 mm). However, the expected integral scale is expected to be greater than 5 mm (see Section 3.2.3). The interrogation box size of the PIV measurements corresponds to a wavenumber of $k = 44$, and all scales up to this value of k are resolved. Although scales corresponding to wavenumber $k > 44$ are computed due to the 75% overlap used in vector calculations, they are not fully resolved due to the averaging process inherent to the PIV method. A top-hat filter of the

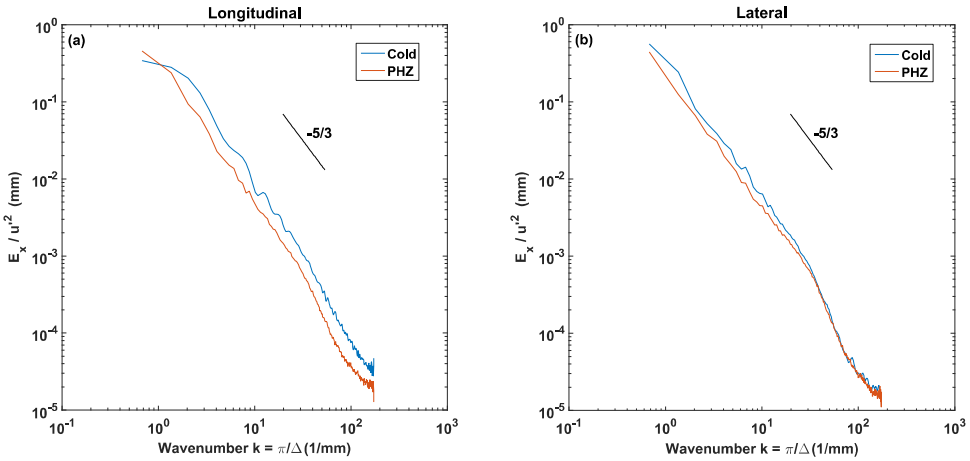

Figure 6.16: Turbulent kinetic energy in the (a) longitudinal and (b) lateral direction. Energy spectra are normalized by the square of the rms velocity in the cold flow and preheat regions, respectively.

size of the interrogation window was applied to processed vectors in order to eliminate high frequency noise.

It is observed in Fig. 6.16 that for most wavenumbers the shape of the spectrum is approximately the same in the cold flow and the preheat zone. The lateral spectra converge for $k > 25$, although the spectrum taken in the cold flow is shifted up slightly from the measurement in the preheat layer for lower k. However, the longitudinal energy spectra in the preheat layer and the cold flow upstream have a very different shape at low wavenumber, which corresponds to the large scales of the flow. The longitudinal spectra in the cold flow and the preheat layer indicate a change in slope for $k < 3$, indicating the start of the inertial range. However, the cold flow bends much more sharply, and is nearly horizontal for $k \sim 1$. The integral length scale cannot be obtained from the turbulent kinetic energy spectra given in Fig. 6.16, due to the limited range of scales imposed by the small field of view. However, it is clear the inertial range begins at larger k in the cold flow as compared to the preheat layer. In the cold flow upstream, it appears that the inertial range starts for $k = 1 - 2$, while in the preheat layer it begins at some value of k less than 0.6. This implies that the integral

length scale is larger in the preheat zone, because the start of the inertial range marks the end of the energy-containing range of scales. This result suggests that dissipation of the smallest eddies is occurring, and supports the conditional integral scale measurements discussed previously.

6.4.4 Evolution of the dissipative structures

Kinetic energy dissipation occurs predominantly in sparsely packed, layer-like structures. The dissipation structures are generally long and thin with a cross-sectional thickness that is very close to the strain-limited vorticity diffusion scale, called the viscous scale λ_ν [128]. These structures therefore correspond to fine scale elements in the flow, and they might be expected to grow larger if dissipation of small-scale features is occurring. Therefore this may provide another measurement of the hypothesis that the small-scale eddies are being attenuated.

In order to measure the fine-scale structures, the dissipation of kinetic energy was computed from the 2-D PIV vectors. Because any terms in the kinetic energy dissipation equation involving the vector normal to the plane of the laser sheet cannot be measured, a two-dimensional analog is derived following Tsurikov and Clemens [128], which is given below in Eqn. 6.4. Note that although $\partial w/\partial z$, cannot be directly measured, it is obtained by applying mass conservation, $\partial w/\partial z = -\partial u/\partial x - \partial v/\partial y$.

$$\epsilon = 2\nu\left[\left(\frac{\partial u}{\partial x}\right)^2 + \left(\frac{\partial v}{\partial y}\right)^2 + \left(\frac{\partial w}{\partial z}\right)^2 + \frac{1}{2}\left(\frac{\partial u}{\partial x} + \frac{\partial v}{\partial y}\right)^2 + \frac{1}{2}\left(\frac{\partial u}{\partial z} + \frac{\partial w}{\partial x}\right)^2 + \frac{1}{2}\left(\frac{\partial v}{\partial z} + \frac{\partial w}{\partial y}\right)^2\right] \quad (6.3)$$

Table 6.1: Estimated values of ν in the cold flow, preheat layer, and products

Region	T (K)	$\nu\ (m^2/s)$
Cold flow	300	15.68e-6
Preheat layer	850	90.61e-6
Products	1900	323.4e-6

$$\begin{aligned}\epsilon_{2D} &= 2\nu\left[\left(\frac{\partial u}{\partial x}\right)^2+\left(\frac{\partial v}{\partial y}\right)^2+\left(\frac{\partial w}{\partial z}\right)^2+\frac{1}{2}\left(\frac{\partial u}{\partial x}+\frac{\partial v}{\partial y}\right)^2\right] \\ &= 2\nu\left[\left(\frac{\partial u}{\partial x}\right)^2+\left(\frac{\partial v}{\partial y}\right)^2+\left(-\frac{\partial u}{\partial x}-\frac{\partial v}{\partial y}\right)^2+\frac{1}{2}\left(\frac{\partial u}{\partial x}+\frac{\partial v}{\partial y}\right)^2\right]\end{aligned} \tag{6.4}$$

Only Case 3b was selected for analysis, as Case 4b had much coarser resolution of the small scales. As for the turbulent energy spectra, a smaller interrogation window of 16x16 pixels was used. The viscous length scale is estimated to be approximately 110 μm for this case, and the PIV spatial resolution is 72 μm. Thus, though there may be resolution limits introduced in the measurement, it should be sufficient to indicate any changes in the dissipative structures before and after passage through the preheat layer. Structure thicknesses are measured by finding the skeleton of each element, which is facilitated by the layer-like shape. The nearest structure edge from each skeleton point is found, the array is averaged, and multiplied by two to provide the layer thickness. The kinematic viscosity ν in Eqn. 6.4 poses a challenge, since it is expected to change by over an order of magnitude from the reactants to the products. It was handled by digitizing the domain according to cold flow upstream of the preheat layer, the preheat layer, and the products region. The assumptions for temperature in these regions, and therefore ν, are given in Table 6.1.

The resulting PDF's of structure size are presented below in Fig. 6.17. The mean dissipation element is 138.2 μm in the reactants upstream of the preheat layer, and increases to 139.6 μm in the preheat zone. The change in layer thickness between the two regions is not outside of the measurement uncertainty, and therefore we cannot conclusively say

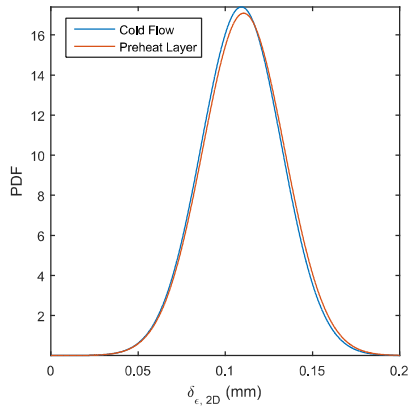

Figure 6.17: PDF's of dissipation structures

that the measurement shows that the small scale eddies are being attenuated. Nonetheless, the measurement appears to suggest that there is some dissipation of the finer scales of turbulence.

6.5 Discussion of results

This thesis has reported a very large variation of turbulence conditions in the Hi-Pilot burner; u' was varied by a factor of 20 from 2 m/s to 40 m/s, and Karlovitz and Reynolds numbers were as high as $Ka_T = 503$ and $Re_T = 99,000$. However, despite these extreme conditions, the thickness of the reaction layers remain approximately unchanged, as was verified with both CH PLIF and the overlap of OH and CH_2O PLIF. The conditional integral scale measurements showed that the smaller scales of turbulence may disappear in the very broad preheat layers, but the turbulence level u' is determined by the large eddies in the flow that remain present. Therefore u' is not attenuated in the thick preheat layers, as described in Section 6.3, despite the possible attenuation of small eddies. This means that the high-temperature chemical reactions are strong enough to resist broadening from turbulence levels at least as large as 40 m/s, which conflicts with previous predictions by Peters and others.

To resolve this discrepancy, we can speculate that the strength of the reaction zone is the characteristic velocity u^*, which is:

$$u^* = D_{OH}/\delta_{RZ} \tag{6.5}$$

Where D_{OH} is the diffusivity of the major radical in the reaction zone, OH, at 2,200 K, which is approximately 3 cm^2/s. The turbulent reaction zone thickness was shown in Chapter 4 $0.6\,mm < \delta_{RZ} < 1\,mm$. Similarly, we can define the velocity fluctuation at the scale of the reaction zone as:

$$u'_{RZ} = u'(\delta_{RZ}/L_x)^{1/3} \tag{6.6}$$

The integral scale may be approximately 30 mm for the most turbulent Hi-Pilot test cases. It is often assumed that the reaction zone thickness is an order of magnitude smaller than the preheat layer, that is $\delta_F = \delta_{RZ} + \delta_{PHZ}$ and $\delta_{RZ} = 0.1\delta_F$. We will also make a simplification for the flame thickness, and re-write D_{OH} as:

$$\delta_F = \alpha_0/S_L \tag{6.7}$$

$$D_{OH} = (D_{OH}/\alpha_0)\alpha_0 \tag{6.8}$$

Where $\alpha_0 = 0.15\,cm^2/s$. We can then speculate that the criterion for broadening of the reaction zone begins when

$$u'_{RZ} > u^* \tag{6.9}$$

Combining equations 6.5-6.8 and substituting into 6.9, we have the critical turbulence intensity required to disrupt the flame chemistry:

$$u'/S_L > \left(\frac{D_{OH}}{\alpha_0}\right)\left(\frac{\delta_{RZ}}{\delta_F}\right)^{-1}\left(\frac{\delta_{RZ}}{L}\right)^{-1/3}$$

Since the measured reaction layer thicknesses reported here vary between 0.6 and 1 mm, there is a range of possible values of the critical u'/S_L between 620 and 740, which is significantly larger than the most turbulent Hi-Pilot run conditions. Clearly this analysis only provides an order of magnitude estimate of the required turbulence intensity necessary for broken or distributed reactions. However, it suggests that the required value of u'/S_L is very large, and may be a factor of 6 greater than previous estimates by Peters.

6.6 Conclusions from the simultaneous PIV-PLIF measurements

The goal of this chapter was to determine to what extent the turbulence upstream of the flame is dissipated in the broadened preheat layers of the Hi-Pilot. To this end, conditional velocity statistics were obtained as a function of η, the local distance from the reaction zone. The measurements showed that the mean and fluctuating components of velocity are both essentially homogeneous through the region upstream of the preheat layer. The mean velocity was seen to decrease rapidly at approximately $\eta = \delta_{PHZ,T}$, indicating that the flame is positioned near the shear layer that lies between the main flow of reactants and the outer co-flow of hot products. However, the turbulence level u' did not change appreciably in the preheat zone, and only increased in the final 1 mm before the reaction zone, due to thermal expansion at the flame front. This indicates that the flame is not in fact in the shear layer, rather the shear layer is positioned immediately downstream of the flame. Therefore, although the shear layer affects the turbulence level just downstream of the flame, it does not affect the turbulence level that is upstream and is incident upon the flame. This was confirmed through measurement of the average eddy velocity U_θ, which indicated that no

significant decay in the eddy strength occurs in the preheat region of the flame.

Despite little change in the turbulence levels incident on the flame, measurements of the conditional integral length scale in the preheat layer and the cold flow upstream showed that some attenuation of the smallest turbulent scales may be occurring. Because u' is largely determined by the larger scales of the flow, this does not effect the magnitude of velocity fluctuations that interact with the flame surface. However, if the critical element in flame broadening or extinction depends on the strength of the smallest eddies of the flow, this preheat attenuation of the may be an important clue as to why broken layers are not observed in the Hi-Pilot.

The results of this chapter show that the turbulence issuing from the Hi-Pilot burner are essentially identical to the conditions impinging on the flame surface. Attenuation of the small scales of the flow may be one possible explanation as to why the very large turbulence levels are unable to modify the reaction layer structure. However, an alternative explanation may be that the reaction layer may be much more resilient to turbulent strain than previously understood. The reasoning requires consideration of the turbulent diffusivity of the limiting reactant in the high temperature reaction zone, which in this case may be the OH molecule. This analysis shows that the critical value of u'/S_L for broken reactions may be approximately 620, which is several times greater than the value predicted by Peters.

CHAPTER 7

Conclusions and Future Work

7.1 Summary

This work has explored various aspects of high Reynolds number combustion that have received much previous speculation. A new high-Reynolds number premixed Bunsen burner, called Hi-Pilot, was designed to produce turbulence intensities in the extreme range of turbulence. The burner was modified several times in order to prevent boundary layer separation in the nozzle, and a large co-flow was designed that was capable of maintaining reactions over the entire flame surface. Velocity and turbulence characteristics were measured using a combination of Laser Doppler Velocimetry and Particle Image Velocimetry.

Flame structure was studied using a combination of formaldehyde, OH, and CH Planar Laser Induced Fluorescence. The spatial Overlap of formaldehyde and OH PLIF qualitatively measures the reaction rate between formaldehyde molecules and OH radicals, and is a measure of the reaction layers of the flame. CH PLIF provides an alternative measure of the reaction zone, and was measured to compare with the Overlap PLIF results. Reaction layers are the full-width at half-maximum of the Overlap or CH PLIF signal, and extinction events were defined as regions where the PLIF signal drops below this threshold. Preheat structures were measured using formaldehyde PLIF, and are defined as beginning at 35% of the local maximum PLIF signal, and continue up to the leading edge of the reaction layer.

Previous predictions of regime diagram boundaries were tested at the largest values of

Re_T to date. The Klimov-Williams criterion for broadened preheat layers was evaluated using the preheat structure measurements, and the Overlap and CH PLIF diagnostics allowed extensive testing of the predicted broken reaction zones boundary of Peters. Several measures of the turbulent burning velocity, including the global consumption speed and the extent of flamelet wrinkling, were measured at these conditions. Reaction layers for the burning velocity measurements were provided by the OH PLIF. The flame structure and burning velocity measurements motivated the final part of this work, which measured the evolution of turbulence through regions of very thick preheat layers. This measurement utilized simultaneous PIV and formaldehyde PLIF in order to obtain conditioned statistics of the turbulence as a function of η, the distance from the reaction layer. Together, the results tell a consistent story, and deepen our understanding of premixed combustion at large Re_T.

7.2 Conclusions

The primary findings of this thesis are the following:

7.2.1 Flow and turbulence characterization

1. Laser Doppler Velocimetry measurements characterized the mean and fluctuating components of the axial velocity, and temporal autocorrelations and temporal integral scales τ were computed from the data. LDV data demonstrated the extreme turbulence of the Hi-Pilot burner, with turbulence levels u' approaching 40 m/s and turbulence intensities u'/U exceeding 35%. Due to the large turbulence, Taylor's hypothesis would underpredict the integral length scales; instead, a common correction to Taylor's hypothesis was applied assuming isotropic flow. Integral scales are found to be very large, ranging from 6 mm to 41 mm.

2. Particle Image Velocimetry measurements were performed to characterize the asymmetry in the turbulent structures (i.e., $u' \neq v'$), and to evaluate the accuracy of the cor-

rection to Taylor's hypothesis used in the LDV measurements. PIV results showed that the turbulence remains approximately homogeneous across the central ~80% of the jet within the first 20 mm of the jet exit. Significant anisotropy in both integral length scales and turbulence levels were observed, however the anisotropy did not change with turbulence level u'. The isotropic correction to Taylor's hypothesis utilized in the LDV data was found to be superior to Taylor's hypothesis alone. Taylor's hypothesis underpredicts the length scales by nearly 50%, while the isotropic correction can overestimate it by 35% for $u'/U > 30\%$. These results reinforce that single-component measurements of velocity are not ideal in highly turbulent flows.

7.2.2 Flame structure measurements and evaluation of regime boundaries

1. Flame structure measurements showed that the preheat layers became fully broadened as the turbulence level increased. Fully broadened preheat layers exist when all reactants are in the preheat region. The preheat layers increased with integral scale, and residence time effects were important as downstream regions exhibited greater thickening. The Klimov-Williams criterion for broadened preheat layers appears to be supported by experimental data in the Hi-Pilot, although the boundary cannot be conclusively tested in this work since no run conditions fall below the predicted boundary.

2. In contrast, the reaction layers did not show any significant variation in structure or thickness with increasing turbulence, and remained below two times the measured laminar thickness at all conditions. Based on these measurements, it is concluded that all Hi-Pilot run conditions fall in the broadened preheat-thin reaction layers regime.

3. A number of Hi-Pilot run conditions are well beyond the predicted boundary for broken reactions, yet the layers remain continuous. Peters predicts that broken reac-

tions will occur when the turbulent Karlovitz number $Ka_T = 100$. In this, work, Ka_T reaches 503, which indicates a problem with the theory of Peters.

4. The results show that flamelet sub-models can still be used for very large Re_T, as well as for $Ka_T > 100$, as the reaction layers retain their laminar structure throughout the measurement domain. This is an important finding that greatly expands the domain of flamelet models. However, it is noted that any model must be able to reproduce both the thin reaction layers and the broadened preheat layers seen in this experiment.

7.2.3 Turbulent burning velocity measurements

1. The global consumption speeds $S_{T,GC,1}$ and $S_{T,GC,2}$ were based on the flame area that is defined by the contours where $\overline{c}_{OH}$ was 0.5 and 0.2, respectively. $\overline{c}_{OH}$ is the progress variable of OH defined in section 2.4.2. Measurements were performed for turbulence intensities up to $u'/S_L = 163$, which is more than six times that of the most turbulent study prior to this work. The results showed that the global consumption speeds continued to increase at all conditions, despite some predictions that the burning velocity would plateau in extreme turbulence due to extensive flamelet merging. However, significant bending in the consumption speeds was observed in the range of extreme turbulence, $u'/S_L > 25$, where the consumption speed became less sensitive to turbulence intensity..

2. Several measures of the flame surface wrinkling A_T/A_L were performed, including the integral of flame surface density $\int \Sigma d\eta$ and the direct computation of A_T/A_L. The results show that the flame surface area rapidly increases to approximately 4-5 times the laminar value, but becomes insensitive to further increases in u'/S_L. This implies that there is a limit to how much flamelet wrinkling can occur, and beyond this point flame surface destruction (through flamelet merging, for example) will counteract any further wrinkling.

3. The global consumption speed continues to increase with turbulence level, despite the fact that the flame surface area remains constant. This indicates that the local consumption rate of the exothermic layers must be enhanced. This corresponds to Damköhler's second hypothesis, and may be an explanation for the large scale bending observed in the global consumption speed profiles. This is because the burning velocity was predicted by Damköhler to scale as $S_T/S_L \sim \sqrt{D_T} \sim \sqrt{u'L}$, where D_T is the turbulent diffusivity. These results agree well with other experimental data, however there is some discrepancy with DNS that may be due to the different integral length scales used in the simulations, highlighting the importance of Reynolds number.

4. A correlation for the turbulent burning velocity was developed that utilizes Damköhler's two hypotheses and is able to reproduce the experimental data. The model consists of the product of a flamelet wrinkling term, which is independent of length scales, and a turbulent diffusivity component that accounts for increases in the local consumption rate per unit area.

5. The flame structure measurements indicated that flamelet models would still be useful in the extreme range of turbulence ($u'/S_L > 25$), and this is confirmed by the burning velocity measurements. However, we note that there are two contributions to the burning velocity in this regime: increases in the area of the exothermic layers, and increases in the local consumption rate per unit area (which is proportional to the turbulent diffusivity). The former is typically modeled in the sub-grid scales of LES studies, and this approach should continue to be used. However, in order to obtain an accurate measure of the burning velocity, a model of the turbulent diffusivity must also be included, as this component becomes dominant at large Re_T once flame surface wrinkling has become saturated.

7.2.4 Conditioned velocity measurements through the flame

1. Conditional velocity statistics were obtained as a function of η, the local distance from the reaction zone. Measurements showed that the mean velocity U and the turbulence level u' were approximately constant in the region upstream of the preheat layer approaching the flame.

2. Inside the preheat zone, measurements showed that U decreased substantially beginning at approximately $\eta = \delta_{PHZ,T}$. However the turbulence level u' and turbulent kinetic energy $k = \frac{1}{2}u' + v'$ remained approximately constant throughout the preheat layer until the final 1 mm ahead of the reaction zone, where thermal expansion began to increase the turbulence level.

3. In the region downstream of the reaction zone, U continued to decrease at approximately the same gradient $dU/d\eta$. The turbulence level u' increased slightly in the near flame region ($-1 < \eta < 1$), but then decayed to its upstream value for Case 3b. For Case 4b, $u'$and k also increased over $-1 < \eta < 1$ due to the thermal expansion, but in the post-flame region the turbulence dropped more significantly. Because the turbulence levels do not change significantly until the post-flame region, it indicates that the shear layer lies just downstream of the flame brush, but it is relatively close to the downstream boundary of the flame. Thus the shear layer affects the turbulence level just downstream of the flame, but does not affect the turbulence level that is upstream and is incident upon the flame.

4. The average eddy velocity was computed by taking the product of the average vorticity of a vortical structure and its hydraulic diameter, $U_\theta = \overline{\omega} D_{HD}$. Conditioned measurements of U_θ as a function of η showed that the eddy velocity decreased slightly through the flame, but the magnitude of change is small. This result suggests that expansion of the eddies in the preheat gases does not significantly reduce the strength of the eddies impinging on the reaction layer.

5. The conditional integral length scale was computed in the products, the preheat layer, and in the cold flow upstream of the flame. Results indicate that the integral scales increase slightly in the preheat layer, which is presumably due to dissipation of the smallest scales of turbulence. Thus, although the turbulence level u' is not changing through the flame, it is primarily determined by scales of turbulence greater than the Taylor scale. However, predictions for the onset of broken reactions are conditional on the presence of small scale eddies (of size η_k) that disrupt the chemistry. These measurements show that the smallest scales of the flow may not survive through the elevated temperature and viscosity of the preheat layer. Therefore, this is a possible explanation for the flame structure measurements discussed in Chapter 4.

6. Lastly, it is theorized that the reaction layer may be much more resilient to turbulent strain than previously expected. The reasoning is the consideration of the turbulent diffusivity of the limiting reactant, which in this case may be the OH molecule. This analysis shows that the critical value of u'/S_L for broken reactions is approximately 620, which is 6.2 times greater than predicted by Peters. This is an additional possible explanation for the lack of broken reactions observed in the extreme turbulence levels of this experiment.

7.3 Future Work

This work marks the first experimental study of premixed combustion in the Bunsen geometry at large Re_T. Therefore, it is not surprising that many important research questions remain unanswered. For instance, the DNS community and some experiments have demonstrated the possibility for broken and distributed reactions, but these have been confined to extremely small geometries ($L/\delta_{F,L} < 10$). It remains unknown what values of Ka_T and Re_T are required in order to produce such flames, and they must be replicated at more realistic scales of turbulence. However, this work suggests that the necessary turbulence levels

to produce broken or distributed layers is very large, as $Ka_T = 503$ produced no change in reaction layer structure. Although the turbulent jet flames of Zhou et al [143,144] produced distributed zones for $Ka_T > 500$, it is noted that the geometry of shear-generated turbulence in such a small diameter jet is significantly different from a Bunsen flame, where all turbulence is generated within the reactants. Carryover between these different geometries is currently unknown and must be explored.

Future work should build on these results to construct a more accurate regime diagram. Such a diagram should have boundaries that are both grounded in theory and validated by experiment. An accurate diagram may require additional parameters that are commonly missing; such parameters include preheat temperature, residence time of the turbulence in the flame, and geometry of the turbulence-flame interaction. All measurements here were performed with methane-air reactants; it may be that the Lewis number, a chemistry parameter not captured by the equivalence ratio, has a significant effect. Indeed, the DNS work of Aspden et al [5] has shown that variations in Le in turbulent flames can produce large changes in flame structure and burning velocity. Future work should explore these effects.

Another open question is why DNS studies seem to show that the flame surface area continues to increase with turbulence, even up to $u'/S_L > 30$, while most experiments show that flame surface area A_T/A_L saturates for much lower turbulence. The DNS results report laminar flamelets, whose burning velocity is directly determined by the increase in flame surface area. Integral length scale is very important in this situation, because the turbulent diffusivity scales with $\sqrt{L}$. Therefore, the very small domains of the DNS may not be capable of producing a significant increase in the consumption rate per unit area that is seen in experiments due to their limited integral scales. It may be that the ability of turbulence to wrinkle a flame surface increases with the integral scale; for instance, the stretch efficiency of an eddy increases approximately logarithmically with integral scales [79]. Therefore, the small integral scales inherent to DNS studies may not be able to wrinkle the flame to

the saturation point that seems to occur for $A_T/A_L \sim 5$. A parametric study that measured the flame surface wrinkling parameter A_T/A_L over a range of turbulence intensities and integral scales, possibly by varying the burner diameter, could test this theory directly.

Bibliography

[1] R. G. Abdel-Gayed, Derek Bradley, and F. K K Lung. Combustion regimes and the straining of turbulent premixed flames. Combustion and Flame, 76(2):213–218, 1989.

[2] R.G. Abdel-Gayed and D. Bradley. A Two-Eddy Theory of Premixed Turbulent Flame Propagation. Philosophical Transactions of the Royal Society of London. Series A, Mathematical and Physical Sciences, 301(1457):1–25, 1981.

[3] Patton Manuel Allison. Experimental Characterization of Combustion Instabilities and Flow-Flame Dynamics in a Partially-Premixed Gas Turbine Model Combustor by. PhD thesis, 2013.

[4] G.E. Andrews, D. Bradley, and S.B. Lwakabamba. Turbulence and turbulent flame propagation: A critical appraisal. Combustion and Flame, 24:285–304, feb 1975.

[5] A J Aspden. A numerical study of diffusive effects in turbulent lean premixed hydrogen flames. Proceedings of the Combustion Institute, 36(2):1997–2004, 2017.

[6] A. J. Aspden, J. B. Bell, M. S. Day, and F. N. Egolfopoulos. Turbulence flame interactions in lean premixed dodecane flames. Proceedings of the Combustion Institute, 36(2):2005–2016, 2015.

[7] A. J. Aspden, M. S. Day, and J. B. Bell. Turbulence flame interactions in lean premixed hydrogen: transition to the distributed burning regime. Journal of Fluid Mechanics, 680:287–320, may 2011.

[8] A.J. Aspden, M.S. Day, and J.B. Bell. Lewis number effects in distributed flames. Proceedings of the Combustion Institute, 33(1):1473–1480, 2011.

[9] A.J. Aspden, M.S. Day, and J.B. Bell. Lewis number effects in distributed flames. Proceedings of the Combustion Institute, 33(1):1473–1480, 2011.

[10] B.O. Ayoola, R. Balachandran, J.H. Frank, E. Mastorakos, and C.F. Kaminski. Spatially resolved heat release rate measurements in turbulent premixed flames. Combustion and Flame, 144(1-2):1–16, jan 2006.

[11] R Balachandran, B Ayoola, C Kaminski, a Dowling, and E Mastorakos. Experimental investigation of the nonlinear response of turbulent premixed flames to imposed inlet velocity oscillations. Combustion and Flame, 143(1-2):37–55, oct 2005.

[12] B. Bedat and R. K. Cheng. Experimental Study of Premixed Flames in Intense Isotropic Turbulence. Combustion and Flame, 100:485–494, 1995.

[13] John B. Bell, Marcus S. Day, Joseph F. Grcar, Michael J. Lijewski, James F. Driscoll, and Sergei A. Filatyev. Numerical simulation of a laboratory-scale turbulent slot flame. Proceedings of the Combustion Institute, 31:1299–1307, 2007.

[14] L H Benedict, H Nobach, and C Tropea. Estimation of turbulent velocity spectra from laser Doppler data. Measurement Science and Technology, 11(8):1089–1104, aug 2000.

[15] R. W. Bilger, S. B. Pope, K. N C Bray, and J. F. Driscoll. Paradigms in turbulent combustion research. Proceedings of the Combustion Institute, 30(1):21–42, 2005.

[16] Stefan Böckle, Jan Kazenwadel, Thomas Kunzelmann, Dong-Ill Shin, Christof Schulz, and Jürgen Wolfrum. Simultaneous single-shot laser-based imaging of formaldehyde, OH, and temperature in turbulent flames. Proceedings of the Combustion Institute, 28(1):279–286, 2000.

[17] B. Böhm, D. Geyer, a. Dreizler, K.K. Venkatesan, N.M. Laurendeau, and M.W. Renfro. Simultaneous PIV/PTV/OH PLIF imaging: Conditional flow field statistics in partially premixed turbulent opposed jet flames. Proceedings of the Combustion Institute, 31(1):709–717, jan 2007.

[18] B. Böhm, C. Heeger, I. Boxx, W. Meier, and a. Dreizler. Time-resolved conditional flow field statistics in extinguishing turbulent opposed jet flames using simultaneous highspeed PIV/OH-PLIF. Proceedings of the Combustion Institute, 32(2):1647–1654, 2009.

[19] R Borghi. On the structure and morphology of turbulent premixed flames. Recent Advances in the Aerospace Sciences, pages 117–138, 1985.

[20] R Borghi. Turbulent combustion modelling. Progress in Energy and Combustion Science, 14:245–292, 1988.

[21] D. Bradley, A. K. C. Lau, and M. Lawes. Flame stretch rate as a determinant of turbulent burning velocity. Philosophical Transactions: Physical Sciences and Engineering, 338:359–387, 1992.

[22] K. N. C. Bray and R. S. Cant. Some applications of Kolmogorov's turbulence research in the field of combustion. Proceedings of the Royal Society A: Mathematical, Physical and Engineering Sciences, 434:217–240, 1991.

[23] K. N. C. Bray, P. A. Libby, Goro Masuya, and J. B. Moss. Turbulence Production in Premixed Turbulent Flames. Combustion Science and Technology, 25(3-4):127–140, 1981.

[24] K. A. Buch and W. J. A. Dahm. Experimental study of the fine-scale structure of

conserved scalar mixing in turbulent shear flows. Part 1. Sc>>1. Journal of Fluid Mechanics, 364(1998):1–29, 1998.

[25] K. A. Buch and W. J. A. Dahm. Experimental study of the fine-scale structure of conserved scalar mixing in turbulent shear flows. Part 2. Sc˜1. Journal of Fluid Mechanics, 364(1998):1–29, 1998.

[26] A Buschmann, F Dinkelacker, T Schafer, M Schafer, and J Wolfrum. Measurement of the Instantaneous Detailed Flame Structure in Turbulent Premixed Combustion. In Twenty-Sixth Symposium on Combustion/The Combustion Institute, pages 437–445, 1996.

[27] C D Carter, J M Donbar, and J F Driscoll. Simultaneous CH planar laser-induced fluorescence and particle imaging velocimetry in turbulent nonpremixed flames. Applied Physics B, 66:129–132, 1998.

[28] Campbell D. Carter, Stephen Hammack, and Tonghun Lee. High-speed planar laserinduced fluorescence of the CH radical using the C2Sigma X2Pi band. Applied Physics B, 116(3):515–519, jul 2014.

[29] Campbell D. Carter, Stephen Hammack, and Tonghun Lee. High-speed flamefront imaging in premixed turbulent flames using planar laser-induced fluorescence of the CH C-X band. Combustion and Flame, 168:66–74, 2016.

[30] Yung-Cheng Chen and Robert W. Bilger. Experimental investigation of threedimensional flame-front structure in premixed turbulent combustion. Combustion and Flame, 131:400–435, 2002.

[31] Yung-Cheng Chen and Robert W. Bilger. Experimental investigation of threedimensional flame-front structure in premixed turbulent combustion. Combustion and Flame, 138(1-2):155–174, jul 2004.

[32] Yung-cheng Chen and Robert W Bilger. Experimental Investigation of Three-Dimensional Flame- Front Structure in Premixed Turbulent Combustion I : Hydrocarbon Air Bunsen Flames. Combustion and Flame, 131:400–435, 2006.

[33] R K Cheng, I G Shepherd, B Bédat, and L. Talbot. Premixed turbulent flame structures in moderate and intense isotropic turbulence. Combustion Science and Technology, 174:29–59, 2002.

[34] N. T. Clemens and M. G. Mungal. A planar Mie scattering technique for visualizing supersonic mixing flows. Experiments in Fluids, 11(2-3):175–185, 1991.

[35] Noel T. Clemens. Flow Imaging. pages 390–419.

[36] G. Damkohler. Der Einflu_ der Turbulenz auf die Flammengeschwindigkeit. Z.

Elektrochem, 46:601–652, 1940.

[37] Sulabh Kumar Dhanuka. An experimental study of the stable and unstable operation of an LPP gas turbine. 2008.

[38] F Dinkelacker, A Soika, D Most, D Hofmann, A Leipertz,WPolifke, and K Dobbeling. Structure of locally quenched highly turbulent lean premixed flames. Twenty-Seventh Symposium (International) on Combustion/The Combustion Institute, pages 857–865, 1998.

[39] Jeffrey M. Donbar, James F. Driscoll, and Campbell D. Carter. Reaction zone structure in turbulent nonpremixed jet flames from CH OH PLIF images. Combustion and Flame, 122(1-2):1–19, jul 2000.

[40] J. F. Driscoll and A. Gulati. Measurement of various terms in the turbulent kinetic energy balance within a flame and comparison with theory. Combustion and Flame, 72(2):131–152, 1988.

[41] James F Driscoll. Turbulent premixed combustion: Flamelet structure and its effect on turbulent burning velocities. Progress in Energy and Combustion Science, 34(1):91–134, feb 2008.

[42] J. M. Duclos, D. Veynante, and T. Poinsot. A comparison of flamelet LES models for premixed turbulent combustion. Combustion and Flame, 95(January):101–117, 1993.

[43] Matthew J. Dunn, Assaad R. Masri, and Robert W. Bilger. A new piloted premixed jet burner to study strong finite-rate chemistry effects. Combustion and Flame, 151(1-2):46–60, oct 2007.

[44] M.J. Dunn, a.R. Masri, R.W. Bilger, R.S. Barlow, and G.-H. Wang. The compositional structure of highly turbulent piloted premixed flames issuing into a hot coflow. Proceedings of the Combustion Institute, 32(2):1779–1786, 2009.

[45] Alan C. Eckbreth. Laser diagnostics for combustion temperature and species.

[46] EIA. Electric Power Monthly: with data for January 2015. U.S. Energy Information Administration, (August), 2015.

[47] a. Fayoux, K. Zähringer, O. Gicquel, and J.C. Rolon. Experimental and numerical determination of heat release in counterflow premixed laminar flames. Proceedings of the Combustion Institute, 30(1):251–257, jan 2005.

[48] Sergei A Filatyev, James F Driscoll, Campbell D Carter, and Jeffrey M Donbar. Measured properties of turbulent premixed flames for model assessment, including burning velocities, stretch rates, and surface densities. Combustion and Flame,

141:1–21, apr 2005.

[49] Jonathan H Frank, Peter A M Kalt, and Robert W Bilger. Measurements of Conditional Velocities in Turbulent Premixed Flames by Simultaneous OH PLIF and PIV. 232(1999):220–232, 2006.

[50] C. A. Friehe, C. W. Van Atta, and C. H. Gibson. Jet turbulence: dissipaiton rate measurements and correlations. AGARD Turbulent Shear Flows1, pages 1–7, 1971.

[51] Mirko Gamba and Noel Clemens. Requirements, Capabilities and Accuracy of Time-Resolved PIV in Turbulent Reacting Flows. 49th AIAA Aerospace Sciences Meeting including the New Horizons Forum and Aerospace Exposition, (January):1–32, 2011.

[52] Carlos M. García and Marcelo H. García. Characterization of flow turbulence in large-scale bubble-plume experiments. Experiments in Fluids, 41(1):91–101, 2006.

[53] F. C. Gouldin. An application of fractals to modeling premixed turbulent flames. Combustion and Flame, 68(3):249–266, 1987.

[54] X. J. Gu, M. Z. Haq, M. Lawes, and R. Woolley. Laminar burning velocity and Markstein lengths of methane-air mixtures. Combustion and Flame, 121(1-2):41–58, 2000.

[55] Anil Gulati and James F Driscoll. Velocity-Density Correlations and Favre Averages Measured in a Premixed Turbulent Flame. Combustion Science and Technology, 48(5-6):285–307, 1986.

[56] Ö.L. Gülder, G.J. Smallwood, R. Wong, D.R. Snelling, R. Smith, B.M. Deschamps, and J.-C. Sautet. Flame front surface characteristics in turbulent premixed propane/air combustion. Combustion and Flame, 120(4):407–416, mar 2000.

[57] Omer L. Gulder and Gregory J. Smallwood. Flame surface densities in premixed combustion at medium to high turbulence intensities. Combustion Science and Technology, 179:191–206, 2007.

[58] W. H. Harch and S. C. Favaloro. A time interval sampling method for the removal of velocity bias in LDV measurements in turbulent flows.pdf. In 9th Australasian Fluid Mechanics Conference, pages 541–544, 1986.

[59] Gunnar Heskestad. A Generalized Taylor Hypothesis with Application for High Reynolds Number Turbulent Shear Flows. Journal of Applied Mechanics, 32(4):735–739, 1965.

[60] J. O. Hinze. Turbulence. 2nd edition, 1975.

[61] J. Kariuki, a. Dowlut, R. Yuan, R. Balachandran, and E. Mastorakos. Heat release imaging in turbulent premixed methane-air flames close to blow-off. Proceedings of the Combustion Institute, 35(2):1443–1450, 2014.

[62] J. Kiefer, Z.S. Li, J. Zetterberg, X.S. Bai, and M. Aldén. Investigation of local flame structures and statistics in partially premixed turbulent jet flames using simultaneous single-shot CH and OH planar laser-induced fluorescence imaging. Combustion and Flame, 154(4):802–818, sep 2008.

[63] Hideaki Kobayashi, Katsuhiro Seyama, Hirokazu Hagiwara, and Yasuhiro Ogami. Burning velocity correlation of methane-air turbulent premixed flames at high pressure and high temperature. Proceedings of the Combustion Institute, 30:827–834, 2005.

[64] H. Kolla, J. W. Rogerson, and N. Swaminathan. Validation of a Turbulent Flame Speed Model across Combustion Regimes. Combustion Science and Technology, 182(3):284–308, 2010.

[65] Fridolin Krausmann, Simone Gingrich, Nina Eisenmenger, Karl Heinz Erb, Helmut Haberl, and Marina Fischer-Kowalski. Growth in global materials use, GDP and population during the 20th century. Ecological Economics, 68(10):2696–2705, 2009.

[66] Suzanne M. Kresta and Philip E. Wood. The flow field produced by a pitched blade turbine: Characterization of the turbulence and estimation of the dissipation rate. Chemical Engineering Science, 48(10):1761–1774, 1993.

[67] Kenneth K. Kuo. Principles of Combustion. 2005.

[68] LaVision. FlowMaster Manual. 2016.

[69] P. Lavoie, G. Avallone, F. De Gregorio, G. P. Romano, and R. A. Antonia. Spatial resolution of PIV for the measurement of turbulence. Experiments in Fluids, 43(1):39–51, 2007.

[70] Chung K Law. Combustion Physics.

[71] Z.S. Li, B. Li, Z.W. Sun, X.S. Bai, and M. Aldén. Turbulence and combustion interaction: High resolution local flame front structure visualization using simultaneous single-shot PLIF imaging of CH, OH, and CH2O in a piloted premixed jet flame. Combustion and Flame, 157(6):1087–1096, jun 2010.

[72] a. N. Lipatnikov and J. Chomiak. Molecular transport effects on turbulent flame propagation and structure. Progress in Energy and Combustion Science, 31:1–73, 2005.

[73] E. Mallard and HL Le Chatelier. Thermal model for flame propagation. Annales des Mines, 1883.

[74] B. B. Mandelbrot. On the geometry of homogeneous turbulence, with stress on the fractal dimension of the iso-surfaces of scalars. Journal of Fluid Mechanics, 72(03):401, 2006.

[75] Mohy S. Mansour, Norbert Peters, and Yung-Cheng Chen. Investigation of scalar mixing in the thin reaction zones regime using a simultaneous CH-LIF/Rayleigh laser technique. Symposium (International) on Combustion, 27:767–773, 1998.

[76] A. Marshall, P. Venkateswaran, D. Noble, J. Seitzman, and T. Lieuwen. Development and characterization of a variable turbulence generation system. Experiments in Fluids, 51(3):611–620, apr 2011.

[77] W. T. Mayo. A discussion of limitations and extentions of power spectrum estimation with burst-counter LDV systems. In Proceedings of the International Workshop on Laser Velocimetry, 1974.

[78] A Melling. Tracer particles and seeding for particle image velocimetry. Measurement Science and Technology, 8:1406–1416, 1997.

[79] C. Meneveau and T. Poinsot. Stretching and Quenching of Flamelets in Premixed Turbulent Combustion. Combustion and Flame, 86:311–332, 1991.

[80] Fernand Meyer. Topographic distance and watershed lines. Signal Processing, 38(1):113–125, 1994.

[81] Charles J. Mueller, James F. Driscoll, David L. Reuss, Michael C. Drake, and Martin E. Rosalik. Vorticity generation and attenuation as vortices convect through a premixed flame. Combustion and Flame, 112(3):342–358, 1998.

[82] H. N. Najm, O. M. Knio, P. H. Paul, and P.S.Wyckoff. A Study of Flame Observables in Premixed Methane - Air Flames, volume 140. dec 1998.

[83] Habib N Najm, Phillip H Paul, Charles J Mueller, and Peter S Wyckoff. On the Adequacy of Certain Experimental Observables as Measurements of Flame Burning Rate. Combustion and Flame, 113(3):312–332, may 1998.

[84] Zacharias M. Nikolaou and Nedunchezhian Swaminathan. Heat release rate markers for premixed combustion. Combustion and Flame, 161(12):3073–3084, dec 2014.

[85] Girish V Nivarti and R Stewart Cant. Direct Numerical Simulation of the Bending Effect in Turbulent Premixed Flames. Proceedings of the Combustion Institute, 36:1903–1910, 2017.

[86] H. Nobach and C. Tropea. A statistical method for transforming temporal correlation functions from one-point measurements into longitudinal spatial and spatio-temporal correlation functions. Experiments in Fluids, 53(6):1815–1821, 2012.

[87] P.L. O'Neill, D Nicolaides, D. R. Honnery, and Julio Soria. Autocorrelation Functions and the Determination of Integral Length with Reference to Experimental and Numerical Data. 15th Australasian Fluid Mechanics Conference, 1(December):1–4, 2004.

[88] Jeffrey R Osborne, Sarah A Ramji, Campbell D Carter, and Adam M Steinberg. Relationship between local reaction rate and flame structure in turbulent premixed flames from simultaneous 10 kHz TPIV, OH PLIF, and CH2O PLIF. Proceedings of the Combustion Institute.

[89] F. O'young and R.W. Bilger. Scalar gradient and related quantities in turbulent premixed flames. Combustion and Flame, 109(4):682–700, jun 1997.

[90] Phillip H. Paul and Habib N. Najm. Planar laser-induced fluorescence imaging of flame heat release rate. Symposium (International) on Combustion, 27(1):43–50, 1998.

[91] N. Peters. Laminar flamelet concepts in turbulent combustion. Symposium (International) on Combustion, 21(1):1231–1250, 1988.

[92] N. Peters. Length Scales in Laminar and Turbulent Flames. AIAA, A 92-16977:155–182, 1991.

[93] N. Peters. The turbulent burning velocity for large-scale and small-scale turbulence. Journal of Fluid Mechanics, 384:107–132, apr 1999.

[94] N. Peters. Turbulent combustion. 2000.

[95] Per Petersson and Marcus Alden. Laser based velocity measurement techniques (LDV and PIV), 2015.

[96] T. Poinsot, D. Veynante, and S. Candel. Diagrams of premixed turbulent combustion based on direct simulation. Symposium (International) on Combustion, 23(1):613–619, 1991.

[97] A.Y. Poludnenko and E.S. Oran. The interaction of high-speed turbulence with flames: Turbulent flame speed. Combustion and Flame, 158(2):301–326, feb 2011.

[98] Stephen B. Pope. Turbulent Flows. Cambridge University Press, 2000.

[99] Markus Raffel, Christian E Willert, Steve T Wereley, and Jürgen Kompenhans. Particle Image Velocimetry - A Practical Guide.

[100] Mattias Richter, Robert Collin, Jenny Nygren, Marcus Aldén, Leif Hildingsson, and Bengt Johansson. Studies of the Combustion Process with Simultaneous Formaldehyde and OH PLIF in a Direct-Injected HCCI Engine. JSME International Journal Series B, 48(4):701–707, 2005.

[101] M. Roder, T. Dreier, and C. Schulz. Simultaneous measurement of localized heat release with OH/CH 2O-LIF imaging and spatially integrated OH* chemiluminescence in turbulent swirl flames. Applied Physics B: Lasers and Optics, 107(3):611–617, 2012.

[102] M. Roder, T. Dreier, and C. Schulz. Simultaneous measurement of localized heat release with OH/CH 2O-LIF imaging and spatially integrated OH* chemiluminescence in turbulent swirl flames. Applied Physics B: Lasers and Optics, 107(3):611–617, 2012.

[103] Paul D. Ronney and Victor Yakhot. Flame Broadening Effects on Premixed Turbulent Flame Speed. Combustion Science and Technology, 86(1-6):31–43, nov 1992.

[104] Pentti Saarenrinne, Mika Piirto, and Hannu Eloranta. Experiences of turbulence measurement with PIV*. Measurement Science and Technology, 12(11):1904–1910, 2001.

[105] Ramanan Sankaran, Evatt R. Hawkes, Jacqueline H. Chen, Tianfeng Lu, and Chung K. Law. Structure of a spatially devloping turbulent lean methane-air Bunsen flame. Proceedings of the Combustion Institute, 31:1291–1298, 2007.

[106] Ramanan Sankaran, Evatt R. Hawkes, Chun Sang Yoo, and Jacqueline H. Chen. Response of flame thickness and propagation speed under intense turbulence in spatially developing lean premixed methane-air jet flames. Combustion and Flame, 162(9):3294–3306, 2015.

[107] Bruno Savard and Guillaume Blanquart. Broken Reaction Zone and Differential Diffusion Effects in a High Karlovitz n-C7H16 Premixed Turbulent Flame. Combustion and Flame, 162:2020–2033, 2015.

[108] Bruno Savard, Brock Bobbitt, and Guillaume Blanquart. Structure of a high Karlovitz n-C7H16 premixed turbulent flame. Proceedings of the Combustion Institute, 35:1377–1384, 2014.

[109] Stephen Alexander Schumaker. An Experimental Investigation of Reacting and Nonreacting Coaxial Jet Mixing in a Laboratory Rocket Engine by. PhD thesis, 2009.

[110] Sergei A. Filatyev. Burning Velocity Measurements in Turbulent Premixed Flames. PhD thesis, 2006.

[111] K. I. Shchelkin. NACA Tech. Technical report, 1947.

[112] I G Shepherd, R K Cheng, T Plessing, C Kortschik, N Peters, and Lawrence Berkeley. Premixed flame front structure in intense turbulence. Combustion Institute, 29:1833–1840, 2002.

[113] I.G. Shepherd and R.K. Cheng. The burning rate of premixed flames in moderate and intense turbulence. Combustion and Flame, 127(3):2066–2075, nov 2001.

[114] I.G. Shepherd and R.K. Cheng. The burning rate of premixed flames in moderate and intense turbulence. Combustion and Flame, 127(3):2066–2075, nov 2001.

[115] K. Singh. Engineering Mathematics. Tata McGraw-Hill, 6 edition, 2003.

[116] G.J. Smallwood, O. L. Gulder, D. R. Snelling, B. M. Deschamps, and I. Gokalp. Characterization of flame front surfaces in turbulent premixed methane-air combustion. Combustion and Flame, 101:461–470, 1995.

[117] Armin Soika, Friedrich Dinkelacker, and Alfred Leipertz. Measurement of the resolved flame structure of turbulent premixed flames with constant reynolds number and varied stoichiometry. Symposium (International) on Combustion, 27(1):785–792, 1998.

[118] Adrian Spencer and David Hollis. Correcting for sub-grid filtering effects in particle image velocimetry data. Measurement Science and Technology, 16(11):2323–2335, nov 2005.

[119] Adam M Steinberg. THE DYNAMICS OF TURBULENT PREMIXED FLAMES : MECHANISMS AND MODELS FOR TURBULENCE-FLAME by. PhD thesis, 2009.

[120] Adam M. Steinberg and James F. Driscoll. Straining and wrinkling processes during turbulence: premixed flame interaction measured using temporally resolved diagnostics. Combustion and Flame, 156(12):2285–2306, dec 2009.

[121] C. J. Sung, K. M. Yu, and C. K. Law. On the Geometry and Burning Intensity of Bunsen Flames. Combustion Science and Technology, 100(1-6):245–270, 1994.

[122] Parsa Tamadonfar and Ömer L. Gülder. Flame brush characteristics and burning velocities of premixed turbulent methane/air Bunsen flames. Combustion and Flame, 161(12):3154–3165, 2014.

[123] Parsa Tamadonfar and Ömer L Gülder. Effects of mixture composition and turbulence intensity on flame front structure and burning velocities of premixed turbulent hydrocarbon / air Bunsen flames. Combustion and Flame, 162(12):4417–4441, 2015.

[124] J.E. Temme, T.M. Wabel, A.W. Skiba, and J.F. Driscoll. Measurements of premixed turbulent combustion regimes of high reynolds number flames. In 53rd AIAA

Aerospace Sciences Meeting, 2015.

[125] Guido Troiani, Francesco Battista, and Francesco Picano. Turbulent consumption speed via local dilatation rate measurements in a premixed bunsen jet. Combustion and Flame, 160(10):2029–2037, 2013.

[126] P.J. Trunk, I. Boxx, C. Heeger, W. Meier, B. Böhm, and a. Dreizler. Premixed flame propagation in turbulent flow by means of stereoscopic PIV and dual-plane OHPLIF at sustained kHz repetition rates. Proceedings of the Combustion Institute, 34(2):3565–3572, jan 2013.

[127] TSI. Phase Doppler Particle Analyzer (PDPA)/ Laser Doppler Velocimeter (LDV) Operations Manual. 2001.

[128] M. S. Tsurikov and N.T. Clemens. The structure of dissipative scales in axisymmetric turbulent gas-phase jets (AIAA). 40th AIAA Aerospace Sciences Meeting & Exhibit, 2002.

[129] M J Tummers and D M Passchier. Spectral estimation using a variable window and the slotting technique with local normalization. Measurement Science and Technology, 7(11):1541–1546, 1996.

[130] Christina M. Vagelopoulos and Jonathan H. Frank. An experimental and numerical study on the adequacy of CH as a flame marker in premixed methane flames. Proceedings of the Combustion Institute, 30(1):241–249, jan 2005.

[131] H R E van Maanen, H. Nobach, L. H. Benedict, H R E Van Maanen, H. Nobach, and L. H. Benedict. Improved estimator for the slotted autocorrelation function of randomly sampled LDA data. Measurement Science and Technology, 10(1):L4—-L7, 1999.

[132] Denis Veynante and Luc Vervisch. Turbulent combustion modeling. Progress in Energy and Combustion Science, 28(3):193–266, 2002.

[133] Timothy M. Wabel, Aaron W. Skiba, and James F. Driscoll. Turbulent burning velocity measurements: Extended to extreme levels of turbulence. Proceedings of the Combustion Institute, 36:1801–1808, 2017.

[134] Timothy M. Wabel, Aaron W. Skiba, Jacob E. Temme, and James F. Driscoll. Measurements to determine the regimes of premixed flames in extreme turbulence. Proceedings of the Combustion Institute, 36:1809–1816, 2016.

[135] Haiou Wang, Evatt R. Hawkes, Bo Zhou, Jacqueline H. Chen, Zhongshan Li, and Marcus Alden. A comparison between direct numerical simulation and experiment of the turbulent burning velocity-related statistics in a turbulent methane-air premixed jet flame at high Karlovitz number. Proceedings of the Combustion Institute, 35:1–9, 2015.

[136] E. S.Wernersson and C. Tragardh. Measurements and analysis of high-intensity turbulent characteristics in a turbine-agitated tank. Experiments in Fluids, 28(6):532–545, 2000.

[137] F A Williams. Recent Advances in Theoretical Descriptions of Turbulent Diffusion Flames. In Turbulent Mixing in Nonreactive and Reactive Flows, pages 189–208. 1975.

[138] H. Wu and G.K. Patterson. Laser-Doppler measurements of turbulent-flow parameters in a stirred mixer. Chemical Engineering Science, 44:2207–2221, 1989.

[139] R. Yuan, J. Kariuki, A. Dowlut, R. Balachandran, and E. Mastorakos. Reaction zone visualization in swirling spray n-heptane flames. Proceedings of the Combustion Institute, 35(2):1649–1656, 2015.

[140] Frank T. C. Yuen and Ömer L. Gülder. Dynamics of Lean-Premixed Turbulent Combustion at High Turbulence Intensities. Combustion Science and Technology, 182(4-6):544–558, jun 2010.

[141] Frank T C Yuen and Omer L. Gulder. Turbulent premixed flame front dynamics and implications for limits of flamelet hypothesis. Proceedings of the Combustion Institute, 34:1393–1400, 2013.
213

[142] Frank T.C. Yuen and Ömer L. Gülder. Premixed turbulent flame front structure investigation by Rayleigh scattering in the thin reaction zone regime. Proceedings of the Combustion Institute, 32:1747–1754, 2009.

[143] Bo Zhou, Christian Brackmann, Qing Li, Zhenkan Wang, Per Petersson, Zhongshan Li, Marcus Aldén, and Xue-song Bai. Distributed reactions in highly turbulent premixed methane/air flames: Flame structure characterization. Combustion and Flame, 162:2937–2953, 2015.

[144] Bo Zhou, Christian Brackmann, Zhongshan Li, Marcus Alden, and Xue Song Bai. Simultaneous multi-species and temperature visualization of premixed flames in the distributed reaction zone regime. Proceedings of the Combustion Institute, 35(2):1409–1416, 2015.

[145] Bo Zhou, Qing Li, Yong He, Per Petersson, Zhongshan Li, Marcus Aldén, and Xue Song Bai. Visualization of multi-regime turbulent combustion in swirlstabilized lean premixed flames. Combustion and Flame, 162(7):2954–2958, 2015.